

Development of a bio-inspired *in silico-in vitro*
platform: towards personalised healthcare through
optimisation of a bone-marrow mimicry bioreactor

A thesis submitted to Imperial College London for the degree of Doctor of Philosophy

By

Mark Colin Allenby

Biological Systems Engineering Laboratory, Centre for Process Systems Engineering,

Department of Chemical Engineering, Imperial College London, United Kingdom.

July 2017

Acknowledgements

This thesis represents a body of research taken place between October 2013 and September 2017 and captures periods of personal struggle, success, and growth in my life. This internal growth was both dictated by and manifested in experiences with the wonderful people surrounding an often arrogant, vain, often confused, and very naïve young researcher. These brilliant people deserve more thanks than this brief page could convey.

Foremost, this thesis belongs to my supervisors: Sakis and Nicki. Both of whom provided immense support, patience, and assurance throughout such a stressful and uncertain period of self-examination. Sakis always told me I would end up hating him by the end of the PhD, and I am happy this hasn't proven true. Both Sakis and Nicki's guidance has rarely been wrong, and although my impatience often brought us to arguments, their expert mentorship in knowing when to pressure, steer, or let my curiosity drift to new explorations has allowed for this PhD to not only be an enjoyable experience at so many moments, but also allow me to call it my own. Thank you for your mentorship, your passion, but most influentially: your open-mindedness. If I did it again I would still choose both of you as my mentors. Please just return revisions faster, Sakis!

I would not be here without Claudia Menichini, whose continuous, every-day support and care over more than 5 years in London encouraged me to explore life when I would otherwise spend all of my time in the lab and brought so many happy adventures to this memory. You shine light in the dark. I would like to thank the close friends I found in London whose everyday interactions at coffees, lunches, dinners, beers, parties, and holidays never failed to restore my happiness. I am extremely thankful for my friends: Franky, Diego, Marie, Manuela, Nick, Saulius, and Assen among others. Conversations at the bar, at 5am on a bus, or in Tyrone Park in Colombia helped me learn more about myself than any length of time at the bench did.

I would like to thank my colleagues in my laboratory, BSEL. Primarily Susana, as we have shared years of labwork, projects, examinations, presentations, and moments of scrutiny together; you are one of the most kind, helpful people I know. I would like to thank the masters and undergraduate student's I have mentored: especially José and Joana among others, for coping with my often unrelenting demands, and supporting our work with your excitement and willingness to learn new things. Acknowledging my support system at BSEL could not end without mentioning: Joana S, Maria Papas, Ruth, Mauricio, Marias F and R, David, Lia, Spyros, Magic Mike, Asma, and many others, for maintaining a continuous stream of jokes, gossip, and karaoke in the lab.

Most importantly, I would like to thank my parents, Greg and Patricia, and my sister, Kate, whose support has been unwavering for 28 years of my life now, who have completely shaped me into a person for 18 years, and who have supported me to move out away from Ohio and into the world for the last 10. I was always your lazy child whose head was distracted and in the clouds, and I will do my best not to change. I am blessed to have such a inspiring family.

Mark

Declarations

Originality

I hereby declare that this is my own work and any published and unpublished work used here has been cited in the text and in the list of references in the bibliography section at the end of this thesis.

Copyright

The copyright of this thesis rests with the author and is made available under a Creative Commons Attribution Non-Commercial No Derivatives license. Researchers are free to copy, distribute, or transmit the thesis on the contribution that they attribute it, that they do not use it for commercial purposes and that they do not alter, transform or build upon it. For any reuse or redistribution, researchers must make clear to others the license terms of this work.

Mark Colin Allenby

List of Publications

Thesis publications: primary-author peer-reviewed full-length publications submitted or in print

[1] **Allenby, M.C.**, Tahlawi, A., Morais, J.F.R., Li, K., Panoskaltsis, N., Mantalaris, A. ‘Ceramic hollow fibre constructs for continuous perfusion and cell harvest from 3D hematopoietic organoids.’ *Submitted to Stem Cells International*.

[2] **Allenby, M.C.**, Misener, R., Panoskaltsis, N. Mantalaris, A. 2017, ‘A quantitative three-dimensional image analysis tool for maximal acquisition of spatial heterogeneity data.’ *Tissue Engineering Part C: Methods*, vol. 23, no. 2, pp. 108-117.

[3] **Allenby, M.C.**, Tahlawi, A., Santos, S.B., Panoskaltsis, N., Mantalaris, A. ‘An *ex vivo* model of multi-lineal human umbilical cord erythropoiesis in a 3D perfusion hollow fibre bioreactor.’ *In preparation*.

[4] **Allenby, M.C.**, Santos, S.B., Mantalaris, A. ‘Differentiation of pluripotent stem cells towards red blood cell production.’ *Submitted to Gene & Cell Therapy, CRC Press*.

Thesis conference publications : primary-author peer-reviewed submitted or in print

[1] **Allenby, M.C.**, Tahlawi, A. Santos, S.B., Misener. R., Hwang, Y.S., Panoskaltsis, N. Mantalaris, A. ‘Development of a hematopoietic microenvironment for the production of red blood cells (RBCs) in a novel 3D hollow fibre bioreactor.’ *Tissue Engineering Part A*, vol. 21, pp. S15-S16. Presented at: Tissue Engineering and Regenerative Medicine International Society World Congress, 2015, Boston, USA.

[2] **Allenby, M.C.**, Tahlawi, A. Santos, S.B., Misener. R., Hwang, Y.S., Panoskaltsis, N. Mantalaris, A. ‘Development of an *ex vivo* bone marrow mimicry microenvironment in a novel 3D hollow fibre bioreactor.’ *Experimental Hematology*, vol. 43, pp. S51. Presented at: International Society for Experimental Hematology, 2015, Kyoto, Japan.

[3] **Allenby, M.C.**, Tahlawi, A. Santos, S.B., Misener. R., Panoskaltsis, N. Mantalaris, A. ‘Spatiotemporal mapping of erythroid, stromal, and osteogenic niche formation to support physiologic red cell production in a three-dimensional hollow fibre perfusion bioreactor.’ *Blood*, vol. 128, no. 22, pp. 3885. Presented at: American Society of Hematology, 2016, San Diego, USA.

[4] **Allenby, M.C.**, Tahlawi, A. Santos, S.B., Panoskaltsis, N. Mantalaris, A. ‘Quantitative imaging of *ex vivo* niche formation within a hollow fibre bioreactor for physiological *in vitro* human red cell production.’ *European Cells and Materials Journal*, preprint online. Presented at: Tissue and Cell Engineering Society, 2017, Manchester, UK.

Non-thesis publications: peer-reviewed full-length publications in print

- [5] Allison, B.J., **Allenby, M.C.**, Bryant, S.S., Min, J.E. Hieromnimon, M., Joyner, P.M. 'Antibacterial activity of fractions from three Chumash medical plant extracts and in vitro inhibition of the enzyme enoyl reductase by the flavonoid jaceosidin.' *Natural Product Research*, vol. 31, no. 6, pp. 707-12.
- [6] Shah, U.V., **Allenby, M.C.**, Williams, D.R., Heng, J.Y.Y. 'Crystallization of proteins at ultralow supersaturations using novel three-dimensional nanotemplates.' *Crystal Growth & Design*, vol. 12, no. 4, pp. 1772-7.

Non-thesis conference publications: peer-reviewed in print

- [5] dos Santos, S.B., **Allenby, M.C.**, Mantalaris, A., Panoskaltis, N. 'Early erythroid development is enhanced with hypoxia and terminal maturation with normoxia in a 3D ex vivo physiologic erythropoiesis model.' *Blood*, vol. 128, no. 22, pp. 2453. Presented at: ASH 2016, San Diego, USA.
- [6] Totti, S., **Allenby, M.C.**, dos Santos, S.B. Velliou, E. 'On the evaluation of long term ex vivo cultivation of pancreatic cancer in a 3D scaffolding system.' Presented at: TERMIS-EU 2016 in Upsala, Sweden.
- [7] dos Santos, S.B., **Allenby, M.C.**, Mantalaris, A. Panoskaltis, N. 'Effect of oxygen and 3D microenvironment on physiologic erythropoiesis.' *Blood*, vol. 124, no. 23, pp. 3600. Presented at: ASH 2015, Miami, USA.
- [8] dos Santos, S.B., **Allenby, M.C.**, Panoskaltis, N., Mantalaris, A. 'In vitro physiologic erythropoiesis in a 3D bone marrow biomimicry.' *Tissue Engineering: Part A*, vol. 21, pp. S228. Presented at: TERMIS 2015, Boston, USA.
- [9] Allison, B.J., Hester, V., Fleming, M., **Allenby, M.C.**, Bryant, S., Joyner, P.M. 'Investigation of in vitro bioactivity of extracts and secondary metabolites of Chumash native American medical plants.' *Planta Medica*, no. 81, vol. 11, pp. PM2.
- [10] Misener, R. **Allenby, M.C.**, Gari, M.F., Rende, M., Velliou, E., Panoskaltis, N., Pistikopoulos, S., Mantalaris, A., 'Optimisation under uncertainty for a bioreactor that produces red cells.' Presented at: TERMIS 2014.
- [11] **Allenby, M.C.**, Louie, K., Masaki, M., Lucas, T., Bertozzi, A.L., 'A point process model for stimulating gang violence.' Presented at: the Joint Mathematics Meeting 2010.

This publication list was last updated 10/2017.

Abstract

Human red blood cell production, or erythropoiesis, occurs within bone marrow. Living animal and human cadaver models have demonstrated the marrow production of red blood cells is a spatially-complex process, where cells replicate, mature, and migrate between distinct niches defined by biochemical nutrient access, supportive neighboring cells, and environmental structure.

Unfortunately, current research in understanding normal and abnormal human production of blood takes place in petri dishes and t-flasks as 2D liquid suspension cultures, neglecting the role of the marrow environment for blood production. The culture of blood on marrow-mimetic 3D biomaterials has been used as a laboratory model of physiological blood production, but lacks characterization. In this work, a 3D biomaterial platform is developed and to capture the *in vivo* blood production process and manufacture red blood cells from human umbilical cord blood.

First ceramic hollow fibres were designed and tested to be incorporated and perfused in a 3D porous scaffold bioreactor to mimic marrow structure, provide a better expansion of cell numbers, a better diffusion of nutrients, and allow for the continuous, non-invasive harvest of small cells in comparison to static, unperfused biomaterials. Quantitative 3D image analysis tools were developed to spatially assess bioreactor distributions and associations of and between different cell types. Using these tools, the bioreactor distribution of red blood cell production were characterized within niches in collaboration with supportive, non-blood cell types and designed miniaturised, parallelised mini-bioreactors to further explore bioreactor capabilities.

This thesis presents a hollow fibre bioreactor able to produce blood cells alongside supportive cells at 1,000-fold higher cell densities with 10-fold fewer supplemented factor than flask cultures, without serum, with one cell source, and continuously harvest enucleate red blood cell product to provide a physiologically-relevant model for cell expansion protocols.

Table of Contents

| | |
|---|-----|
| Acknowledgements | ii |
| Declarations | iii |
| List of Publications | iv |
| Abstract..... | vi |
| Table of Contents | vii |
| Table of Tables..... | ix |
| Table of Figures..... | x |
| 1. Introduction | 1 |
| 2. Review of in vivo and ex vivo models of the human marrow environment | 4 |
| 2.1. Bone Marrow Structure | 4 |
| 2.1.1. Physical Properties | 4 |
| 2.1.2. Chemical Factors..... | 6 |
| 2.1.3. Extracellular matrix proteins | 6 |
| 2.2. Hematopoiesis | 7 |
| 2.2.1. Hematopoietic progenitor hierarchy | 7 |
| 2.2.2. Hematopoietic niche environment..... | 8 |
| 2.2.3. Hematopoietic Growth Factors | 9 |
| 2.3. Erythropoiesis | 10 |
| 2.3.1. Erythroid hierarchy..... | 10 |
| 2.3.2. Erythroid niche environment | 11 |
| 2.3.3. Erythroid Growth Factors..... | 12 |
| 2.3.4. Transendothelial migration | 13 |
| 2.4. Erythropoiesis Ex Vivo | 14 |
| 2.4.1. 2D: Human erythroid massive amplification (HEMA) cultures | 14 |
| 2.4.2. 3D: Mimicking physiological hemato-erythroid niches..... | 18 |
| 2.5. Analysing Erythropoiesis in 3D..... | 25 |
| 2.5.1. Methods of 3D imaging..... | 25 |
| 2.5.2. In vivo 3D image analyses..... | 26 |
| 2.5.3. Ex vivo 3D image analyses | 27 |
| 3. Aims and Objectives..... | 29 |
| 4. Incorporation of hollow fibres able to perfuse nutrients and harvest cells within a 3D porous scaffold | 32 |

| | | |
|--------|---|-----|
| 4.2. | Introduction..... | 33 |
| 4.3. | Methodology | 35 |
| 4.4. | Results | 41 |
| 4.4.1. | Phase-inversion bore fluid controls ceramic fibre micropore structure | 41 |
| 4.4.2. | Cross-flow filtration enriches enucleate fractions | 43 |
| 4.4.3. | Dead-end filtration filters large numbers of enucleate red cells | 47 |
| 4.4.4. | Continuous fibre perfusion increases nutrient exchange and cell proliferation in a 3D porous scaffold..... | 48 |
| 4.5. | Discussion | 52 |
| 4.6. | Conclusion | 54 |
| 5. | Development of an image analysis tool to spatially quantify 3D cellular distribution and association. | 55 |
| 5.2. | Introduction..... | 56 |
| 5.3. | Methodology | 59 |
| 5.4. | Results | 68 |
| 5.4.1. | Enhanced Utilization of Imaged Data..... | 68 |
| 5.4.2. | Comparison of 3D Distance Analysis against Manual Scoring | 69 |
| 5.4.3. | Random Sampling Accuracy | 71 |
| 5.4.4. | 3D Distribution with Regional Asymmetries | 71 |
| 5.5. | Discussion | 73 |
| 5.6. | Conclusion | 75 |
| 6. | Characterization of structured, niche-like HSC and erythroid microenvironments within the marrow-mimetic bioreactor | 76 |
| 6.2. | Introduction..... | 77 |
| 6.3. | Methodology | 79 |
| 6.4. | Results | 89 |
| 6.4.1. | A perfused HFR established CBMNC hypoxic gradients | 89 |
| 6.4.2. | Organization of an interactive hematopoietic environment..... | 96 |
| 6.4.3. | Production of a supportive stromal environment | 101 |
| 6.4.4. | Genesis and harvest of red cells | 108 |
| 6.4.5. | Increasing cell density enhances erythropoiesis..... | 113 |
| 6.5. | Discussion | 117 |
| 6.6. | Conclusion | 118 |
| 7. | Development of high-cell-density mini-bioreactors toward producing blood..... | 120 |
| 7.2. | Introduction..... | 121 |

| | | |
|--------|---|-------|
| 7.3. | Methodology | 123 |
| 7.4. | Results | 131 |
| 7.4.1. | Mathematical design of mini-bioreactor (BR) fabrication | 131 |
| 7.4.2. | Mini-BR culture of hUCB MNCs forms large, confluent cell clusters in 3D | 132 |
| 7.4.3. | Exclusion of hollow fibre improves phenotypic RBC egress..... | 136 |
| 7.5. | Discussion..... | 140 |
| 7.6. | Conclusion | 141 |
| 8. | Conclusions | 142 |
| 9. | Future Work..... | 147 |
| 9.2. | Identify and exploit biomarkers in proliferative hUCB donations | 147 |
| 9.3. | Further develop the a mini-BR for dense hUCB MNC expansion and RBC egress | 148 |
| 9.4. | Qualitatively assess RBC product quality | 149 |
| 9.5. | Quantify and exploit endogenous hematopoietic support provided by accessory cells | 149 |
| 9.6. | Model and treat abnormal hematopoiesis ex vivo | 150 |
| 10. | References | xii |
| 11. | Figure reprint permission | xxiii |

Table of Tables

| | | |
|-----------|---|-------|
| Table 1: | List of abbreviations | xi |
| Table 2: | In vivo HSPC niche factors | 10 |
| Table 3: | In vivo erythroid niche (erythroblastic island) factors..... | 14 |
| Table 4: | Current HEMA liquid suspension culture state-of-the-art. | 17 |
| Table 5: | Selected examples of marrow-mimicry biomaterial culture systems. | 25 |
| Table 6: | Primary antibody stains implemented for confocal detection in Figure 16C and Figure 17. . | 39 |
| Table 7: | Filtrate collected within 6 hours of cross-flow and dead-end filtration for Water and DMSO fibre types. | 45 |
| Table 8: | Confocal 3D immunofluorescent microscopy primary antibody staining protocol. | 60 |
| Table 9: | Mathematical parameters used..... | 61 |
| Table 10: | Comparison of calculating 3D cell density distributions..... | 70 |
| Table 11: | List of primary and secondary antibodies and counterstains implemented in confocal microscopy analysis..... | 84 |
| Table 12: | List of threshold DAPI to stain co-localisation distances and internal image replicates for each analysed stain. | 84 |
| Table 13: | Mathematical parameters for krogh cylinder BR model. | 124 |
| Table 14: | Summary of successful design mini-BR medium profiles implemented up to 04/2017. | 129 |
| Table 15: | Summary of figure reprint permissions..... | xxiii |

Table of Figures

| | |
|--|-----|
| Figure 1: Environmental factors influencing marrow blood production. | 2 |
| Figure 2: Human bone marrow structure as understood from three-dimensional imaging. | 5 |
| Figure 3: A subset of antigen markers that denote the hematopoietic lineage..... | 8 |
| Figure 4: A subset of growth factors (cytokines) which promote hematopoietic cell expansion. | 10 |
| Figure 5: Antigen expression during the process of HSC-derived erythropoiesis. | 11 |
| Figure 6: An illustration of selected growth and transcription factors within erythropoiesis..... | 13 |
| Figure 7: Example outputs of major advancements in HEMA culture. | 15 |
| Figure 8: Examples of marrow-mimicking 3D biomaterial cultures..... | 23 |
| Figure 9: Quantitative 3D confocal imaging analysis state-of-the-art..... | 28 |
| Figure 10: Schematics for hollow fibre cell filtration experiments. | 37 |
| Figure 11: Fibre fabrication parameters producing structural differences in porosity and pore size. .. | 42 |
| Figure 12: Ceramic hollow fibre structure. | 43 |
| Figure 13: Cross-flow filtration efficiency. | 44 |
| Figure 14: Cross-flow cell filtrate cell types..... | 46 |
| Figure 15: Dead-end filtration efficiency. | 48 |
| Figure 16: Long-term 3D perfusion hollow fibre bioreactor culture..... | 50 |
| Figure 17: Expression of hematopoietic, osteogenic, and endothelial markers within the scaffold region of day 21 HFBR cross-sections..... | 51 |
| Figure 18: Imaging regions of the 3D culture device. | 58 |
| Figure 19: A visualization of the 2D distance cell density analysis. | 63 |
| Figure 20: 2D tissue distance cell density analysis. | 65 |
| Figure 21: A visualization of the 3D cell clustering density analysis in confocal images..... | 67 |
| Figure 22: Convex hulls illustrating the cell clustering 50 μ m neighborhood estimation..... | 68 |
| Figure 23: Comparison of algorithm efficiency in comparison with manual scoring. | 70 |
| Figure 24: Assessment of methods and applications for calculating 3D cell clustering density. | 72 |
| Figure 25: Manual measurement and scoring of cell-to-HFR surface distances..... | 86 |
| Figure 26: HFR mechanical structure and function. | 90 |
| Figure 27: HFR culture medium replenishment, cell viability, and metabolism. | 91 |
| Figure 28: A hollow fibre bioreactor (HFR) structures hUCB MNC distribution. | 92 |
| Figure 29: HFR hUCB culture DAPI and ATP distributions. | 93 |
| Figure 30: Distribution of cellular hypoxia. | 95 |
| Figure 31: Distribution statistics of HIF-1 α , Pimo, and Ki-67 co-localised MNCs. | 96 |
| Figure 32: Hematopoietic organization and interaction. | 99 |
| Figure 33: Distribution statistics of CD45, CD34, C-KIT, and VCAM-1 at days 0, 14, and 28. | 100 |
| Figure 34: Stromal proliferation generates an erythroid-interactive mesenchymal-osteogenic matrix. | 103 |
| Figure 35: Distribution statistics of Stro-1, OSx, and OPN..... | 105 |
| Figure 36: Distribution statistics of SDF-1, collagen type 1 (Col-1), laminin type 2 (Lam-2), and fibronectin (Fibr). | 106 |
| Figure 37: Differentiation and harvest of enucleated red cells. | 109 |
| Figure 38: Distribution statistics of erythroid markers: enucleated CD235a and CD71 (eCD235a, eCD71), nucleated CD235a, CD71, EPO-R, CD45, and enucleate cell membranes (Enucleate)..... | 112 |
| Figure 39: Increased cell density enhances RBC production. | 114 |
| Figure 40: Comparisons of HFR inoculum densities..... | 116 |

| | |
|--|-----|
| Figure 41: Mathematical design and fabrication of mini-BRs. | 127 |
| Figure 42: Mini-BR culture formed dense cellular clusters in 3D. | 134 |
| Figure 43: Comparison of mini-BR cultures with and without hollow fibres. | 138 |

Table 1: List of abbreviations

| Abbreviation | Full | First pg. |
|----------------|---|-----------|
| RBC | Red blood cell | 1 |
| HEMA | Human Erythroid Massive Amplification | 2 |
| ECM | Extracellular matrix | 4 |
| HS(P)C | Hematopoietic stem (and progenitor) cell; with varied prefixes (e.g. Long term HSC: LT-HSC) | 7 |
| GF | Growth factor; with varied prefixes (e.g. fibroblast growth factor: FGF) | 7 |
| BMP | Bone morphogenic proteins | 7 |
| MPP | Multi-potent progenitors | 7 |
| SCF | Stem cell factor | 9 |
| IL | Interleukens, with varied suffix numbers | 9 |
| CSF | Colony stimulating factors, with varied prefixes (e.g. granulocyte: G-CSF) | 9 |
| OPN | Osteopontin | 9 |
| SDF-1 | Stromal derived factor-1 (a.k.a. CXCL-12) | 9 |
| VLA-4 | Very late antigen-4 | 9 |
| VCAM-1 | Vascular cell adhesion molecule-1 | 9 |
| CD | Cluster of differentiation | 11 |
| CFU/BFU | Colony/burst forming unit, with suffixes (erythroid: CFU-E) | 11/12 |
| EPO | Erythropoietin | 12 |
| MSC | Mesenchymal stem cell | 19 |
| PU | Polyurethane | 20 |
| hUCB/CB | Human umbilical cord blood / cord blood | 20 |
| hBM/mBM | Human bone marrow / murine bone marrow | 20 |
| hPB | Human peripheral blood | 20 |
| MNC/CBMNC | Mononuclear cell / cord blood mononuclear cell | 20 |
| CT | Computerised tomography | 26 |
| HF/H(F)BR/BR | Hollow fibre / hollow fibre bioreactor / bioreactor | 32 |
| DMSO | Dimethyl sulfoxide | 35 |
| MIP | Mercury intrusion porosimetry | 35 |
| CFP | Capillary flow porometry | 35 |
| SEM | Scanning electron microscopy | 35 |
| PFA | Polyfluoro-alkoxy | 36 |
| TIPS | Thermally induced phase separation | 36 |
| PBS | Phosphate buffered saline | 36 |
| UV | Ultraviolet (light) | 36 |
| IMDM | Iscove's Modified Dulbecco's Medium | 37 |
| FBS | Fetal bovine serum | 37 |
| CSB | Cell staining buffer | 38 |
| CSMB | Cell staining microscopy buffer | 38 |
| DAPI | 4',6-diamidino-2-phenylindole | 39 |
| OSx | Osterix | 48 |
| AF | Alexa Fluor | 57 |
| Pimo | Pimondiazole (Hypoxypore Inc.) | 91 |
| HIF-1 α | Hypoxia inducible factor-1 α | 91 |

1. Introduction

Bio-mimetic cell culture platforms investigate normal biological processes, model diseases, screen drugs and treatments, and manufacture cell therapies to provide cost-efficient and physiologically-relevant solutions in clinical trials and stem cell bio-manufacturing. Major pharmaceutical R&D has declined by 80-fold since 1950 due to high clinical trial expenses, which account for approximately £700 million annually, or 63% of the total development cost for new pharmaceuticals (Paul et al. 2010; Scannell et al. 2012). The development of a single successful therapeutic requires more than a decade of research, and costs approximately \$2.6 billion (Peng et al. 2016). Most drug candidates fail in clinical trials due to low efficacy and adverse effects, failures whose cost could be mitigated by screening therapeutic hopefuls on bio-mimetic platforms faithfully modelling the complex bodily *in vivo* environment (Lane et al. 2014).

Red blood cell production represents a bodily process rich in therapeutic potential if able to be mimicked *ex vivo*. Hospitals throughout the United Kingdom require 8000 units of peripheral blood per day at a cost of £2.25 billion per annum, with \$225.42 per typical blood unit in the USA or £125 in the UK (Blood & Transplant 2010; Blood & Transplant 2013; Whitaker & Henry 2012). This demand can only be satiated by blood donation, as 92 million units of whole donor blood are globally collected yearly but still 3.3% of hospitals delay surgery due to a lack of blood and 10.3% of hospitals experience at least one day per year where blood needs cannot be met (Timmins & Nielsen 2009; Whitaker & Henry 2012). These shortages are further exacerbated by patients with rare blood types and/or diseases (e.g. sickle cell disease), who must undergo regular transfusions at higher expense due to low availability: between \$1150 to \$3025 per unit rare blood in the USA, and up to £25,000 in the UK (Whitaker & Henry 2012; Blood & Transplant 2010; Timmins & Nielsen 2009). Red blood cell (RBC) manufacture *in vitro* has been studied to fulfil blood donation shortages, but remains infeasible due to high costs and might be made more efficient by implementing physiological features of *in vivo* blood production.

Current methods of *ex vivo* blood production methods vary greatly from *in vivo* hematopoiesis, limiting clinical relevance. Current blood culture typically takes place in liquid suspension, or 2D

culture, where a purified stem cell source is expanded at low densities within a vat of liquid supplemented with expensive growth factors more than 10-100 fold more concentrated than what is present in the human body. This has been defined as a human erythroid massive amplification (HEMA) culture, and has been optimised to produce very large quantities of immature red blood cells (reticulocytes) per stem cell input (order of 10^6 reticulocytes produced per stem cell), with well characterized phenotype, oxygen carrying capacity, and deformability, and have been transfused into a human patient to undergo final functional red blood cell maturation (Rousseau et al. 2014). These advances in HEMA culture, and the recent red blood cell production from immortalised erythroblast cell lines (Trakarnsanga et al. 2017), have removed the burden of cost from the stem cell starting material and shifted it towards medium, growth factor, and platform costs, which remain 40-fold greater than clinical costs by conservative estimates (Timmins & Nielsen 2009).

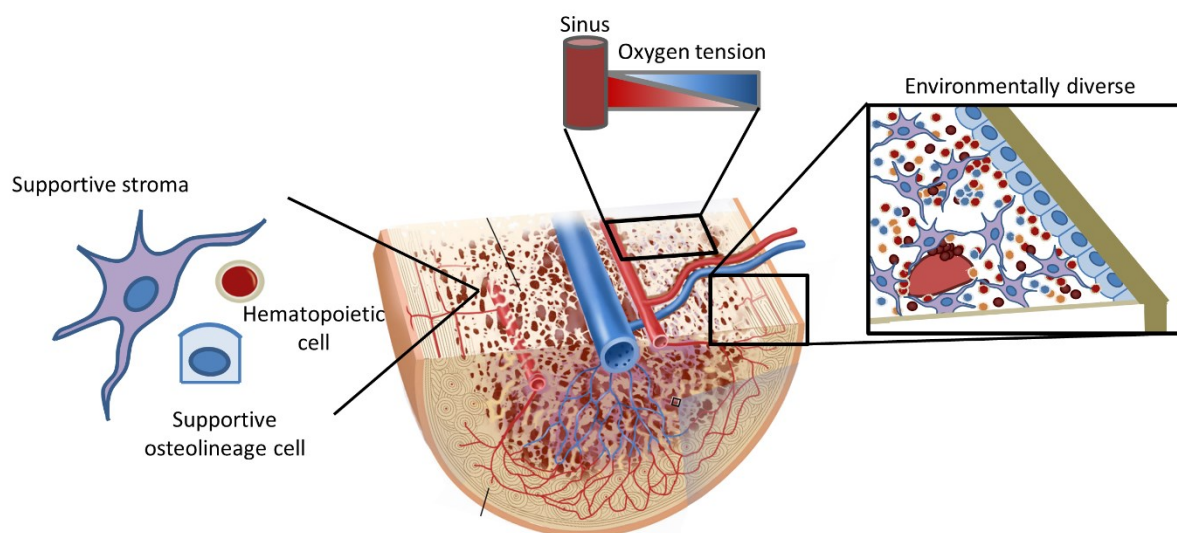


Figure 1: Environmental factors influencing marrow blood production.

(Centre) Cellular distribution within the marrow is influenced by (top) sinus vasculature: the source of nutrients and oxygen which diffuse into the marrow spaces to create environments of different oxygen tensions, nutrients, and metabolites for unique cell types. (Left) Hematopoietic cells exist in interactive niches comprised of stromal and osteolineage cells which form (right) an environmentally diverse environment amongst the marrow structure of vasculature and bone. Centre image is adapted from (U.S. National Cancer Institute 2017).

Many blood production shortcomings could be remedied by culture platforms which better mimic aspects of *in vivo* hematopoiesis, as illustrated in Figure 1. Current attempts to mimic marrow structure *in vitro* use 3D cell-scaffoldings and mimic marrow function by imparting continuous

perfusion as an approximation of engineered “vasculature” to permit 10-100x higher cultured cell densities or using lower concentrations of expensive growth factors (Mantalaris et al. 1998) than unperfused systems due an enhanced diffusion of nutrients reducing the volume and cost of the culture medium required for blood production. While 3D perfusion cultures limit invasive culture handling, they are much more complex systems than 2D suspension cultures to characterize, model, and optimize: unable to be continuously monitored, with more complex considerations for fluid dynamics, nutrient diffusion-reaction, and the impact of cell-cell and cell-environment interactions (e.g. adherence, paracrine stimulation, migration) (Allenby et al. 2017). A critical limitation of 3D cell cultures is their inability to easily and continuously harvest cell therapy product: where 2D platforms can easily extract cells by extracting a fraction of medium, 3D cultures must be invasively aspirated for cells, requiring culture termination. In summary, bio-mimetic hematopoietic culture must be improved by: developing biomaterials which can further enhance platform nutrient exchange and continuously harvest cell therapy products, developing analytical tools to better characterize the interaction of cells within their environments, and designing culture platforms which can optimize scheduling of exogenous nutrient supplementation alongside paracrine and juxtacrine cell stimulation.

2. Review of *in vivo* and *ex vivo* models of the human marrow environment

Hematopoiesis is defined as the renewal of hematopoietic stem cells and their differentiation into lymphoid and myeloid components of blood. The ability to up-regulate hematopoietic cell survival and production of blood is dependent its surrounding microenvironment, or hematopoietic niche, within the adult human bone marrow. Different niches have been implicated in the growth of specific hematopoietic stem, lymphoid, and myeloid, and therein, erythroid subpopulations, as each niche allows the appropriate nutrients and physiochemical factors to reach its cells, including secreted and membrane-bound cytokines, stromal and neighboring cell types, and a diverse extracellular matrix (ECM) (Klein 1995; Kfoury & Scadden 2015). This range of environmental niche conditions is necessary for hematopoietic, and erythropoietic, homeostasis: the maintenance of a blood cell production steady-state which allows for continuous basal production and for stressed production in times of demand, and is the blueprint for three-dimensional hematopoietic cultures *ex vivo*.

The majority of hematopoietic niche understanding has been derived from non-human animal models. As the hematopoietic niche is spatially defined and must be observed unseparated from its native environment, human experiments are impractical to perform. While animal models provide limited clinical insight due to confounding deviations from human erythropoiesis at phenotypic and genetic levels (An et al. 2014), they have become surrogates to a non-existent human model. In addition, the lack of a human model makes generating an *ex vivo* bone marrow-mimetic culture platform all the more necessary to better understand and treat normal and abnormal human hematopoiesis.

2.1. Bone Marrow Structure

2.1.1. Physical Properties

Adult hematopoiesis exists within the marrow: the trabecular region of long bones. These trabeculae are 75-90% porous with pore diameters of 300-900 μm on average (Lee et al. 2012; Duchey & Healy 2015), whose mechanical properties, biochemical concentrations, and cellular composition is typically segregated into distinct zones or “niches” as illustrated in Figure 2. Within the trabecular bone a range of material stiffnesses exist between the outer endosteal bone surface, which encases the marrow (>35 kPa), perivascular regions (2-10 kPa), and vascular spaces (0.3 kPa) (Nelson & Roy 2016). The

marrow is well-vascularised by one large central sinus, 1700 venous sinusoids, 101 arterial capillaries, and 30 arterioles per cm² of cross section surface where cell nutrients are perfused and diffuse into the marrow trabeculae structure (Bartl & Frisch 2012; Schoutens 1993).

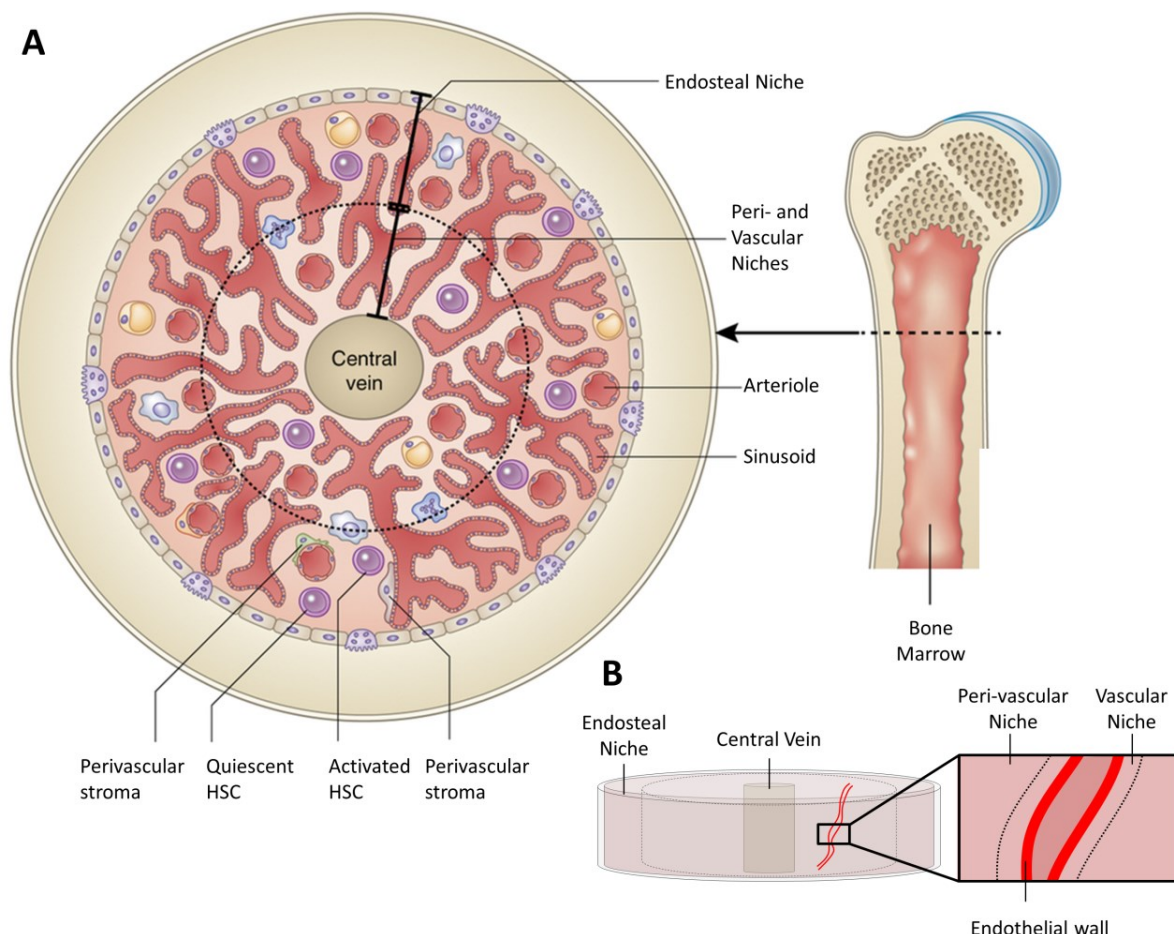


Figure 2: Human bone marrow structure as understood from three-dimensional imaging.

(A) A cross section of adult human marrow within long bones containing a large central vein surrounded by a vascular network of arterioles and sinusoids and encased within cancellous bone. These architectural components make three well-defined environments for hematopoietic cell growth: the endosteal niche, near cancellous bone, and peri-vascular and vascular niches, which are detailed in (B) as vascular niches within a few cell distances from any given vein's endothelial wall, or peri-vascular otherwise. Adapted from (Mendelson & Frenette 2014).

Maturing blood cells (e.g. RBCs, platelets) exit the marrow into peripheral circulation through transendothelial migration. As these cells are deformable, they can squeeze through tight junctions between endothelial cells comprising marrow vasculature to enter bodily circulation. This process of cellular trafficking in and out of the marrow predominately takes place through “leaky” sinusoids with endothelial pores near 2-3 μm which cells can compress through (Itkin et al. 2016). The process of

murine marrow egress provides a sinusoidal wall shear stress of 150 mPa, which may contribute towards mature RBC and platelet remodelling towards functional maturation (Leblond et al. 1971).

2.1.2. Chemical Factors

The marrow concentration of chemical nutrients and metabolites is dependent on two metrics: their distance from vasculature, acting as the source of nutrients and outlet of metabolites; and their distance from other cell types which consume nearby nutrients and produce metabolites. Oxygen tension is an important determinant of proliferation and differentiation of hematopoietic cells. Despite being well-vascularised, *in vivo* murine marrow oxygen tension remains quite low, as intravascular oxygen is delivered at a tension of only 2.7% O₂, making average extravascular oxygen 1.8% O₂. Recent studies have demonstrated higher oxygen climates reside near arteriolar endosteal marrow regions, and decrease with distance towards a more hypoxic sinusoidal region during hematopoietic homeostasis, while, during periods of murine marrow remodelling after radiation and chemotherapy, the oxygen gradient between endosteal and perisinusoidal regions was abolished due to low marrow cellularity (Spencer et al. 2014).

It has long been established hematopoietic progenitors proliferate at increased capacities *in vitro* in low oxygen environments (<5% O₂), while higher efficiencies of RBC production occur at high oxygen environments (20% O₂) (Chow et al. 2001). This positive effect of oxygen on late erythropoiesis could explain traditional examinations of higher numbers of erythroid colonies nearer higher marrow oxygen climates, and greater numbers of dormant marrow stem cells in lower oxygen climates (Weiss 1984; Cui et al. 1996; Frassoni et al. 1982). Although cellular consumption of other common nutrients, e.g. glucose, glutamine, and the removal of metabolite waste, e.g. lactate, ammonia have been considered in previous models of physiological hematopoiesis, oxygen has been identified as the limiting factor for viable cell growth, and during healthy hematopoiesis other nutrients would follow similar but less critical reaction-diffusion gradients (Chow et al. 2001a; Misener et al. 2014).

2.1.3. Extracellular matrix proteins

The trabeculae and vascular marrow structure is coated with ECM proteins native to the marrow environment which include various subtypes of collagen (I, III, IV), fibronectin, and laminin, amongst others. (Nilsson et al. 1998). HSCs have been shown to bind to fibronectin and immature myeloid and

erythroid cells have been shown to bind to both fibronectin and collagen type 1, with fibronectin theorized to prevent erythroblast apoptosis and assist in nuclear expulsion (Nilsson et al. 1998; Williams et al. 1991; Eshghi et al. 2007; Ji et al. 2011). Collagen type 1, produced by osteoblasts, is primarily distributed in the marrow-peripheral endosteal niche. Fibronectin, produced by fibroblasts, remains well distributed in both endosteal and perivascular niches within the central marrow. Laminin, produced by fibroblasts and endothelial cells, are predominately expressed near and on marrow vessels, both sinuses and arteries (Nilsson et al. 1998). ECM proteins do not only act as sites for cell anchorage and biomechanical forces, but also can bind and present growth factors (GFs) to neighbouring cells, especially collagens and fibronectin which can bind fibroblast- (FGFs), hepatocyte- (HGF), vascular endothelial- (VEGFs), transforming- (TGFs) growth factors, and bone morphogenic proteins (BMPs) (Gattazzo et al. 2014).

2.2. Hematopoiesis

2.2.1. Hematopoietic progenitor hierarchy

Blood production occurs by cell replication, where the symmetric division of identical cells is known as proliferation or self-renewal, and the asymmetrical division of a new progeny from a parent cell is known as differentiation, forming a family tree, or hierarchy, of “immature” hematopoietic stem cells (HSCs) able to populate all mature blood cell types, as proposed in Figure 3. HSCs exist as three successive maturations: long-term renewing HSCs (LT-HSCs) which are thought to differentiate into short-term renewing HSCs (ST-HSCs) followed by multipotent progenitors (MPPs) (Cabrita et al. 2003; Reya et al. 2001). In theory, LT-HSCs can self-renew for the entire lifetime of the organism whereas ST-HSCs have more limited renewal, only able to restore hematopoiesis in a lethally irradiated mouse for up to four months. Both ST-HSCs and their MPP progeny undergo cell division much more frequently than LT-HSC precursors and continue differentiation to progenitors constrained to repopulate lymphoid and myeloid lineages.

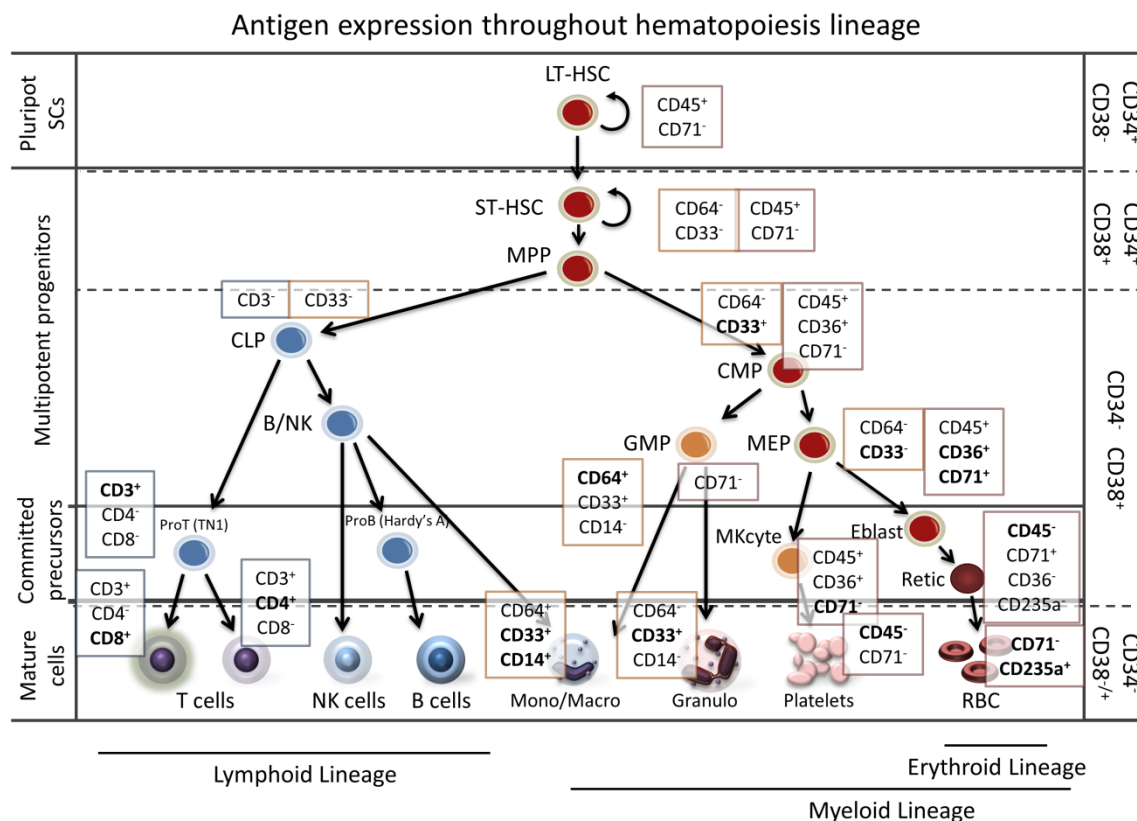


Figure 3: A subset of antigen markers that denote the hematopoietic lineage. (Handel et al. 2010; Doulatov et al. 2012; Kondo et al. 2003)

2.2.2. Hematopoietic niche environment

The factors which drive *in vivo* haematopoiesis occur at subcellular (chemical, metabolomics; protein, proteomic) and intercellular (niche cell-cell adherence) scales. The exposure of a cell to each stimulating factor is dependent on its niche environment within the marrow. The most studied hematopoietic environment is the HSPC niche, summarised in Table 2. The classical structure of hematopoiesis places the most immature HSCs in endosteal niches far from vasculature where areas of hypoxia were thought to occur near bone cells (osteoblasts) known to secrete factors maintaining quiescence (Schofield 1978; Parmar et al. 2007; Allen & Henshaw 2001). During cell differentiation toward mature blood types, cells sequentially organize themselves in areas closer to marrow sinusoids in vascular and peri-vascular niches containing higher oxygen tensions, mesenchymal stromal cell types, and stimulatory factors produced from other organs (EPO) (Yokoyama et al. 2003; Mohandas & Prenant 1978). Once mature, these sinus-adjacent positions would be advantageous for marrow egress into peripheral circulation.

Recently, this traditional view has been challenged as LT- and ST-HSCs have been found in different marrow microenvironments, and it is unclear whether the cellular kinetics separating fast-dividing ST-HSCs from largely quiescent LT-HSCs are a result of their environment, or their genetic programming (Nombela-Arrieta et al. 2013). The majority of HSCs (85%) within murine marrow were within 10 μm of a venous sinusoids and distant from endosteal arterioles (Acar et al. 2015), while more quiescent “LT-HSC” populations distribute near less permeable arterial vessels (Itkin et al. 2016; Kunisaki et al. 2013). The more permeable or “leaky” veous sinusoids, as well as cell-adhesive proteins or molecules, control the majority of cellular trafficking out of and into the marrow.

2.2.3. Hematopoietic Growth Factors

Soluble growth factors, e.g. cytokines and migratory chemokines, can direct HSC proliferation or quiescence, promote erythroid differentiation, and influence interactions of many other surrounding niche cell neighbours, a subset of which are represented in Figure 4. Near the top of the hematopoietic hierarchy, stem cell factor (SCF) regulates HSC proliferation through binding to the C-KIT receptor and stimulating HSCs to enter and proceed through the cell cycle by inhibition of p27 and upregulation of Cyclin E (Tamir et al. 2000). Many pro-inflammatory cytokines, including members of the interleukin (IL) and hematopoietic colony stimulating factor (CSF) families, also act as mitogenic factors and differentiation agents of hematopoietic stem cells toward a myeloid lineage. Endosteal agents, such as osteopontin (OPN), promote HSC quiescence in the marrow for long-term hematopoietic repopulation during times of stress. Nearly all these HSC-acting factors are secreted by neighbouring fibroblasts and osteolineage stromal cells that, when upregulated in the murine marrow, increase the frequency of LT-HSCs, and when depleted, cause a loss of cellularity and an immunophenotypic reduction in hematopoietic and erythroid progenitors (Kfoury & Scadden 2015). Neighboring niche cells, both stromal and hematopoietic, also express chemoattractant cytokines such as stromal derived factor 1 (SDF-1; CXCL-12) and very late antigen-4 (VLA-4) as well as adhesive motifs including vascular cell adhesion molecule-1 (VCAM-1) amongst others, to recruit, migrate, and mediate adhesion of HSCs and other hematopoietic cells.

Cytokine stimulation throughout hematopoiesis lineage

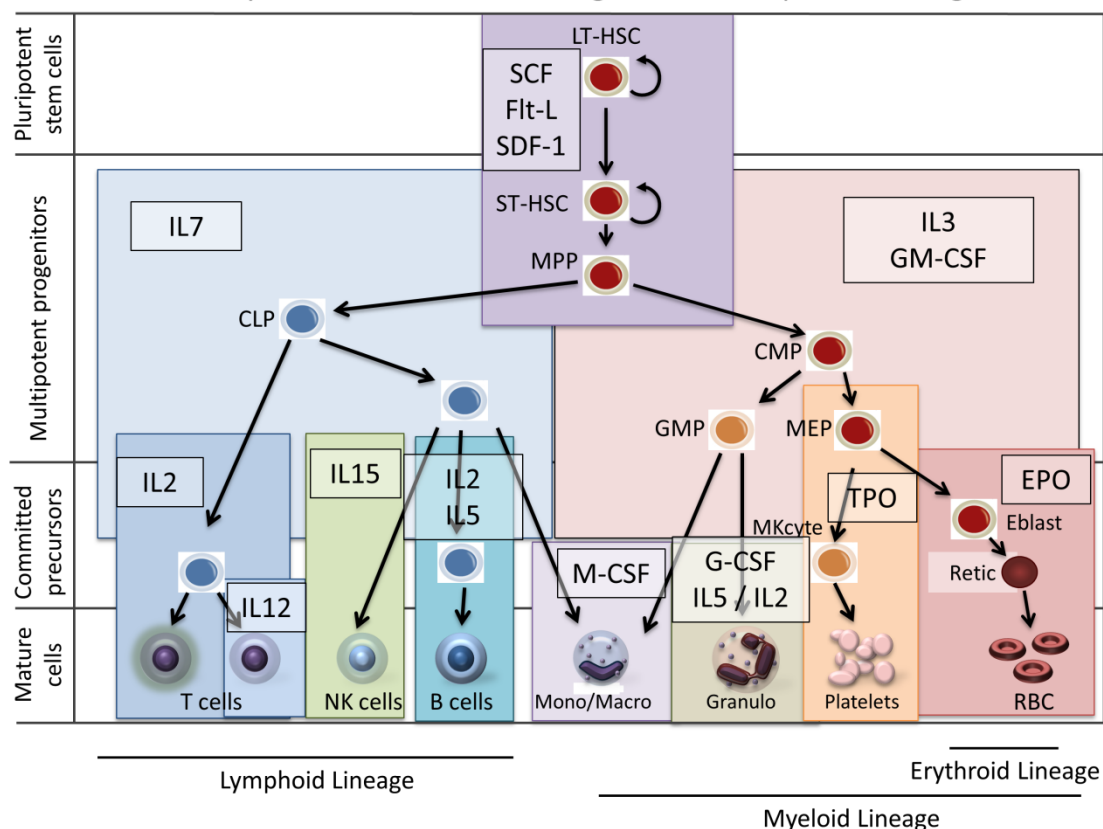


Figure 4: A subset of growth factors (cytokines) which promote hematopoietic cell expansion.

Table 2: *In vivo* HSPC niche factors

| Primary Cells | Accessory Cells | Structural cues | Humoral cues | Biochemical Cues |
|------------------------|--|---|--|--|
| LT-HSCs, ST-HSCs, MPPs | Mesenchymal stromal cells, osteoprogenitors, osteoblasts, stroma and endothelial cells | Matrix stiffness collagen-1 (ECM protein) VCAM-1, VLA-4 (cell adhesion markers) | SCF (proliferation) OPN (quiescence) SDF-1 (migration) CSFs, ILs (differentiation) | Oxygen: Lower for LT-HSCs, higher for ST-HSCs and MPPs |

2.3. Erythropoiesis

2.3.1. Erythroid hierarchy

Hematopoietic MPP cells can differentiate into immature blood precursor cells confined to produce a single cell type, such as erythroblasts, and mature into terminal cell types (erythrocytes) which exit the marrow and enter blood circulation. Erythropoiesis defines the sub-process of red blood cell production within myelopoiesis, within hematopoiesis. Hematopoietic cell types have been well characterized by the expression (+) or the absence (-) of specific antigen “markers” on their surface,

many of which provide functionality to cells such as adhesive motifs (VCAM-1), for protein uptake and transport (C-KIT, CD71), or the induction of differentiation (EPO-R). Most hematopoietic mononuclear cells are characterized by the expression of cluster of differentiation (CD)45, and are CD45⁺ (Migliaccio et al. 2012). Many other antigen surface markers exist and are specifically used to characterize stages of erythropoiesis from HSCs to RBCs, such as CD34, CD38, CD45, CD36, CD71, and CD235a (Rappold et al. 1997; Bertrand et al. 2007) and are outlined in Figure 5. *Ex vivo* erythropoietic cultures traditionally focus on the expansion capacity of erythroid progenitors (Doulatov et al. 2012; Cabrita et al. 2003). However, recent studies have emphasized the benefit of simultaneously maintaining HSC pools to continuously produce red cells in long-term cultures (Mortera-Blanco et al. 2011; Serafini et al. 2007).

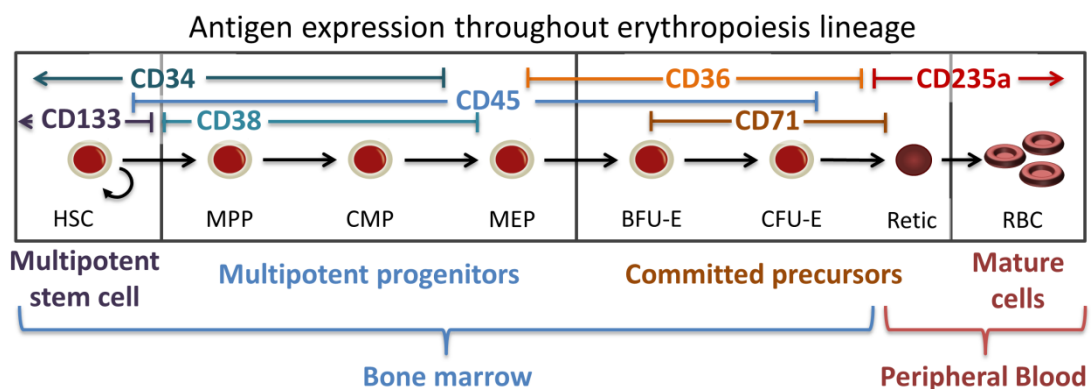


Figure 5: Antigen expression during the process of HSC-derived erythropoiesis.
(Chesney et al. 2011)

2.3.2. Erythroid niche environment

Upon commitment to myelo-erythroid lineages, HSCs differentiate through several colony-forming-unit (CFU) stages, named for their high proliferative capacity that form hematopoietic colonies when plated in methylcellulose assays *ex vivo*. These differentiation stages amplify replicate cell numbers, with granulocytic colonies appearing near bone surfaces and erythroid colonies appearing perivascular, with more mature erythroid colonies approaching closer and closer to the sinusoidal wall, as noticed in animal stereologic studies (Weiss 1984; Yokoyama et al. 2003; Frassoni et al. 1982). Erythroid colonies contain erythroblasts, cells which have committed to the erythroid fate with proliferative potential until nuclear expulsion at a late erythroblast stage (normoblast) whereupon the remaining enucleate reticulocyte must undergo membrane remodelling as an essential step to resemble

a mature erythrocyte (Weiss 1965). These erythroid maturation steps include physical interaction with a macrophage, and many erythroid cells typically assemble into an “erythroblastic island” surrounding a central macrophage, which supplies specific factors and adhesive signals to promote enucleation as outlined below (Manwani & Bieker 2008). Erythroid colonies are not found in direct contact with the wall of the sinus, as platelet-producing megakaryocytes are, but exist 15-40 μm (1 to 4 cell-distances) away from rat marrow sinuses (Mohandas & Prenant 1978). The unique distribution of LT-HSC, ST-HSC, MPP, and erythroid niches impact their exposure to biochemical factors (nutrients, metabolites, growth factors) as well as their niche-neighboring cells which is summarized in Table 3.

2.3.3. Erythroid Growth Factors

Erythropoietin (EPO), the essential growth factor for erythropoiesis, is almost completely produced from the kidney during oxygen demand, and rises from basal serum concentrations of 15 IU/mL to stress concentrations up to 10,000 IU/mL (Jelkmann 2011). EPO induces an erythroid lineage bias and rescues cells at the colony forming unit-erythroid (CFU-E) stage from apoptosis (Grover et al. 2014) by interacting with EPO-receptors (EPO-Rs) present on BFU-E and CFU-E cell surfaces (Misener et al. 2014). EPO is provided to marrow erythroblasts via the central sinus, and may influence how more mature erythroblastic islands distribute closer to marrow sinuses for egress (Yokoyama et al. 2003; Weiss 1984). Recent studies have indicated EPO can also be secreted by murine marrow osteoblasts, if in much lower concentrations (Singbrant et al. 2011; Shiozawa et al. 2010). In these mature erythroblastic islands, characteristic macrophage-erythroblast interactions may augment the response of maturing erythroblasts to EPO (Tordjman et al. 2001; Muta et al. 1995), while also providing iron, erythroid and angiogenic factors (VEGF-A), and presenting adhesive motifs (fibronectin, VCAM-1) (Manwani & Bieker 2008; Tordjman et al. 2001). The presence of adhesive motifs on macrophages promotes erythroblast nuclear expulsion to become reticulocytes, whose nuclei are then phagocytosed by contacting macrophages (Pallotta et al. 2011). A summary of growth factors in erythropoiesis are presented in Figure 6.

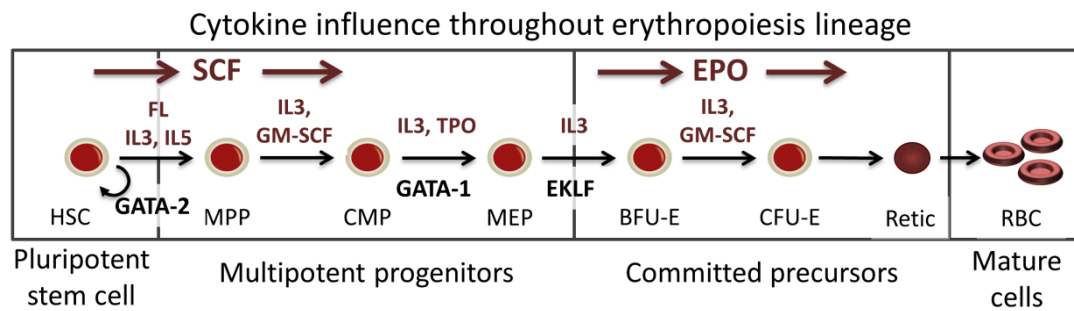


Figure 6: An illustration of selected growth and transcription factors within erythropoiesis.

2.3.4. Transendothelial migration

Once enucleated, reticulocytes cease production of adherent surface markers and depart from erythroid islands and travel to sinuses for marrow egress toward bodily circulation. Although enucleated, the reticulocyte is not considered a functionally mature erythrocyte (red blood cell) and cannot bind oxygen or undergo deformation similar to erythrocytes. Final erythrocyte maturation is a time-dependent process of membrane remodelling, and occurs while reticulocytes are in bodily circulation and is aided during the stressful process of egress, and has corresponded to a decreasing phenotypic expression of CD71 (Liu et al. 2010; Malleret et al. 2013). During marrow egress, reticulocytes must deform through the tight endothelial wall gaps of marrow sinuses, typically 2-3 μm , although sub-1 μm transendothelial migration has been witnessed in murine models (Waugh & Sassi 1986; Silber et al. 1978; Lichtman 1978). This egress aids in shedding excess reticulocyte membrane proteins which, with time, leaves a functional and deformable erythrocyte (Johnstone 1992).

Physiological haematopoiesis and therein, erythropoiesis, is spatially reliant on both its (1) environmental distribution near vasculature or bone surfaces and also its (2) local organization near surrounding niche cells. Where vasculature provides a site for nutrient and EPO supply, metabolite and erythrocyte removal, and mechanical stimulation, neighbouring niche cells provide paracrine supportive factors and physical interaction through adhesive motifs. These neighboring niche cells can include macrophages, megakaryocytes, mesenchymal, and osteoblastic cells that secrete supportive growth factors and produce adhesive extracellular matrix (ECM) proteins (Boulais & Frenette 2015; Kunisaki et al. 2013; Zhu & Emerson 2002; Kfoury & Scadden 2015; Ehninger & Trumpp 2011). While detailed information regarding the *in vivo* distributions and niche interactions of the hemato-erythroid

environment is only available for animal models, many culture platforms have implemented bio-mimetic 3D geometries and co-cultures to study *ex vivo* human hematopoiesis.

Table 3: *In vivo* erythroid niche (erythroblastic island) factors.

| Primary Cells | Accessory Cells | Structural cues | Humoral cues | Biochemical Cues |
|--|---|---|--|---|
| Erythroblasts (multiple stages), reticulocytes: CD36, CD71, CD44, CD235a | Macrophages (erythroid island): CD68, CD169 | Fibronectin (ECM protein) VCAM-1 (cell adhesion) Compression (egress) | EPO (from sinuses) VEGF (accessory cells) | Iron, increasing concentrations of oxygen with maturity |

2.4. Erythropoiesis *Ex Vivo*

Current methods in recapitulating hematopoiesis and, specifically, erythropoiesis in the laboratory have two goals: either to efficiently produce cell therapies (e.g. red blood cells in this review) or to create bio-mimicry platforms to study the progression of normal and abnormal hematopoiesis. The pursuit of an *ex vivo* method to produce RBCs at clinically relevant numbers and costs have taken place almost entirely in liquid suspension culture systems, which along with monolayer cultures, are classified as two-dimensional (2D). State of the art 2D cultures have created 10^6 enucleated red cells per CD34⁺ hematopoietic stem cell (Timmins et al. 2011) which have been further transplanted into a human subject to terminally and functionally mature into adult RBCs (Giarratana et al. 2011). The design of physiologically relevant platforms to recreate and study mechanisms *ex vivo* theorized to occur *in vivo* (as human models are non-existent) frequently implement 3D culture geometries, either as co-culture, encapsulates, or porous scaffoldings. These 3D platforms may provide bio-mimetic attributes to reduce 2D RBC production cost which remain conservatively 40-fold higher than donation costs (Rousseau et al. 2014).

2.4.1. 2D: Human erythroid massive amplification (HEMA) cultures

The production of human RBCs from CD34⁺ hematopoietic stem cells was first accomplished through the use of murine or human stromal layers, which allowed for high expansion rates (10^6 -fold increase in cell number) and enucleate purity (95% of expanded cells) which exhibited all the functionality of mature RBCs: biconcave morphology, deformability, haemoglobin expression (adult globin for adult peripheral blood or marrow CD34⁺ sources, fetal globin for umbilical cord CD34⁺

sources), phenotype (CD235a⁺CD71⁻), and oxygenation uptake, and could be functionally transfused into mice with normal lifespans (~120 days) (Giarratana et al. 2005). This first 21-day HEMA culture relied on 3 steps: (1) 8 days of cell proliferation and erythroid differentiation in serum-free medium supplemented with SCF, IL-3, and EPO, (2) 3 days of co-culture only with EPO either on a murine MS-5 stromal cell line or human mesenchymal cells, (3) 10 days of co-culture without exogenous factors on a stromal layer as above.

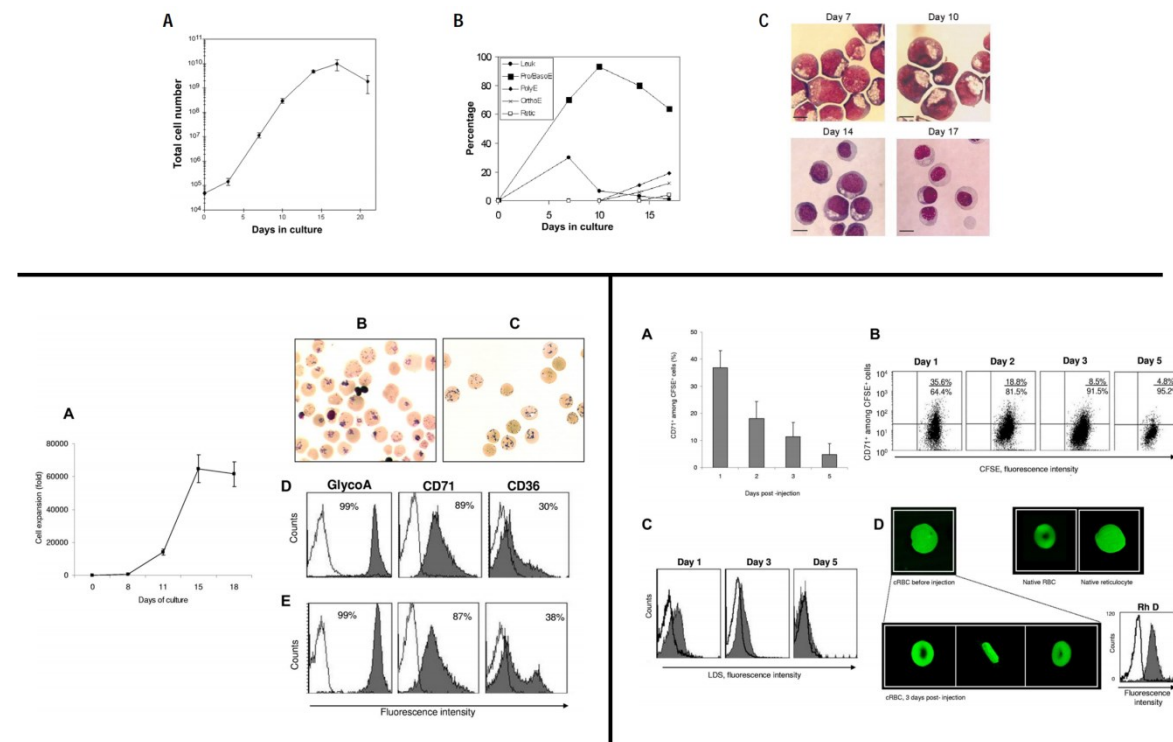


Figure 7: Example outputs of major advancements in HEMA culture.

(top) The massive expansion of nucleated erythroblasts in 2002, whereupon stromal feeder layers were required for enucleation. (bottom, left) The massive expansion of enucleated reticulocytes using stroma-free and serum-free conditions and (bottom, right) maturation into biconcave RBCs after successful transfusion into a human patient (Neildez-Nguyen et al. 2002; Giarratana et al. 2011).

While the use of xenogenic (murine) stromal line co-culture limited the clinical applications of RBC product from these early HEMA cultures, direct stromal contact was required for erythroblast enucleation as physical separation from the murine stromal layer by a transwell plate abrogated enucleation, and prior stroma-free erythroid production failed to fully mature *ex vivo* (Neildez-Nguyen et al. 2002). Allogeneic hUCB and hBM-derived stromal cells or hUCB-derived macrophages had subsequently been used to replace xenogenic murine stromal layers for erythroblast enucleation in HEMA co-culture (Fujimi et al. 2008; Baek et al. 2008).

This second major advancement of this protocol was made in 2006 by successfully replacing the co-culture system with serum (Miharada et al. 2006) with a four-passage culture protocol across 20 days. While enucleation efficiency was significantly less than when using co-culture (77.5% versus >90%), the supplementation of VEGF and IGF-II early in culture enhanced expansion and enucleation. The third major advancement came by transfusing autologous cultured reticulocytes into a human patient, which were expanded from peripheral blood HSCs from the same patient. To accomplish this, 10^{10} enucleated cells were produced from 10^6 CD34⁺ cells over 18 days using a 13 litre liquid suspension culture platform and were injected and found to mature from a pre-injection reticulocyte stage into a mature red blood cell *in vivo*, with normal RBC lifespan (Giarratana et al. 2011). Others improved RBC yield by increasing proliferation at the HSC expansion step with different steroid combinations, and could increase culture duration to 50 days and scaled-up culture size to a 1 litre stirred tank bioreactor, providing 10^9 red cells/initial HSC and 90% enucleation efficiency (von Lindern et al. 1999; Leberbauer et al. 2005; Timmins et al. 2011). The major advancements toward HSC-derived RBC production are summarised in Figure 7 and in Table 4.

Since 2011, advances in RBC production have focused on the use of induced pluripotent stem cells (iPSCs) as a source. Recently, an immortalised adult human erythroid line has been developed that produces normal adult human red cells with adult, not fetal or embryonic, haemoglobin for oxygen transport, and without terminal differentiation defects. The ability to produce RBCs from immortalised progenitors allows for the unlimited cultivation of source material towards expansion when necessary. Although this study was limited to low enucleation efficiency (30%), produced reticulocytes were able to bind oxygen and deform similar to native erythrocytes (Trakarnsanga et al. 2017).

Liquid suspension, or “2D”, culture systems have provided sufficient reticulocyte production per HSC input, and have proven the clinical utility of these reticulocyte products as transfusable, functional cells for human use. Even moreso from the successful generation of reticulocyte-producing immortalised cell lines, the clinical limitation of *ex vivo* red blood cell production is no longer production efficiency per HSC input, but is now bioprocess cost (medium, cytokine requirements), scalability (volume and RBC quantity needed), and product quality (producing immature reticulocytes versus functional erythrocytes). Liquid suspension cultures are currently limited to densities of $2\text{-}5 \cdot 10^6$

cells/mL, should that limit be lifted to 10^7 cells/mL, estimates predict the HEMA production of one unit of RBCs ($2 \cdot 10^{12}$ cells) would cost \$8330, 40-fold higher than clinical costs for normal RBC units (\$225.42) and rare RBC units (approx. \$1000-3000) (Timmins & Nielsen 2009; Rousseau et al. 2014; Misener et al. 2014), and the majority of these HEMA production costs can be attributed to culture medium and cytokine supplementation. Bio-mimetic, 3D culture systems may alleviate these constraints by implementing: supportive co-culture cells as surrogates for expensive cytokine supplementation, higher cell densities to promote cell-cell adhesion for enucleation, and complex culture platform topologies: with a variety of niche environments and biomechanical forces to support physiological culture homeostasis alongside terminal cell maturation.

Table 4: Current HEMA liquid suspension culture state-of-the-art.

Pink is 4-step method from (Miharada et al. 2006) which is similar to and was adapted for (Giarratana et al. 2011). Grey is 1-step method from (Timmins et al. 2011)

| Culture Stages | Cell Input | Cell Output | Growth Factors | Biochemicals |
|--|-------------------------------------|--|---|--|
| Passage I [6 days] | 10^4 /mL 95% CD34 ⁺ | 9×10^6 /mL 65% CD235a ⁺ 0% enucleate 167.5-fold | 10^{-3} M hydrocortisone 50 ng/mL SCF 10 ng/mL IL-3 6 IU/mL EPO 10 ng/mL VEGF 250 ng/mL IGF-2 | 20 ng/mL α -tocopherol 4 ng/mL linoleic acid 200 ng/mL cholesterol 2 ng/mL sodium selenite 200 ng/mL transferrin 10 μ g/mL insulin 10 μ M ethanolamine 0.1 mM 2-mercaptoethanol 5% Plasmanate cutter In StemSpan H3000 |
| Passage II [4 days] | 3×10^4 /mL From I | 2.5×10^7 /mL 86% CD235a ⁺ 2% enucleate 86.4-fold | 50 ng/mL SCF 6 IU/mL EPO | Same as above |
| Passage III [6 days] | 5×10^4 /mL From II | 5×10^7 /mL 87% CD235a ⁺ 14% enucleate 49.6-fold | 50 ng/mL SCF 2 IU/mL EPO | Same as above |
| Passage IV Enucleation [4 days] | 5×10^5 /mL From III | 5×10^5 /mL 94% CD235a ⁺ 78% enucleate 1-fold | None | 14.57 mg/m D-mannitol 0.14 mg/mL adenine 0.94 mg/mL disodium hydrogenphosphate dodecahydrate 1 μ M mifepristone 0.5% Plasmanate cutter In StemSpan H3000 |
| Direct HSC to Retic. differentiation [21 to 33 days] | 10^4 /mL CD34 ⁺ | 10^5 /mL cells 95% CD235a ⁺ 92% enucleate $2.25 \cdot 10^8$ -fold expansion | 10^{-3} M HC 100 ng/mL SCF 5 ng/mL IL-3 3 IU/mL EPO | 1% BSA 120 μ g/mL donor-derived transferrin 10 μ g/mL insulin 900 ng/ml ferrous sulphate |

| | | | | |
|--|--|--------------------------|--|------------------------------------|
| | | 1 litre bioreactor scale | | 90 ng/mL ferric nitrate In IMDM |
|--|--|--------------------------|--|------------------------------------|

2.4.2. 3D: Mimicking physiological hemato-erythroid niches

HEMA liquid suspension expansion of HSCs, the differentiation of HSCs into erythroid cells, and the maturation of functional RBCs have shown proof of clinical principle for *ex vivo* RBC production and transfusion. However these liquid suspension cultures are limited by low cell density requirements, and therefore, steep costs exist from the quantity of medium and growth factors needed for producing clinically-useful numbers of RBCs. These costs could be salvaged implementing cultures with lower cytokine requirements, higher cell densities, and implementing materials for the continuous harvest of cell products. 3D cultures can implement these attributes through the use of co-culture models, biomaterial scaffolds, and dynamic culture platforms.

2.4.2.1. Co-culture models

The original marrow mimicry predates 2D liquid suspension culture and was developed from murine bone marrow aspirate, whose cells autonomously formed a co-culture as an adherent monolayer of stromal cells and collagen nursing hematopoietic cells when cultured in 30% serum across multiple months (Dexter et al. 1977). Attempts to adapt these foundational long-term “Dexter” cultures to a humanised model were unsuccessful, despite advances in short-term cell output when supplementing various CSF and IL growth factors, and human progenitors exponentially decreased with time and never maintained the expansion found in murine HSCs (Coutinho et al. 1990; Bronzino 1999).

The co-culture of accessory cell types (e.g. stroma, other hematopoietic cells) with HSCs over 7 or 14 days allow for HSC proliferation (3.2-fold) and a more consistent output with regard to donor-to-donor variability, whereas HSC culture within identical conditions (serum, cytokines) in the absence of stroma led to culture decline, spontaneous HSC differentiation, and variable phenotypic and clonogenic cell output (Koller et al. 1996; Koller et al. 1995; Breems et al. 1998). The proliferative contribution of HSC-neighbouring cells (e.g. stroma) was found to be critically dependent on physical contact through adhesion molecules (e.g. VCAM-1), which alters HSC migratory behaviour and gene expression profile (Alakel et al. 2009), and also could be otherwise effected through the range of secretory molecules and factors mesenchymal stromal cells produce (Wagner et al. 2007). A detailed

analysis of the impact and distribution of HSCs during a 7-day MSC co-culture provided three distinct MSC-related micro-environments for HSCs: (1) non-MSC-adherent HSCs, (2) HSCs adherent to MSC feeder surface, (3) HSCs that had migrated beneath the MSC feeder layer. HSCs adherent to the MSC feeder surface were more proliferative, while more immature (CD34⁺CD38⁻) HSCs migrated below the feeder surface where they maintained their more immature phenotype long-term (Jing et al. 2010). HSC-MSC interactions are most commonly studied through soluble factors (SCF, SDF-1) and adhesion molecules (VCAM-1); and while chemoattractant SDF-1 does not mediate HSC-MSC adhesion *ex vivo*, the stromal-secreted factor plays essential roles in HSC migration *in vitro*, and retains HSCs within the marrow *in vivo* (Anthony & Link 2014).

Co-culture has long been essential for complete erythropoiesis *ex vivo*. As discussed above, the *in vitro* final maturation and enucleation of erythroblasts toward becoming reticulocytes and thereafter, mature erythrocytes was critically dependent on an adherent stromal layer (Neildez-Nguyen et al. 2002). Although many RBC-production studies implement stromal layers, the correct *in vivo* analogy would be an *ex vivo* erythroblast enucleation culture with macrophages. Whereas erythroblast-macrophages adherent interactions which lead to nuclear expulsion are thought to result from VLA-4 or phosphatidylserine (PS) erythroblast adhesion molecules binding to VCAM-1, CD51, or CD61 on macrophages (Manwani & Bieker 2008), recent *in vitro* co-culture found the essential factor was none of these, but rather was heparin-binding protein erythroblast macrophage protein (Emp) on erythroblasts, which limited erythroblast differentiation, expansion, and enucleation when blocked (Fujimi et al. 2008; Hanspal & Hanspal 1994). The liquid suspension culture of late erythroblasts at high densities (10⁷ MNCs/mL) to form aggregate cell clusters enhanced enucleation efficiencies, demonstrating that mechanical adherence alone was sufficient to promote enucleation (Lee et al. 2014). However, this effect could be recapitulated through the use of 3D biomaterial substrates, coated with adhesive proteins, and cultured with cells at high density.

2.4.2.2. Biomaterial scaffolds

Although co-culture platforms provide a niche bio-mimicry of neighboring cells towards hematopoietic proliferation, maintenance of stemness, erythroid differentiation, or erythroblast

enucleation; their dependence on physical monolayer-contact limits scalability, requires low cell densities to maintain culture viability, and their use of two separate cell sources limits clinical utility.

A wide variety of materials, surface modifications, cellular input, and medium considerations have been investigated for the *ex vivo* expansion of hematopoietic cells as analogues to the marrow microenvironment. Briefly, the most common materials include natural polymers (e.g. gels such as alginate and ECM proteins) which better recapitulate adhesive motifs and mechanical forces provided *in vivo*, or synthetic polymers (e.g. polyurethane (PU), amongst many others), which have been approved for clinical use without xenogeneic complications, and ceramics have also been used (e.g. calcium, glass, hydroxyapatite). These materials must be formed by a variety of methods into useful structural templates, including monolayers, hydrogels, microcarriers, encapsulates, and porous or fibrous matrices; where influential properties include porosity, pore size, and interconnectedness. The surfaces of these architected materials may be modified chemically (e.g. aminated, made hydrophilic, etc.) and coated with adhesive peptides (e.g. RGD) and proteins (e.g. collagen type-1, fibronectin, laminin) to improve cell adhesion and function (Nelson & Roy 2016; Choi et al. 2015).

Human hematopoietic cell sources are typically derived from bone marrow (hBM), umbilical cord blood (hUCB), and stem-cell-mobilised peripheral blood (hPB). While hBM is difficult to donate due to collection by invasive aspiration, hUCB and hPB are popular as *in vitro* HSC sources, with hUCB-derived HSCs providing better expansion rates than hPB. These cell sources are isolated typically for mononuclear cells (MNCs) by ficoll-paque, and can be further refined for only progenitor populations based on phenotypic separation (CD38, CD34, CD133), typically by immunomagnetic bead separation prior to culture inoculation. The co-culture of hematopoietic cells with stromal cells, or of specific hematopoietic subsets, provides a more bio-mimetic environment, but incorporating cells from multiple sources limits clinical application due to xenogeneic or allogeneic immunoresponses (Sharma et al. 2012; Ventura Ferreira et al. 2012; Ventura Ferreira et al. 2016).

The initial 3D scaffold cultures provided an alternative to murine Dexter cultures by creating perfused plug-flow-reactors of collagen microspheres which expanded murine bone marrow cells nearly 20-fold across 120 days of viable culture (Wang & Wu 1992). Recently after, a 2D perfusion culture of human mononuclear bone marrow cells autonomously formed a stromal layer while expanding total

cell output 6-fold and CFU-GM content 22-fold after 16 days (Palsson et al. 1993). Thereafter, the collagen microsphere bioreactor of Wang and Wu was implemented for 6.5-week culture of human bone marrow MNCs additionally supplemented with low-doses (0.2 IU/mL) of EPO in addition to basal SCF, IL-3, GM-CSF, and IGF-1, and populated the pores of the microspheres with intimate cell-cell contact and a high cell density. In comparison with identically stimulated Dexter cultures, whose primary hematopoietic output consisted of granulocytes instead of erythrocytes (90% vs. 6%), nonadherent cells within the bioreactor consisted of 43% erythrocytes, 43% granulocytes, 8% lymphocytes, and 5% monocyte-macrophage cells. When EPO was raised from 0.2 IU/mL to concentration near prior Dexter concentrations and current HEMA concentrations (2 IU/mL), culture output only increased 50% and the output expression of erythroid phenotypes declined after week 3. These results by Mantalaris using the Wu lab bioreactor from 1998 may abnormally high EPO doses appeared to stunt erythropoiesis by stimulating the early differentiation and exhaustion of EPO-responsive erythroid progenitors. Whereas, in contrast, lower and more physiological EPO doses may have maintained such EPO-responsive erythroid progenitors during later time points in culture. This was the first proof that 3D biomaterials cultures could operate at less-expensive and more-physiological cytokine supplementations for long-term, multilineal, bio-mimetic cell culture (Mantalaris et al. 1998). In the same year, the first commercial human umbilical cord blood perfusion bioreactor from Aastrom Biosciences exhibited a 390% total and 93% erythrocyte growth over 12 days in serum without the addition of any exogenous cytokines (Koller et al. 1998).

While perfusion systems allowed for a more efficient exchange of nutrients and growth factors, static systems allowed for a high-throughput analysis of culture parameter and material effects on cell output. The 6-week expansion of hBM hematopoietic progenitors in cytokine-free, 10% serum-containing medium was made much more efficient when using porous 3D scaffold foams (tantalum-coated porous biomaterial; 90% porous, 300 μ m pores) in comparison with a fibronectin monolayer, a bone marrow stromal monolayer, dextran microbeads, and calcium-based ceramic matrix (60% porous, 700 μ m channels) (Bagley et al. 1999). Similar recent 3D static biomaterials have optimised the 28-day expansion (54-fold) of hUCB MNCs in cytokine-free conditions using collagen type-1 coated polyurethane porous scaffolds where in identical medium conditions 2D cultures would fully apoptose

after 7 days (Mortera-Blanco et al. 2011). While this collagen coating best expanded general hUCB MNCs in a cytokine-free polyurethane scaffold culture, porous scaffolds formed of fibrin outperformed collagen for the 14-day cytokine-supplemented expansion of small CD34⁺ hUCB HSPC numbers (10⁶- vs. 10⁴-fold starting with 10⁴ cells/mL; Ventura Ferreira et al. 2012). As detailed in Section 2.2.2, more proliferative BM HSPCs reside in peri-vascular niches *in vivo*, with a higher fibronectin ECM composition than collagen-containing quiescent endosteal niches, while other BM MNCs contain a much smaller proliferative potential.

The incorporation of marrow-like biomechanical form and function has allowed for the study of physiological hematopoietic stages *in vitro*. Recent scaffolds include hollow channels for the static inclusion (Rnjak-Kovacina et al. 2014; Rodenhizer et al. 2016) or continuous perfusion (Kolesky et al. 2016; Zhang et al. 2016; Di Buduo et al. 2015) of fresh media, producing biochemical gradients of nutrients and proteins to study and maintain a distribution of microenvironmental conditions and cell types. Recently, wall shear stress (WSS) within perfusion HFRs has been studied to promote the short-term (≤ 1 day) production and harvest of functional human platelets from a silk scaffold or microfluidic chip containing hUCB-derived megakaryocytes (Di Buduo et al. 2015; Thon et al. 2014). This shear has been implemented in cell-encapsulate cultures during stirred-tank bioreactor scale-up, whose impeller stir rate must be carefully controlled to optimise nutrient diffusion alongside cell culture viability (Levee et al. 1994; Jelined et al. 2002; Cabrita et al. 2003). Bioprocesses have additionally begun mimicking the marrow separation of terminally differentiated blood cells ready for marrow egress into circulation from proliferative progenitors which remain within the marrow by incorporating material designs which can filter biologics products (typically mAb or viral products) from cells for continuous bioreactor harvest (Sheu et al. 2015). Biomaterial mechanisms for cell separation have proven useful in static 3D biomaterials where less-adhesive red cell product egress from foam scaffolds containing more-adhesive progenitors (Severn et al. 2016). Three of these 3D culture platforms are shown in Figure 8 and described in Table 5.

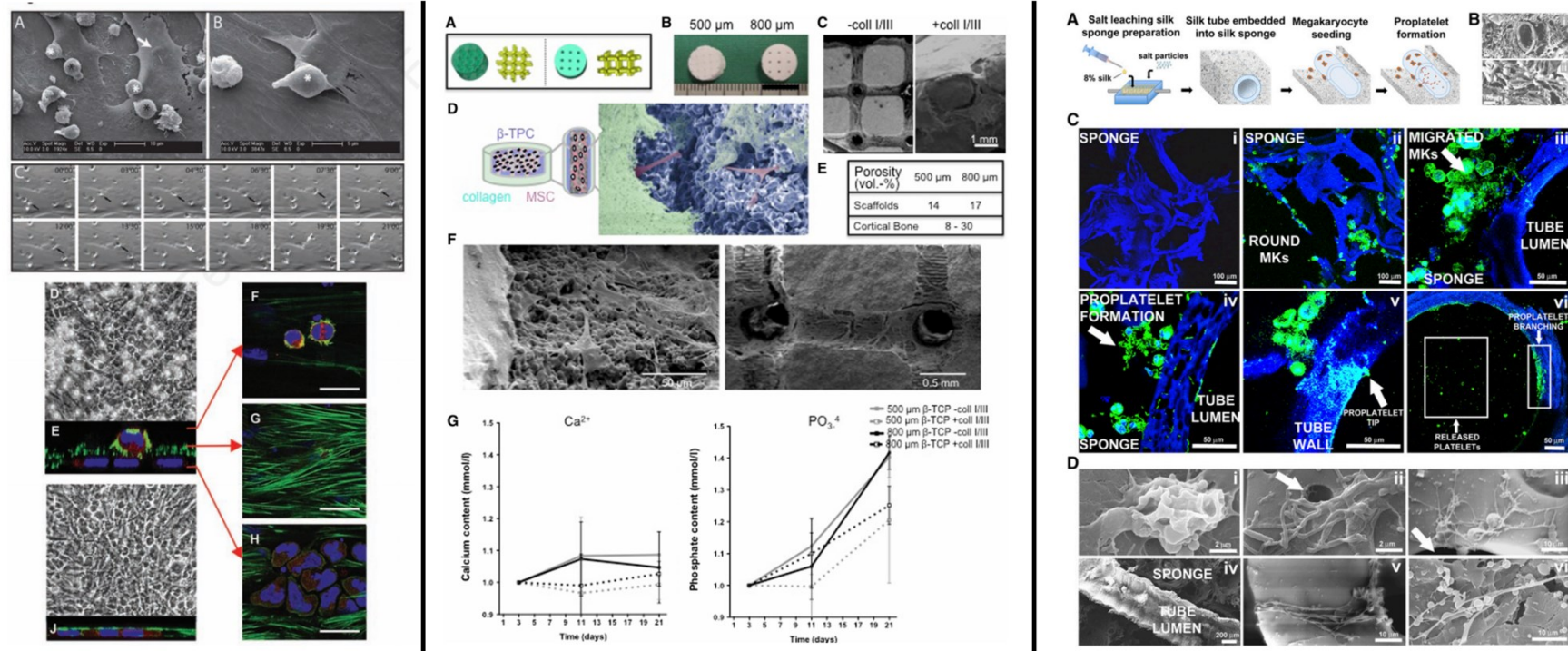


Figure 8: Examples of marrow-mimicking 3D biomaterial cultures.

(left) Hematopoietic cells migrating between a monolayer of co-culture stromal cells, (center) a β -tricalcium phosphate ceramic porous scaffold inoculated with a HSC-MSC co-culture, and (right) a perfusion silk bioreactor inoculated with hUCB-derived megakaryocytes for platelet production (Jing et al. 2010; Ventura Ferreira et al. 2016; Di Buduo et al. 2015)

Although countless 3D biomaterial platforms have been engineered for the expansion of hematopoietic stem and progenitor cells, or total hematopoietic cells, relatively very few have focused on the role of biomaterials specifically for erythropoiesis. Biomaterials implemented for erythroid cultures frequently leverage adhesion molecules (e.g. VCAMs, VLA_s) present on hematopoietic and erythroid progenitors (Chow et al. 2013; Silberstein et al. 2016) by modifying biomaterial surfaces chemically (amine functional groups (Cells et al. 2014; Chua et al. 2006)) or with cell-adherent peptides (CS-1, RGD (Jiang et al. 2006; Chen et al. 2012)) and proteins (fibronectin, collagen type-1 (Lee et al. 2014; Feng et al. 2006; Mortera-Blanco et al. 2011; Dao et al. 1998)). As erythroid cell mature *in vivo*, their cell adhesive proteins are lost after enucleation for departure from erythroblastic islands (Manwani & Bieker 2008). Therefore, biomaterials leveraging adhesion molecules may retain productive hematoerythroid progenitor cells while separating more mature red cell egress (Severn et al. 2016). Nanorough biomaterial substrate topologies further increase coatable surface area and the number of HSC-adhesive sites to increase HSC expansion and maintenance of potency (Chen et al. 2012; Muth et al. 2013). These erythroid-adhesive contacts have not only been mimicked *ex vivo* by adhesive coatings, but also by promoting intercellular associations. Late-stage erythroblasts plated at high densities (10^7 /mL) in a variety of 2D and 3D platforms were found to be making intercellular contacts, and exhibited enhanced terminal differentiation (13% vs 22%) and enucleation (23% vs 46%) toward red blood cell production when compared with a low-density controls (10^6 /mL) (Lee et al. 2014).

Many scaffold and carrier constructs utilizing the different properties detailed above have been implemented for the expansion of HSCs, however very few have investigated their use in erythropoiesis. In 2014, Arterioocyte, Inc. patented an aminated PAAc-grafted PES nanofibre mesh scaffold for the production of RBCs from UCB CD34⁺CD133⁺ HSCs. Within 18 days of culture, the scaffold reached a 2630-fold increase in total cell number with 95% enucleation rate, producing $35 \cdot 10^6$ RBCs per HSC input (Cells et al. 2014). In 2013, a perfusion 3D hollow fibre bioreactor design was patented which allowed for the high-density production of RBCs from hUCB. The reactor implemented ceramic and polymeric hollow fibres perfused with medium within a collagen type-1 coated polyurethane scaffold which was inoculated with 10^8 MNCs/mL and produced a total number of 36 billion cells across 31 days, including 830 million enucleate red blood cells (Macedo 2011). These two culture platforms aim

to produce RBCs from UCB through the use of shear stress, nanoroughness and different surface modifications to cope with three major challenges restricting commercialization of RBC production *ex vivo*: expansion, culture density, and quality, all which influence cost per product RBC.

Table 5: Selected examples of marrow-mimicry biomaterial culture systems.

| Culture Platform | Environment | Cell Input | Growth Factors | Conclusions |
|--|---|--|--|--|
| Co-Culture (Jing et al. 2010) | 2D monolayer | 10 ⁴ HSCs/cm ² on confluent MSC monolayer | 10% FCS 150 ng/mL Flt3L 150 ng/mL SCF 50 ng/mL IL-3 CellGrow SCGM | MSC associations promote HSC proliferation or quiescence through SDF-1 |
| 3D Static Biomaterial (Mortera-Blanco et al. 2011) | 3D porous collagen-coated PU scaffolds | 2x10 ⁷ hUCB MNCs/mL injected into scaffold | 30% FBS IMDM Half-medium exchanges | High density, 54- fold expansion, in absence of cytokines |
| Co-Cultured 3D Static Biomaterial (Ventura Ferreira et al. 2016) | 3D porous bioceramic scaffold | 4.5x10 ⁵ MSCs + 10 ⁶ HSCs / mL | 50 ng/mL Flt3L 50 ng/mL SCF 20 ng/mL TPO 10 ng/mL IL-6 | 8 week HSC expansion/ granulopoiesis alongside MSC osteogenesis/matrix deposition |
| 3D Perfusion Bioreactors (Mantalaris et al. 1998) (Macedo 2011) (Di Buduo et al. 2015) | Plug flow through microsphere chamber containing horse serum | 6x10 ⁷ murine BM MNC / mL | 0.2 v 2 IU/mL EPO 50 ng/mL SCF 10 ng/mL IL-3 5 ng/mL GM-CSF 200 ng/mL IGF-1 Fetal calf serum Fisher's medium | 17+ week culture. 3-fold expansion Low-dose EPO did not decrease expansion, but increased longevity |
| | Ceramic hollow fibres within collagen-coated PU scaffold | 10 ⁸ hUCB MNCs/mL | 30% FBS 100 ng/mL SCF 3 IU/mL EPO IMDM | Reached 33.5-fold total and 14-fold RBC expansion at densities >10 ⁹ /mL |
| | Silk hollow fibres within silk scaffold | 5x10 ⁶ hUCB Mks /mL | 10 ng/mL TPO, IL- 6, IL-11 StemSpan SFEM | Mk-derived platelet production in a short term shear platform |

2.5. Analysing Erythropoiesis in 3D

2.5.1. Methods of 3D imaging

The spatial structure of hematopoiesis within *in vivo* marrow and *in vitro* engineered environments has been captured through recent advances in 3D imaging, but data defining the interaction of cells within their environment has been largely unquantified. This is especially true for animal and *ex vivo* marrow models, wherein current imaging research is primarily focused towards designing instruments and probes to enhance imaging depth, spatial resolution, speed, and specificity,

but typically do not improve the postanalysis quantitation of imaged data (Allenby et al. 2017). Postanalysis quantitation of a cell's distribution within its local environment is applicable to many 3D imaging platforms: magnetic resonance imaging (MRI), computed tomography (CT), and optical imaging (UV, Visible, IR) due to their use of cellular or environmental markers to discern a region of interest. Studies employing these platforms include *in vivo* animal models, or *in vitro* 2D cell cultures, which can be performed continuously (intravital) during study. Most *in vitro* 3D cultures must be terminated for spatial analyses, and as such, the extraction of maximal quantitative, spatial data from these rare, expensive 3D analyses must drive new postimaging quantitation algorithms.

2.5.2. *In vivo* 3D image analyses

Most knowledge of the bone marrow environment, and in the last decade, recent advances in understanding marrow niche distributions during normal and abnormal hematopoiesis, have come from intravital confocal microscopy imaging of murine marrow calvarium (Hawkins et al. 2016; Lo Celso et al. 2009), or fixed imaging of murine marrow in long bones (Nombela-Arrieta et al. 2013). Immunofluorescence imaging provides the broadest catalogue of cell and environmental probes as fluorochromes: fluorescence molecules that bind to cell receptor and environmental proteins, and although traditionally limited by a 100-200 μm tissue imaging depth, current bone clearing techniques have allowed for millimetres scale penetration and complete imaging of murine marrow (Greenbaum et al. 2017).

These imaging methods of animal models have rewritten the understanding of cellular microenvironments and their organization within marrow niches. Designing new oxygen reactive probes, the exact oxygen concentration of vasculature, peri-vascular and endosteal spaces could be measured, demonstrating cells near marrow endosteum experienced the highest oxygen tension, a gradient which was cell-consumption dependent (Spencer et al. 2014). The distribution of HSC niches was demonstrated to not simply exist within peri-endosteal regions of low oxygen concentrations, but were divided into HSC subtypes which laid in vascular and peri-vascular space, and near endosteal arterioles (Nombela-Arrieta et al. 2013; Kusumbe et al. 2014; Itkin et al. 2016). These new HSC niches were supported by neighbouring mesenchymal and osteolineage cells which were genetically and functionally different than phenotypically identical cells further away (Silberstein et al. 2016). These

HSC-neighboring osteolineage and mesenchymal cells supported hematopoietic function through physical contact and the secretion of growth and migratory factors (Greenbaum et al. 2013; Kfoury & Scadden 2015).

The quantitative image analyses of erythroid niche distributions remains disputed, as no detailed murine studies have implemented 3D confocal imaging to define the marrow erythropoietic niche, and most knowledge of marrow erythroblast island distribution is currently derived from stereological studies (Mohandas & Prenant 1978; Weiss 1983; Weiss 1984). However, current calculations of cell distributions amongst their environment are typically constrained if the complete organ is not able to be imaged, or if regions of interest are spatially complex. Recent studies have compensated for this by normalizing against a uniform distribution of cell positions within a similar tissue topology (Acar et al. 2015; Takaku et al. 2010), or by only analysing phenomena that exist within the central fraction of the image (Delarue et al. 2014; Meddens et al. 2013; Bjornsson et al. 2008). Examples of current quantitative *in vivo* and *in vitro* image analyses are provided in Figure 9.

2.5.3. *Ex vivo* 3D image analyses

The recreation of a physiological environment in the laboratory requires an *in situ* assessment of the *de novo* tissue architecture formed. Therefore, analyses of cell association, distribution, and migration has been increasingly studied for continuous time frames in 2D culture systems (Thon et al. 2014), or for fixed time frames in 3D culture systems. While 3D culture systems have typically represented “black boxes” as only extracellular medium could be continuously monitored with no spatial insight into the scaffolding constructs, new confocal analyses have allowed for the realisation of cell distributions at multiple time points through culture. Recently, these analyses have proven essential in thick tissue engineered constructs, which typically promote multilineal cell growth as a function of distance from medium inclusion (Kolesky et al. 2016; Zhang et al. 2016; Rnjak-Kovacina et al. 2014; Rodenhizer et al. 2016). Spatially-homogenous 2D culture systems lack multilineal cell growth, stimulating all cells to simultaneously undergo differentiation or proliferation equally, preventing homeostatic stem cell renewal during progenitor differentiation for continuous growth. Quantitative image analyses have proven useful for high-throughput multiwell culture screening experiments (Mahadik et al. 2017; Müller et al. 2016), but have not been effectively to assess reproducible and

physiological cell distributions and associations for thick, cell-laden tissue constructs (Kolesky et al. 2016; Rnjak-Kovacina et al. 2014), if image quantitation occurs, average cell expressions over the similar image volumes have been analysed (Rodenhizer et al. 2016).

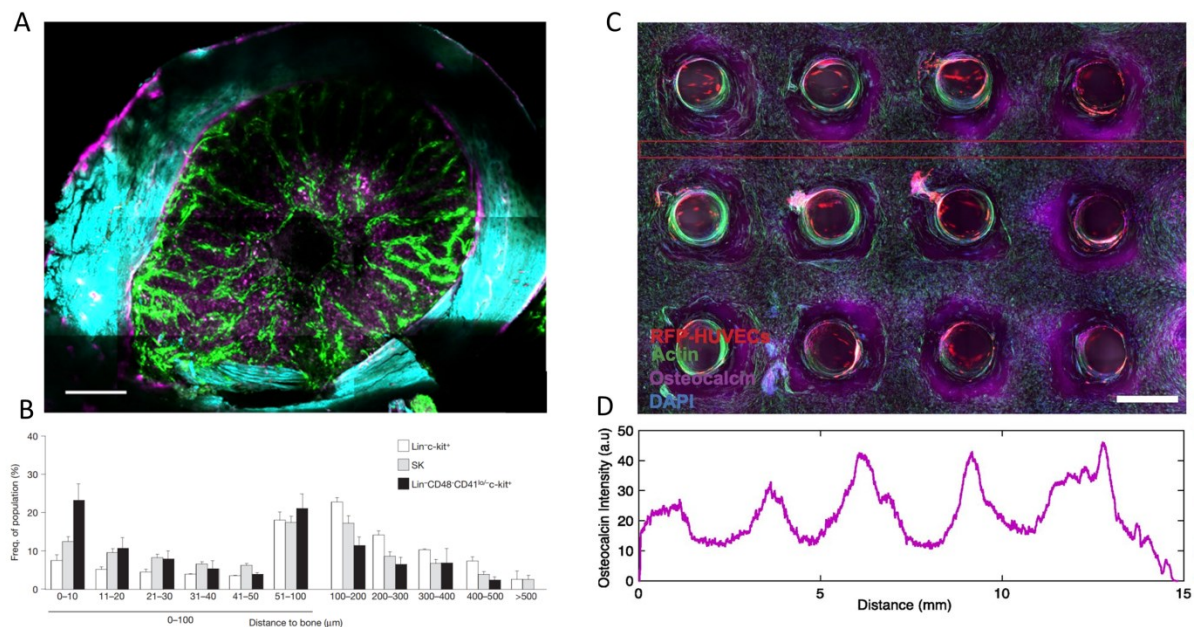


Figure 9: Quantitative 3D confocal imaging analysis state-of-the-art.

(A) Imaging vascular (green, pink) and endosteal (cyan) structure within a cross section of murine trabecular bone marrow, adapted from (Lassailly et al. 2013). An example of quantitating the percent expression of HSCs phenotypes at different distances from bone surfaces, adapted from (Nombela-Arrieta et al. 2013). (C) Imaging multilineal cell distributions within vascularised tissue engineering constructs, and quantitative results of fluorescence intensity along a highlighted plane adapted from (Kolesky et al. 2016).

Therefore, new quantitative 3D image analyses tools must be developed to maximize data output for these expensive, destructive, native or engineered tissue analyses. These tools would have important application toward the understanding of normal hematopoietic development, wherein assessments detailing specific cell densities at different regions of interest could describe cell distributions and associations as compared to current understandings of HSC niche formation. In addition, these tools could help define more current knowledge of erythropoietic niche development, which has not been addressed during this decade of immunofluorescent image development.

3. Aims and Objectives

The development of an *ex vivo* model which faithfully recapitulates the bone marrow environment would allow both for the characterization of and be able to leverage efficient *in vivo* human red blood cell production mechanisms *in vitro*. The physiological process of erythropoiesis takes place in multiple marrow cell niches: from HSC niches which control kinetics of proliferation, quiescence, and differentiation, to erythroid niches which expand and mature erythroblasts into reticulocytes, and later, functional red blood cells. These niches are complex, requiring a careful balance of mechanical forces, biochemical factors, and supportive cell signals, and *in vitro* studies have demonstrated each factor produces significant outcomes on red blood cell quantity and quality. A successful marrow-mimetic device would serve both as a hematopoietic platform for translational cell-expansion protocols, and also for the study and treatment of abnormal hematopoiesis *ex vivo*.

Prior studies have demonstrated the faithful recapitulation of some marrow functions: co-culture of accessory niche cells (Jing et al. 2010), marrow trabeculae-mimetic structure and surface chemistry (Nelson & Roy 2016), and biomechanical forces such as perfusion for product harvest (Di Buduo et al. 2015). But few have demonstrated single-step, long-term production without allogeneic co-culture (Mantalaris et al. 1998), and none have done so under defined conditions nor have characterized the spatial niche development of their *ex vivo* marrow model in detail. Herein, the objective of this thesis is the creation of 4 products which seek to better model and characterise the marrow environment *ex vivo*, starting from a first generation bioreactor (Macedo 2011):

Objective 1: Incorporate medium-perfused hollow fibres which can locally deliver nutrients, growth factors, and harvest cells within a 3D porous scaffold as a marrow-mimetic bioreactor.

First, the fabrication of ceramic hollow fibres is detailed. When perfused, these ceramic hollow fibres allow for the passage of nutrients, metabolites, and proteins, while acting as leukoreduction filters: allowing for the selective filtration of hematopoietic enucleate and not nucleated cells. The major innovation of these fibres are their ability to be incorporated into 3D polymeric foam biomaterials, which allows for enhanced nutrient diffusion, cell harvest, and scaffold volume scale-up for better cell expansion in comparison to static systems. After 21 days of hollow fibre perfusion, immunofluorescent

images of the porous biomaterial scaffolding demonstrated multilineal hematopoietic, osteogenic, and endothelial cell phenotypes *in situ*.

Objective 2: Develop a quantitative image analysis tool which can spatially quantify cellular gradients and associations within the marrow-mimetic bioreactor.

Second, the development of quantitative image analysis tools provides spatial insight into environmental and cellular interactions. Where current methods have misrepresented or underutilized cellular phenomena captured, these image postprocessing algorithms quantitatively assess 3D cell-to-cell and cell-to-microenvironmental phenomena of interest while utilizing, for the first time, the entire 3D image captured. These advancements allow for the calculation of marrow niche association and distribution densities, even in complex spatial geometries.

Objective 3: Characterize the formation of niche-like cellular microenvironments formed within the bioreactor.

Third, the design, fabrication, culture, and the characterisation of a marrow-mimicry bioreactor are described. The bioreactor design, improved from objective 1, is inoculated with unselected hUCB MNCs and perfused with chemically defined medium with physiological doses of only EPO and SCF for 28 days. UCB MNC stromal proliferation, osteogenic differentiation, ECM protein deposition is, for the first time, spatiotemporally characterized in defined conditions by detailed quantitative image analyses. Stromal components provide structural as well as humoral support for hematopoietic cells, secreting growth factors and interacting at close local densities with erythroblasts, while phenotypically mature enucleate red cells are continuously harvested through the engineered reactor hollow fibres.

Objective 4: Explore the capabilities of marrow-mimetic bioreactors towards producing blood.

Fourth, the development towards an optimized marrow-mimicry miniature bioreactor is described. This mini-reactor, envisioned from objective 3, leverages an increased erythroid cell output found from higher hUCB MNC inoculum densities made possible by a small reactor volume. The mini-reactor has been designed from assembled diffusion and cell distribution models derived from experimental data from objective 3, and fabricated to allow for mini-reactor parallelisation. Preliminary analyses have demonstrated these mini-reactors can achieve 3D confluent-like cell densities under lower cytokine stimulation and nutrient demand.

Altogether, these objectives and their outcomes highlight the importance of faithfully mimicking the marrow environment *ex vivo*, through (1) structure and perfusion, (2) imaging analysis, (3) characterisation, and (4) exploration of a marrow-mimicry hollow fibre bioreactor platform. While acting as novel platforms for analysis of more physiological marrow erythropoiesis, these platforms could be further developed to reach clinically-relevant costs of RBC production, to produce other hematopoietic cell therapies, and be used as a platform to model and treat abnormal hematopoiesis and erythropoiesis for pre-clinical studies prior to use of such agents in clinical trials.

4. Incorporation of hollow fibres able to perfuse nutrients and harvest cells within a 3D porous scaffold.

Tissue vascularisation efficiently distributes nutrients, removes metabolites, and possesses selective cellular permeability for tissue growth and function. Current engineered tissue models have been limited by ineffective nutrient perfusion and product separation to small volumes, low cell densities, and invasive cell extraction. Here, engineered hollow fibre “vasculature” are described which can be incorporated into 3D tissue models to improve nutrient and metabolite exchange while continuously filtering out mature red blood cells during perfusion. These ceramic hollow fibres can filter enucleate and reticulocyte red cells from below 20% of impure human umbilical cord blood (hUCB) mononuclear cell (MNC) fractions to enriched suspensions above 90%. When incorporated into a 3D porous scaffold, medium-perfused hollow fibres maintained nontoxic glucose, lactate, and pH values and expanded cells to 1.6-fold higher densities over 21 days of culture in comparison to static matrices. This hollow fibre bioreactor (HFBR) required a smaller per-cell medium requirement and operated at cell densities 10-fold above current 2D methods while allowing for continuous cell harvest through hollow fibres. This study identifies key fabrication parameters for hollow fibres useful as engineered “vasculature” to better mimic native tissue for *ex vivo* cell therapy biomanufacturing and disease modelling.

In this section, Asma Tahlawi performed all hollow fibre fabrication. Hollow fibre filtration testing with performed jointly between Mark C. Allenby, Asma Tahlawi, and José C.F. Morais (supervisor: Mark C. Allenby), and bioreactor fabrication and culture was performed by Mark C. Allenby. Prof Kang Li assisted in final manuscript revision.

4.2. Introduction

Manufactured culture platforms for cell therapy production, disease modelling, and tissue regeneration have been limited by nonphysiological structure and ineffective nutrient diffusion to small biomaterial volumes, sparse cell densities, and impure cell product harvests (Webber et al. 2015). Human cell culture within liquid suspension and 2D platforms have been restricted to densities below 10^6 cells/mL (Rousseau et al. 2014) which improve under an enhanced biochemical nutrient transfer provided by stirred-tank or rocking bioreactors to 10^7 cells/mL (Ratcliffe et al. 2012). Higher culture density has been incorporated within a tissue mimetic 3D structure for porous scaffolds (Mortera-Blanco et al. 2011), while perfused hollow fibre bioreactors (HFBRs) have reached the highest human cell culture densities reported, similar to native tissue (10^{8-9} cells/mL) (Rnjak-Kovacina et al. 2014; Rodenhizer et al. 2016; Housler et al. 2012). Although providing a biosimilar structure and cell density, 3D cultures require termination for product harvest, and harvests are frequently contaminated with cells of other lineages and maturations than desired cell therapy products. While HFBRs have been applied to continuously extract viral cell products by filtration through polymeric hollow fibres (Sheu et al. 2015), no polymeric fibre BR has been implemented with pore size large enough to filter cell products for continuous 3D culture biomanufacturing.

Red blood cells (RBCs) represent a cell therapy with high clinical demand: RBCs are required at a rate of 8000 blood units per day in the United Kingdom at a cost of 250 million GBP per year (Hamlyn 2016). Human umbilical cord blood (hUCB)-derived RBC production has demonstrated clinical utility for human transfusion (Giarratana et al. 2011) but remains limited by unnaturally low production densities which create exorbitant medium and cytokine costs (Rousseau et al. 2014). Physiological blood production takes place within the human bone marrow (hBM) and is supported by a complex vascular and trabecular architecture to nourish a dense, multilineal, spatially-heterogeneous distribution of RBC stem, progenitor, and precursor cells (Nombela-Arrieta et al. 2013). Leaky marrow sinusoids allow for mature cell egress into peripheral blood circulation, where maturing reticulocytes can cross its endothelial wall by deforming through tight gaps between cells ($3 \mu\text{m}$) (Leblond et al. 1971; Itkin et al. 2016). Therefore, this endothelial sinus not only diffuses nutrients into the marrow, but also acts as a natural filter to allow the passage of small, deformable reticulocytes out of the marrow

while retaining other mononuclear cells (MNCs), as enucleate red cells comprise <25% of marrow cells, but >95% of peripheral blood cells (Lansdorp & Dragowska 1992). A HFBR comprised of medium-perfused cell-filtering fibres integrated within a porous scaffold could support tissue-like culture densities, allow for the study of biomimetic microenvironments and human cell to cell interactions, and continuously harvest mature RBCs similar to the hBM (Webber et al. 2015; Kolesky et al. 2016; Zhang et al. 2016; Rodenhizer et al. 2016).

Herein, the fabrication of ceramic hollow fibres are described which can be incorporated as engineered “vasculature” within a 3D porous scaffolding. These fibres have previously demonstrated an unrestricted filtration of pico- (ions and glucose) and nano- (cytokines) scale nutrients, with average pore sizes above 0.1 μm (Macedo 2011; Misener et al. 2014), and are now investigated for their performance in the filtration of enucleate red cells from impure human umbilical cord blood (hUCB) mononuclear cell (MNC) fractions in three filtration formats: passive shell-to-lumen filtration (“cross-flow”), forced lumen-to-shell filtration (“dead-end”), and long-term perfused hollow-fibre-bioreactor culture within a 3D scaffolding (“HFBR”) useful for long-term hUCB MNC expansion and erythropoiesis (Mortera-Blanco et al. 2011). Whereas other studies have fabricated microfluidic devices as effective high-throughput leukoreduction filters (Xia et al. 2016), these ceramic hollow fibres can be modular biomaterials which can also be incorporated into tissue engineered scaffolds serving both as a source of nutrient incorporation and cell therapy harvest.

4.3. Methodology

Current 3D biomaterials provide physiologically relevant platforms for translational cell expansion protocols, however, their use for high-density cell therapy production is limited by a lack of biochemical nutrient diffusion and continuous cell therapy harvest. In this section, the examination of several hollow fibres are described, produced by Ms. Asma Tahlawi, for their ability to filter enucleated red cell product and their incorporation into a 3D porous scaffolding for long-term hematopoietic culture. In addition to allowing the continuous harvest of cells, hollow fibre-perfused bioreactors better diffused nutrients, reached higher cell expansions and densities, while requiring small quantities of medium in comparison to static scaffolds. These initial steps demonstrate the utility of hollow fibre bioreactors for cell therapy bioprocesses, and provide insight for future development.

4.3.1. Ceramic hollow fibre fabrication and characterisation

Ceramic hollow fibres were fabricated and assessed by Ms. Asma Tahlawi by the preparation of a mixture of 58.6 wt% 1 and 4 μm aluminium oxide powders (VWR, Lutterworth, UK), 1.3 wt% Arlcel P135 (polyethylene glycol 30-dipolyhydroxystearate; Uniqema, Yorkshire, UK) and 15-30 wt% polyethersulfone (PES) in N-methylpyrrolidone (Sigma-Aldrich, Dorset, UK). This gradual dissolution was accomplished through milling with zirconium balls (Across International, Livingston, NJ) for 48 hours and degassing for 2 hours. The resulting dope solution was extruded through a tube-in-orifice spinneret of outer diameter 3 mm and inner diameter 1.2 mm around an inner bore fluid of water of DMSO (Sigma-Aldrich), which fell into a water bath with an air gap of 1 to 15 cm. Eight different hollow fibres were fabricated by adjusting aluminium oxide powder, particle size, PES binder content, type of bore fluid, flow rates of both bore fluid and dope solutions, spinneret-to-water-bath air-gap, as well as sintering temperatures on an apparatus previously described (Kingsbury et al. 2010). Fibres were first screened for structural integrity and shape before assessing porosity by mercury intrusion porosimetry (MIP), capillary flow porometry (CFP) and scanning electron microscopy (SEM) by Asma Tahlawi.

4.3.2. Filtration and culture platform assembly

To assess the utility of these ceramic hollow fibres to filter nucleated and enucleated cell fractions isolated from human umbilical cord blood, three different filtration platforms were

constructed: (1) a cross-flow filtration platform, (2) a dead-end filtration platform, and (3) a long-term HFBR culture platform (depicted in Figure 10).

In cross-flow filtration (Figure 10A): four hollow fibres were adhered within a polyfluoroalkoxy (PFA) fine thread flare tee (Swagelok, London, UK) applying a rapid drying two-component resin (Araldite, Basel, Switzerland) on both the inlet or outlet of the reactor. Medium could then be perfused from the inlet of the reactor, through hollow fibre lumens, to the exit.

In dead-end filtration (Figure 10B): a custom-built shell was machined in-house from a PFA rod (ThePlasticShop, Coventry, UK) containing inlet and outlet barbed perfusion caps, and shell-release caps. A single hollow fibre was adhered inside the shell with resin, then the fibre was blocked at the perfusate outlet with resin, and tubing was attached to collect medium flowing out of the shell-release cap.

In long-term 3D HFBR culture (Figure 10C): a single hollow fibre made with water-bore fluid was adhered within cross-flow filtration PFA shell (Swagelok), and a solution of 5% polyurethane (PU; Noveon, Brussels, Belgium) in 1,4-dioxane (Sigma-Aldrich) was dissolved at 60°C, then 5 mL was injected into the extraluminal shell space and frozen at -80°C for 2 hours. The 1,4-dioxane was selectively sublimed through thermally induced phase separation (TIPS) by applying a vacuum pressure of 0.01 mbar at -15°C to leave a porous PU scaffold, subsequently coated with bovine collagen type 1 (Sigma-Aldrich) by thoroughly immersing, mixing, and perfusing the HFBR with phosphate buffered saline (PBS, Life Technologies, Paisley, UK), 70% ethanol (VWR), 62.5 ug/mL bovine collagen type 1 (Sigma-Aldrich) in PBS at a pH of 7.0, then PBS again.

Prior to cell inoculation, all platforms were sterilized by perfusing and washing the shell-side with PBS, ethanol (2 hours), and PBS in multiple washes accompanied by UV sterilization. The perfusion bioreactor platform was compared to a static PU scaffold platform in the form of 0.125 mL cubes prepared, coated, and sterilized similarly as previously described (Mortera-Blanco 2008). All platforms were then conditioned in cell culture medium for at least 24 hours.

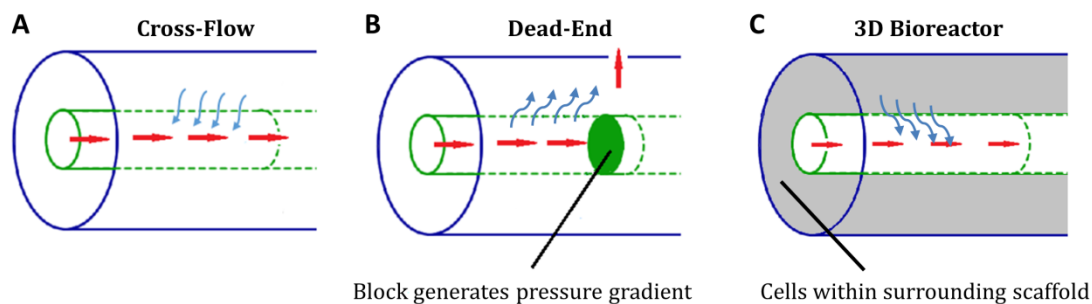


Figure 10: Schematics for hollow fibre cell filtration experiments.

(A) Cross-flow filtration: cells are inoculated within the abluminal, shell region and filter through the fibre into the perfused lumen, and are collected at the fibre effluent. (B) Dead-end filtration: a solution of cells are perfused into fibre lumens, which are blocked at the exit with a resin solution so cells must pass through the fibre into the shell and are collected at an opening in the shell. (C) HFBR culture: cells are inoculated into a 3D porous scaffold formed around the fibre, which is perfused for 21 days. Red and blue arrows indicate flow direction and cell movement, respectively. Figure schematic drawn by José C.F. Morais.

4.3.3. Isolation and inoculation of hUCB

MNC fractions were isolated from freshly-collected hUCB (National Health Service Blood & Transplant (NHSBT), Colindale, UK) by Ficoll-Paque (Sigma Aldrich) yielding approximately 70-80% MNCs and 20-30% enucleate cells. For filtration experiments, cells were then stored in 90% human serum at 4°C for up to 10 hours and re-counted prior to inoculation. hUCB cell suspensions were inoculated into platforms as enumerated below, and all the systems were perfused at a rate of 20 mL/hour.

- Cross-flow filtration: $3 \cdot 10^7$ cells/mL were seeded into the 5 mL PFA shell and perfused for 24 hours.
- Dead-end filtration: $5 \cdot 10^6$ cells/mL were seeded into a 480 mL reservoir and perfused into four platforms for 6 hours.
- HFBR culture: $4 \cdot 10^7$ cells/mL were seeded into 5 mL of porous scaffolding and perfused for 21 days.

HFBR culture medium consisted of a 60 mL recycled batch of IMDM supplemented with 30% fetal bovine serum (FBS; Life Technologies), 1% penicillin-streptomycin (ATCC, Maryland, USA), and 100 ng/mL stem cell factor (SCF; R&D Systems, Abingdon, UK). From day 2, the recycled batch was exchanged for fresh medium with 1 IU/mL erythropoietin (EPO; R&D Systems) and without SCF at a continuous rate of 0.5 mL/h from a 100 mL solution of fed medium replenished weekly.

The quantity of total, viable, and mononuclear cells were counted on hemocytometer using trypan blue (StemCell Technologies, Grenoble, France) and methylene blue (StemCell Technologies) dye-exclusion stains.

4.3.4. Flow cytometry

Suspensions of 10^6 cells were stained with 1 mL solution of Hoescht 33342 (300 $\mu\text{g}/\text{mL}$, Thermo-Fisher) and Calcein AM (2.5 $\mu\text{g}/\text{mL}$, Thermo-Fisher) in PBS for 45 minutes at room temperature, prepared according to manufacturer's specifications. Suspensions were then washed with Cell Staining Buffer (CSB, described below) and stained with mouse anti-human monoclonal antibodies 1.5 μL CD235a-PE and 5 μL CD61-APC or isotype antibodies 1.5 μL IgG2b-PE and 5 μL IgG1-APC (BD Biosciences, Oxford, UK) in 100 μL of CSB and 20 μL of FBS and incubated for 1 hour at 4°C. Suspensions were then washed with CSB, with PBS, and filtered prior to the analysis of 50,000 events on a LSR Fortessa Flow Cytometer (BD Biosciences) with detection of Hoescht (405 laser, 450-50 filter midpoint-bandwidth), Calcein AM (488, 530-30), CD235a or IgG2b-PE (561, 582-15), and CD61 or IgG1-APC (640, 670-14). Fluorochrome detection spillover was compensated in comparison with single-stain controls, and positive marker detection was compared with isotype and unstained controls as presented.

CSB was prepared by adding 1wt% bovine serum albumin (BSA; Sigma Aldrich) and 0.01wt% NaN_3 (Sigma-Aldrich) to PBS.

4.3.5. Confocal microscopy

To assess viability, frozen fibre or reactor sections were immediately incubated at 37°C in 4 μM ethidium homodimer-1 (Invitrogen) and 2 μM Calcein AM (Invitrogen) in culture medium for 1 hour followed by washes with PBS and imaging on a Leica SP5 upright confocal microscope with Leica LAS AF software (Leica, Milton Keynes, UK).

To assess cell type, frozen sections were immediately fixed with a 4% paraformaldehyde solution (Sigma-Aldrich) in PBS for at least 12 hours, permeabilised with 0.1% Triton X-100 (Sigma-Aldrich) in Confocal Microscopy Stain Buffer (CMSB, described below) for 2 hours, blocked with 10% donkey serum (AbCam, Cambridge, UK) in CMSB for 4 hours at 4°C, followed by an overnight incubation with primary antibodies or isotype controls in CSMB at 4°C, a 6-hour incubation with

secondary antibodies in CMSB at 4°C, an overnight incubation in 1:200 DAPI (Life Technologies) and 1:1000 cell membrane (CellMask, Life Technologies) counterstain solution in PBS, then storage in a 0.01% NaN₃ in PBS solution at 4°C. Each step was separated by single or multiple 15 minute washing steps in appropriate buffer. Sections were then imaged on a Leica SP5 inverted confocal microscope as above. Acquired images were manipulated within figures by adjusting contrast and brightness of both sample and negative (isotype) controls identically as presented.

CMSB contained 1wt% BSA, 0.5wt% Tween-20, 0.01wt% NaN₃ in PBS. Primary antibodies used include CD235a or IgG2b rat anti-human (ab33386, ab18541) at 1.7 µg/mL and CD61 or IgG rabbit anti-human (ab75872, ab172730) at 8.4 µg/mL (AbCam). Secondary antibodies include donkey anti-rat Alexa Fluor 488 and donkey anti-rabbit Alexa Fluor 555 at 1:1000 dilutions (Thermo Fisher). Details regarding primary antibody stains used during confocal microscopy detection for HFBR experiments (in Figure 16C and Figure 17) are provided in Table 6.

Table 6: Primary antibody stains implemented for confocal detection in Figure 16C and Figure 17.

Becton-Dickenson (BD) stains (CD235a, CD36) were recommended for flow cytometry but here implemented for immunofluorescent imaging.

| Antibody | Concentration (µg/mL) | Product number |
|-----------------|-----------------------|----------------|
| Mouse CD235a-PE | 2.5 | BD 555570 |
| Mouse EPO-R | 33.3 | AbCam ab56310 |
| CD36-APC | 1:24 dilution | BD 550956 |
| Rabbit CD71 | 8.3 | AbCam ab84036 |
| Rabbit OSx | 8.3 | AbCam ab94744 |
| Mouse OPN | 3.3 | AbCam ab69498 |
| Mouse CD31 | 1:30 dilution | AbCam ab9498 |
| Rabbit IgG | 8.3 | AbCam ab172730 |
| Mouse IgG | 33.3 | AbCam ab37355 |
| Mouse IgG2b-PE | 2.5 | BD 555743 |
| Mouse IgM-APC | 1:24 dilution | BD 555585 |

4.3.6. Scanning Electron Microscopy

Frozen sections were immediately fixed with a 3% glutaraldehyde solution (Sigma-Aldrich) in Sorenson's buffer (described below) for at least 12 hours. Sections were then washed twice, and post-fixed in 1% OsO₄ (Sigma-Aldrich) in Sorenson's buffer for one hour, then washed twice. Sections were then dehydrated in an increasing gradient of absolute ethanol diluted with Sorenson's buffer at 0.067 M, pH 7.4 (50:50, 70:30, 90:10, 95:5, and 100:0 twice, respectively), followed by further drying in an

increasing gradient of hexadimethylsilazane (Sigma-Aldrich) in absolute ethanol (70:30, 90:10, 95:5, 100:0 twice, respectively, Sigma-Aldrich), and left to air-dry overnight. After solvent evaporation, sections were adhered to SEM stubs with carbon tape (Elektron Technology, Stansted, UK), sputter-coated with gold (20 mA, 30 s) prior to imaging on a JSM-6010LA scanning electron microscope (SEM; JOEL, Watchmead, UK).

Sorenson's buffer was prepared by titrating solutions of 0.067 M Na_2HPO_4 in DI water with 0.067 M KH_2PO_4 (Sigma-Aldrich) in DI water to a pH of 7 directly before use.

4.3.7. Extracellular metabolite and protein analysis

Perfused HFBR medium was collected from 3-way stopcocks (Smith's Medical, Watford, UK) directly before entering and directly after leaving the HFBR. Extracellular nutrients and metabolites, pH, and dissolved gases were analysed by electrochemical sensors and averaged over 3 identical replicates (Bioprofile 400, Nova Biomedical, Runcon, UK).

4.4. Results

4.4.1. Phase-inversion bore fluid controls ceramic fibre micropore structure

Eight different types of ceramic hollow fibres were fabricated by Asma Tahlawi through steps of dope preparation, fibre extrusion, phase inversion, and sintering by adjusting dope alumina particle size and PES binder composition, bore fluid, dope and bore fluid flow rate, and sintering temperatures. Dope and bore flow rates were controlled to maintain a stable fibre extrusion and probably played a minor role influencing fibre pore architecture. Otherwise, these parameters altered average fibre pore sizes from 0.2 to 2 μm along outer surfaces and from 0.35 to 11.5 μm along inner surfaces with porosities of approximately 45-80%. Amongst fabrication parameters inspected by Asma Tahlawi (Figure 11), choice of bore fluid most significantly influenced fibre porosity, followed by spinneret to water bath air-gap distance, while the addition of 4% ethanol or altering maximal sintering temperature held no microscale differences. Observation of fibre cross sections by Asma Tahlawi (Figure 12) demonstrated finger-like voids formed within an otherwise tortuous ceramic sponge whose diameter, length, and frequency also appeared primarily dependent on bore fluid and air-gap distance.

The use of a solvent (DMSO) as a bore fluid instead of water produced larger outer surface pore sizes, inner surface pore sizes, and fibre porosity (0.18 μm , 0.43 μm , 62%: Fibre 1 versus 0.62 μm , 5.04 μm , 80%: Fibre 5). Fibres spun around a DMSO bore fluid (Fibre 5-8) contained larger pore sizes and porosity (up to 2 μm , 11.77 μm , 80%) but frequently disintegrated during phase inversion or later handling; specifically, Fibre 6 was not structurally useful for filtration. Fibre structure could be stabilised by increasing PES binder concentration which led to larger outer surface pore sizes (1.84 μm , 7.28 μm , 71%; Fibre 7). The use of larger particle sizes in Fibre 8 increased limiting pore diameters: from 2.5-fold (Fibre 7) to 4-fold (Fibre 8) in comparison with Fibres 1 and 5 as measured by capillary flow porometry (Figure 12) by Asma Tahlawi and José C.F. Morais.

Four representative fibres (Fibres 1, 5, 7, and 8) were selected to be further tested towards cell filtration from the eight fibres successfully fabricated. However, the pore architecture of Fibres 7 and 8 was unable to filter cells and caused platform blockage and rupture for Fibre 7 (after 0.5h), and Fibre 8 (after 2h) during dead-end filtration. Fibre 1 and Fibre 5 successfully filtered cells in both platforms, and are further described as “Water Fibres” and “DMSO Fibres”, respectively.

A

| Fibre# | 1/2 | 3/4 | 5/6 | 7 | 8 |
|--|------------------|------------------|------------|----------|----------|
| Particle Size(μm) | 1 | 1 | 1 | 1 | 4 |
| PES Binder (%) | 15 | 15 | 15 | 22.5 | 30 |
| Additive | -- | Eth (4%) | -- | -- | -- |
| Bore Fluid | Water | Water | DMSO | DMSO | DMSO |
| Air-gap (cm) | 12 | 12 | <u>0/1</u> | 15 | 15 |
| Flow Rate (Dope/Bore) | 15/18 | 7/9 | 8/16-20 | 8/15 | 8/15 |
| Sintering temperature ($^{\circ}\text{C}$) | <u>1350/1450</u> | <u>1350/1450</u> | 1350 | 1450 | 1700 |
| Porosity (%) | 62/47 | 59/61 | 80/66 | 71 | 72 |

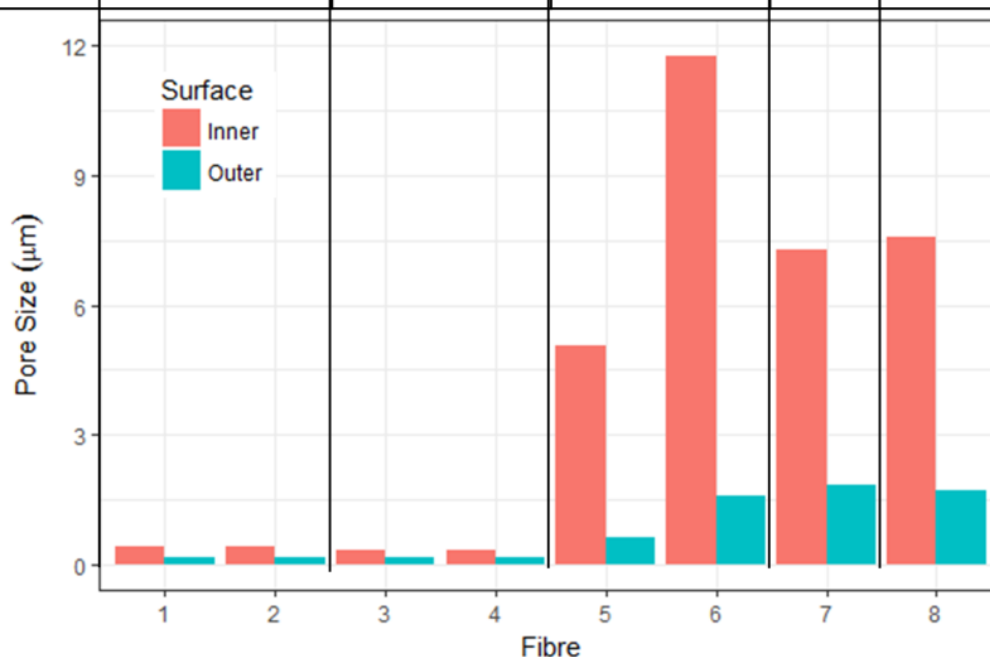
B

Figure 11: Fibre fabrication parameters producing structural differences in porosity and pore size.

(A) Parameters modified, parameters which are highlighted in bold/italic identify varied parameters of the fibre/group. (B) Outer and inner surface average pore diameter measured by MIP. Fibres 1 and 5 were defined as the “Water Fibre” and “DMSO Fibre” respectively. This figure was made with fabrication and fibre characterization data generated by Asma Tahlawi.

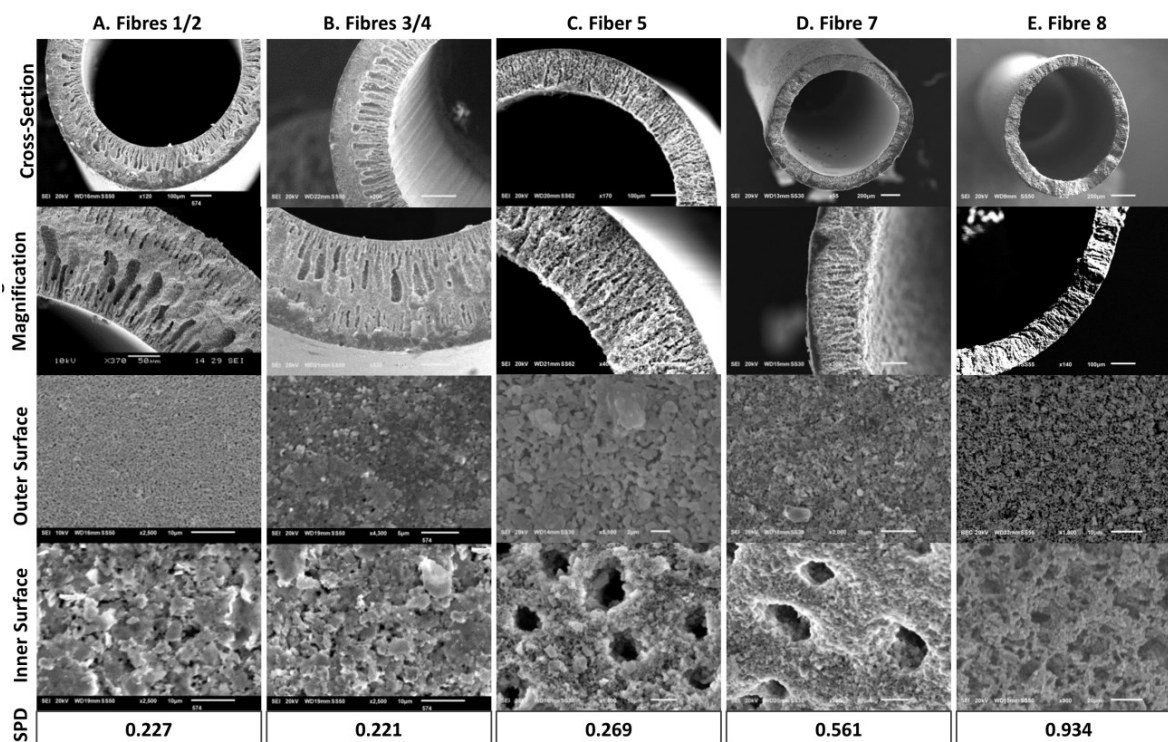


Figure 12: Ceramic hollow fibre structure.

SEM images representative of (A) fibres 1 and 2, (B) fibres 3 and 4, (C) fiber 5, (D) fiber 7, and (E) fiber 8. Filtration is described and limited by the smallest section of open pores: Smallest Pore Diameter (SPD). Fibres 1 and 5 are the “Water Fibre” and “DMSO Fibre”, respectively. This figure was made with fabrication and fibre characterization data generated by Asma Tahlawi.

4.4.2. Cross-flow filtration enriches nucleate fractions

Cross-flow filtration demonstrated that a 6-fold higher quantity of cells permeated larger-pore DMSO Fibres across 24 hours in comparison with Water Fibres (Figure 13A), but DMSO Fibres had an 11% lower selectivity for nucleate cells (Figure 13B). The number of viable cells filtered through Water Fibres increased throughout the timepoints sampled, while DMSO Fibres decreased in viable cell numbers collected at successive timepoints. Filtered cell viability decreased from 90% to almost 60% between hour 5 and 24 of filtration for both fibres. Nucleate fractions were purified from 30% of inoculum hUCB cells to 92% (Water Fibre) or 81% (DMSO Fibre) for all filtrate timepoints. Inoculum hUCB reticulocyte fractions were reduced from 18% to 8.6% (Water Fibre) or to 5.7% (DMSO Fibre) after 24 hours of filtration. However, a majority of the filtrate collected was neither phenotypically nucleate red blood cells nor platelets (<20% CD235a⁺ or CD61⁺; Table 7, Figure 14).

After 24 hours of filtration, fibres were sectioned for confocal microscopy, and larger quantities of MNCs were observed within DMSO Fibres in comparison with Water Fibres. Cells which remained inside hollow fibres appeared viable and expressed Calcein AM (Figure 13C). Less than 1% of cells

contained within Water Fibres expressed enucleate cell phenotypes CD235a and CD61, while DMSO Fibres contained a higher number of cells expressing platelet marker CD61 (Figure 13D).

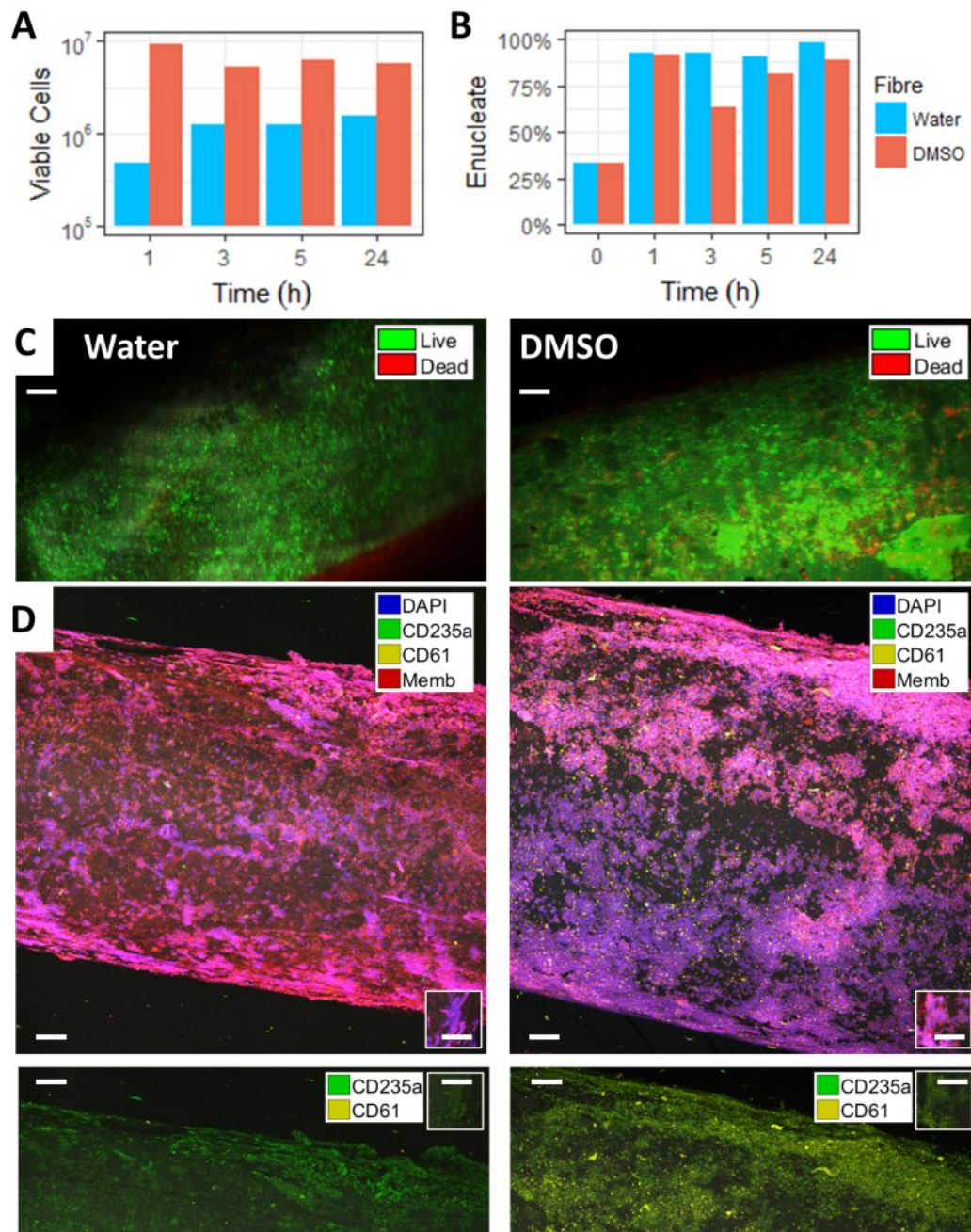


Figure 13: Cross-flow filtration efficiency.

(A) Number of viable and (B) percent enucleate cells collected at fibre outlets counted by trypan blue and methylene blue dye-exclusion at different time points of filtration. (C) Comparison of cell viability within Water (left) and DMSO (right) fibres after 24 hours of perfusion using confocal microscopy by detection of calcein-AM (green), ethidium homodimer-1 (red), and laser reflectance (grey) (100 μ m scale). (D) Comparison of cells types remaining within fibres by detection of (top) DAPI (blue), red blood cell marker CD235a (green), platelet marker CD61 (yellow), cell body stain CellMask (red), and laser reflectance (grey) or (bottom) only CD235a and CD61 (100 μ m scale).

Table 7: Filtrate collected within 6 hours of cross-flow and dead-end filtration for Water and DMSO fibre types.

Filtration rate, viability, and enucleate purity was assessed by manual cell counting on a hemocytometer using trypan blue or methylene blue dye-exclusion. Reticulocyte purity was measured by flow cytometry and corresponded to a Calcein AM-gated Hoescht and CD235a positive fraction as demonstrated in Methods and Figures.

| Platform Fibre | Cross-filtration | | Dead-end filtration | |
|---------------------------|------------------|------------------|---------------------|-------------------|
| | Water | DMSO | Water | DMSO |
| Filtration rate (cells/h) | 7×10^5 | 44×10^5 | 1.6×10^8 | 1.8×10^8 |
| Cell viability (%) | 88 | 89 | 96 | 99 |
| Enucleate purity (%) | 92 | 81 | 84 | 81 |
| Reticulocyte purity (%) | 1 | 9 | 74 | 71 |

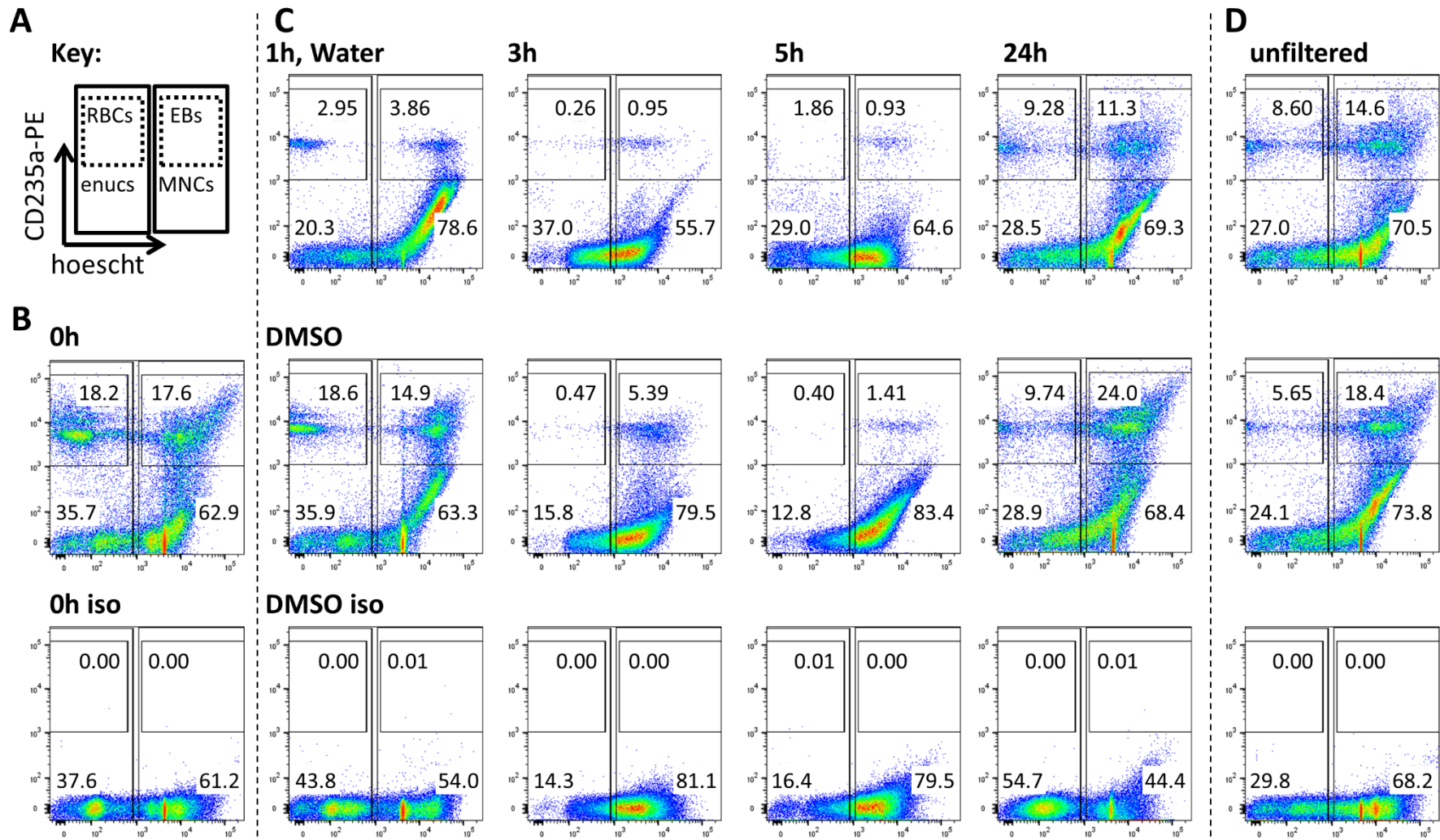


Figure 14: Cross-flow cell filtrate cell types.

(A) Schematic of flow cytometry gating procedure employing CD235a-PE and hoescht. (B) Inoculated hUCB phenotype pre-filtration with isotype. (C) Collected filtrate cell types at 1, 3, 5, and 24-hour timepoints for water (top) and DMSO (middle) fibres with DMSO fibre filtrate isotype (bottom). (D) Cell types remaining in the shell-side after 24 hours. Numbers within flow cytometry gates represent percent distribution of Calcein-AM⁺ gated cells.

4.4.3. Dead-end filtration filters large numbers of enucleate red cells

Dead-end filtration filtered 100-fold greater quantities of cells in comparison to the passive cross-flow filtration platform ($2 \cdot 10^9$ versus $2 \cdot 10^7$) in one-fourth the amount of time for both fibre types (6h versus 24h; Figure 15A). The manually counted enucleate purity of all filtered cells was 50% (Water Fibre) and 67% (DMSO Fibre). Phenotypically red blood cells were better purified using dead end filtration, as the original hUCB solution perfused was comprised of 19% reticulocytes (Calcein AM⁺CD235a⁺Hoescht⁻), and then both fibres purified reticulocyte content to over 70% of collected cells, peaking at 89% between hours 1 and 2.5, as measured by flow cytometry (Table 7; Figure 15B).

Fibres imaged at the end of the 6-hour dead-end filtration indicated that a similarly large number of cells were found within both Water and DMSO fibre types. While a greater number of cells in cross-flow filtration remained within DMSO Fibres, dead-end filtration promoted a similar filtration rate for both fibres (Figure 15C), and CD235a⁺ enucleate and nucleated erythroblasts could be found in the process of filtration through transverse sections of DMSO Fibres (Figure 15D). The viability of cells imaged in the process of dead-end filtration was noticeably less than cross-flow filtration, especially for Water Fibres, with a higher expression of ethidium homodimer-1 (Figure 15E). For both fibres, small cells could be imaged on the abluminal fibre surface after filtration (Figure 15F). While filtered cell viability remained >97% for the first 4-hours of filtration, the viability of cells filtered by Water Fibres decreased to 83% at hour 6 while DMSO Fibres remained at 99%, in agreement with cells imaged within Water Fibres (Table 7).

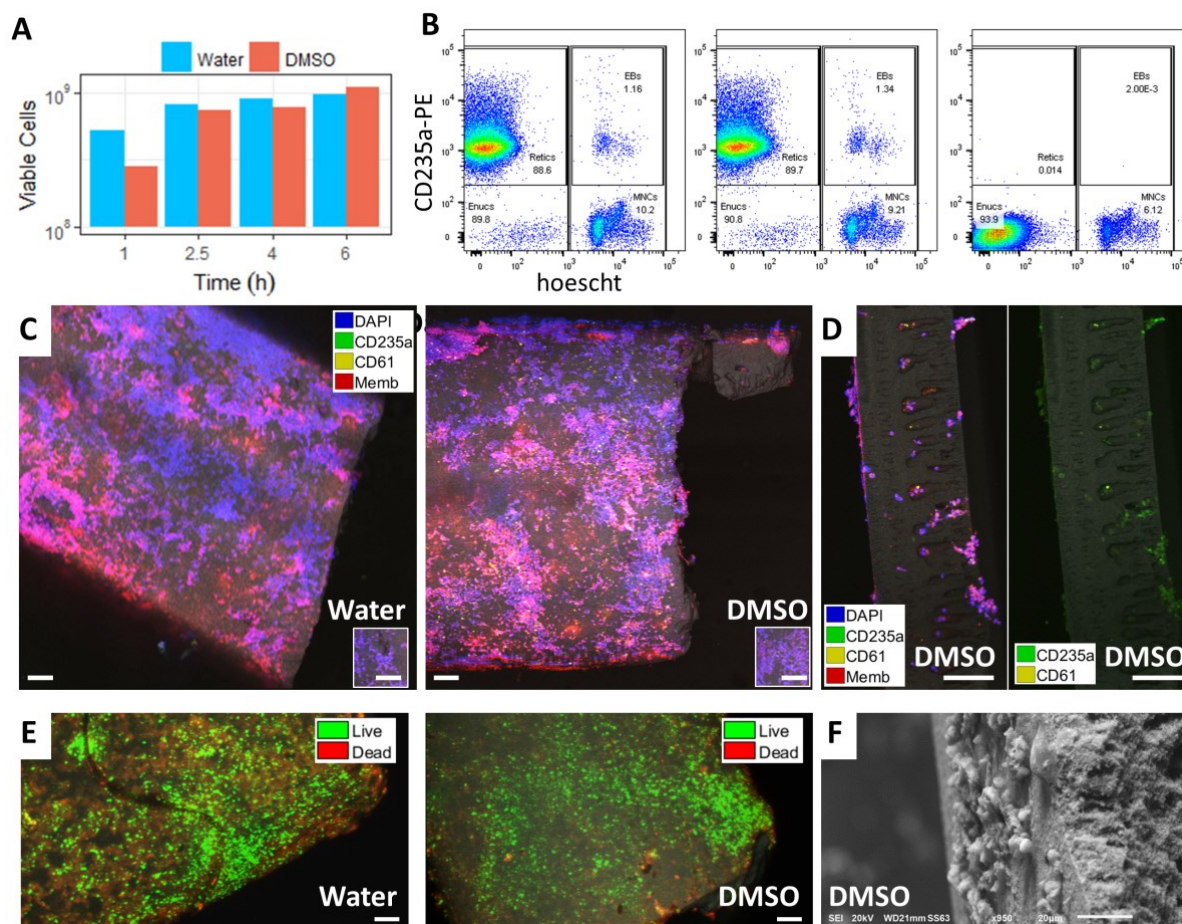


Figure 15: Dead-end filtration efficiency.

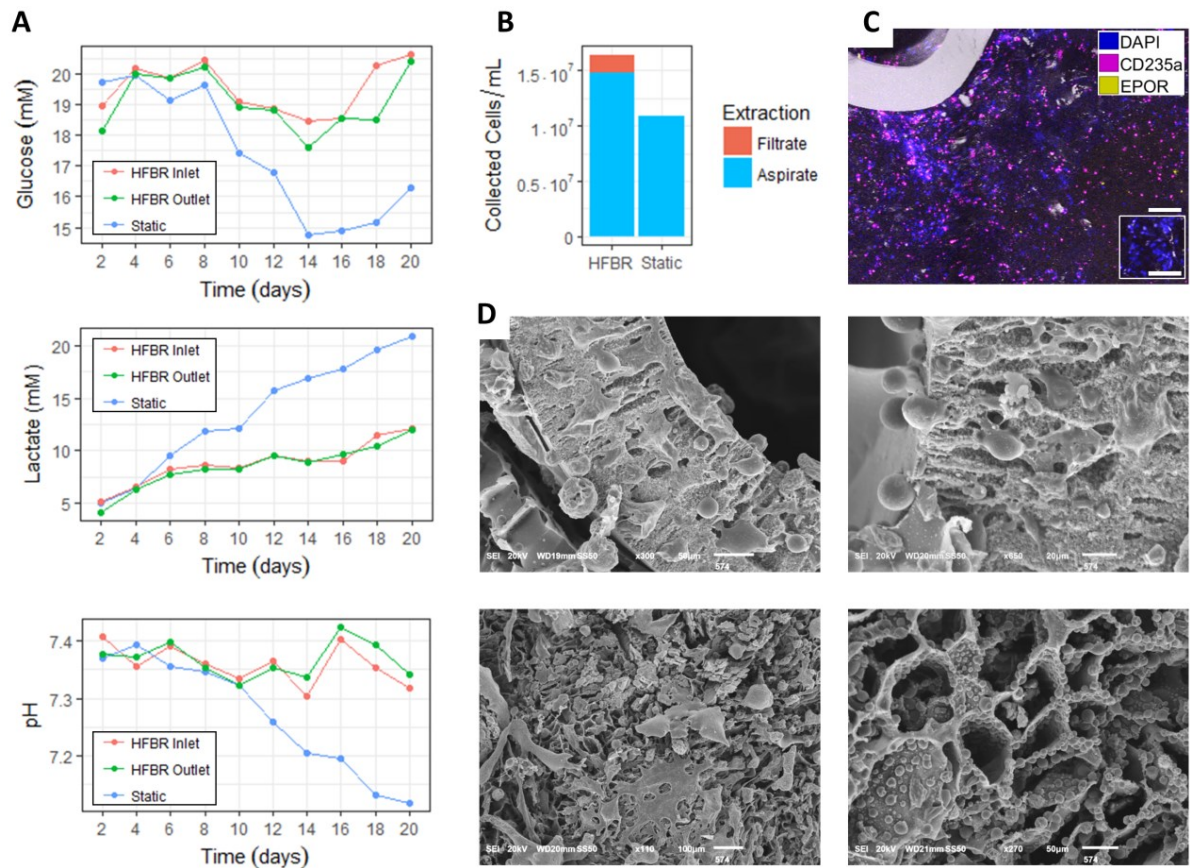
(A) Viable cell filtrate collection at 1, 2.5, 4, and 6-hours of filtration. (B) Filtrate cell types after 2.5-hours of perfusion for (left) water fibre and (center) DMSO fibre with (right) DMSO fibre isotype. (C) Comparison of cells remaining within fibres after 6 hours of perfusion within the Water (left) and DMSO (right) fibre by confocal microscopy detection of DAPI (blue), red blood cell marker CD235a (green), platelet marker CD61 (yellow), cell body stain CellMask (red), and laser reflectance (grey) (100 μm scale). (D) Confocal images of a magnified traverse section of the DMSO fibre after 6 hours of filtration with (left) identical marker detection and (right) detecting only CD235a (green), CD61 (yellow), and laser reflection (grey) (100 μm scale). (E) Comparison of cell viability within Water (left) and DMSO (right) fibres using confocal microscopy with calcein-AM (green), ethidium homodimer-1 (red), and laser reflectance (grey) (100 μm scale). (F) SEM of outer, abluminal surface of DMSO fibre after 6 hours of dead-end filtration (20 μm scale)

4.4.4. Continuous fibre perfusion increases nutrient exchange and cell proliferation in a 3D porous scaffold

The perfusion HFBR maintained a more stable extracellular glucose, lactate, and pH profile over 21 days in comparison with static culture, with pH and lactate of supernatant static culture medium reaching toxic levels by the end of culture (pH 7.1, >20 mM lactate; Figure 16A). Recycled nutrients and metabolites entering the inlet and outlet of the bioreactor fibre varied <5% in concentration, signifying perfusion was rapid enough to approximate pseudo-steady state conditions. 50% more cells per scaffold volume were extracted from the HFBR platform in comparison with the static platform,

10% of which were continuously harvested by filtration (Figure 16B). The HFBR was replenished with half the amount of medium (1.56 mL versus 3.3 mL per 10^6 cells inoculated over 21 days of culture) in comparison with the static culture throughout the culture duration.

Erythroblasts ($CD235a^+DAPI^+$) and reticulocytes ($CD235a^+DAPI^-$) were imaged by confocal microscopy near the HFBR Water Fibre (Figure 16C), and cells could be observed crossing the hollow fibre in SEM images (Figure 16D). In addition, high cell densities were imaged within the bulk scaffold surrounding the hollow fibre which included small spherical erythroid morphologies in addition to large, spread, adherent morphologies (Figure 16D) where erythroid ($CD235a$, $CD71$, EPO-Receptor or EPO-R), hematopoietic ($CD36$, SCF-Receptor: SCF-R or C-KIT), endothelial ($CD31$), and osteogenic phenotypes (osterix or OSx, osteopontin or OPN) were imaged (Figure 17). This demonstrates the utility of ceramic hollow fibres as a modular installation within long-term 3D cell culture platforms in order to enhance nutrient transport, cell proliferation, and incorporate continuous, purified cell harvest, and should be investigated for their role in generating biochemical gradients preferential for diverse cell morphologies.



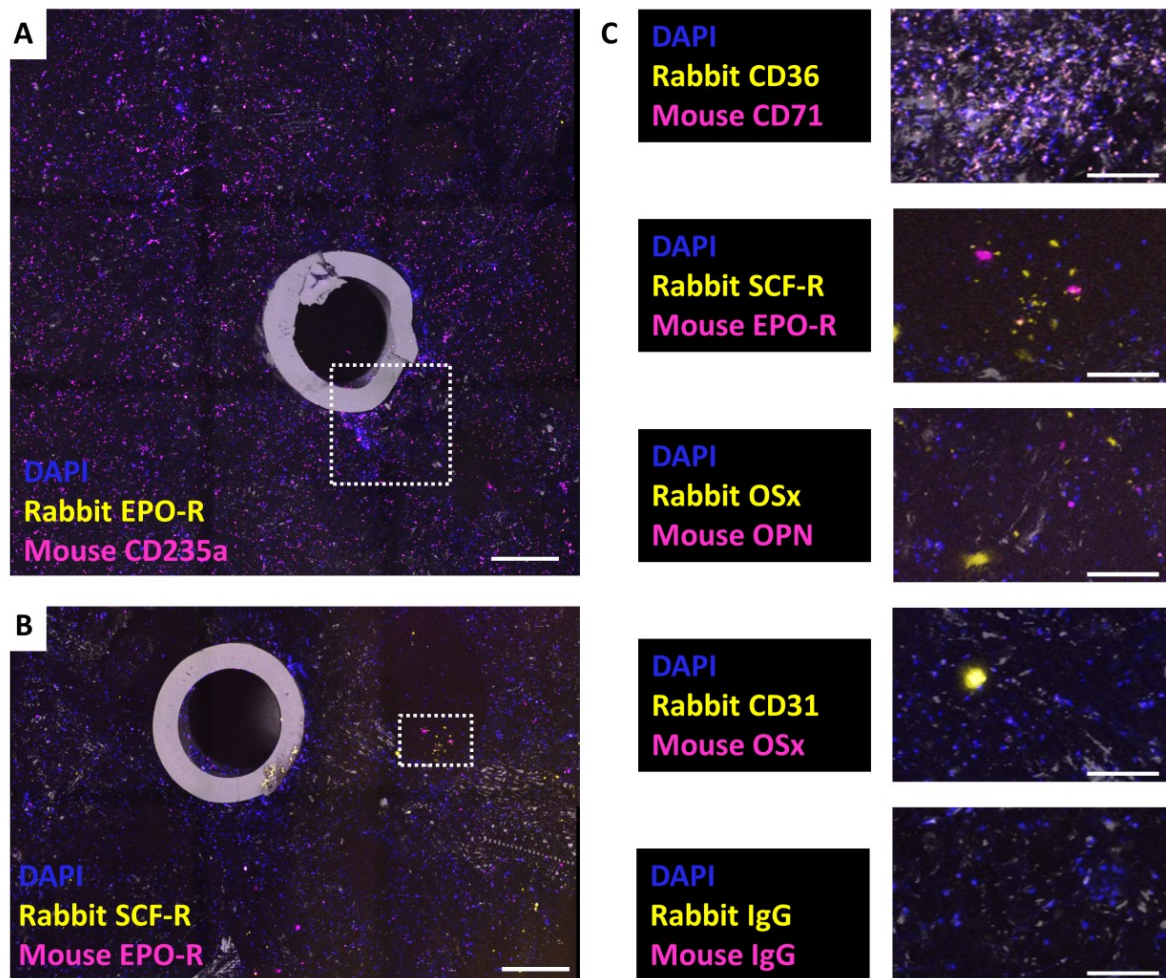


Figure 17: Expression of hematopoietic, osteogenic, and endothelial markers within the scaffold region of day 21 HFBR cross-sections.

(A) A large-scale 3D confocal image highlighting the inset cropped for Figure 16C (500 µm scale bar). (B) A large scale 3D confocal image (500 µm scale bar) of demonstrating inset volumes represented in (C) with erythroid, hematopoietic, osteogenic, and endothelial phenotype markers expressed on nucleated cells within HFBR sections at day 21 (100 µm scale bars), with the bottom image representing a negative isotype control of a static scaffold at day 21. Laser reflection was captured in grey on all images to demonstrate fibre and scaffold structure.

4.5. Discussion

Hollow fibres are currently used in biologics, viral, and cell therapy bioreactors to enhance biochemical nutrient diffusion and to isolate viral or antibody products (Usuludin et al. 2012; Housler et al. 2012; De Bartolo et al. 2009; Sheu et al. 2015). Ceramic hollow fibres have been extensively characterized for chemical filtration (Faiz et al. 2013; M. Lee et al. 2014; Gouveia Gil et al. 2015; Melanie Lee et al. 2015), and have been recently used for the filtration of proteins (Liu et al. 2006). However, current biomedical progress in ceramic filtration has been focused into nano- and reverse osmosis filtration to separate biological products from cells, and few studies have investigated the role of ceramics in the microscale separation of cellular fractions (M. Lee et al. 2015; Afonso & Yaez 2001; Schaefer et al. 2005). Microporous cell filtration has typically been performed by dead-end filtration through polymeric meshes or microfluidic separations (Xia et al. 2016), neither of which have been incorporated into 3D cell culture scaffoldings as a source of continuous perfusion. Recently, the BSEL laboratory has employed hollow fibres 3D perfusion bioreactors to continuously harvest cells (Misener et al. 2014), but no comparison of the fabrication methods, cell-filtering properties, or long-term 3D culture benefits of these fibres has been carried out.

Presented parameters for hollow fibre fabrication and subsequent analysis by Asma Tahlawi imparted a wide range of pore sizes, structures, and filtration efficiencies, and parameters effecting mechanisms of spinning and phase inversion seemed especially sensitive (Schaefer et al. 2005). During spinning; bore fluid can penetrate the hollow fibre membrane, forming large fibre-like voids in the ceramic structure which stops upon contact with the water bath during phase inversion. Therefore, altering bore fluid or time-of-flight between spinneret and water bath (air-gap distance) produced longer finger-like void pores: decreasing tortuosity but also structural integrity of the fibre.

Spinning fibres around a DMSO bore fluid produced average pore sizes more similar to those found within bone marrow sinus wall, where reticulocytes egress through endothelial gaps of 2-3 μm (Lichtman 1978). However, these large pores often rendered fibres structurally unstable to be used (Fibre 6) and others contained a larger, tortuous sponge layer, occluding cell passage and causing rupture (Fibres 7 and 8). Therefore, stability and tortuosity and not pore size became the critical factor for cell filtration, and as cells could only be filtered using fibres that had uniformly smooth finger-like

channel voids. Filtrate yield may be further increased if fibres with larger pore sizes could be fabricated, but a tight control on pore size distributions must be implemented to not dilute filtrate purity.

The small average pore sizes of examined fibres did not prohibit the passage of cells, but may have limited filtration efficiency especially through fouling. Two centimetres of examined ceramic fibres filtered nearly half a billion RBCs per hour despite having an average pore size below 1 μm . Although MIP only provided an average pore size, variability in pore sizes could be observed during imaging, and it's likely that cells successfully egressed through larger-than-average pore sizes, while cells became trapped and clogged in smaller-than-average pores. In cross-flow filtration, larger-pore DMSO fibres (Fibre 5) filtered a greater number of cells than Water fibres (Fibre 1). However, DMSO fibre filtration proceeded at a successively slower rate with time, suggesting the greater quantity of larger, nucleated cells imaged within DMSO fibres may have become trapped and fouled fibre filtration. In dead-end filtration, larger pores on the inner hollow fibre surface may have allowed more cells to enter and, unable to pass through smaller outer surface pores, remain trapped within the fibre wall causing a reduction of *in situ* viability. While cells could be imaged filtering through fibres after 21 days of HFBR culture, a much smaller number of cells were found in the HFBR filtrate relative to those aspirated from the scaffold, indicating that while small pore sizes did not prohibit the passage of cells, their filtration may have been hampered during long-term culture.

Our scaled-up HFBR platform demonstrated hollow fibre perfusion improved nutrient diffusion, metabolite removal, and cell expansion at culture termination while allowing continuous cell harvest by filtration throughout culture. The HFBR operated at a 40-fold increased scaffold volume (5 mL HFBR vs. 0.125 mL static cubes) and incorporated only one hollow fibre when many more could be incorporated in a similar scaffold volume. Even so, the platform demonstrated the perfusion of one hollow fibre reduced toxic metabolite accumulations found in static scaffold culture. These toxic metabolites may have limited the scaffold culture from reaching the higher day 21 aspirate cell numbers found within the HFBR, which contained a visibly dense number of cells.

Hollow fibre perfusion may help mimic the physiological harvest of cells and structuring of cell environments. Marrow egress is a process thought to restructure RBC membrane proteins towards final maturation (Leblond et al. 1971), as the stress created by sinus blood flow and the tight pore

geometries provides mechanical stimuli. This process has been mimicked *in vitro* for the mechanistic study and production of other cell types, such as platelets stripped from megakaryocyte cytoskeletons at the sinusoidal wall (Di Buduo et al. 2015; Thon et al. 2014). In addition, the impact of vessel placement on cell and cell niche distribution within the hBM has been well-documented, both for hematopoietic stem and progenitor cell niches, as well as more mature erythroid niches, or erythroblastic islands, and stems from the distribution of biochemical gradients between nutrition provided by vascular perfusion, and stimuli generated from cell-cell interactions within the marrow (Itkin et al. 2016; Mohandas & Prenant 1978; Weiss 1984). The distribution of different cell phenotypes and morphologies within the HFBR could indicate that hollow fibre nutrient perfusion could be similarly structuring a multi-lineal environment for 3D red blood cell production.

4.6. Conclusion

In summary, 8 novel microporous ceramic hollow fibres were fabricated and structurally analysed by Asma Tahlawi, 4 of which were examined for cell filtration, 2 of which successfully filtered cells, whereupon 1 was incorporated into a porous 3D scaffolding for long-term culture. These HFfs allowed for the continuous filtration of RBCs from hUCB and improved nutrient diffusion for dense hUCB MNC 3D cultures. Two operation modes using ceramic fibres have been implemented with different objectives: cross-flow filtration for a better viable enucleate purity, and dead-end filtration for a much higher, faster reticulocyte product yield. Incorporation of ceramic hollow fibres into a 3D porous scaffolding not only improved diffusion and cell density, but also populated the scaffold with cells of different lineages. Biochemical and cellular 3D scaffold gradients imposed from perfused hollow fibres during long-term culture should be further characterized to optimize reactor, fibre, and scaffold dimensions and medium composition and perfusion for cell therapy output.

5. Development of an image analysis tool to spatially quantify 3D cellular distribution and association.

Three-dimensional imaging techniques provide spatial insight to environmental and cellular interactions and are implemented in various fields, including tissue engineering, but have been restricted by limited quantification tools which misrepresent or underutilize the cellular phenomena captured. This study develops image post-processing algorithms pairing complex Euclidean metrics with Monte Carlo simulations in order to quantitatively assess cell and microenvironment spatial distributions while utilizing, for the first time, the entire 3D image captured. While current methods only analyze a central fraction of presented confocal microscopy images, the proposed algorithms can utilize 210% more cells to calculate 3D spatial distributions which can span a 23-fold longer distance. These algorithms seek to leverage the high sample cost of 3D tissue imaging techniques by extracting maximal quantitative data throughout the captured image.

In this section, Mark C. Allenby performed all experiments, instrumental analyses, and wrote all computational postanalyses. Dr. Ruth Misener assisted in the revision of the final manuscript.

5.2. Introduction

Native and engineered tissues maintain spatial architecture of cells, extracellular matrix proteins and humoral factors via interactive adhesive motifs, paracrine niche interaction, and soluble factor gradients. The interplay of these factors promotes *de novo* cell and tissue formation, pathogen response, cellular chemotaxis, and tissue homeostasis (Cha et al. 2012; Pampaloni et al. 2007; Baker & Chen 2012; Khademhosseini & Bong 2009; Niklason et al. 2010). Developments for the *in situ* capture of these cell-environment processes are focused on designing instruments and probes to enhance imaging depth, spatial resolution, speed, and specificity (Appel et al. 2013; Weissleder & Nahrendorf 2015; Ntziachristos 2010; Flower 2012; Ntziachristos 2006). However, the quantitative characterization of imaged tissue environments is often constrained by spatially selective or underutilized image analyses that discard data that are expensive to acquire, which inherently limits the applicability of these algorithms (Bjornsson et al. 2008; Delarue et al. 2014; Meddens et al. 2013; Acar et al. 2015; Takaku et al. 2010; Nombela-Arrieta et al. 2013). Therefore, image analysis tools that enable quantitating spatial heterogeneity by unbiasedly utilizing the complete tissue sample image thus maximizing information output are required.

Quantitative image analysis has been applied in various systems to determine how spatial tissue organization influences cell activity and fate. Studies include *in vivo* animal models, centered around intravital imaging at continuous but short (<24 hours) durations limited to the few animals or tissues (zebrafish, murine calvarial marrow) able to be imaged while alive (Lo Celso et al. 2009; Spencer et al. 2014; Khorshed et al. 2015; Bertrand et al. 2007; Binder & Zon 2013), or *in vitro* 2D cell cultures appropriate for studies of spatial organization and cell-cell association (Thon et al. 2014; Ma et al. 2015; Toh et al. 2015). Most *in vivo* and *in vitro* 3D cultures are not able to implement intravital imaging throughout growth area of interest and require invasive techniques or culture termination to characterize the formation of cell-environment tissue networks *in situ* (Di Buduo et al. 2015; Rodenhizer et al. 2016; Eng et al. 2013; Rnjak-Kovacina et al. 2014; Liu et al. 2015; Takaku et al. 2010; Nombela-Arrieta et al. 2013). Maximizing extraction of data from these rare, expensive 3D analyses has been a major driver to develop new imaging instruments and techniques rather than the postimaging algorithms that

quantitate their output (Appel et al. 2013; Weissleder & Nahrendorf 2015; Ntziachristos 2010; Flower 2012; Ntziachristos 2006).

Varied instruments exist for imaging analysis of tissue constructs, including magnetic resonance imaging, computed tomography (CT), and optical imaging. The utility of these imaging techniques are expanded through the use of spatially “tagged” contrast agents or probes (e.g. nanomaterials, labelled small and large molecules, fluorescent proteins), where discrete cells, phenomena, or regions of interest can be spatially identified (Weissleder & Nahrendorf 2015). Magnetic resonance and CT imaging allow for full specimen penetration but lack multiplexed probe detection, have poorer sensitivity, and lower resolution; only recent advancements have allowed imaging at single-cell resolution (Appel et al. 2013). Optical imaging allows for the quantitative analysis of a wide variety of cell-environment interactions and can characterize multiple phenotypes, organelle, and matrix proteins simultaneously by implementing light microscopy (LM) with immunohistochemistry (IHC) or immunofluorescence (IF) imaging of probes and chemicals delineating cell or tissue type, status, and their interactions to quantify the effects of the tissue environment on cell differentiation, proliferation, and stimulation spatially at multiple aspect sizes (Ntziachristos 2006; Bjornsson et al. 2008). The versatility of optical imaging is frequently implemented to determine quantitative co-localization from the subcellular protein scale up to multicellular and tissue scales, and is implemented here as an application for image postanalysis algorithms.

Herein, quantitative tools are developed to analyze 3D spatial heterogeneity throughout the entire captured image in order to maximize data output for expensive, destructive imaging analyses. They work by dividing the full image space into regions, counting the number of cells within each region, and calculating the volume of each region so that regional cell density can be determined. The novel algorithms enable the assessment of complex volumes in regions towards the periphery of the image thus increasing analysis distance (range) as well information content (number of cells surveyed). Nonetheless, the proposed 3D analysis represents an estimation whose accuracy is dependent on user-defined inputs. Therefore, results must be validated against controls, such as regions of known volume and data of known density.

Two algorithms to quantify full-image spatial heterogeneity are presented and applied to immunofluorescent (IF) images of a 3D culture system consisting of a synthetic scaffold impregnated with hollow fibres (Panoskaltsis et al. 2012). The first algorithm quantifies the distribution of cellular density from a region of interest and is applicable to recent *in vivo* studies, including the measurement of oxygen and cellular phenotype, stress, and depiction of regional niches of cell activity and migration (Acar et al. 2015; Takaku et al. 2010; Nombela-Arrieta et al. 2013; Lo Celso et al. 2009; Spencer et al. 2014; Khorshed et al. 2015). The second algorithm quantifies cellular association by calculating the distribution of cellular density from each cell imaged. Cell association metrics have been useful to assess roles of cell-cell communication, cell attraction and repulsion, as well as cell co-localization (Bjornsson et al. 2008; Delarue et al. 2014; Meddens et al. 2013; Ma et al. 2015; Liu et al. 2015). While current cellular distribution algorithms only analyze a central fraction of imaged data, the method presented herein allows for the utilization of all cells and environmental space imaged (Bjornsson et al. 2008; Delarue et al. 2014; Meddens et al. 2013). Specifically, the presented algorithms utilize 3.6-fold more 2D area or $2.5 \cdot 10^4$ -fold more 3D volume and survey 1116 cells instead of 235 cells using the 2D analysis or 524 cells using the 3D analysis to help leverage the high cost of tissue culture.

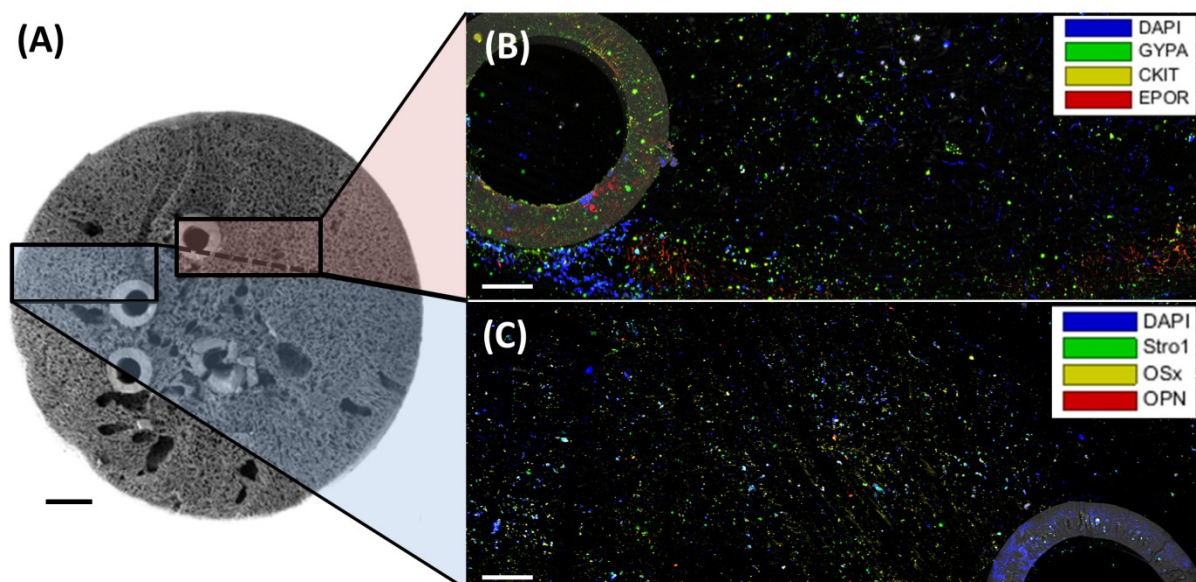


Figure 18: Imaging regions of the 3D culture device.

(A) The topology of the hollow fiber bioreactor as a representative SEM cross-section, and (B, C) surveyed 5-color confocal images. Scale bar in (A) is 1 mm and in (B) and (C) are 100 μ m, and bioreactor material reflection is represented in greyscale. Markers analyzed were DAPI for cell nuclei, and cell phenotypes: glycoprotein-A (GYPA), erythropoietin receptor (EPO-R) and stem cell growth receptor (c-kit) in Fig. 1B, and Stro-1 (Stro1), osterix (OSx), and osteopontin (OPN) in Fig. 1C.

5.3. Methodology

The incorporation of perfused hollow fibres in long-term hUCB MNC cultures maintained multiple different cell lineages by day 21 (Figure 17) that appeared to be uniquely distributed away from hollow fibre perfusion in the bioreactor scaffold. This heterogeneous distribution could be due to the different mechanical, biochemical, and cellular gradients formed as a function of distance from hollow fibres. The description of these *in situ* cellular gradients could provide an *ex vivo* model for the physiological distribution of human marrow cells, and lead to further development of an optimised hollow fibre bioreactor for blood production: eliminating spatial regions unnecessary for blood development. Therefore, quantitative post-analyses of 3D confocal microscopy images were written to describe spatial cell locations within the reactor.

5.3.1. 3D Cultures

Mononuclear cells (MNCs) from human umbilical cord blood were cultured in a hollow fiber bioreactor as previously described in Section 4. In brief, a polyurethane scaffold was formed around ceramic hollow fibers and coated with collagen. Cord blood MNCs were inoculated into the scaffold while hollow fibers were perfused with serum-free medium for 28 days, when a representative SEM to demonstrate bioreactor topology was taken (Figure 18A).

5.3.2. Immunofluorescent Sample Preparation

For analyses, the 3D cultures were snap-frozen in liquid nitrogen and preserved at -80°C until sectioning. Sectioning occurred at -20°C into thick histological sections of approximately 1mm. The frozen sections were directly fixed in ice cold 4% paraformaldehyde (BDH Laboratory Sciences, Poole, Dorset, UK) in PBS (Life Technologies, Paisley, UK) overnight followed by a 2-hour permeabilization with 0.1% Triton X-100 (Sigma-Aldrich, Poole, Dorset, UK) in staining buffer [1% BSA (Sigma-Aldrich), 0.5% Tween-20 (Promega, Southampton, Hampshire, UK), 0.01% NaN₃ (Sigma-Aldrich) in PBS]. This was followed by a 4-hour blocking step with 10% donkey serum (AbCam, Cambridge, UK) in staining buffer and overnight incubation with primary antibodies and isotype controls (Table 8; AbCam) in staining buffer at 4°C. Thereafter, 6-hour staining was undertaken with secondary antibodies: donkey anti-rat Alexa Fluor 488, donkey anti-sheep Alexa Fluor 488 (AF488), donkey anti-rabbit Alexa Fluor 555 (AF555), and donkey anti-mouse Alexa Fluor 647 (AF647) all at 1:500 dilution

in staining buffer at 4°C (Life Technologies). These steps were followed by a DAPI counterstain (Fisher Scientific, Loughborough, Leics, UK) overnight at 50 µM in PBS at 4°C, and samples were stored in 0.01% NaN₃ in PBS at 4°C. Each step was separated by single or multiple 15 minute washing steps in appropriate buffer.

Table 8: Confocal 3D immunofluorescent microscopy primary antibody staining protocol.

All products were obtained from AbCam with product number stated. The two samples presented in Figures 1-7 were prepared alongside appropriate isotype and unstained controls.

| Fig. 1B | Fig. 1B Isotype | Fig. 1C | Fig. 1C Isotype | Unstained |
|---|----------------------------------|---|----------------------------------|-----------|
| 1.7 µg/mL rat anti-human glycoporphin-A (ab33386) | 1.7 µg/mL rat IgG2b (ab18437) | 6.7 µg/mL sheep anti-human Stro-1 (ab192766) | 6.7 µg/mL sheep IgG (ab37385) | None |
| 8.3 µg/mL rabbit anti-human C-Kit (ab111033) | 8.3 µg/mL rabbit IgG (ab172730) | 8.3 µg/mL rabbit anti-human osterix (ab94744) | 8.3 µg/mL rabbit IgG (ab172730) | None |
| 33.3 µg/mL mouse anti-human erythropoietin-receptor (ab56310) | 33.3 µg/mL mouse IgG2a (ab91361) | 3.33 µg/mL mouse anti-human osteopontin (ab69498) | 33.3 µg/mL mouse IgG2a (ab91361) | none |

5.3.3. Confocal Microscopy Image Acquisition

The fixed, stained microscope sections were imaged on a Leica SP5 inverted confocal microscope with Leica LAS AF software (Leica, Milton Keynes, UK) using 405, 453, 488, 543, and 633 nm lasers and filters for DAPI, reflectance, AF488, AF555, and AF647 stains in 2 sequences of excitation for 2- then 3-color collection without any detectable spill-over. Images were taken at 512x512 pixel resolution using a 10x dry microscope lens for a resolution of approximately 3.03 µm per pixel with Z-stacks acquired in 5 µm slices, selected as the minimum lens magnification to ensure single-cell stain recognition (Khorshed et al. 2015). All laser voltage, filter wavelength, and capture settings were identical for corresponding samples and controls. Each sample was captured as three adjacent 3D images with 7% overlap to allow collation of three individual 1551 x 1551 µm² square images into a 4437 x 1551 µm² rectangular image with a depth of 350 µm for Figure 18B, and 230 µm for Figure 18C. Unstained and isotype controls were captured under identical conditions. Images were not manipulated.

5.3.4. Confocal Cell Localization

Once captured, images were analyzed using the Fiji image processing package of ImageJ: (1) the *grid/collection* package collated together adjacent 3D images, (2) the *subtract background* package decreased auto-fluorescence and self-absorbance, and, finally (3) the *3D object counter* package located the center of each individual fluorescence stain, $(X, Y, Z)_c$, which was exported into MATLAB for further analysis (The MathWorks, Inc., Natick, USA) (Schindelin et al. 2012; Preibisch et al. 2009; Bolte & Cordelieres 2006). Representative confocal images are shown in Figure 18B and Figure 18C with stain localization for Figure 18B in Figure 19A and Figure 19B. The presence of each fluorescent antibody stain, $(X, Y, Z)_c$, was biologically validated in comparison to isotype controls, which contained less than 1% of detected sample stains. All computational post processing was run on a 3.4 GHz machine with 8 GB RAM and an Intel® Core™ i7-4770 CPU. Processing times are provided and correspond as 1 second to $1.2 \cdot 10^8$ random points sampled from a uniform distribution in MATLAB on this machine.

Table 9: Mathematical parameters used.

| Parameter | Description | Ref |
|---------------------------|-------------------------------------|----------|
| $(X, Y)_c ; (X, Y, Z)_c$ | 2D/3D cell position | [1], [3] |
| $(X, Y)_a ; (X, Y, Z)_a$ | Line or point of interest | [1], [3] |
| R_f | Cell to region of interest distance | [1], [3] |
| R_{\max} | Maximum surveyable distance | - |
| A_i | Examined region area | [2] |
| $R_i ; R_{i-1}$ | Bin of examinable region | [2] |
| $A_e ; A_{ee}$ | Extraneous binned region area | [2] |
| $V_L ; (X, Y, Z)_L$ | Total image volume; limits | [4], [5] |
| $V_i ; V_{i-1}$ | Examined region volume | [4], [5] |
| $V_{LS} ; (X, Y, Z)_{LS}$ | Subset volume; limits | [5] |

5.3.5. 2D Distance Distribution

Assessing cell density as a function of distance from an environmental region of interest is useful in examining cellular gradients across tissue sections [14-19]. In order to determine cellular distribution in 2D, 3D confocal image z-stacks (Figure 18B) were compressed into 2D so that a given line of interest running perpendicular to the image plane becomes a point $(X, Y)_a$. Cellular heterogeneity was studied as a function of XY distance from this point of interest (Figure 19C and Figure 19D), where individual cell position $(X, Y)_c$ and its distance from the point of interest $(X, Y)_a$ was defined as 2D Euclidean distance:

$$R_c = \sqrt{(X_c - X_a)^2 + (Y_c - Y_a)^2} \quad [1]$$

The full image field distance was defined as the distance from the fiber to the furthest pixel of the image, R_{max} . The full distance was then discretized into bins of equally spaced radii, R_i , which form concentric circles of area $\pi(R_i^2 - R_{i-1}^2)$. However, if the circle of radius R_i centered at $(X, Y)_a$ encompassed space outside of the cubic image limits, the extraneous volume, A_e , must be subtracted off:

$$A_e = \frac{R_i^2}{2} \left(\frac{\pi S_i}{180} - \sin(S_i) \right) \quad [2]$$

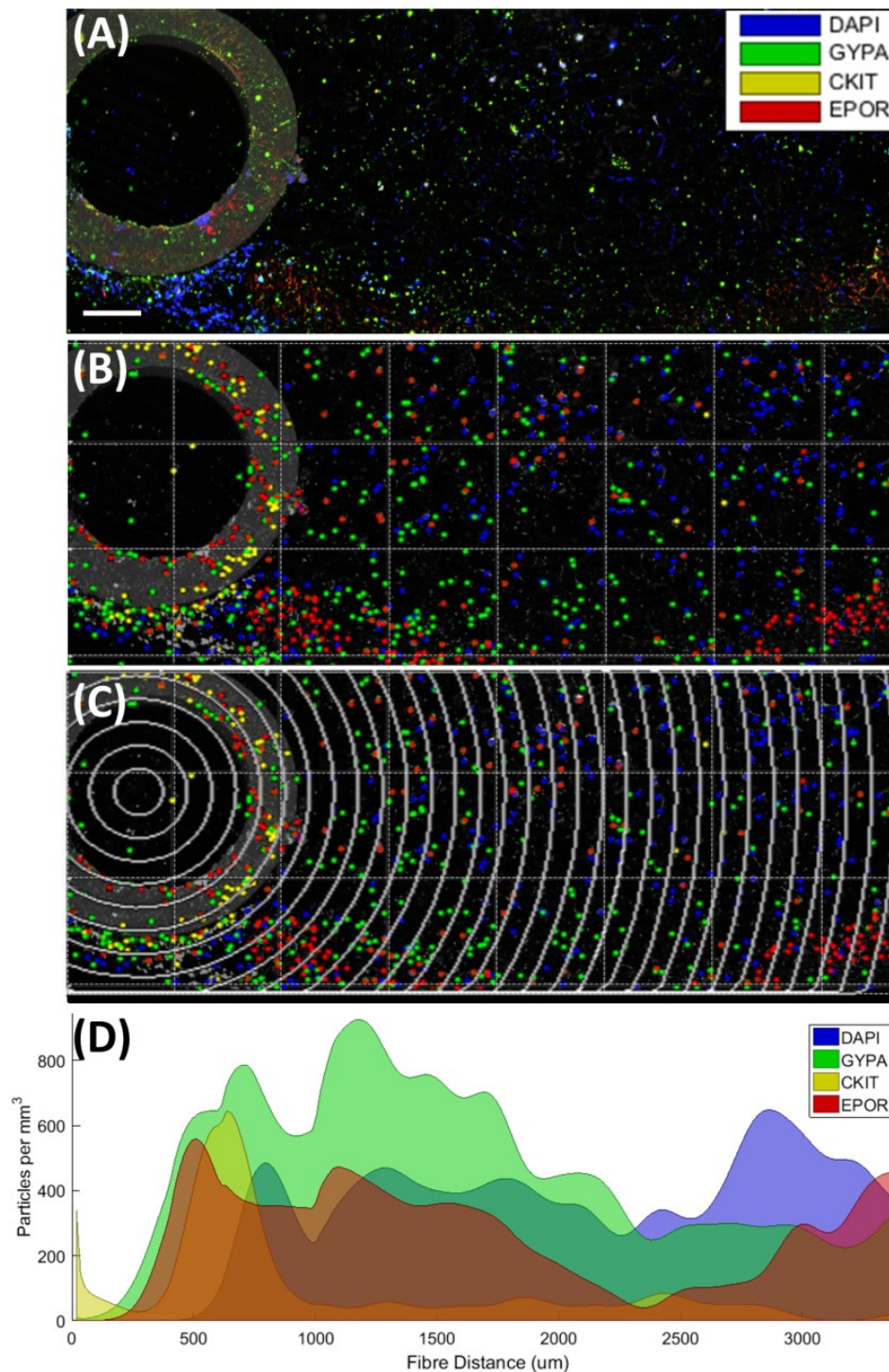


Figure 19: A visualization of the 2D distance cell density analysis.

(A) Immunofluorescent images were captured and (B) fluorescent markers were identified by object-based co-localization. The fiber center was defined and (C) volumes of concentric spaces confined to image limits were calculated explicitly or estimated probabilistically in order to determine (D) cell and phenotype density at all distances captured by confocal microscopy. Scale bar in (A) is 100 μm .

The arc angle of the circle area segment protruding out of the image, S_i , is calculated through trigonometric identities:

$$S_i = \cos^{-1} \left(\frac{D_{a \rightarrow k1}^2 + D_{a \rightarrow k2}^2 - (Y_{k1} - Y_{k2})}{2D_{a \rightarrow k1} D_{a \rightarrow k2}} \right) \quad [3]$$

Where $D_{a \rightarrow k1}$ represents the 2D Euclidean distance between point $(X, Y)_a$ and $(X, Y)_{k1}$, see Figure 20A for terminology.

In cases where the extraneous circle area included a vertex of the rectangular image limits, two overlapping extra-image volumes have been subtracted from the circular area which must be corrected by adding back the overlapping extraneous area A_{ee} :

$$A_{ee} = S_i - \sqrt{P_A(P_A - D_{a \rightarrow k2})(P_A - D_{a \rightarrow i})(P_A - D_{i \rightarrow k2})} - \sqrt{P_B(P_B - D_{a \rightarrow j2})(P_B - D_{a \rightarrow i})(P_B - D_{i \rightarrow j2})} \quad [4]$$

Where S_i , from Equation 4, here describes the arc angle of the circle slice inscribing A_{ee} , while P_A and P_B are triangle perimeters which exclude the overlapped circle section A_{ee} , described as:

$$P_A = 0.5D_{a \rightarrow k2} + D_{a \rightarrow i} + D_{i \rightarrow k2} \quad [5]$$

$$P_B = 0.5D_{a \rightarrow j2} + D_{a \rightarrow i} + D_{i \rightarrow j2} \quad [6]$$

So that the final volume of the concentric circles constrained to rectangular image limits is:

$$A_i = \pi(R_i^2 - R_{i-1}^2) - A_e + A_{ee} \quad [7]$$

With all terms corresponding to the diagram in Figure 20A.

In order to assess complex 3D geometries that can also be validated against analytical 2D solutions, Monte Carlo methods have been employed to estimate complex geometrical spaces by generating points from a uniform distribution within a measureable region, such as the complete image volume (Anon 2017b). However, this method may be inaccurate when insufficient points are generated. Therefore, in the 2D case, *estimation error* was defined as the percent difference of the Monte Carlo estimation from the analytical solution. As there was no analytical solution for many 3D cases, *Monte Carlo convergence* was defined as the percent difference between estimated Monte Carlo solutions when 10^4 additional uniformly generated points were appended (Kathryn et al. 2016).

The Monte Carlo method was validated for the typical 2D distance distribution (Figure 20C) by calculating the average *estimation error* and *Monte Carlo convergence* across 4 image geometries, each broken into 40 equidistant intervals from a point of interest. An estimation error of 2.75% from

the explicit calculation was reached for 10^{-6} % Monte Carlo convergence in iterations of 10^4 points, but required 8.6 minutes. A 10^{-2} % Monte Carlo convergence, which corresponded to an average of 2.4×10^6 generated points or 0.02 seconds per distance interval with estimation error below 5% in the 2D distance distribution, was utilized for all subsequent distance distribution analyses.

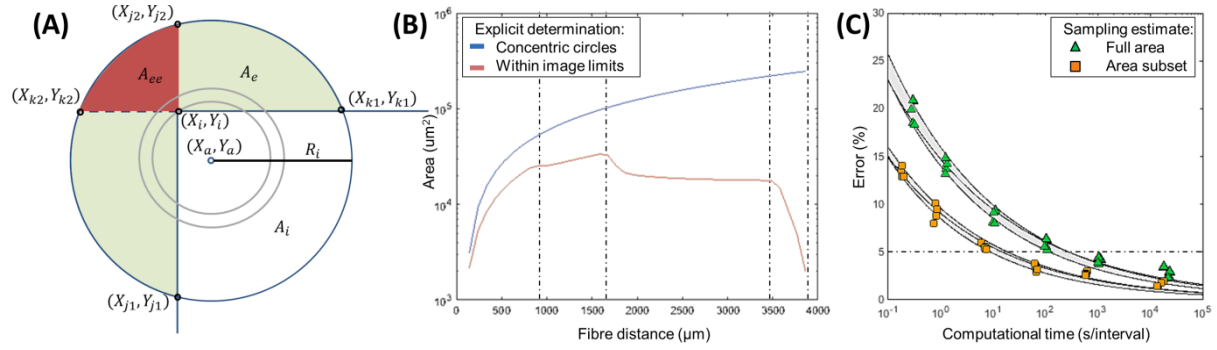


Figure 20: 2D tissue distance cell density analysis.

(A) Mathematical notations used for 2D concentric neighborhoods surrounding the point of interest. (B) A visualization of concentric circle area (blue) and the area confined to discontinuous image limits (red) with iterative radii of $50 \mu\text{m}$. (C) Monte Carlo estimation error from explicit solutions for successively tighter iterative Monte Carlo convergences ($10^{-1}, \dots, 10^{-6}$) averaged over 4 image geometries and 40 distance intervals per image inside (green) the full image cuboid or (orange) the smallest subset cuboid where trend lines were fitted to $E = k_1 t^{-k_2}$ for the mean, m_E , and the 95% confidence interval, $m_E \pm 1.96 \frac{\sigma_E}{\sqrt{n}}$ for $n=4$, shaded in grey.

5.3.6. 3D Distance Distribution

The analysis of 3D cell distributions away from a specific point of interest is often utilized for cell co-localization studies, but is currently limited to cells either near the center of the image or only for very close cell proximities, creating regional bias in analysis (Bjornsson et al. 2008; Delarue et al. 2014; Ma et al. 2015; Liu et al. 2015). To analyze 3D cell distribution from a point of interest $(X, Y, Z)_a$ throughout the entire image, the distance from $(X, Y, Z)_a$ to the furthest pixel imaged was divided into intervals, R_i . Cell $(X, Y, Z)_c$ exists within the interval (R_{i-1}, R_i) if:

$$R_{i-1} < R_c = \sqrt{(X_c - X_a)^2 + (Y_c - Y_a)^2 + (Z_c - Z_a)^2} \leq R_i \quad [8]$$

Therefore, cell density within neighborhood (R_{i-1}, R_i) can be calculated as the quantity of all cells within (R_{i-1}, R_i) divided by the neighborhood's volume, V_i . If this neighborhood exists entirely within image boundaries then the neighborhood volume is $V_i = \frac{4}{3} \pi (R_i^3 - R_{i-1}^3)$. However, if a portion of this neighborhood exists outside of the image boundaries, then calculation of V_i may not hold an explicit solution. In this case, Monte Carlo point sampling methods were implemented to estimate volume V_i :

random 3D points $P_N = (X, Y, Z)_N$ were generated from a uniform distribution (known as Monte Carlo sampling) across the entire imaged space, such that: $P_N \in [(0,0,0), (X, Y, Z)_L]$. Then, P_n is defined as the fraction of P_N within the sphere volume of interest, such that $P_n \in ((X, Y, Z)_a \pm R_i)$, and an estimate of concentric neighborhood volume is provided as:

$$V_i = V_L \frac{\sum P_n}{\sum P_N} - V_{i-1} \quad [9]$$

Where, V_L is the full image volume and the concentric neighborhood volume of the prior radial interval R_{i-1} is given by V_{i-1} . This process of uniform point generation and volume calculation was repeated and appended until iterations of calculated V_i vary less than a chosen Monte Carlo convergence limit, as discussed above. The estimation of a 100 μm cell neighborhood (100 μm , $4.2 \times 10^{-3} \text{ mm}^3$) inside a large image volume, V_L (2.4 mm^3), required sampling 5.8×10^7 uniformly distributed random points and 0.49 seconds, or 9.1 minutes if repeated for the 1,116 cells within Figure 18B.

Computational time decreased by 96% from 9.1 minutes to 22 seconds when Monte Carlo point sampling methods were applied within small regions around each cell rather than across the entire image space. A smaller cuboid of known volume, V_{LS} , was constructed to exactly encase the cell neighborhood (volume $(2R_i)^3$ centered on cell $(X, Y, Z)_c$) that was then confined within the image limits ($V_{LS} \leq 8 \times 10^{-3} \text{ mm}^3$ for $R_i = 100 \mu\text{m}$ cell neighborhood). Points, P_{NS} , were sampled within the cuboid sub-volume such that $P_{NS} \in V_{LS} \subset V_L$, and the fraction of P_{NS} within the sphere volume of interest, $P_{nS} \in ((X, Y, Z)_a \pm R_i)$, provided a more efficient estimate of concentric neighborhood volume than sampling points within the entire image limits as:

$$V_i = V_{LS} \frac{\sum P_{nS}}{\sum P_{NS}} - V_{i-1} \quad [10]$$

Fewer sampled points were required within V_{LS} compared to V_L to reach the same Monte Carlo convergence: 2.4×10^6 uniformly distributed random points required 0.02 seconds per cell neighborhood, or 22 seconds for all 1,116 cells in Figure 18B. Using the proposed method, 3D cell density distributions can be quickly analyzed at distances up to half the diagonal image distance, or $0.5\sqrt{X_L^2 + Y_L^2 + Z_L^2}$, for every cell present in the image.

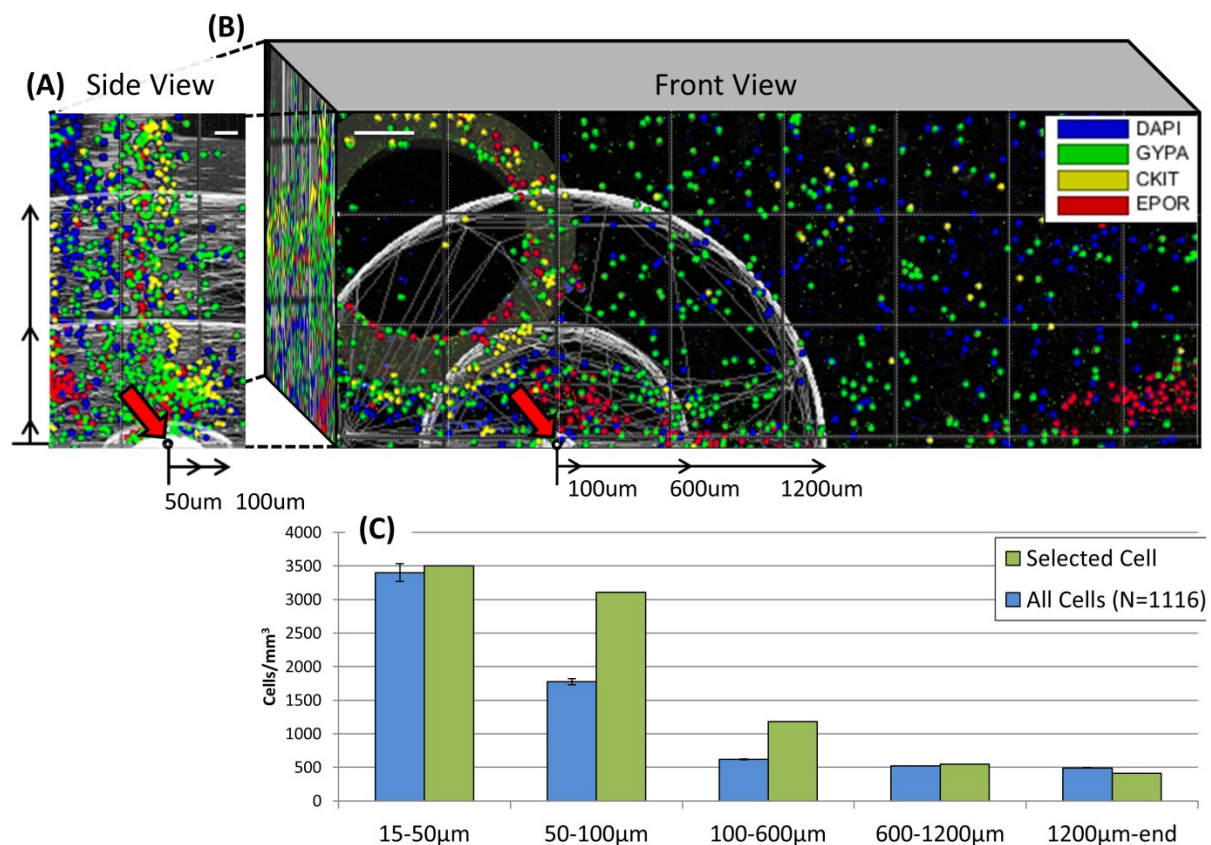


Figure 21: A visualization of the 3D cell clustering density analysis in confocal images.

(A, B) A cell of interest was defined and volumes of concentric spheres confined to image limits were estimated through point sampling in order to determine (C) cell density at any imaged neighborhoods away from a given cell (red arrow, green bars), which can then be iterated for all 1,116 (+/- SEM) cells throughout the image (blue bars). Scale bars in (A, B) are 100 μm.

Alternatively, an equally spaced 3D grid of k points across the image volume, V_L , or a similar image subvolume, V_{LS} , can be used to estimate cell neighborhoods. However, iterative grid generations must be performed with $(2k)^3$ additional points, which greatly increases computational time, and is discussed as a different method to random point generation from a uniform distribution.

Volume estimation by sampling random points from a uniform distribution within a known area converged much more quickly than dividing the image space or subset space into a grid of evenly-spaced points. Uniform random point generation required 1.3 ± 0.2 milliseconds per cell to reach 1% estimated volume convergence ($n = 1,000$ cells) while grid point generation required 7.9 ± 10.8 minutes per cell to reach the same convergence ($n = 10$ cells). The large time and variability for grid point generation may be attributed to the $(2k)^3$ additional points that must be generated for each subsequent iteration of k points so that an evenly-spaced grid would be generated at identical limits for unbiased

point generation. A visual comparison of volume estimations by their convex hulls can be found in Figure 22.

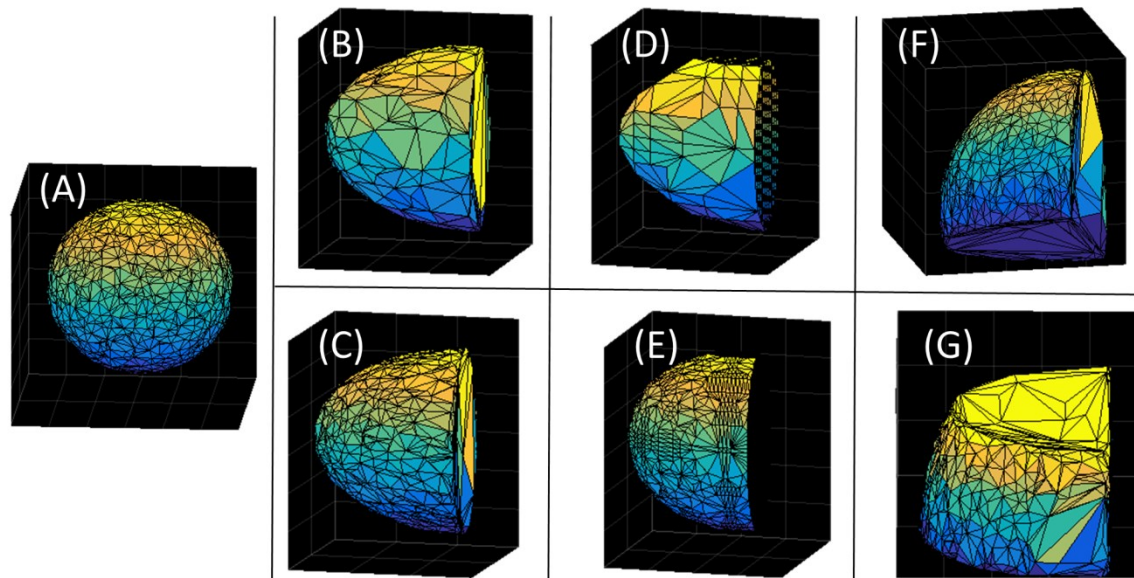


Figure 22: Convex hulls illustrating the cell clustering 50 μm neighborhood estimation.

For (A) a full sphere by 17 generations of 10,000 uniform random points, (B) a sphere's intersection with the image limits with 10,000 uniform and (C) 100,000 uniform points or (D) 10,000 evenly-spaced points and (E) 100,000 evenly-spaced points. Larger, 600 μm cell neighborhoods tend to intersect 2 or 3 planes of image limits, defined by (F) 17 and (G) 13 generations of 10,000 uniform points.

5.3.7. Statistics

Quantitative results are represented as mean \pm standard error of 4 replicate experimental samples prepared and assessed identically (Figure 18B), or 4 replicate computationally generated samples as stated.

5.4. Results

5.4.1. Enhanced Utilization of Imaged Data

The presented algorithms completely assess 2D and 3D cell density distributions of imaged histological data whereas current methods disregard data near image boundaries (Bjornsson et al. 2008; Delarue et al. 2014; Meddens et al. 2013). Therefore, the algorithms herein enhance utilization of image data in two ways: a) by surveying more points of interest, and b) by probing further distances from each point of interest. With current approaches, an ideally centered point of interest within Figure 18B could

only be inspected up to a maximum 2D distance of 775 μm (the closest image boundary); in contrast, using the presented algorithms, a 2D distribution of at minimum 2300 μm (the furthest imaged pixel) can now be calculated from any point within the image.

Cell density distribution algorithms are typically repeated for multiple points, or cells, of interest. A conservative comparison with current methods was performed by analysing 3D cell density distributions within a 100 μm neighborhood around every cell to demonstrate cell to cell association in Figure 18B (Bjornsson et al. 2008). Current methods utilize only cells further than 100 μm from an image boundary as points of interest (N=524) while with the presented approach all imaged cells were utilised (N=1116) at a 23-fold greater distance. The inclusion of these cells improved cell density estimations by 26% and 23% within 15-50 and 50-100 μm intervals, respectively.

Accurate manual scoring allows for the exact measurement of cell positions and cell-to-cell distances, but would be infeasible to manually pinpoint thousands of cells in a large image and infeasible to measure the hundreds of thousands of intracellular distances and the volumetric neighborhoods to calculate cellular density distributions within. The proposed algorithm was compared to manual scoring of random fractions of the entire image in Figure 18B, which revealed that partial manual scoring reduced accuracy due to the non-uniform distribution of cells and was unable to analyze cell distributions at long distances, while still reducing analysis time from 30 min down to 1 min.

5.4.2. Comparison of 3D Distance Analysis against Manual Scoring

The calculation of 3D cell density distribution using the proposed algorithm greatly saved time in comparison to a manual scoring method. For instance, the algorithm was able to calculate the distribution of cells in 4 concentric regional neighborhoods (0-15 μm , 15-50 μm , 50-100 μm , >100 μm) around each of the 1116 cells in Figure 18B within 62 seconds. This analysis was compared against the manual scoring of 3D cell density within random fractions of the image, another method to hasten analysis. To do this, Figure 18B was divided into 100 equal parts, and 5 image parts of this 100 were randomly selected (using MATLAB's random number generator). The image parts were then manually scored for cell position, then cell to cell distances were measured and sorted into 2 partitions (15-50 μm , 50-100 μm), and the average volume of these partitions within the partial, 1%, image boundaries was approximated (437,500 μm^3 , 2,700,000 μm^3) in order to calculate density. Surveying 5x 1% image

parts required 30 minutes for manual scoring (N=1), or 10.2 seconds for the algorithm (N=20), illustrated in Figure 23.

Table 10: Comparison of calculating 3D cell density distributions.

Comparison between (left) manually scoring 5 random image parts against (right) utilising the proposed algorithm across the entire image.

| | Manual Scoring of 5x 1% image parts | Automated estimation of the entire image |
|--|--|---|
| Time of Analysis | 30 minutes | 1 minute |
| Cells Utilized | 67 | 1116 |
| 15-50 μm neighborhood density (cells/ mm^3) | 25600 +/- 11300 | 3400 +/- 131 |
| 50-100 μm neighborhood density (cells/ mm^3) | 2220 +/- 832 | 1776 +/- 46 |

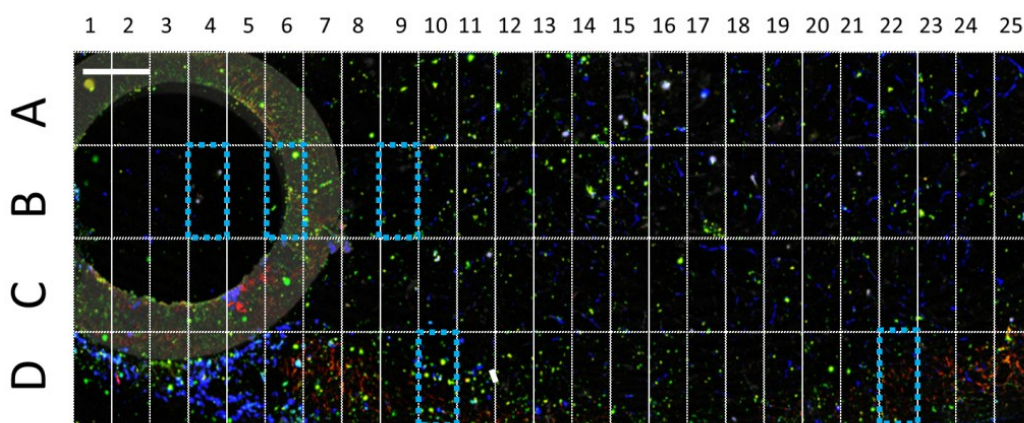


Figure 23: Comparison of algorithm efficiency in comparison with manual scoring.

Figure 18B was partitioned into 100 equal regions, and 5 parts were selected by random number generation (MATLAB), highlighted in blue as partitions B4, B6, B9, D10 and D22 which represented 5% of the full image area. Cells were manually identified within each partition, 3D cell to cell distances were identified if within 15-50 or 50-100 μm , and the average 3D volume of concentric spheres 15-50 or 50-100 μm away from cells of interest were manually estimated to calculate cell densities, and reported in Table 10.

Surveying 5 image parts comprising 5% of the entire image was an imprecise method to calculate 3D cell density distribution. Manual scoring provided inconsistent results, with standard errors of 44% and 38% about a mean which was 750% and 25% different than when using the proposed algorithm across the complete image (Table 10). These differences were likely due to both a large variability between image parts, and the lower number of cells utilized. When manually scoring, there existed between 2 and 28 cells per image (average of 13.4), and when applying the algorithm to 20 replicates of this 5 image parts method, there existed between 0 and 24 cells per image (average of 13.3

+/- 3.2), demonstrating the 5 parts only had 5.9% of the total 1116 cells in the complete image. The lack of cells and inconsistency of regions surveyed increased standard error significantly, from 2.9% to 29% and from 1.3% to 20.3% for the 15-50 μm and 50-100 μm regions when limiting the algorithm to 5x 1% image parts.

Analysing segmented image fractions reduces time while greatly reducing precision and also limiting features of the presented algorithm. This algorithm is unique in its ability to determine cell density at the furthest distance possible, and when Figure 18B is segmented into 100 parts of 388 x 177 x 350 μm^3 , the furthest distance between two points that the algorithm could analyze cell density would be 550 μm , instead of 4700 μm when implementing the full image. Furthermore, implementing a manual scoring method to measure complex image partition volumes is tedious and difficult to approximate. Therefore, the proposed algorithm reduces calculation time while maintaining a higher precision and functionality in comparison to methods of random image scoring.

5.4.3. Random Sampling Accuracy

The point sampling algorithm was validated by assessing uniformly generated random cell distributions, as shown in Figure 24A. These data sets were comprised of 4 types of 500 computationally generated cells which were uniformly distributed within a 4437 x 1551 x 230 μm^3 space in order to produce a known cell density while replicating the number of cells and image geometry of experimental samples, as performed in current studies (Acar et al. 2015; Takaku et al. 2010). The sampling method accurately analyzed the uniform distribution of cells, where 2,000 uniformly generated cell positions were found to have an average of 1257.6 ± 44.8 , 1244.8 ± 22.4 , and 1297.2 ± 2.0 cells per mm^3 in 15-50, 50-100, and 100-600 μm neighborhoods of all other cells, and 1297.0 ± 0.2 cell per mm^3 throughout the remaining 2300 μm of the image space ($n = 2,000$ cells). Small 50 μm and 100 μm neighborhoods contained significantly smaller numbers of cells, and may have accounted for their higher variability, but even so, the density of cells was found to closely approximate a uniform distribution of 2000 cells in the image volume of 1.54 mm^3 .

5.4.4.3D Distribution with Regional Asymmetries

Many histological images contain gaps or spaces without cells, such as vessels, areas of decalcified bone, or the edge of the sectioned sample. These voids may underestimate cell density

during computational analysis if they are averaged into dense cellular neighborhoods. However, if significantly larger numbers of cells could be assessed with full image field analysis, regional asymmetries might be more accurately determined. Cell clustering density analyses were run on an identical image including or excluding regions with engineered void space (Figure 24B and Figure 24C), and showed the region containing the voidage played a relatively minor role in influencing paracrine cell-cell niche communication, but a much greater regional effect correlating to its inclusion or exclusion from the 2D distance cell density analysis. There was a 7.8%, 11.1%, 44.6% difference in cell density in 15-50, 50-100, and 100-600 μm neighborhoods between the image with and without the fiber, and a 46.2% difference in cell density throughout the rest of the image, demonstrating that this regional phenomena altered cell localization at large 2D tissue scales, but cell association at close intercellular distances remained consistent throughout the image.

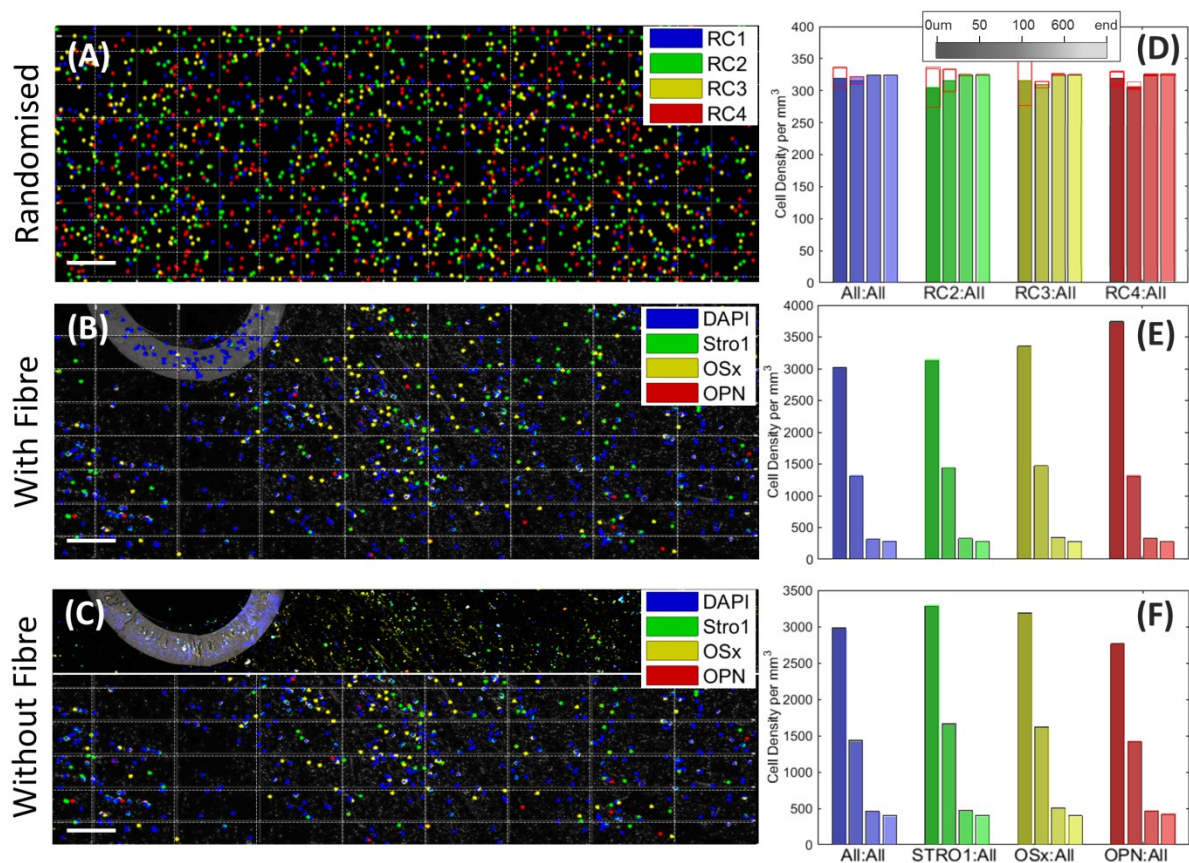


Figure 24: Assessment of methods and applications for calculating 3D cell clustering density.

(A) Cell clustering density estimation for 4 iterations (\pm SEM, red) of 4 types of 500 computationally generated cells, or, for (B) cells imaged from a hollow fiber bioreactor with and (C) without the hollow fiber region, representing a spatial asymmetry. Scale bars in (A, B, C) are 100 μm . Objects analyzed include randomized control cells (RC1-RC4), as well as fluorescent markers.

5.5. Discussion

3D image analyses enable the acquisition of information on spatial cell and tissue heterogeneity due to their quantitative algorithms (Appel et al. 2013; Weissleder & Nahrendorf 2015). However, current calculations of cell distributions are often constrained to a central subset of the image provided, and are further limited when phenomena of interest are off-center or replicate events per image are assessed. When the entire tissue volume of interest is infeasible to image, recent studies have compensated by quantitating images of incomplete tissue subsections either through normalization against uniformly generated random data within a similar tissue topology (Meddens et al. 2013; Acar et al. 2015; Takaku et al. 2010), or by only analysing phenomena that exist within the most central subsection of the image (Bjornsson et al. 2008; Delarue et al. 2014; Nombela-Arrieta et al. 2013). The former method only provides relative quantitation of images while the latter discards nearly half of 3D imaged data (Bjornsson et al. 2008; Delarue et al. 2014). The presented analyses in this study quantitate 2D and 3D distributions of phenomena throughout any full image, providing a minimum 50-fold increase in analytical range (increased distance times increased cells analyzed) throughout coupling complex Euclidean metrics with Monte Carlo point sampling estimations.

The analysis of cell distributions can be parametrically tuned for computational speed and analytical resolution to avoid miscalculation. Analytical resolution is dependent on the quantity of regions the image is partitioned into and, for 3D distributions, the Monte Carlo simulation is also dependent on the quantity of uniformly generated random points. The partitioning of image regions is a balance of precision where larger, coarser partitions may average local spatial phenomena into a larger population of cells, while smaller, finer partitions could provide misleading cell densities due to the sharp geometrical discontinuities that exist at image boundaries and the small number of cells that exist within small partitions. The partition balance is observed as the measurement of small cell-proximal 3D regions held larger error (4% standard error at 0.0042 mm^3) when compared to larger, cell-distal 3D regions (0.015% standard error at 2.4 mm^3). The generation of sufficient quantities of uniformly generated random points to estimate complex 3D volumes is dependent on system and user-specific error tolerance; in the presented case an average of 2.4×10^6 points were generated, which yielded a 5% error when compared against known controls, as discussed above.

Many studies of cell recognition and cell-cell or cell-tissue co-localization have avoided the need for efficient image analysis algorithms by capturing multiple or larger images at lower magnification, increasing the cost and time of these already demanding techniques. Morales-Navarrete *et al* proposed imaging at a moderate resolution (25x, 1 μm^3 voxel), then re-tiling parts of this low-resolution image with high resolution (63x, 0.03 μm^3 voxel) to capture both vasculature of approximately 100-300 μm diameters for murine liver reconstruction followed by cellular and subcellular reconstruction of hepatocytes (Morales-Navarrete *et al.* 2015). Studies by Khorshed *et al* and Sundaramurthy *et al* enumerated intravital murine hematopoietic cells at moderate resolutions (20-40x, 0.2-7.3 μm^3 voxel) in order to inspect intra- and inter-cellular activity for small populations of approximately 25 cells (Khorshed *et al.* 2015; Sundaramurthy *et al.* 2014). The presented study depicts cells at significantly lower resolution (10x, 46 μm^3 voxel), as an optimal balance between image volume analyzed at a tissue scale while still capturing many hematopoietic cells (1000's of 500-33,500 μm^3 cells) at high enough resolution to pinpoint cell nuclei and associated fluorescent markers amongst their environment. This lower magnification and resolution has also been employed in semiautomatic cell and fluorescent marker identification in 3D tissue cultures, to assess megakaryocyte distance from vascularization in murine bone marrow, and used as standard images to compare cell motion tracking algorithms across 14 laboratories (De Boodt *et al.* 2013; Di Buduo *et al.* 2015; Chenouard *et al.* 2014).

The quantitative evaluation of cellular density and heterogeneity is frequently studied and used *in vitro* and *in vivo* 3D applications inspecting roles of cellular and environmental interactions. Many 3D culture systems employ surfaces, scaffolds, carriers, or fibers as an aim to impart spatial heterogeneity to mimic and, upon implantation, integrate with many tissue asymmetries present physiologically (Cha *et al.* 2012; Pampaloni *et al.* 2007; Baker & Chen 2012; Khademhosseini & Bong 2009; Di Buduo *et al.* 2015; Rodenhizer *et al.* 2016; Eng *et al.* 2013; Rnjak-Kovacina *et al.* 2014). Pinpointing cell niche placement and cell association as a tool towards developmental understanding, tracking disease progression, and mammalian cell culture bioprocess design has become increasingly studied in *ex vivo* analogues, however, few intravital analyses have been performed until recently, and none in the adult human. Cell co-localization algorithms frequently inspect small distances from cells or tissues of interest such as the effect of high oxygen tension on cells within 150 μm of a vascular sinus

and the migration of cells within 100 μm of bone surfaces (Nombela-Arrieta et al. 2013; Khorshed et al. 2015). The assessment of spatial heterogeneity away from more complex regions of interest, such as uneven bone surfaces or noncircular vessel walls, could utilize these proposed algorithms to capture the full image-field in one of two ways: in an identical method if these phenomena can be described as a function, or through an iterative process once the complex phenomena of interest have been meshed or mapped similar to the detection of the murine marrow bone surface (Khorshed et al. 2015).

5.6. Conclusion

In summary, new computational algorithms were developed to analyze more 2D and 3D cell distribution and association data from confocal microscopy images than previously possible. This is especially important due to the high cost of native or engineered tissue histology. The study of spatial cellular distributions in tissue constructs has become increasingly popular both due to advancements in 3D culture systems to mimic physiological structures and functions, as well as advancements in imaging technologies able to better define the performance of natural and engineered cellular environments. The presented image analyses, for the first time, pair Euclidean metrics with Monte Carlo estimations to determine co-localization across the entire imaged data set, assessing 2.2-fold more area per frame in 2D distance metrics to depict cell populations in more distant, peripheral imaged areas from phenomena of interest. In 3D distance metrics, all cell neighborhoods can be analyzed to half the maximum image length, whereas previous, basic algorithms may only assess one, perfectly central cell per image; hence, these tools provide 10^2 to 10^4 more replicate cell measurements per image at a similar, if not greater, scope. These image analysis tools aid in the more complete understanding of how 3D tissue culture platforms influence cell distribution and function, and are essential to develop either physiological and translational or optimised therapy production protocols.

6. Characterization of structured, niche-like HSC and erythroid microenvironments within the marrow-mimetic bioreactor

Ex vivo platforms for erythropoiesis are rich in therapeutic potential, but have lacked translational relevance due to varied niche conditions and interactions required for normal maturation and enucleation. Herein, a 3D scaffold hollow fibre bioreactor was engineered which, when inoculated with human umbilical cord blood mononuclear cells (CBMNCs), generates stromal (Stro-1, SDF-1, OSx, OPN) and hematopoietic environments (CD34, C-KIT, CD45, VCAM-1) alongside long-term erythropoiesis (EPO-R, CD71, CD235a). Quantitative image analyses were employed to spatiotemporally map multi-lineal cell distributions and interactions within unique microenvironments which secrete extracellular matrix proteins (collagen type-1, fibronectin) and 23 hematopoietic and stromal growth factors. Viable culture densities above $2 \cdot 10^9$ cells/mL are attained, 1000-fold greater than current flask cultures, which enrich during continuous harvest of enucleated erythroid phenotypes (CD235a⁺CD71⁻). This culture platform provides physiologically-relevant erythroid inductive environments for potential cell expansion protocols and to spatially resolve human erythropoiesis in a marrow-mimetic environment.

In this section, Mark C. Allenby performed all experiments and analyses. Asma Tahlawi fabricated hollow fibres further used towards all other bioreactor fabrication by Mark C. Allenby. Susana S.B. Dos Santos provided advice.

6.2. Introduction

Clinical translation of *ex vivo* human erythropoietic models has been limited as current reductionist liquid suspension cultures fail to conserve *in vivo* environmental conditions found in human bone marrow (hBM) such as: multiple hematopoietic lineages and dynamic maturation, a supportive stromal matrix, and biochemical gradients including oxygen, paracrine and endocrine factors (Lane et al. 2014; Yin et al. 2016). Current human erythroid massive amplification (HEMA) cultures produce 10^{4-6} reticulocytes per CD34⁺ hematopoietic stem cell (HSC) useful for human transfusion (Giarratana et al. 2011; Timmins et al. 2011) and have been adapted to produce reticulocytes from immortalised erythroblast cell lines (Trakarnsanga et al. 2017). However, nonphysiological low cell densities ($\leq 10^6$ /mL) and expensive cytokine supplementations keep HEMA reticulocyte production costs 1- to 2-orders of magnitude above donor-based blood transfusion (Rousseau et al. 2014).

Animal models demonstrate erythropoiesis as a spatially distributed process in heterogeneous microenvironments (Greenbaum et al. 2017), but are limited for understanding human erythropoiesis at phenotypic and genotypic (An et al. 2014). Two frequently studied murine bone marrow (mBM) microenvironments include immature hematopoietic stem and progenitor cell (HSPC) niches and erythroid niches: both distribute within unique oxygen conditions (Spencer et al. 2014; Nombela-Arrieta et al. 2013; Itkin et al. 2016; Parmar et al. 2007; Acar et al. 2015) and interact with neighboring hematopoietic progeny and stromal cells. These niche cells include macrophages, mesenchymal, and osteoblastic cells which secrete supportive growth factors and produce adhesive extracellular matrix (ECM) proteins (Boulais & Frenette 2015; Kunisaki et al. 2013; Zhu & Emerson 2002; Kfoury & Scadden 2015; Ehniger & Trumpp 2011; Nilsson et al. 1998). Erythroid niches distribute with increasing maturation towards marrow sinuses providing a peripheral supply of differentiation factor erythropoietin (EPO) and a location for reticulocyte egress (Grover et al. 2014; Yokoyama et al. 2003; Weiss 1984; Mohandas & Prenant 1978).

An *in vitro* human platform which mimics the spatial distribution of multilineal hBM interactions may represent a physiologically-relevant culture system to test and produce translational therapeutics. Porous scaffold biomaterials provide a 3D structure similar to the marrow trabeculae (Placzek et al. 2009), operate at increased cell densities ($\geq 10^7$ /mL) (Severn et al. 2016; Mortera-Blanco

et al. 2012), and substitute high cytokine supplementation with serum (Mortera-Blanco et al. 2011) or stromal co-culture (Leisten et al. 2012; Schmal et al. 2016; Ventura Ferreira et al. 2016; Holzapfel et al. 2015), where cellular interactions enhance RBC maturation (Lee et al. 2014; Choi et al. 2013). Perfused 3D platforms can further increase culture density ($\geq 10^8/\text{mL}$) (Housler et al. 2012), provide physiological shear (Di Buduo et al. 2015), and impart biochemical gradients to structure cell distribution similar to that found *in vivo* (Rodenhizer et al. 2016; Kolesky et al. 2016; Rnjak-Kovacina et al. 2014).

Herein, an *ex vivo* 3D scaffold continuous perfusion HFR model of erythropoiesis is proposed, inoculated with unselected CBMNCs and perfused with serum-free medium supplemented with near-physiologic concentrations of stem cell factor (SCF) and EPO. With minimal handling, this HFR model maintained immature hematopoietic populations for 28 days, expanded stromal and osteogenic cell types, generated ECM proteins, secreted hematopoietic and stromal factors, and produced enucleated RBCs which were continuously harvested through hollow fibres. The quantity and expression of erythroid phenotypes increased with HFR cell densities similar to that found *in vivo* ($> 2 \cdot 10^9$ cells/mL). Using quantitative image analyses (Allenby et al. 2017), multilineal cells and the spatio-temporal distribution of cells and secreted proteins were analysed at unique distances from medium perfusion. This HFR provides a more physiological human model to spatially study *ex vivo* red cell genesis within stromal and multilineal hematopoietic microenvironments for cell therapy biomanufacturing.

6.3. Methodology

The fabrication of a hollow fibre bioreactor able to expand cells at high densities (Section 4) and the development of tools to characterize this new environment (Section 5) provides the resources to understand the long-term culture development of what appeared to be a spatially-complex, cellularly-diverse system. To characterize the processes occurring, serum was omitted from the media and supplemented growth factors were reduced, replacing them with a defined expansion medium (StemSpan SFEM; StemCell Technologies, Grenoble). These changes allowed for (1) a more accurate understanding of paracrine and autocrine secretory support within the reactor and (2) a stromal proliferation whose phenotypic expression was rare when the reactor was supplemented with higher levels of hematopoietic growth factors. With a better understanding of culture progression, the capabilities of the reactor could be explored by viably increasing cell culture densities 10^3 -fold above 2D limitations.

6.3.1. Study Approval

The study has been conducted in accordance with the Declaration of Helsinki and received the required ethics and local research approvals (reference 05/Q0405/20, London-Harrow NRES Committee, UK).

6.3.2. Fabrication of hollow fibres

Ceramic hollow fibres (HFs) were fabricated by Asma Tahlawi through the dissolution, milling, and degassing of 58.6 wt% $1\ \mu\text{m}$ aluminum oxide powder (VWR, Lutterworth, UK) with 1.3 wt% ArlcelP135 (Sigma-Aldrich, Dorset, UK) in N-methylpyrrolidone (Sigma-Aldrich) solution, followed by extrusion through a tube-in orifice spinneret prior to sintering with a temperature profile rising to 1350°C . HFs were further air-dried and HF porosity was assessed by Asma Tahlawi through mercury intrusion porosimetry (MIP), and scanning electron microscopy (SEM). To assess the permeability of nutrients, proteins, and enucleated and nucleated cells through the HF, four HFs were adhered within a polyfluoroalkoxy (PFA) fine thread flare tee (Swagelok, London, UK) applying a quick drying two-component resin (Araldite, Basel, Switzerland) on both the inlet or outlet of the reactor.

6.3.3. Filtration testing of hollow fibres

A suspension of CB cells in cell culture medium was seeded into the extraluminal space and cell-free medium was perfused at 460 mL/day through the HFs. Perfused medium (filtrate) and medium remaining in the extraluminal space (retentate) were analysed at multiple time points up to 24 hours by electrochemical sensors (Bioprofile 400, Nova Biomedical, Runcon, UK), total protein ELISA, manual counting, and flow cytometry as below.

6.3.4. Fabrication of the hollow fibre reactor (HFR)

Once HFs had been adhered within the PFA tee, a solution of 5% polyurethane (PU; Noveon, Brussels, Belgium) in 1,4-dioxane (Sigma-Aldrich) was dissolved at 60°C, then 5 mL was injected into the extraluminal space, and frozen at -80°C for 2 hours. The 1,4-dioxane was selectively sublimed through thermally induced phase separation (TIPS) by applying a vacuum pressure of 0.01 mbar at -15°C to leave a porous PU scaffold. The porosity of the resultant HFR was assessed by MIP, SEM, and micro-scale computerised tomography (μ CT). The porosity of scaffolding was analysed by MIP separately from the reactor HFs by pouring 60 mL of PU-dioxane solution into a glass petri dish prior to applying TIPS.

This HFR was coated by bovine collagen type 1 (Sigma-Aldrich) by thoroughly immersing, mixing, and perfusing the HFR with PBS, 70% ethanol, 62.5 μ g/mL bovine collagen type 1 in PBS at pH 7.0, then PBS again. The HFR was sterilized through a similar process using 70% ethanol for more than 2 hours, a thorough wash with PBS for 2 hours, UV sterilisation, and then 3-days of conditioning with cell culture medium.

The HFR was fitted into a perfusion assembly of silicon tubing and polycarbonate adapters including 100 mL and 500 mL bottle reservoirs, oxygen permeable tubing, stopcock adapters for sampling, and peristaltic pump tubing and pumps as illustrated in Figure 28D (Cole Parmer, Hanwell, UK; Smith's Medical, Watford, UK; VWR; Instech Technologies, Plymouth Meeting, USA) that were sterilized by either autoclave sterilisation for silicon tubing and bottles or ethanol and UV light sterilisation for polycarbonate adapters and fabricated HFRs as described above.

6.3.5. Culture of primary CBMNCs

Fresh CB units (National Health Service Blood and Transplant, Colindale, UK) were isolated for MNCs by Ficoll-Paque Plus according to manufacturer's instructions (Sigma-Aldrich). A suspension of 10^8 or $2.5 \cdot 10^9$ CBMNCs in culture medium comprised of StemSpan SFEM (StemCell Technologies Grenoble, France) with 1% penicillin-streptomycin (ATCC, Maryland, USA) with 50 ng/mL SCF (R&D Systems, Abingdon, UK) was seeded into 5 mL HFRs and incubated for 1 hour without perfusion. The reactor was perfused with medium at 20 mL/h which was recycled through a reservoir of 30 mL (days 0 to 1) then 60 mL (from day 1), and the 30 mL of medium added at days 0 and 1 was supplemented with SCF.

From day 2, the recycled reservoir was gradually replenished with fresh medium at a rate of 0.8 mL/h (days 2-7), 0.9 mL/h (days 7-14), or 1.5 mL/h (days 14-28) supplemented with 0.5 IU/mL EPO (R&D Systems). Perfused medium was sampled every 2 days for extracellular metabolic and protein analysis, and at days 14 and 28 for filtered cell analysis. Reactors were snap-frozen for sectioning and *in situ* analysis at days 0 (with and without cells, N=4), 14 (N=3), and 28 (N=3 or 4 depending on analysis) of culture after 1 hour perfusion of 0.65 ug/mL Pimondiazole-HCl (Hypoxprobe, Inc., Burlington, USA).

6.3.6. Extracellular metabolite and protein analysis

Perfused HFR medium was collected from 3-way stopcocks (Smith's Medical) directly at the HFR inlet and outlet, from the recycled medium reservoir, and also from the feed medium continuously replenishing the reservoir and waste medium continuously leaving the reservoir. Extracellular nutrients and metabolites, pH, and dissolved gases were analysed by electrochemical sensors (Bioprofile 400, Nova Biomedical). A panel of 27 extracellular proteins were analysed within HFR effluent by bead capture assay and ELISA according to manufacturer's instructions (Biolegend, R&D Systems).

6.3.7. Cell extraction, counting, and cytology

Cell suspensions were obtained pre-inoculation, aspirated from 0.125 mL HFR sections at days 0, 14, and 28, or collected from filtrate within the 60 mL recycled reservoir of medium, or from waste medium removed from the reservoir (100-250 mL per week). Cell suspensions were centrifuged into pellets, suspended in PBS, and assessed for viability and MNC content by trypan blue and methylene

blue differential counts on hemocytometer (StemCell Technologies). Cell morphology was assessed by cytopspin, by smear, or by HFR section imprint onto poly-L-lysine slides (Fisher Scientific, Loughborough, UK), stained with May Grünwald, Giemsa, or Modified Wright Giemsa stains (Sigma-Aldrich) buffered with Sorenson's buffer prepared at 0.0083 M, pH 7, and mounted with DPX, prior to imaging on a BX-51 Olympus microscope (Olympus, UK).

Sorenson's buffer was prepared by dissolving appropriate concentrations of Na_2HPO_4 and KH_2PO_4 (Sigma Aldrich) in two separate solutions of deionised water. The two solutions were then titrated to appropriate pH directly before use.

6.3.8. Flow cytometric analyses

Flow cytometry was performed on isolated MNCs on day 0 prior to inoculation, cells collected from perfused medium at days 14 and 28, and cells aspirated from 0.125 mL HFR cross-sections at days 0, 14, and 28. Flow cytometry was performed on cell aliquots of $2 \cdot 10^5$ viable fresh or fixed cells.

Fresh cells were stained with Calcein Violet, AM (Life Technologies) at a concentration of 2.5 $\mu\text{g}/\text{mL}$ in PBS for 45 minutes at room temperature, washed with cell staining buffer (CSB; PBS with 1% bovine serum albumin (Sigma-Aldrich) and 0.01% sodium azide (Sigma-Aldrich)), then stained with mouse anti-human antibodies (Becton Dickinson, Oxford, UK) in CSB with 10% fetal bovine serum (Life Technologies, Paisley, UK) for 1 hour at 4°C . Samples were then washed with CSB, then PBS twice before analysis on a BD LSR Fortessa (Becton Dickinson) with FACSDiva software.

Becton Dickinson monoclonal mouse anti-human conjugated antibodies employed for flow cytometry include antibodies: 5 μL CD45-FITC (#555482), 1.5 μL CD235a-PE (#555570), 5 μL CD71-PECy5 (#551143), 5 μL CD36-APC (#550956), isotype antibodies: 5 μL IgG1-FITC (#555909), 1.5 μL IgG2b-PE (#555743), IgG2a-PECy5 (#555575), and IgM-APC (#555585). Cells were analysed in 4 combinations: positive sample, fluorescence-minus-one (lacking CD235a-PE), isotype control, and calcein-only control. In addition, single-stain controls were run utilizing compensation beads (Life Technologies).

6.3.9. HFR sectioning, ATP analysis, and confocal microscopy viability analysis

Thin cylindrical cross sections were manually cut from the frozen HFR (9mm diameter, 0.5mm-2mm thick), and immediately immersed in a fixation or assay solution for analysis. These

analyses included 3D Cell Titre Glo (Promega, Southampton, UK) as per manufacturer's instructions. *In situ* cell viability was assessed by incubation at 37°C in 4 µM ethidium homodimer and 2 µM calcein AM in culture medium for 1 hour followed by washes with PBS and imaging on a Leica SP5 upright confocal microscope with Leica LAS AF software (Leica, Milton Keynes, UK). Other HFR sections were fixed for confocal microscopy and SEM.

6.3.10. Scanning Electron Microscopy

Frozen HFR sections were immediately fixed with a 3% glutaraldehyde solution (Sigma-Aldrich) in Sorenson's buffer for at least 12 hours. Sections were then washed twice, and post-fixed in 1% OsO₄ (Sigma-Aldrich) in Sorenson's buffer for one hour, then washed twice. Sections were then dehydrated in an increasing gradient of absolute Ethanol diluted with Sorenson's buffer at 0.067 M, pH 7.4 (50:50, 70:30, 90:10, 95:5, and 100:0 twice, respectively), followed by further drying in hexadimethylsilazane (Sigma-Aldrich) in absolute ethanol (70:30, 90:10, 95:5, 100:0 twice, respectively; Sigma-Aldrich), and left to air-dry overnight. After solvent evaporation, sections were adhered to SEM stubs with carbon tape (Elektron Technology, Stansted, UK), sputter-coated with gold (20 mA, 30 s) prior to imaging on a JSM-6010LA SEM (JOEL, Watchmead, UK).

6.3.11. Fixed confocal microscopy analysis

Frozen HFR sections were fixed, permeabilised, blocked, stained, and imaged as previously described (Allenby et al. 2017). Briefly, HFR sections were fixed in 4% PFA (Sigma-Aldrich) in PBS and kept at room temperature for a minimum of 12 hours, permeabilised with 0.1% Triton X-100 (Sigma-Aldrich) in Confocal Microscopy Stain Buffer (CMSB; contained 1% BSA, 0.5% Tween-20, 0.01% NaN₃ in PBS) for 2 hours, blocked with 10% donkey serum (AbCam, Cambridge, UK) in CMSB for 4 hours at 4°C, followed by an overnight incubation with primary antibodies or isotype controls in CSMB at 4°C, a 6-hour incubation with secondary antibodies in CMSB at 4°C, an overnight 1:200 DAPI (Life Technologies), 1:1000 cell membrane (CellMask, Life Technologies), and/or 1:200 rhodamine B isothiocyanate (Sigma-Aldrich) counterstain solution in PBS, then stored in 0.01% NaN₃ in PBS solution at 4°C. Each step was separated by single or multiple 15 minute washing steps in appropriate buffer, and imaged on a Leica SP5 inverted confocal microscope with LAS AF software (Leica, Milton Keynes, UK). Images were not manipulated for computational analysis and extraction

of cell location. Images were manipulated within all figures by adjusting only contrast and brightness of both sample and negative (isotype) controls identically. Table 11 describes concentrations and product names for all primary and secondary antibodies used.

Table 11: List of primary and secondary antibodies and counterstains implemented in confocal microscopy analysis.

All products were purchased from AbCam unless otherwise stated. Pimodiazole and Dylight 555-HCl was purchased from Hypoxyprobe, Burlington, USA. All other secondary antibodies as well as DAPI and CellMask Deep Red counterstains were purchased from Life Technologies.

| Name | 405 | 488 (Rat/Sheep) | ug/mL | 555 (Rabbit) | ug/mL | 633 (Mouse) | ug/mL |
|------|------|-------------------------------------|-------|---|-------|-----------------------------|--------|
| S1 | DAPI | Ki67 (ab156956) | 100 | Pimondiazole | 25 | HIF1a (ab1) | 25 |
| I1 | DAPI | IgG1 (ab18412) | 100 | - | - | IgG2b (ab91366) | 25 |
| S2 | DAPI | CD45 (ab30446) | 100 | CD71 (ab84036) | 80 | CD34 (ab8536) | 100 |
| I2 | DAPI | IgG2b (ab18541) | 100 | IgG (ab172730) | 80 | IgG1 (ab18437) | 100 |
| S3 | DAPI | CD235a (ab33386) | 100 | C-KIT (ab111033) | 80 | EPO-R (ab56310) | 20 |
| I3 | DAPI | IgG2b (ab18541) | 100 | IgG (ab172730) | 80 | IgG2a (ab91361) | 20 |
| S4 | DAPI | Stro-1 (ab192766) | 80 | OSx (ab94744) | 80 | OPN (ab69498) | 20 |
| I4 | DAPI | Sheep IgG (ab37385) | 80 | IgG (ab172730) | 80 | IgG2a (ab91361) | 20 |
| S5 | DAPI | Laminin-2 (ab11576) | 2,500 | Collagen-1 (ab138492) | 80 | Fibronectin (ab6328) | 25 |
| I5 | DAPI | IgG (ab37361) | 2,500 | IgG (ab172730) | 80 | IgG1 (ab18437) | 25 |
| S6 | DAPI | CD45 (ab30446) | 100 | OSx (ab94744) | 80 | EPO-R (ab56310) | 20 |
| I6 | DAPI | IgG2b (ab18541) | 100 | IgG (ab172730) | 80 | IgG2a (ab91361) | 20 |
| S7 | DAPI | VCAM-1 (ab167095) | 2,500 | Stro-1 (ab108994) | 5 | CD34 (ab8536) | 100 |
| I7 | DAPI | Sheep IgG (ab37385) | 2,500 | IgG (ab172730) | 5 | IgG1 (ab18437) | 100 |
| S8 | DAPI | CD235a (ab33386) | 100 | OSx (ab94744) | 80 | OPN (ab69498) | 20 |
| I8 | DAPI | IgG2b (ab18541) | 100 | IgG (ab172730) | 80 | IgG2a (ab91361) | 20 |
| S9 | DAPI | CD45 (ab30446) | 100 | SDF-1 (ab155090) | 9 | CellMask Deep Red | 1:1000 |
| I9 | DAPI | IgG2b (ab18541) | 100 | IgG (ab172730) | 9 | - | |
| Sec | | Donkey Anti-Rat or Anti-Sheep AF488 | 1:500 | Donkey Anti-Rabbit AF555 or Dylight 555-HCl | 1:500 | Donkey Anti-Mouse AF647 | 1:500 |

6.3.12. Confocal microscopy computational analysis

Once captured, imaged HFR sections were analysed as previously described (Allenby et al. 2017). Once the full image was prepared, the center-point of each individual fluorescence stain was identified. Each MNC was characterized by the identification of DAPI. The MNC was considered “stain-positive” if that stain existed within a threshold distance of the nucleus of interest. As hematopoietic, erythroid, mesenchymal, and osteogenic cells vary in size, different threshold distances (Supplementary Tab. 6) were chosen based on maximum cell sizes imaged during confocal and SEM within this study in agreement with prior literature (Chow et al. 2001b). Two metrics were assessed: the 2D distribution of cells from the abluminal wall of hollow fibres, and the 3D distribution of cells away from each other, and were represented as cell density (/mL) at consecutive distance intervals, fitted by continuous kernel density estimations for the mean and standard error of the measurements.

Table 12: List of threshold DAPI to stain co-localisation distances and internal image replicates for each analysed stain.

| Stain | Type | (μm) | n |
|-------------|---------------|-------------------|---|
| DAPI | Nuclei | N/A | 9 |
| CellMask | Entire cell | 40 | 1 |
| CD235a | Erythroid | 40 | 2 |
| CD71 | Erythroid | 40 | 1 |
| EPO-R | Erythroid | 40 | 2 |
| CD45 | Hematopoietic | 40 | 3 |
| C-KIT | Hematopoietic | 40 | 1 |
| CD34 | Hematopoietic | 40 | 2 |
| Stro-1 | Mesenchymal | 60 | 2 |
| VCAM-1 | Mesenchymal | 60 | 1 |
| OSx | Osteogenic | 60 | 3 |
| OPN | Osteogenic | 60 | 2 |
| Laminin-2 | ECM | 90 | 1 |
| Fibronectin | ECM | 90 | 1 |
| Collagen-1 | ECM | 90 | 1 |
| PIMO | Stress | 90 | 1 |
| Ki-67 | Stress | 90 | 1 |
| HIF-1a | Stress | 90 | 1 |

The confocal microscope was unable to image through the PU scaffolding. Therefore, instead of imaging a confocal z-depth of 100-300 μm as reported for animal tissue (Appel et al. 2013), only superficial cell layers on top of exposed PU scaffolding could be visualised and quantitated. For quantitative analysis, measurement of the imaging z-depth is essential to estimate 3D cell densities. An amine-group stain was employed, rhodamine B isothiocyanate (RBITC) to visualise PU scaffold surface, cell nuclear (DAPI), membrane (CellMask), and phenotypic (e.g. CD45) stains to visualise cell position and morphology as previously described. Higher-magnification images (20x magnification, 1024x1024 resolution) were employed to allow for manual operator measurement of 218 nuclei (DAPI) to scaffold (RBITC) xz-plane distances (Figure 25A), where a subset cross-section is highlighted (Figure 25B). Of these 218 counted cell nuclei, 96% were within 13 μm of a scaffold surface, primarily belonging to a bivariate distribution which would be representative of two cell monolayers, while nuclei at larger distances from scaffold surfaces resembled outliers (Figure 25C). Therefore, a typical imaging depth of 13 μm was adopted for 3D quantitative analyses.

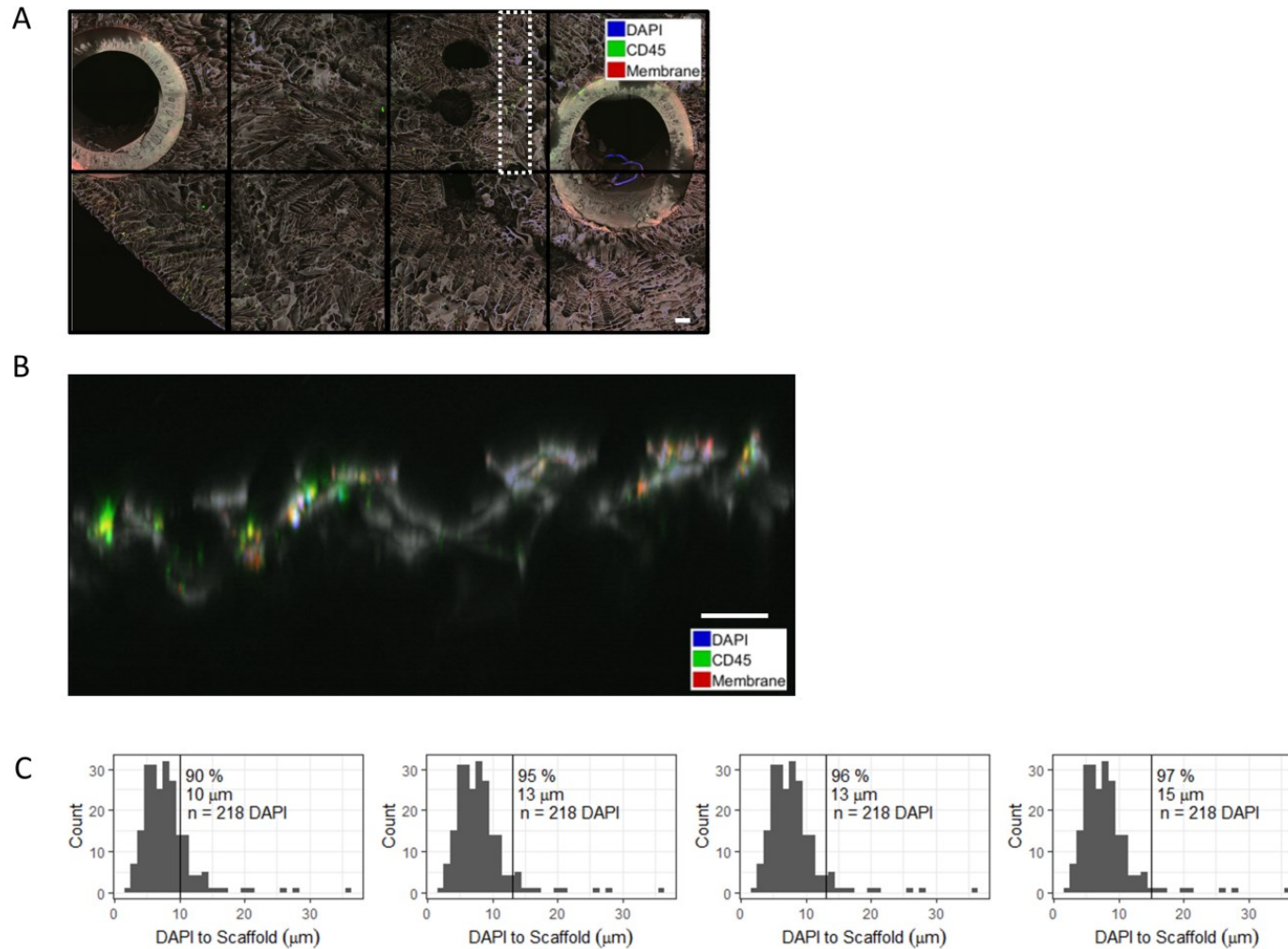


Figure 25: Manual measurement and scoring of cell-to-HFR surface distances.

(A) Employing the RBITC stain, polyurethane amine groups could be detected to image the scaffold surface in detail using confocal microscopy. (B) Different cell stains allowed for the measurement of DAPI nuclear centers (blue) to scaffold surface (grey, 100 μm scale bars in A and B). (C) Cell-to-scaffold distances were manually measured for 218 cells from (A), and 96% of all cell-to-scaffold distances resided within 13 μm.

6.3.13. Comparison of methods to analyse HFR content

The characterization of the HFR is limited by an inability to embed the sample in stabilizing medium and by superficial confocal imaging depths. Confocal imaging could only characterize 1-2 cell layers (13 μm) on top of the PU scaffold surface, both due to cell removal during unembedded preparation and solvent washes and as imaging could not penetrate the PU material. Therefore, the cells imaged, quantitated, and simulated in distribution and association illustrations only account for cells near scaffold surfaces, and not cells within bulk pores. Assuming spherical pore diameters of 180 μm (the average measured pore diameter), 62.6% of void space remains unaccounted for. That is, optimistically, if each pore was 100% confluent populated with cells, only 100 cells could be imaged out of hypothetically 265 per pore.

This limitation could have imaged more cells with PU scaffold-adherent properties, and less thick bodies of associating cell clusters in liquid suspension or with only a portion attached to the scaffold. *In situ* confocal microscopy of HFR sections and flow cytometry of HFR aspirate were compared as methods to analyse CD235a⁺ expression 1 hour after inoculating CB MNC isolate comprising, on average, 4% CD235a⁺ cells (N=4 for all methods, data not shown). Flow cytometry analysis of aspirated cells comprised 50% CD235a⁺ (paired p = 0.04 compared with inoculate) while confocal imaging comprised 2% CD235a⁺ (not significantly different compared with inoculate), demonstrating *in situ* imaging provided a more faithful representation of adherent CD235a⁺ and non-adherent CD235a⁺ cell types than aspiration.

6.3.14. Mathematical model of a projected organizational map

To illustrate the utility of the quantitative confocal analysis in describing cell distributions, a brief mathematical model was constructed to describe (1) the quantity of cells at different abluminal distances and the (2) frequency of these different cells to associate with one another. This model can be described by a single equation:

$$\lambda(x, C_j, C_k) = N(x, C_j) \left[\left(1 - \mu(x, C_j) \right) + \mu(x, C_j) \sum_{d(C_j, C_i) \leq 100 \mu\text{m}} \left(\frac{P(x, C_j, C_k) N(x, C_k)}{\sum_i P(x, C_j, C_i) N(x, C_i)} \right) \right]$$

Where the probability, λ , of a cell type C_j existing within distance x of a hollow fibre abluminal surface and co-localising within 100 μm of cell C_k is equal to the quantity of cell type C_j detected at abluminal

distance x as $N(x, C_j)$. The likelihood of cell type C_j associating within 100 μm of cell type C_k is dependent on the frequency with which cell type C_j associated within 100 μm of any MNCs at abluminal distance x as $\mu(x, C_j)$, and if associating with a MNC, the probability that C_j will uniquely associate within a 100 μm distance of C_k versus all other i cell types illustrated.

To simulate this mathematical representation, the full imaged abluminal distance (1900 μm) was discretised into 100 μm bins, and the number of cells C_j to generate within bin x is equal to the average cell density calculated $N(x, C_j)$ for a 1900x1000x13 μm volume. Each C_j generated is placed randomly within the spatial bin or within 100 μm of other MNCs at interval x with frequency $\mu(x, C_j)$, and further specifically placed within 100 μm of cell type C_k with probability $P(x, C_j, C_k)$. Placed cells were illustrated as circles with radii proportional to their threshold co-localization size.

6.3.15. Statistics and Figure Preparation

Quantitative information on cellular associations can be found within summary, excel files, within supplementary information. All error bars and shaded regions of error represent the standard error about the mean (SEM) of 3-4 independent biological replicates. The number of internal replicates is analysis-specific and reported within the online methods. All p-values were generated as two-tailed comparisons between either paired replicates or replicates of equal variance, as appropriate. Images were not manipulated for quantitative analysis and cell location extraction. ImageJ (U.S. National Institute of Health, Bethesda, USA), FlowJo (TreeStar Inc., Ashland, USA), MATLAB (The MathWorks, Inc., Nantick, USA), R-Project (R Foundation for Statistical Computing, Vienna, Austria), and Microsoft Excel software was employed for data and figure generation.

6.4. Results

6.4.1. A perfused HFR established CBMNC hypoxic gradients

3D HFR systems were produced containing a collagen-coated polyurethane scaffold (87.4% porous, 180 μm pore diameter) surrounding four ceramic hollow fibres (61.7%, 0.2 μm) inoculated with $2 \cdot 10^7$ CBMNCs/mL (Figure 26A-C; Figure 28A). These HF, fabricated and assessed by Asma Tahlawi, demonstrated an unrestricted permeation of metabolites and proteins (>99%) and a similar permeability for enucleated cells as studied in murine marrow sinusoids (Figure 26D) (Itkin et al. 2016). HF placement within the HFR was designed to be equidistant from one another and from the scaffold edge for optimal and balanced medium diffusion. Due to human error, non-optimal HF placement occurred, which could create scaffold regions further from HFs than those analysed during confocal microscopy. These regions would contain lower concentrations of perfused medium components (e.g. O_2 , glucose, EPO, SCF) and higher concentration of cell-secreted components (e.g. lactate, endogenous GFs) and should be considered during future HFR design and optimisation.

For 28 days, HFR fibres were perfused with 460 mL/day of recycled StemSpan Serum-Free Expansion Medium supplemented with 1% penicillin-streptomycin, 0 to 0.23 IU/mL EPO, and 50 to 0 ng/mL SCF (Figure 27A-B). The viability of cells imaged *in situ* or extracted remained above 80% throughout culture (Figure 27C-D), and no difference in nutrient concentration was found between HFR inlet and outlet (<5%; Figure 27E), indicating that perfusate measurements were representative of HF inter-luminal conditions.

Quantitative confocal microscopy analyses signified that CBMNCs were uniformly inoculated at day 0 and then became distributed 2-fold more densely within 500 μm of HF abluminal surfaces at days 14 and 28 (Figure 28E-G). Upon inoculation, CBMNCs were concentrated in dense associations which were maintained over the 28 day culture, with nuclei distributed at 5-fold higher densities within 100 μm “local neighbourhoods” of one another (days 0, 14, 28) peaking at 10-fold higher MNC densities ($\geq 10^8/\text{mL}$) within 1 or 2 cell distances from one another (Figure 28H-I). At day 14 MNCs associated at higher local densities predominately within 350 μm of HFs (Figure 29A). Cellular ATP was initially concentrated in the centre of the HFR scaffold, but then accumulated near the HFR outlet at day 28 (Figure 29B).

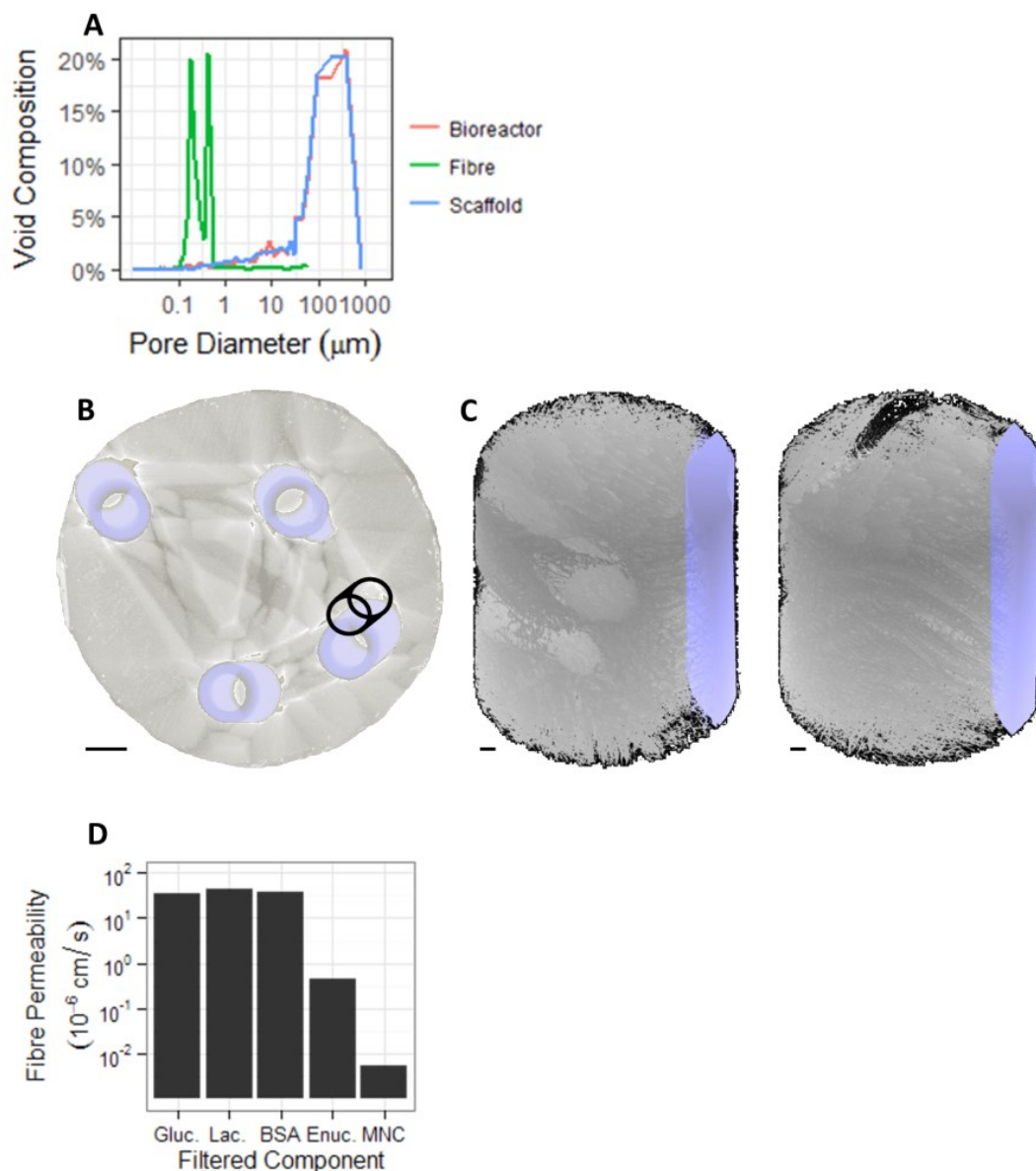


Figure 26: HFR mechanical structure and function.

(A) Pore diameter composition of void space within a representative scaffold (N=6), fibre (N=3), and completely prepared HFR section assessed by mercury intrusion porosimetry. (B) Circumferential bioreactor micro-computerised-tomography images with ceramic fibres (blue) and polymeric scaffold (grey) differentiated by material density (1 mm scale bar, with image distortion by ceramic hollow fibres) with highlighted cylinder representing (C) magnified longitudinal view (100 μm scale bars). (D) Average HF filtration permeability measured at 1, 3, 5, and 24 hours after medium perfusion for glucose and lactate (metabolite sensors), bovine serum albumin (total protein quantitation), viable enucleate and mononuclear cells from CB (differential manual counts employing trypan blue and methylene blue) (Graphical data from (A) is presented as the average of $N \geq 3$ material replicates, (D) represents $N=1$ single experiment for biochemical factors, and $N=1$ single biological replicate for CB cells).

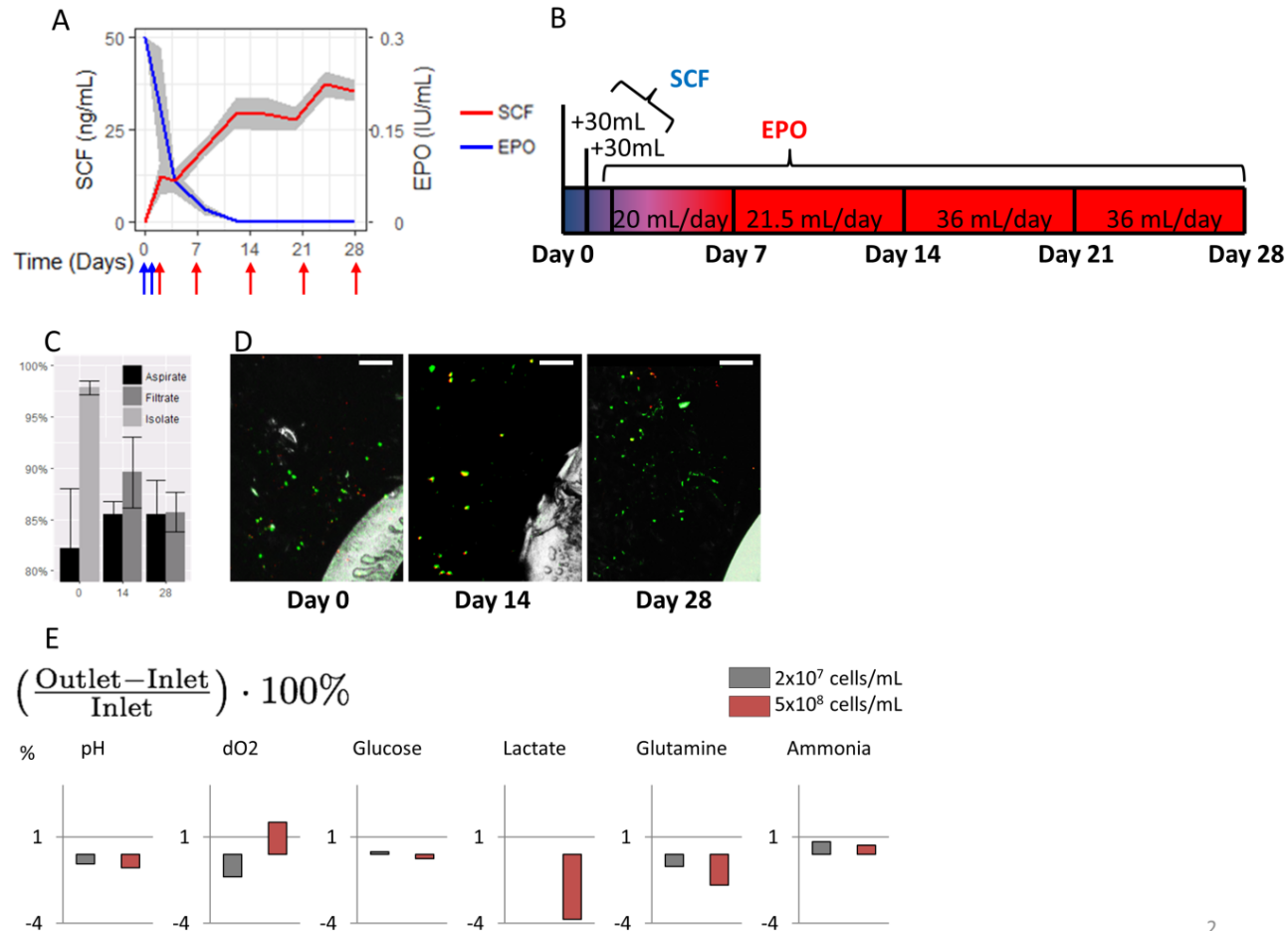


Figure 27: HFR culture medium replenishment, cell viability, and metabolite m.

(A) Supplemented concentrations of SCF and EPO detected at HFR outlet for N=4 biological replicate measurements with shaded standard error; underlying arrows indicate time points of cytokine addition to continuously fed medium. (B) Schedule of cytokine addition, days of fed medium exchange (days 0, 1, 2, 7, 14, 21, 28), and flow rate of replenishment. (C) Viability of extracted cells from day 0 isolate, days 14 and 28 filtrate, and days 0, 14, and 28 aspirate from sectioned reactors manually counted with trypan blue (N≥3 biological replicates). (D) Representative confocal images of frozen and sectioned HFRs; viable cells are identified in green (Calcein-AM) and nonviable cells in red (ethidium homodimer-1) (100 μm scale bars). (E) Average percent change in metabolite, pH, and dO₂ concentrations between HFR inlet and outlet for different inoculum densities, measured every 2 days during culture, as an average of N=4 biological replicates (2x10⁷, in grey) or N=1 (5x10⁸, in red).

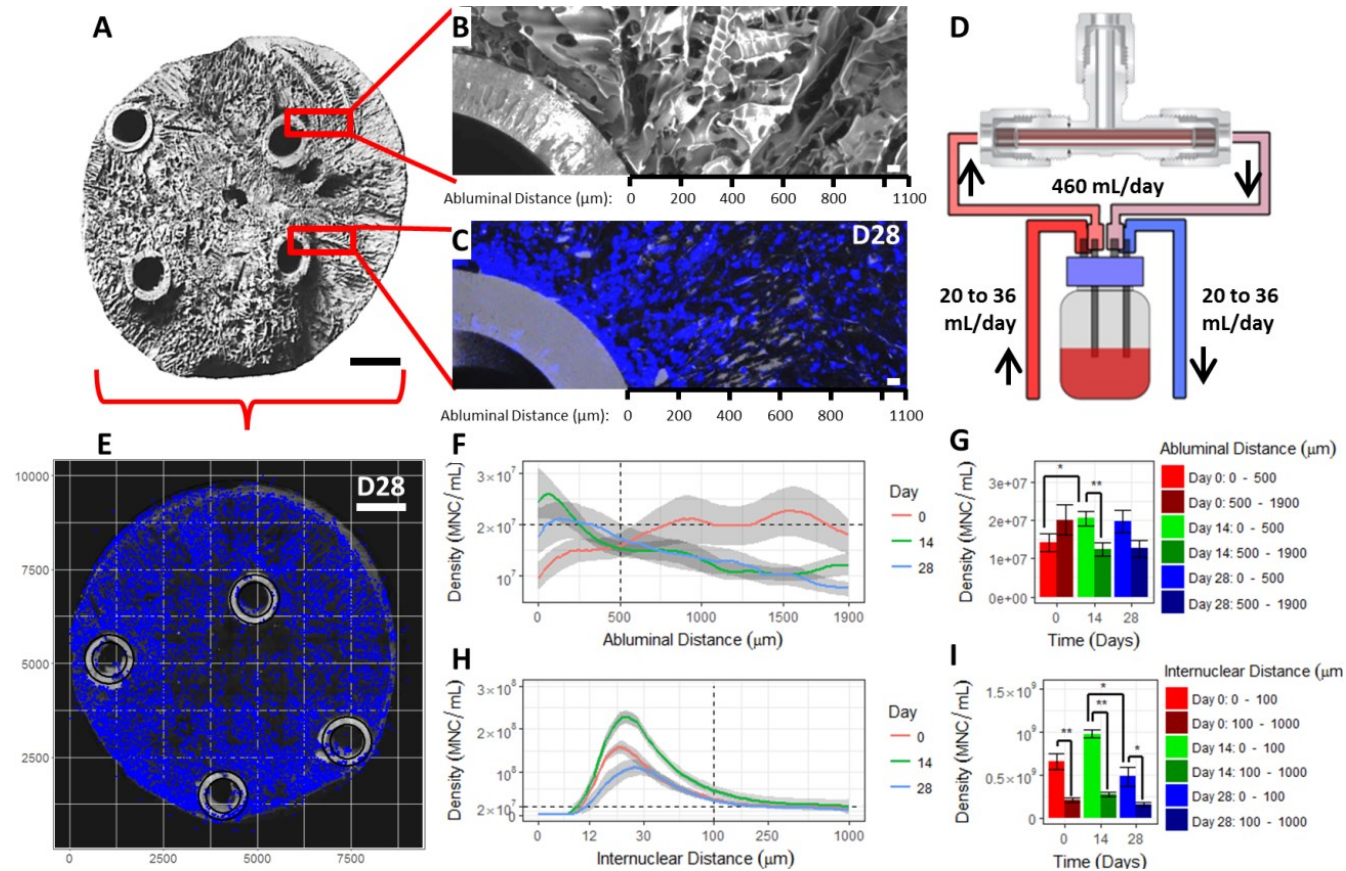


Figure 28: A hollow fibre bioreactor (HFR) structures hUCB MNC distribution.

(A) Representative SEM image of a HFR cross-section (35x magnification, 1mm scale bar). (B) Confocal micrograph of HFR-bound amine groups (RBITC, grey) and of (C) cell nuclei (DAPI, blue) distributed within HFR structure (laser reflection, grey) at day 28 (100 μm scale bars; abluminal HF distances underneath). (D) HFR platform schematic with flow rates for introducing fresh medium, recycling HFR-perfused medium, and removing waste medium and harvest of cells. (E) DAPI localisation from a full HFR cross-section (10x magnification, 1mm scale bar). Cellular distributions in HFR were characterised by: (F) MNC abluminal distribution at days 0, 14, and 28 and highlighting inoculum density (hatched horizontal line) and densities within or further than 500 μm from HF (hatched vertical line) and a (G) comparison of these average densities. (H) Internuclear distribution at days 0, 14, and 28 highlighting inoculum density (hatched horizontal line) and densities within 100 μm of any one nuclei (hatched vertical line) with a (I) comparison of these average densities (N≥3 biological replicates, n=9 image replicates; shaded regions in (F) and (H) represents standard error about the mean from N replicates; *p < 0.05, **p < 0.01 by paired student's t-test from N replicates).

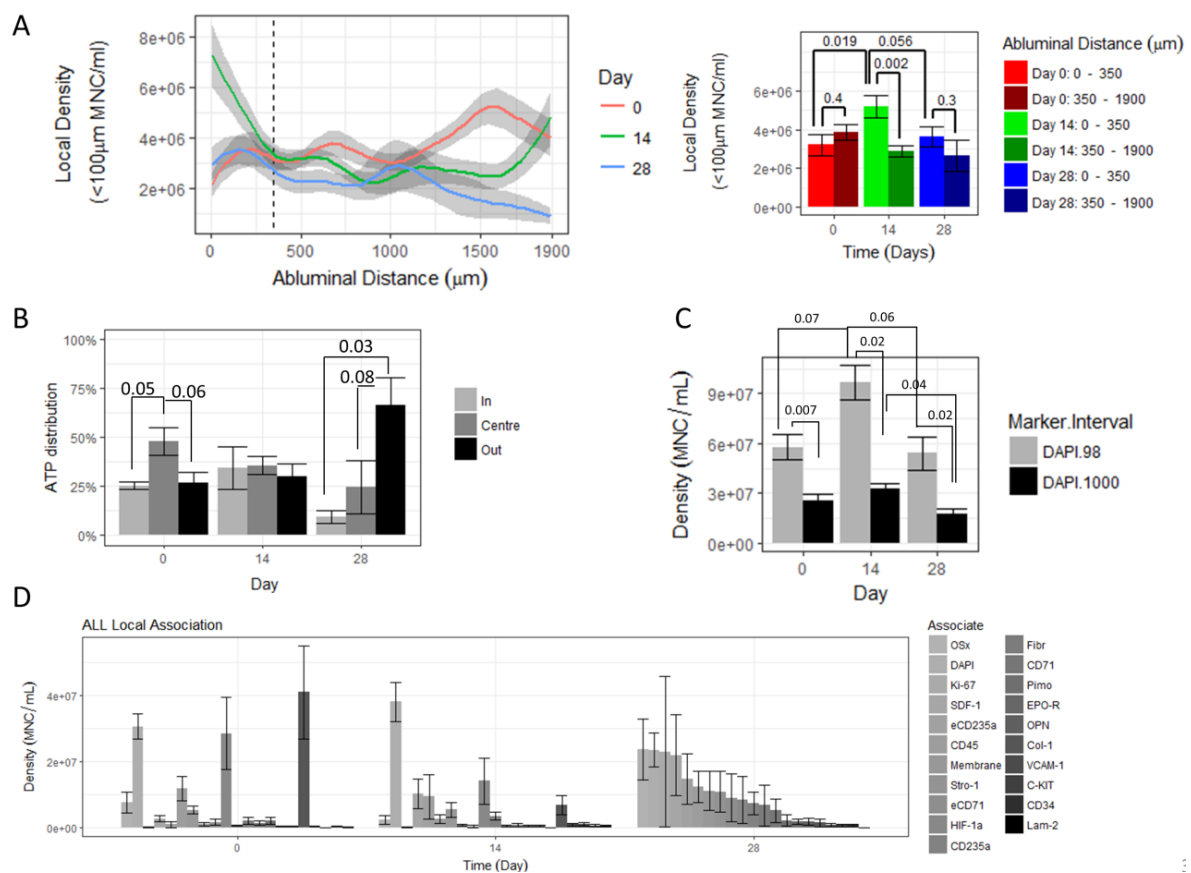


Figure 29: HFR hUCB culture DAPI and ATP distributions.

(A) Abluminal HF distribution of MNC density when within 100 µm of another MNC at days 0, 14, and 28 for $N \geq 3$ biological replicates with shaded standard error alongside corresponding average densities within or outside 350 µm of HF for N replicates with standard error bars and p values from unpaired student's t-test. (B) Distribution of ATP content from 0.125 mL HFBR sections near perfusion inlet, midpoint, and outlet for different time points for $N \geq 3$ biological replicates with standard error bars below selected p values from unpaired student's t-tests. (C) Average distribution of MNCs in local (≤ 98 µm) as compared with bulk (≤ 1000 µm) MNC neighbourhoods at 50% lower radial discretisation than Figure 28I, as used for proceeding supplementary figures, for $N \geq 3$ biological replicates with standard error bars below selected p values from paired student's t-tests. (D) Local (≤ 100 µm) association densities of nucleated cells marked by DAPI with imaged cell types. Statistical significance in (D) was not measured.

Cellular hypoxia was dependent on distance from HF and the local density of surrounding cells. At day 0, inoculated CBMNCs which were co-localised with hypoxia inducible factor 1α ("HIF-1α⁺ MNCs") were evenly distributed throughout the HFR (<6% average difference in expression) and upregulated when within 100 µm of other MNCs (4.2-fold above average density, Figure 31A). At day 28, HIF-1α⁺ MNCs predominately distributed in regions further from HF (12% increase at >1.7mm from HF). Hypoxia marker Pimonidiazole (Pimo) did not follow similar distribution trends, but Pimo⁺ MNC expression increased at day 28 within 1000 µm of HF as did cell proliferation marker Ki-67

(Figure 30A-B; Figure 31B-C). Organizational HFR maps of cell placement were simulated to summarize replicate 3D imaging data including cell number and type, abluminal distribution, and local associations; these maps illustrated a day 28 increase of hypoxic markers far from HF perfusion and within neighborhoods of Ki-67⁺ MNCs (Figure 30C-D, Figure 31D). The perfused HFR distributed cellular microenvironments of association, hypoxia, and proliferation, and its organization of hematopoietic cell maturations was further investigated.

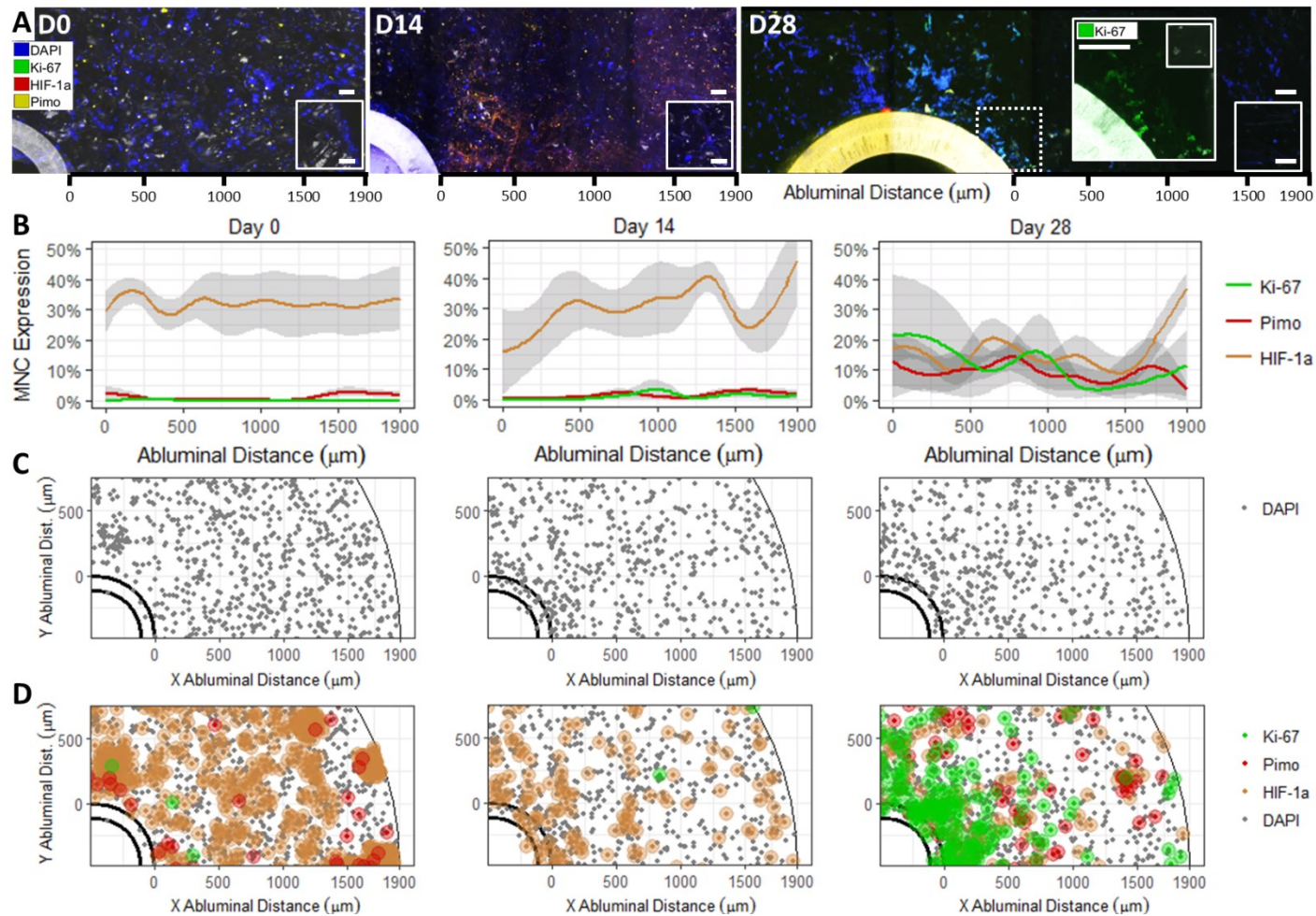


Figure 30: Distribution of cellular hypoxia.

(A) Representative confocal images of DAPI, HIF-1 α , Pimo, and Ki-67 (100 μm scale bars) distribution in HFR at days 0, 14, and 28 with a magnified inset of a highlighted fibre-proximal region of Ki-67. (B) Quantitative image analyses calculate abluminal HF distribution of HIF-1 α ⁺, Pimo⁺, or Ki-67⁺ MNCs. (C, D) Organizational maps illustrating HIF-1 α , Pimo, Ki-67, and DAPI density, HF abluminal distribution, and intercellular associations for a theoretical HFR cross-section cell XY-monolayer simulated from $N \geq 3$ biological replicate measurements at days 0, 14, and 28 ($N \geq 3$ biological replicates; shaded regions in (B) represents standard error about the mean from N replicates).

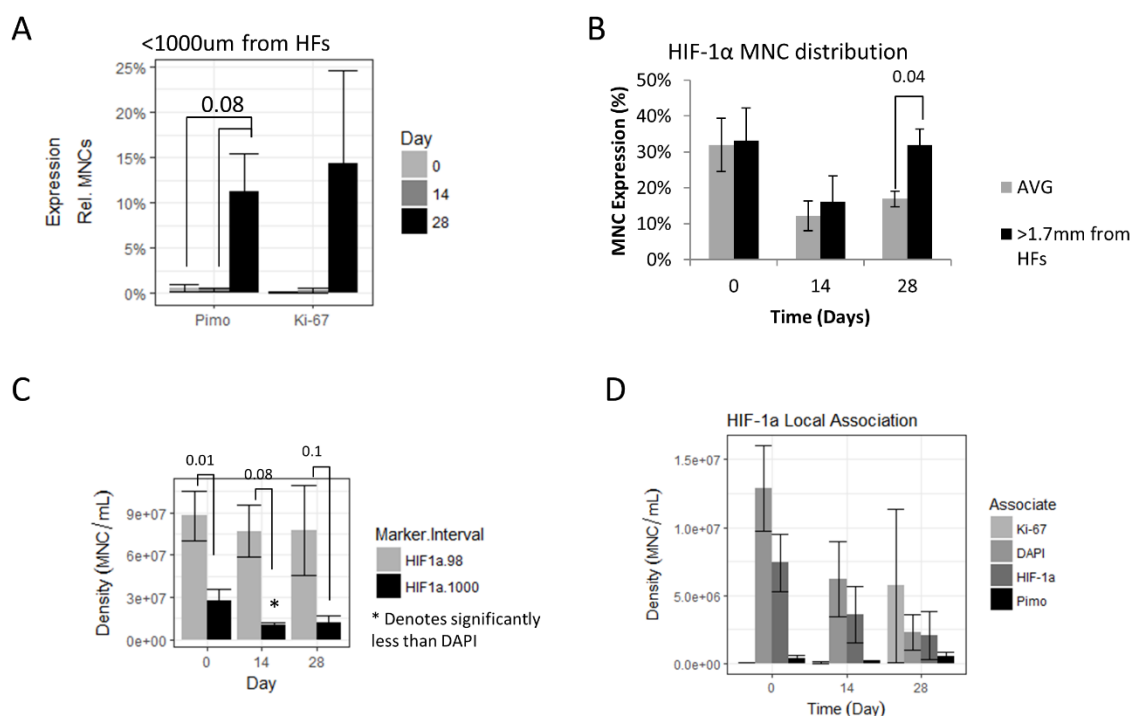


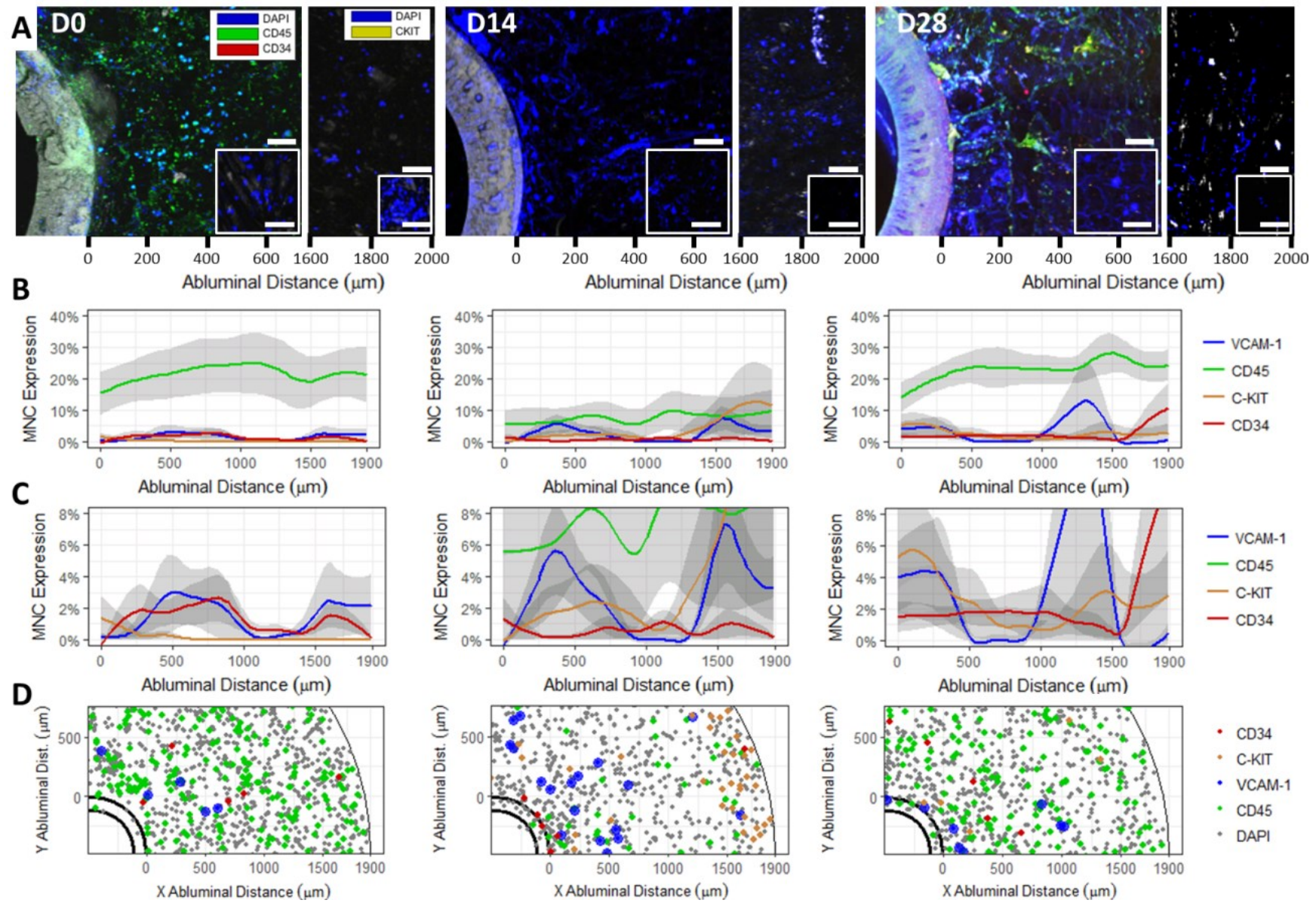
Figure 31: Distribution statistics of HIF-1 α , Pimo, and Ki-67 co-localised MNCs.

(A) Expression of Pimo and Ki-67 within 1000 μm of abluminal hollow fibre surfaces. (B) Expression of HIF-1 α on MNCs throughout the reactor and specifically further than 1700 μm from abluminal hollow fibre surfaces at different time points. (C) HIF-1 α local association densities (DAPI ≤ 98 μm from HIF-1 α MNCs) compared to bulk densities (DAPI ≤ 1000 μm from HIF-1 α MNCs) at days 0, 14, and 28. (D) Local association densities of all, HIF-1 α , Pimo, and Ki-67 co-localised MNCs with HIF-1 α MNCs (all graphs have standard error bars for $N \geq 3$ biological replicates, p values reported in (A) represent paired student's t tests from N, (B) and (C) represent unpaired student's t tests from N, statistical significance not measured in (D)).

6.4.2. Organization of an interactive hematopoietic environment

Cellular C-KIT and CD34 expression increased during culture (1 to 3%, each), whereas pan-hematopoietic marker, CD45, fluctuated from 15-30% of MNCs at days 0 and 28, to as low as 8% at day 14 (Figure 32A; Figure 33A). Whereas CD45⁺ MNCs were evenly distributed throughout HFR space, C-KIT, CD34, and VCAM-1 were expressed in fibre-proximal regions (Figure 32B-C). CD34⁺ and VCAM-1⁺ MNCs distributed within neighbourhoods of 3-fold above average DAPI⁺ densities at days 14 and 28, while between days 0 and 28, CD45⁺ MNCs distributed within 2.5-fold less DAPI dense neighbourhoods (Figure 33B). At day 28, CD34⁺ MNCs were most frequently surrounded by CD45⁺ MNCs (Figure 33C), suggesting hematopoietic colonies were generated during late stages of culture.

Hematopoietic growth factors were continuously secreted throughout HFR culture. Average concentrations of G-, GM-, M-CSF, IL-9, IL-21, ($p < 0.01$) and IL-4, IL-5, IL-6, IL-10, IL-13, IL-17F, IL-22 ($p < 0.05$) were detected above assay baseline with inconsistent detection of IL-2 and IL-17A ($p \leq 0.3$); shed EPO-receptor (EPO-R) was never detected within perfused medium. IL-6 was present above 1.7 ng/mL before decaying to 4.7 pg/mL from day 4 to the second half of culture ($p = 0.006$). Many secreted factors increased in concentration just before a fresh nutrient feed was introduced (days 12, 20, 28), including a 70% G-CSF increase between days 16 and 20 ($p = 0.08$), when unstable nutrients (glutamine, glutamate), metabolites (ammonia), and growth factors (EPO) were at their least supportive concentrations (Figure 32E-G). MNCs expressing hemato-vascular CD34 and VCAM-1 demonstrated stromal morphologies with cell lengths over 100 μm at day 28 near HFVs (Figure 32H). These secretory and morphological profiles indicated hUCB MNCs within the HFRs may have autonomously generated a stromal context for hematopoietic proliferation.



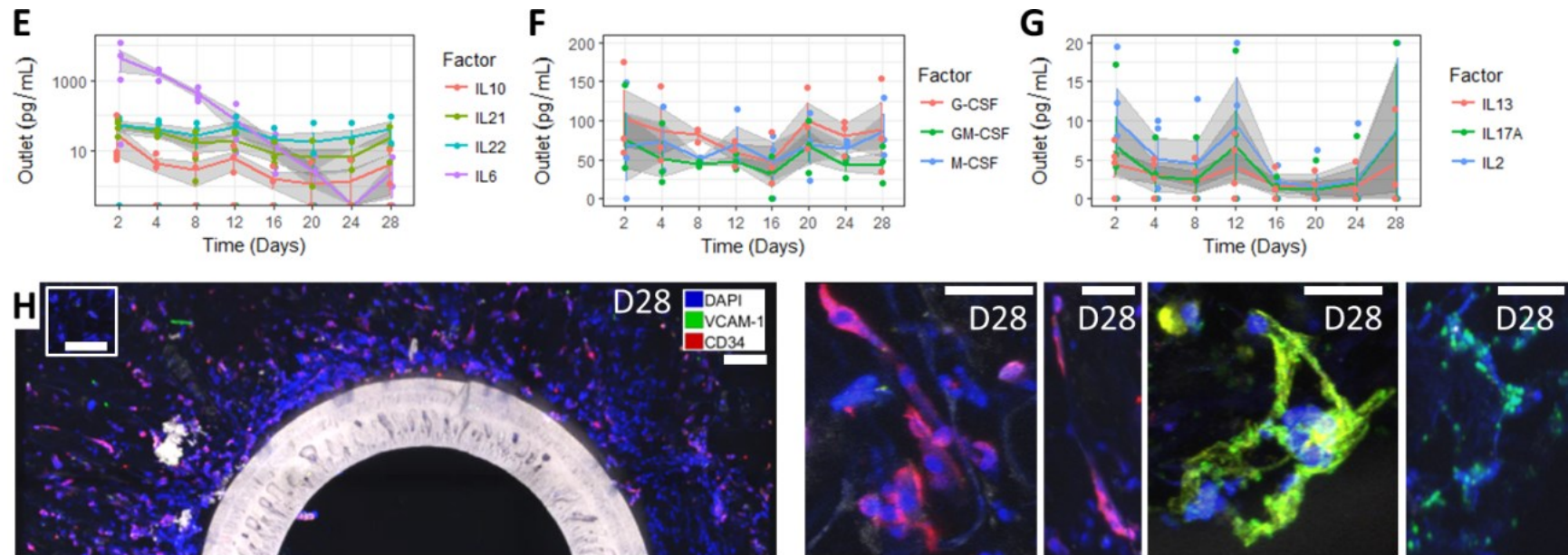


Figure 32: Hematopoietic organization and interaction.

(A) Representative confocal images of HFR distribution of DAPI, CD45, CD34 and C-KIT (100 μm scale bars), with abluminal HF distribution analyses at (B) high and (C) low ranges of phenotype expression on MNCs. (D) Organizational maps illustrating distribution of CD45, C-KIT, CD34, and DAPI for days 0, 14, and 28 of culture. HFR cells produced hematopoietic growth factors *in situ* which were measured at the HFR outlet and included (E) IL-10, IL-21, IL-22, and IL-6, (F) G-CSF, GM-CSF, and M-CSF, and (G) interleukins IL-13, IL-17A, and IL-2. (H) Representative confocal images of CD34 and VCAM-1 phenotypes demonstrating stromal morphologies (left to right: 500 μm, 100 μm, 100 μm, 50 μm, 100 μm scale bars) ($N \geq 3$ biological replicates for (B) and (C), $N = 4$ biological replicates for (E), (F), and (G), all shaded regions represent standard error about the mean from N replicates).

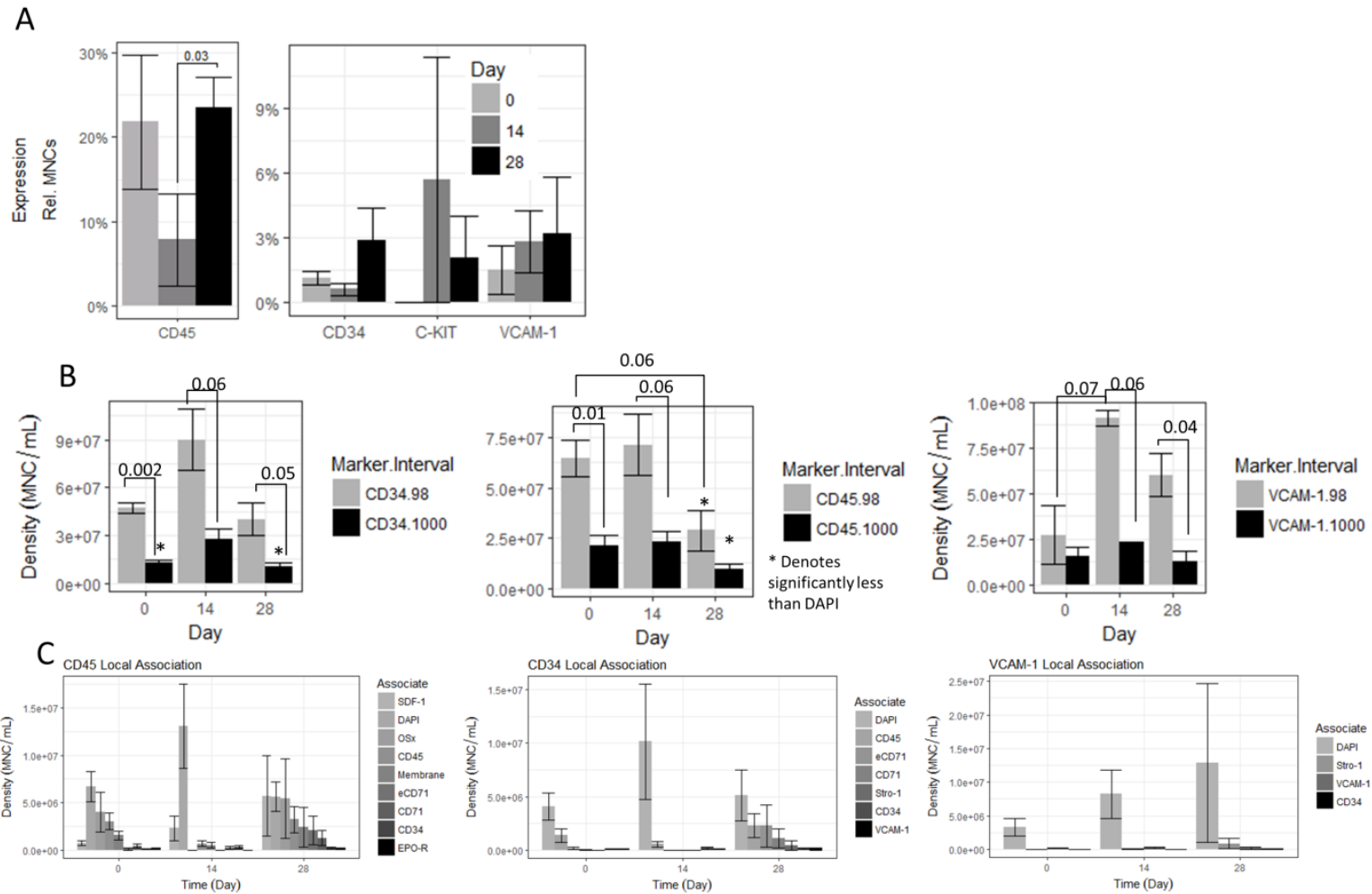


Figure 33: Distribution statistics of CD45, CD34, C-KIT, and VCAM-1 at days 0, 14, and 28.

(A) Overall MNC expression from confocal images at two different y-axis scales. (B) CD45 (left), CD34 (centre), and VCAM-1 (right) MNC local association densities ($\leq 98 \mu\text{m}$ from CD45, CD34, or VCAM-1 MNCs) compared to bulk densities ($\leq 1000 \mu\text{m}$). (C) Local phenotypic association densities of CD45 (left), CD34 (centre), and VCAM-1 (right) with selected markers simultaneously imaged. (all graphs have standard error bars for $N \geq 3$ biological replicates, p values reported in (A) represent unpaired student's t tests from N, (B) represent paired student's t tests from N, statistical significance not measured in (C)).

6.4.3. Production of a supportive stromal environment

Large, stretched, adherent cell morphologies and stromal phenotypes were imaged during HFR culture, and comprised from 10% of inoculated CBMNCs to 35% of the day 28 *in situ* HFR MNC population (Figure A-C). These expanded stromal markers included mesenchymal Stro-1 (4% to 14%), preosteoblast osterix (OSx) (4% to 27%), and mature osteoblast osteopontin (OPN) (0% to 7%). Stro-1⁺ MNCs primarily expanded within 500 μ m of HFs, while generated OPN⁺ MNCs were predominately further than 1 mm away (Figure D-E; Figure 35A). Stro-1 and OSx comprised the most significant markers for MNC association during culture development at days 14 and 28, when Stro-1⁺ and OSx⁺ MNCs were distributed within neighbourhoods of 4 and 5-fold above average DAPI densities (Figure 35B). OSx⁺ MNCs most densely associated with CD45⁺ hematopoietic phenotypes at day 0, and enucleate CD235a⁺ reticulocytes at day 14 before predominately associating with other stromal cells at day 28 (Figure 34F, Figure 35C).

Extracellular matrix (ECM) proteins collagen type 1, fibronectin, and laminin-2, and hematopoietic chemokine SDF-1 (CXCL12) were co-localised with MNCs and expressed on large, stretched cell membranes throughout culture (Figure G-H, Figure 36A). While collagen type 1 MNC expression decreased throughout culture (37% to 6%), fibronectin and SDF-1 increased (1% to 7% fibronectin; 8% to 25% SDF-1) significantly more so within 500 μ m of HFs (Figure I-J; Figure 36B). Collagen type-1 comprised the most significant marker for MNC association upon inoculation, and SDF-1, collagen type-1, and fibronectin expressing MNCs were distributed in dense MNC neighbourhoods at day 0 (6-fold above average DAPI density for SDF-1; 4-fold for collagen type 1 and fibronectin) (Figure 36C). SDF-1 most densely associated in local neighbourhoods with hematopoietic CD45⁺ MNCs at days 0 and 28 (Figure 36D).

Stromal cells were supported by a range of secreted angiogenic and stromal factors, including EGF, HGF, FGF- β , PDGF-AA, PDGF-BB, VEGF, TFN- α ($p < 0.002$), Ang-2, TGF- α , IFN- γ ($p < 0.05$), whose average concentration throughout culture was significantly higher than the baseline. Similar to hematopoietic factors, these secreted, stromal factors were present in significantly higher concentrations at days 2 (IFN- γ), 16 (Ang-2, VEGF, TFN- α), and 20 (TFN- α ; all $p < 0.05$; Figure K-M). The profile of both hematopoietic and stromal cell proliferation, association, and growth factor and ECM protein

secretion followed a similar trend: an early day 0 to 14 decline of MNC progeny (CD45, OSx, OPN) and local associations, followed by the production of mitogenic growth factors and the regeneration of these cells and factors from days 14 to 28. This flux did not noticeably affect red cell output, whose HFR and filtrate content consecutively rose from days 0 to 14 to 28.

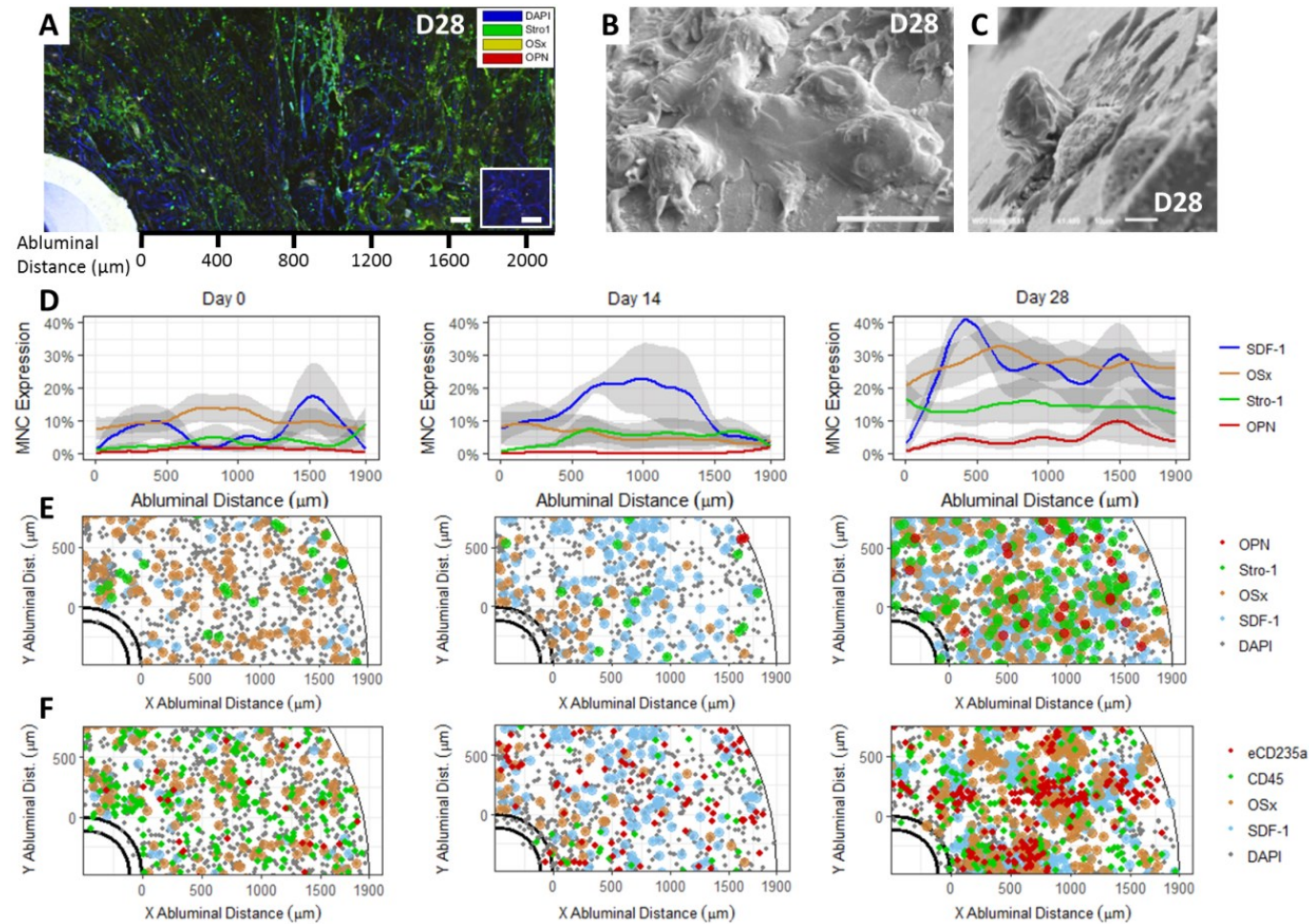


Figure 34: Stromal proliferation generates an erythroid-interactive mesenchymal-osteogenic matrix.

(A) A representative confocal image at day 28 demonstrating dense layers of Stro-1 and OSx stromal cells (100 μm scale bars), and (B, C) SEMs of adherent, stromal-like cells at day 28 (100 μm and 10 μm scale bars). (D) Abluminal HF distributions and (E) organizational maps of SDF-1, OSx, Stro-1, OPN, and DAPI and of (F) enucleate CD235a (eCD235a), CD45, OSx, and DAPI at days 0, 14, and 28.

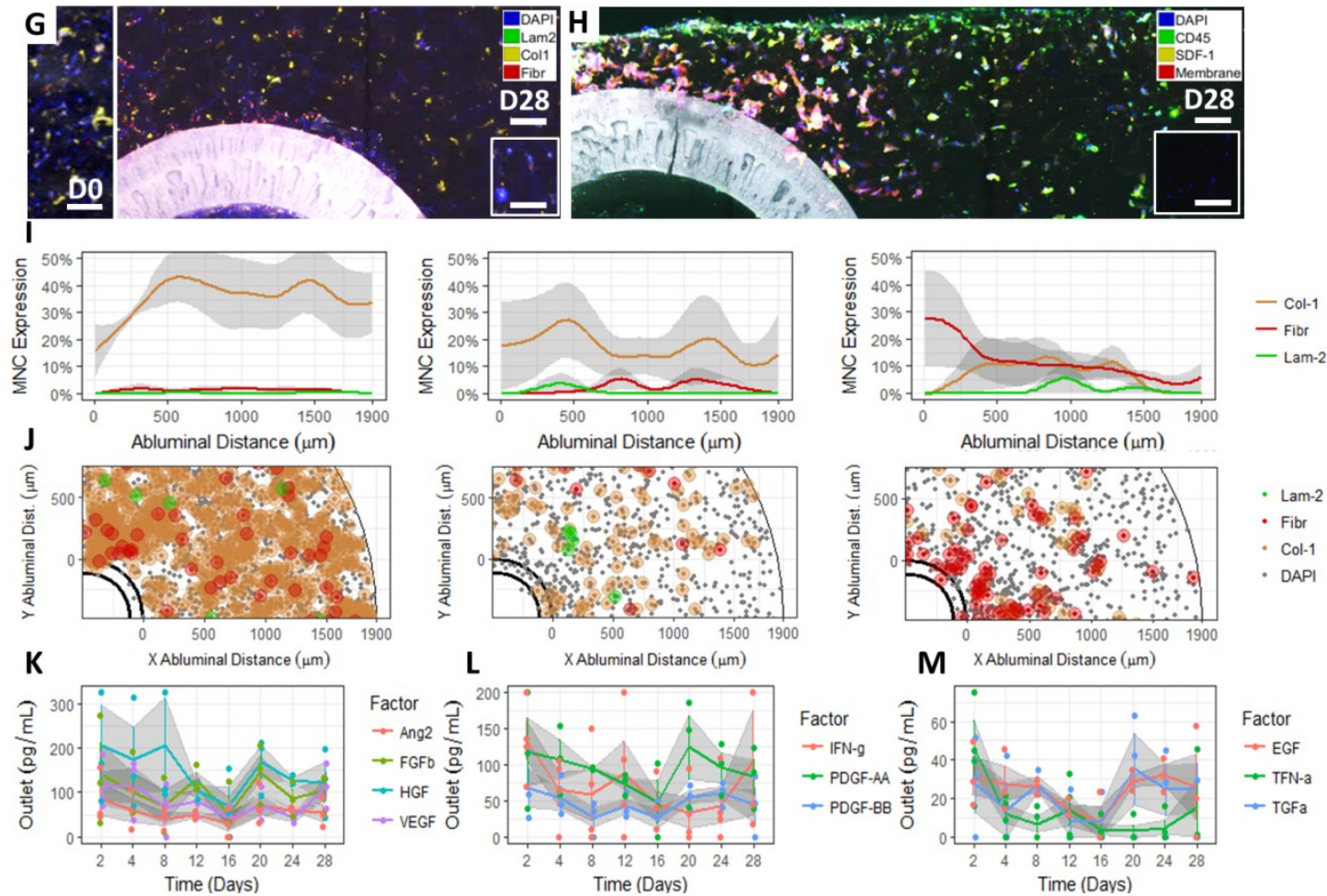


Figure 34 (continued): (G) Confocal images of extracellular matrix (ECM) proteins laminin-2 (Lam2), collagen type 1 (Col1), and fibronectin (Fibr) at days 0 (left), and 28 (right) of culture (100 μm scale bars). (H) A confocal image highlighting CD45⁺ MNCs and stromal cells expressing chemoattractant SDF-1 with nuclear and cell body counterstains at day 28 (100 μm scale bars). (I) Abluminal HF distributions and (J) organizational maps of Laminin-2, Fibronectin, Collagen-1, and DAPI. HFR cells produced stromal growth factors *in situ* which were measured at the HFR outlet and included (K) Ang-2, FGF-b, HGF, and VEGF, (L) IFN-g, PDGF-AA and -BB, and (M) EGF, TFN-a, and TGF-a (N \geq 3 biological replicates for (D), (E), (F), (I), and (J), N=4 biological replicates for (K), (L), and (M), all shaded regions represent standard error about the mean from N replicates).

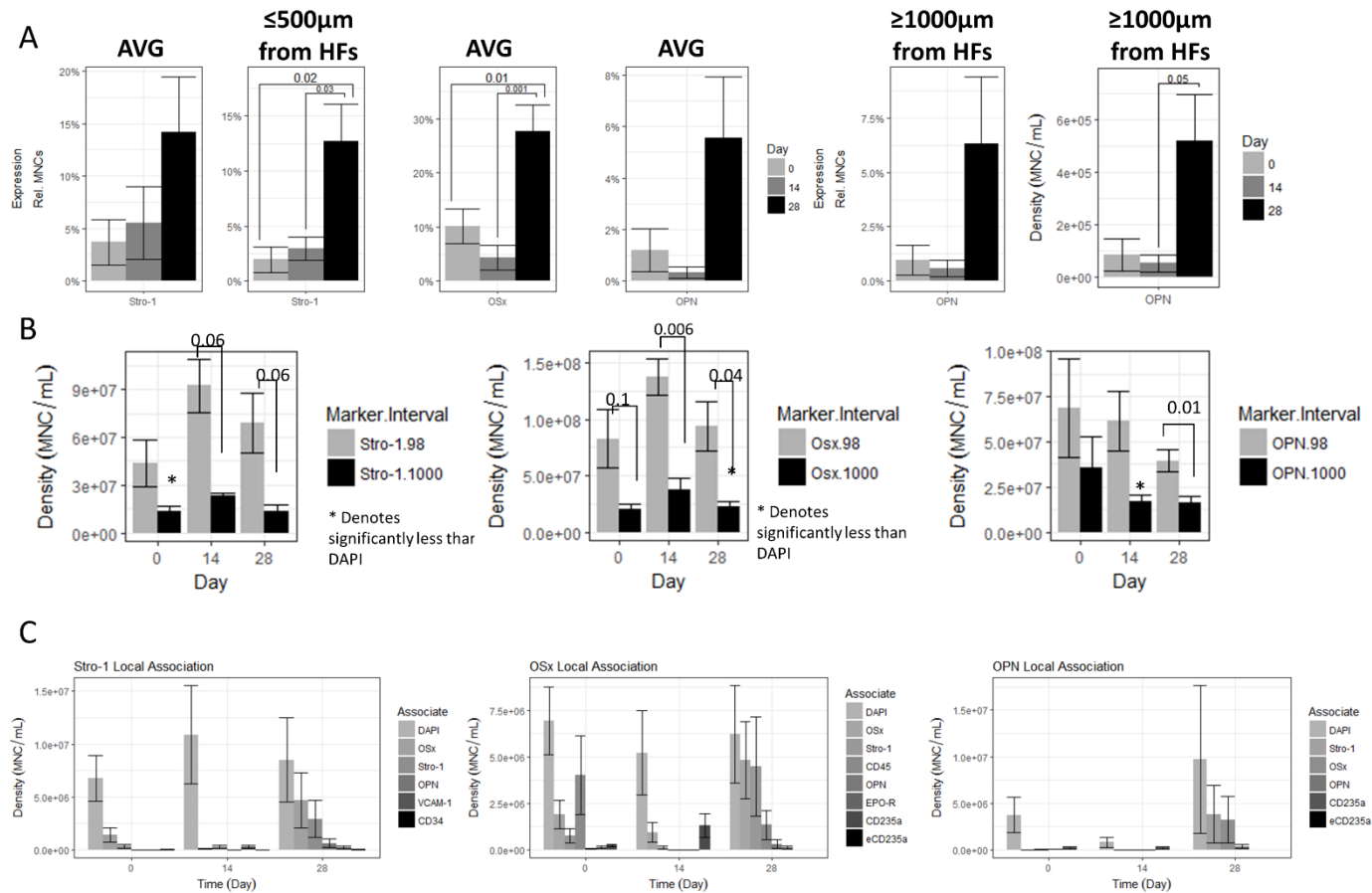


Figure 35: Distribution statistics of Stro-1, OSx, and OPN.

(A) From left, average MNC expression of Stro-1 through bioreactor (first) and when confined to distances within 500 μm of hollow fibre abluminal surfaces (second), average MNC expression of OSx through bioreactor (third), average MNC expression of OPN through bioreactor (fourth), and when confined to distances further than 1000 μm away from hollow fibre abluminal surfaces (fifth) and as an OPN expressing MNC density (sixth). (B) Stro-1 (left), OSx (center), and OPN (right) MNC local association densities ($\leq 98\ \mu\text{m}$ from Stro-1, OSx, or OPN MNCs) compared to bulk densities ($\leq 1000\ \mu\text{m}$). (C) Local phenotypic association densities of Stro-1 (left), OSx (centre), and OPN (right) with selected markers simultaneously imaged (all graphs have standard error bars for $N \geq 3$)

biological replicates, p values reported in (A) represent unpaired student's t tests from N, (B) represent paired student's t tests from N, statistical significance not measured in (C)).

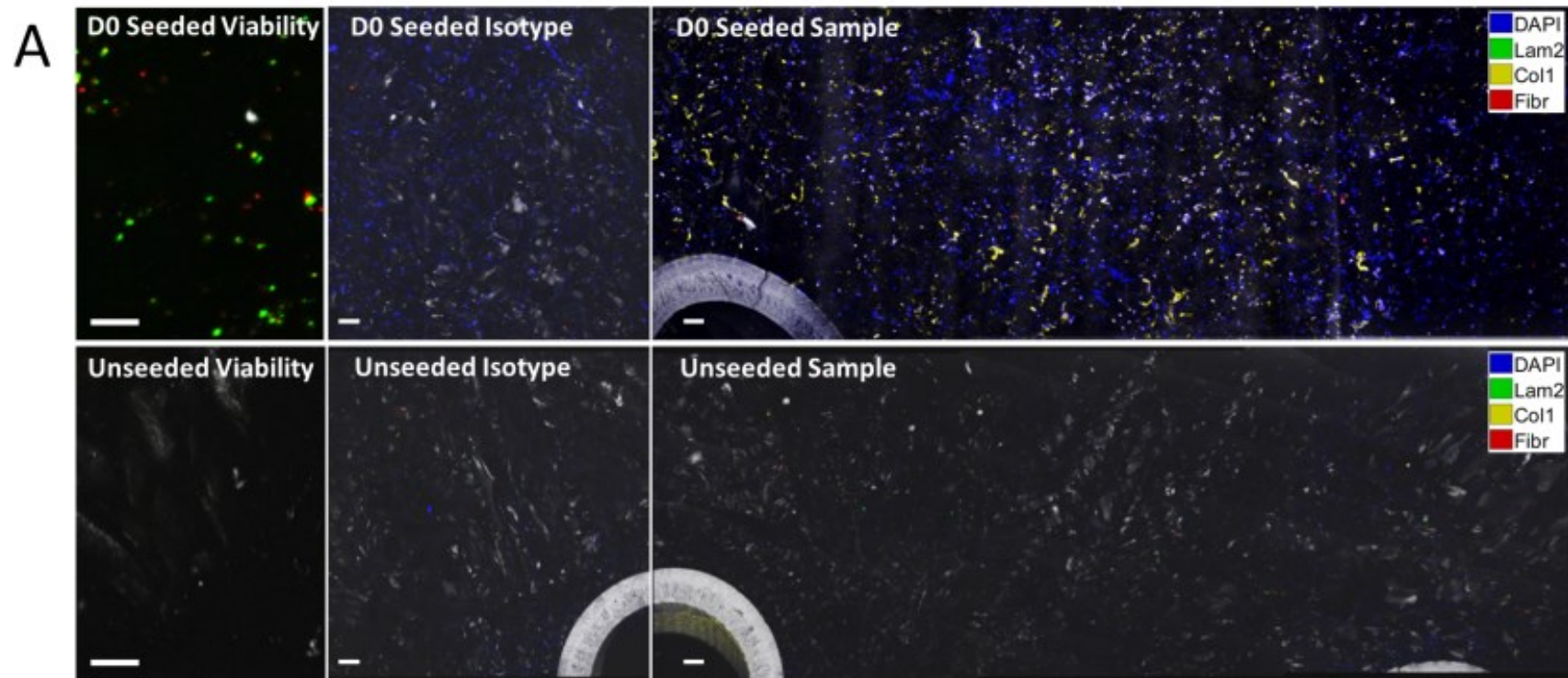


Figure 36: Distribution statistics of SDF-1, collagen type 1 (Col-1), laminin type 2 (Lam-2), and fibronectin (Fibr).
 (A) Demonstrating positive detection of collagen type-1 proteins associating with MNCs upon day 0 seeding as compared to isotype and unseeded controls, where the a cropped section from the top, right sample image was used in Main Fig. 4G.

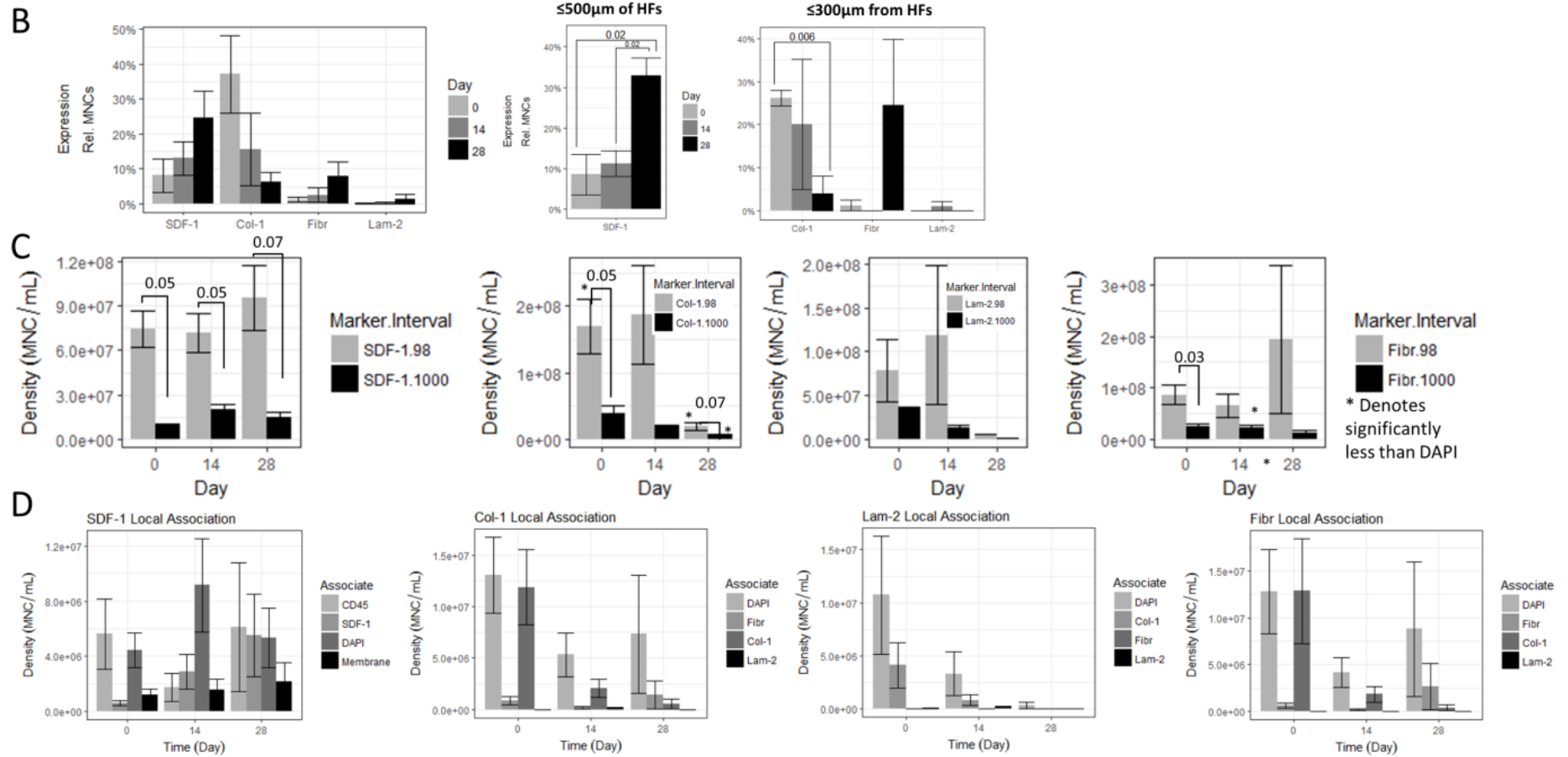


Figure 36 (continued): (B) Average MNC expression of SDF-1, Col-1, Fibr, and Lam-2 throughout reactor at days 0, 14, and 28. (C) MNC expression of SDF-1 within 500 μm (left) and Col-1, Fibr, and Lam-2 within 300 μm (right) of hollow fibre abluminal surfaces. (D) From left, SDF-1 (first), Col-1 (second), Lam-2 (third), and Col-1 (fourth) MNC local association densities ($\leq 98 \mu\text{m}$) compared to bulk densities ($\leq 1000 \mu\text{m}$). (E) From left, local phenotypic association densities of SDF-1 (first), Col-1 (second), Lam-2 (third), and Fibr (fourth) with selected markers simultaneously imaged (all graphs have standard error bars for $N \geq 3$ biological replicates, p values reported in (B) represent unpaired student's t tests from N, (C) represent paired student's t tests from N, statistical significance not measured in (D)).

6.4.4. Genesis and harvest of red cells

Nucleated erythroblasts expressing EPO-R, CD71, or CD235a and enucleate reticulocytes expressing CD71 or CD235a (referred to as eCD71 or eCD235a) increased from days 0 to 28 (Figure 37A; Figure 38A). With the exception of CD235a at day 28, the peak distribution of these 5 erythroid cell types at days 14 and 28 existed within 1 mm of hollow fibres (Figure 37B). EPO-R, CD71, or CD235a nucleated erythroid cells associated near other MNCs at much lower densities than stromal cells, with EPO-R⁺ MNCs being most associative and CD235a⁺ MNCs declining in association by the end of culture (Figure 38B). EPO-R erythroid progenitors most frequently associated in neighborhoods with OSx⁺ preosteoblast phenotypes, while mature CD235a⁺ erythroblasts tended toward intra-lineal erythroid associations (Figure 38C). These erythroid associations were visualised as colonies which included erythroblasts, enucleate cells, and macrophages attached to HFR biomaterials (Figure 38D-E)

Reticulocytes were found filtering through HF's and 10 million viable cells were collected within perfused HFR medium (Figure 37D-G). The number of filtering cells imaged within HF's increased 3 or 2-fold between days 0 and 14 or 28, and were comprised of 1% to 30% total enucleate or 1% to 25% eCD235a (Figure 38D). Collected viable cells were composed of a phenotype and morphology enriched for mature enucleate red cell phenotypes compared to the inoculum (from 3% to 23% CD235a) and not pan-hematopoietic CD45 (from 55% to 7%; Figure 37H-I).

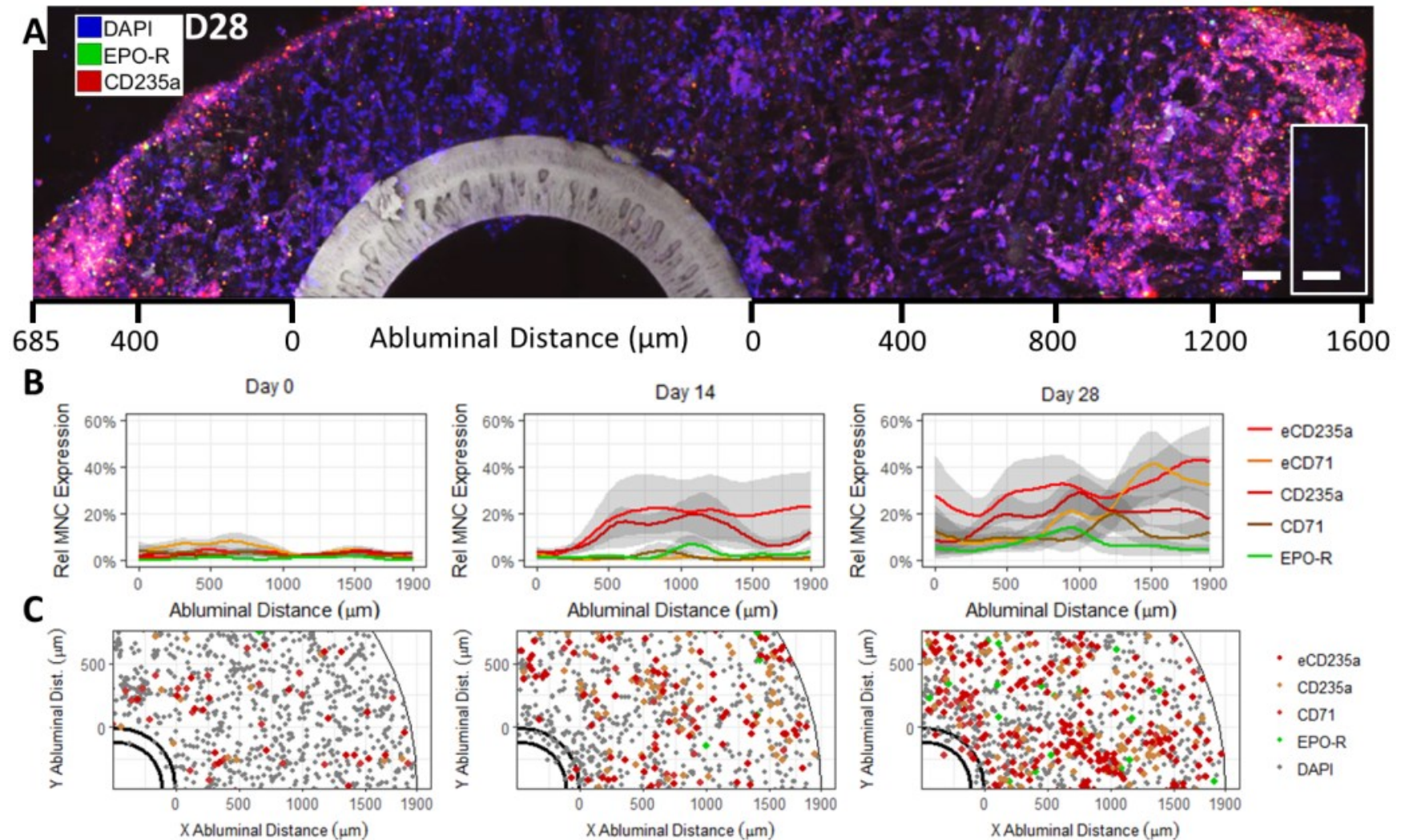


Figure 37: Differentiation and harvest of enucleated red cells.

(A) A representative confocal image at day 28 demonstrating distribution of nuclei, EPO-R, and mature RBC CD235a phenotype (100 μm scale bars). (B) Abluminal distributions of enucleate CD235a and CD71 (eCD235a, eCD71) cells, and nucleated CD235a, CD71, and EPO-R-expressing cells, and (C) projected organizational maps of eCD235a, CD235a, CD71, and EPO-R alongside DAPI.

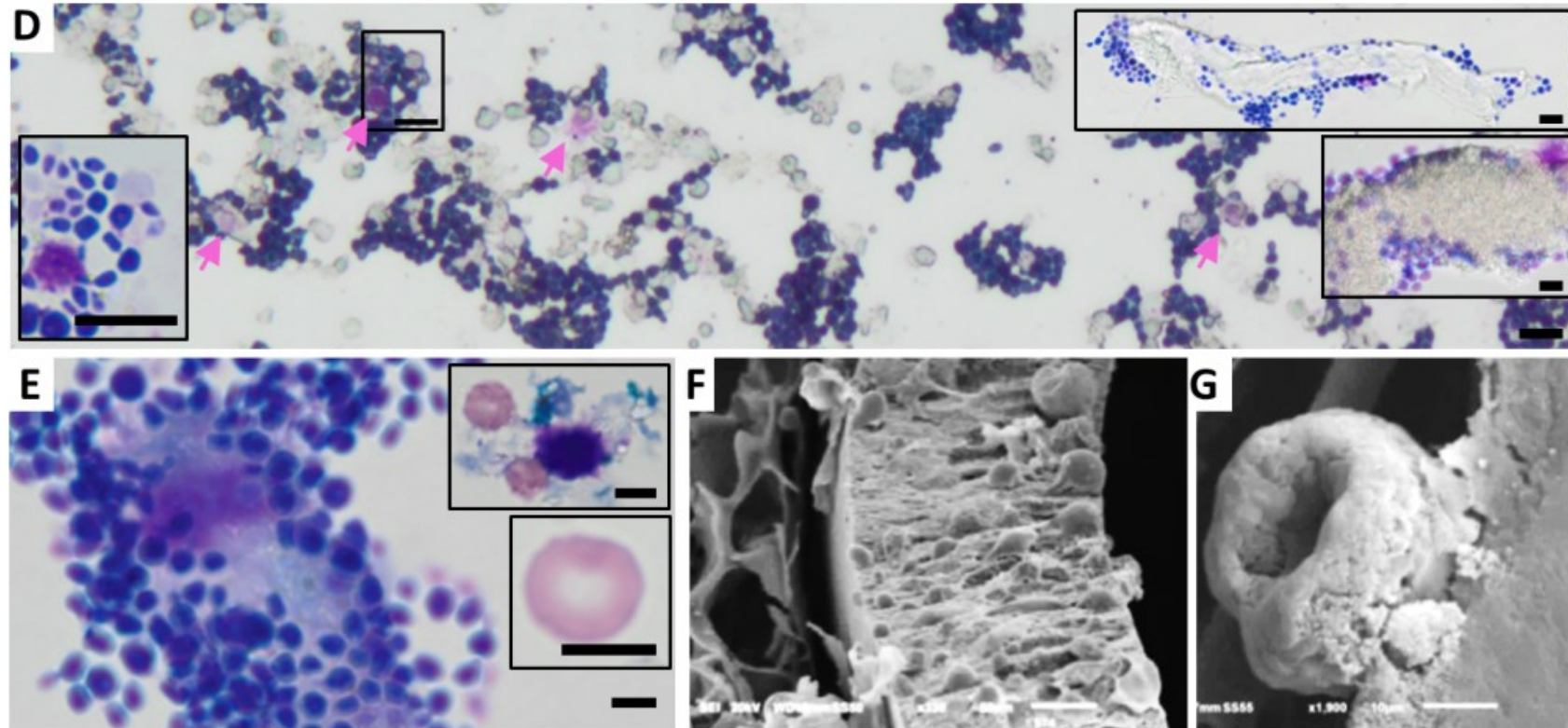


Figure 37 (continued): (D) Wright Giemsa-stained cell distribution from a day 14 HFR cross-section imprint with pink arrows highlighting candidate macrophages and insets of a highlighted colony (left) and of erythroid cell adherence to scaffold biomaterial (right top) and of erythroid cells adhering to and filtering through hollow fibres (right bottom) (20 μm scale bars). (E) May Grünwald Giemsa-stained erythroid colony including a central macrophage from a day 14 HFR aspirate and insets of May Grünwald Giemsa-stained day 14 HFR filtrate reticulocytes connected to a macrophage (top right) and of an isolated biconcave reticulocyte (bottom right) (10 μm scale bars). (F) A SEM showing small round cells filtering through hollow fibres at day 28 (50 μm scale bar) and (G) SEM showing a biconcave cell on hollow fibre adluminal surface (10 μm scale bar).

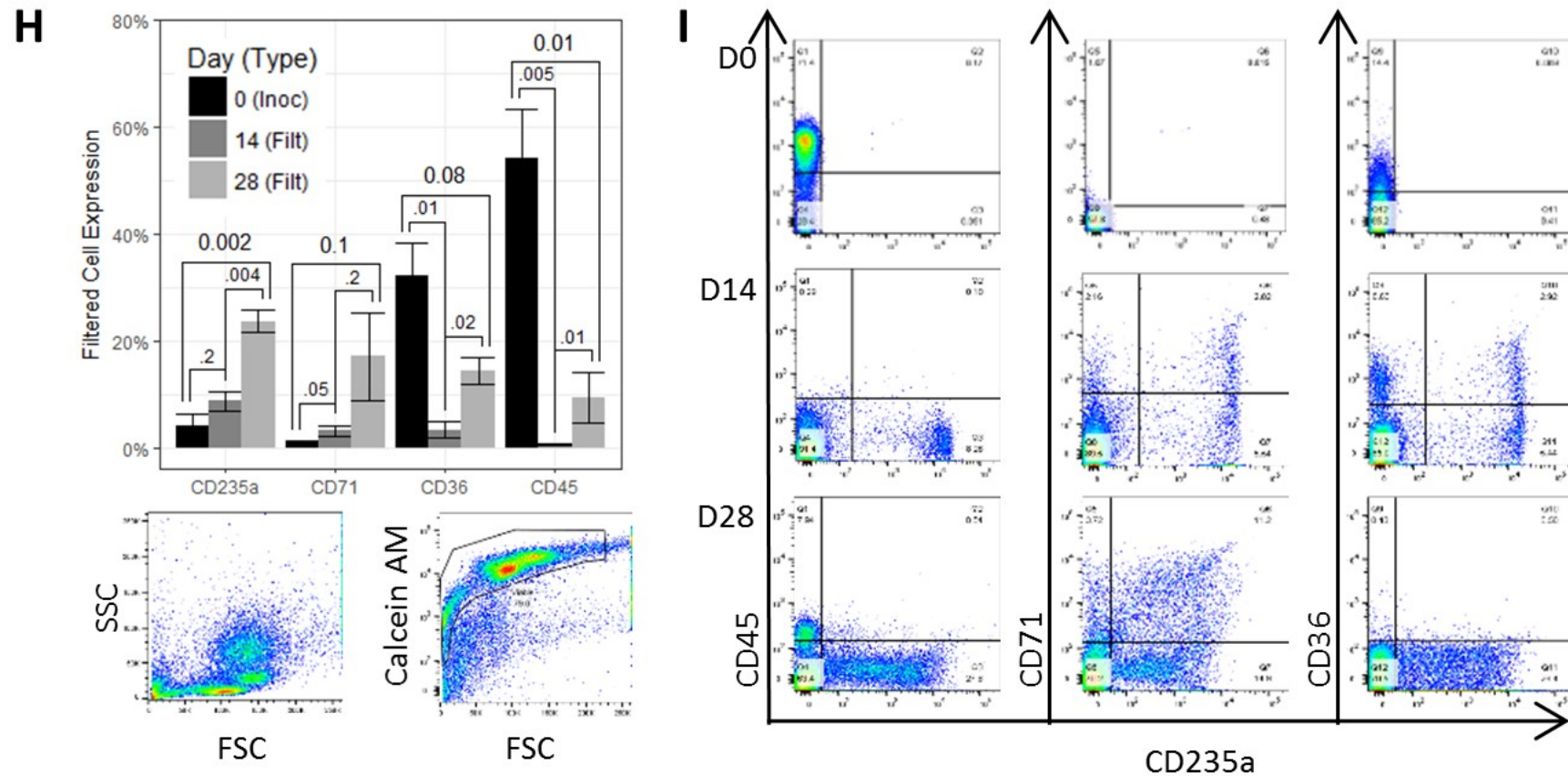


Figure 37 (continued): (H) Inoculated and filtered viable cell phenotypes at days 0, 14, and 28 were gated on Calcein AM Violet and assessed for single-phenotype expression of CD235a, CD71, CD36, and CD45, alongside (I) representative CD235a co-expression plots. ($N \geq 3$ biological replicates for (B), (C), (H), and (I), all shaded regions and error bars represent standard error about the mean from N replicates, p-values in (H) were calculated from unpaired student's t-test from N replicates).

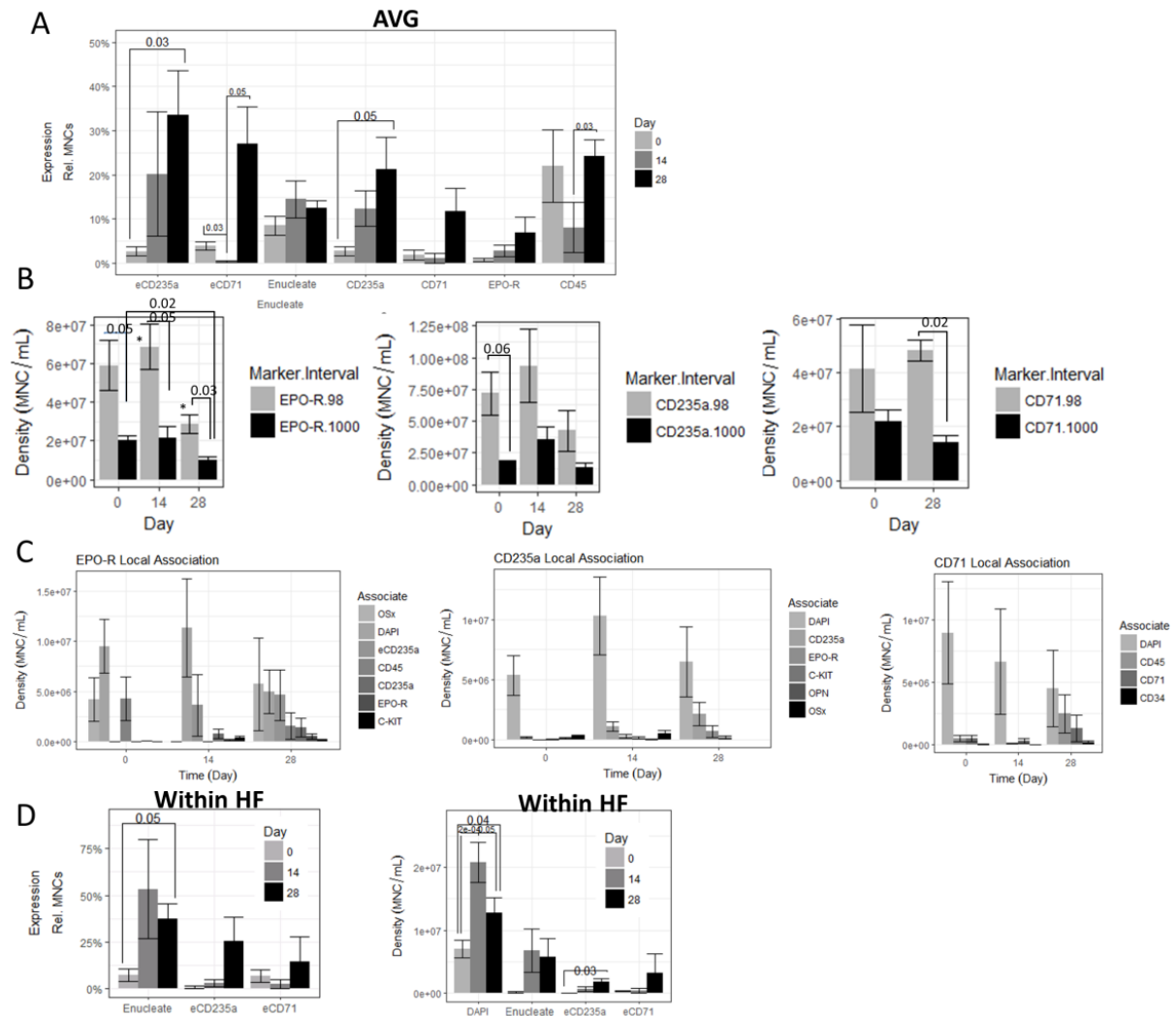


Figure 38: Distribution statistics of erythroid markers: enucleated CD235a and CD71 (eCD235a, eCD71), nucleated CD235a, CD71, EPO-R, CD45, and enucleate cell membranes (Enucleate). (A) Percent expression of erythroid markers throughout HFR. (B) EPO-R (left), CD235a (centre), and CD71 (right) MNC local association densities ($\leq 98 \mu\text{m}$ from EPO-R, CD235a, and CD71 MNCs) compared to bulk densities ($\leq 1000 \mu\text{m}$). (C) Local phenotypic association densities of EPO-R (left), CD235a (centre), and CD71 (right) MNCs with selected markers simultaneously imaged, statistical significance was not measured. (D) Enucleate, eCD235a, and eCD71 distribution within $150 \mu\text{m}$ HF as a percentage of MNCs (left) or as a density as compared with DAPI (right) (all graphs have standard error bars for $N \geq 3$ biological replicates, p values reported in (A) and (D) represent unpaired student's t tests from N, (B) represent paired student's t tests from N, statistical significance not measured in (C)).

6.4.5. Increasing cell density enhances erythropoiesis

Different HFR inoculation densities were compared in parallel: one with the aforementioned inoculum density (10^8 MNCs/HFR), and one with a 25-fold higher inoculum density ($2.5 \cdot 10^9$ MNCs/HFR). At day 28, this high-inoculum HFR provided a 125-fold higher extraction of cells ($1.1 \cdot 10^{10}$ total counted cells (TCC)/HFR) and 25-fold higher filtration of cells ($3.4 \cdot 10^7$ TCC/HFR) with higher cell viability (98%) as compared with the normal-inoculum HFR (Figure 39A-B; Figure 40A). High inoculum HFR MNC density peaked at 550 μm from HF, 66% of which were CD45⁺ MNCs, while normal inoculum HFR MNC density was highest along HF surfaces (Fig. 6C). Despite differences in total culture density and MNC distribution from HF, local 100 μm MNC associations were at similar densities for high and normal inoculum HFRs (Figure 40B).

In situ, the high inoculum HFR had greater MNC expressions of CD45 (55% vs 25%), SDF-1 (45% vs 20%), fibronectin (19% vs 5% co-localised MNCs), and CD235a (39% versus 30%), similar expressions of OSx (20% vs 16%) and OPN (5% vs 2%), but lesser expressions of CD34 (2% vs 4%), Stro-1 (4% versus 16%), collagen type 1 (9% vs 18%), CD71 (1% vs 19%) and EPO-R (3% vs. 12%). MNCs within 500 μm of high inoculum reactor HF were prevalently CD235a⁺ and present at a 10-fold higher density than lower inoculum conditions (Figure 39D; Figure 40C-D). The high inoculum HFR perfusate contained increased concentrations of angiogenic factors, M-CSF, and IL-6, decreased concentrations of interleukins, and an increased consumption of SCF (Figure 39E; Figure 40E).

Viable cells filtered out of the high inoculum HFR contained a greater fraction of mature red cell phenotypes, expressing 57% CD235a⁺ and 39% CD235a⁺CD71⁻ compared to 20% and 13% in the normal inoculum HFR (Figure 39F). Therefore, increasing CBMNC density in the HFR promoted more efficient erythropoiesis, and viable densities >1,000-fold higher than current liquid suspension limitations were reached at day 28.

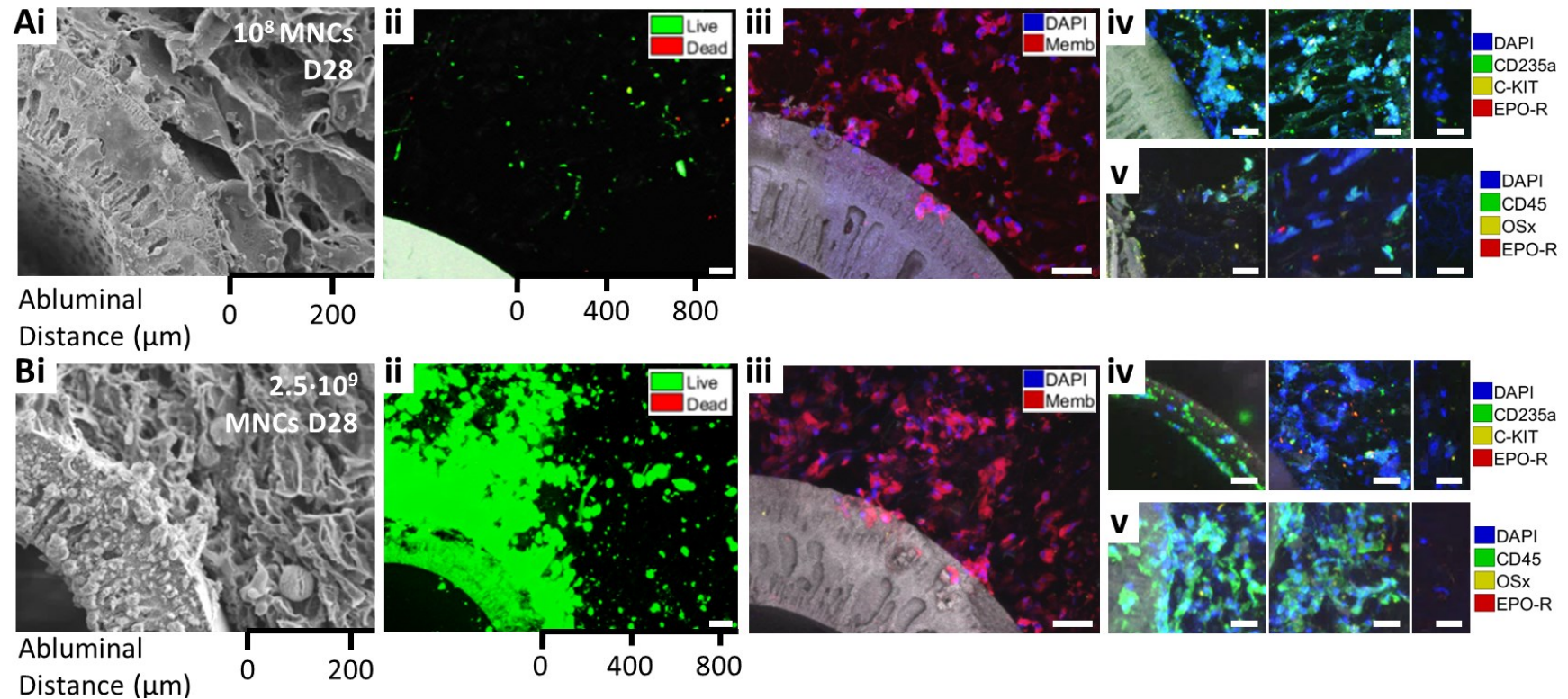


Figure 39: Increased cell density enhances RBC production.

Qualitative comparison of day 28 HFR cultures using CBMNC inoculums of (A) 10^8 and (B) $2.5 \cdot 10^9$ including a representative (i) SEM image with (ii-v) confocal micrographs of (ii) calcein-AM (green, alive with HF autofluorescence) and ethidium-homodimer-1 (red, dead) ($100 \mu\text{m}$ scale bars), (iii) DAPI (blue) and CellMask (red) ($100 \mu\text{m}$ scale bar), (iv) DAPI (blue), CD235a (green), C-KIT (yellow), and EPO-R (red) or (v) DAPI (blue), CD45 (green), OSx (yellow), and EPO-R (red) at fibre-adjacent (left) and distal (center) neighborhoods with isotype (right) ($50 \mu\text{m}$ scale bars), these images are not from the same CB donations, and (Aiii) represents a magnified sub-image of Figure 34.

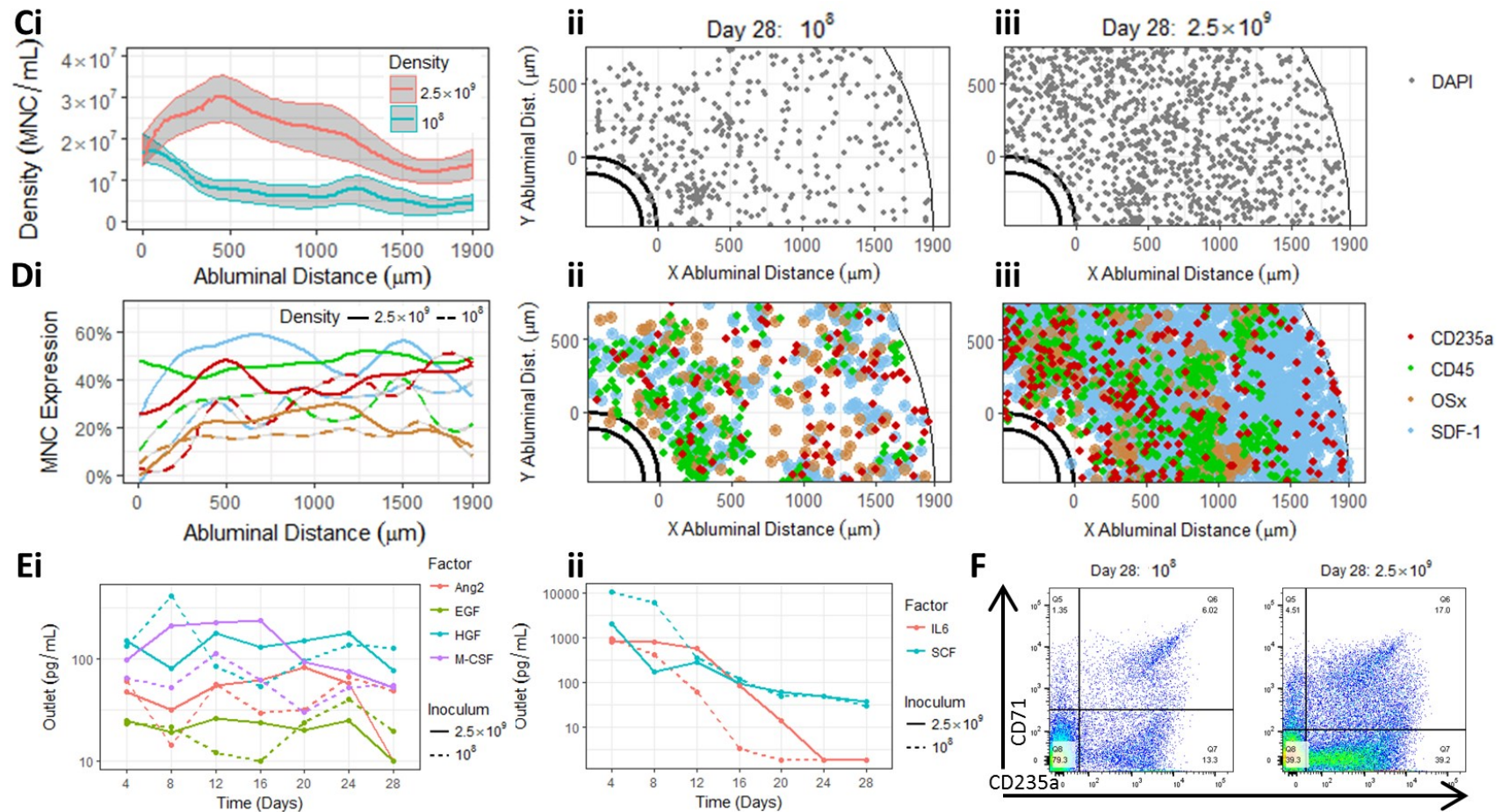


Figure 39 (continued): (Ci) HFR abluminal distribution of DAPI nuclei and (Cii-Ciii) projected organizational maps at different inoculum densities from the same CB donation with (Di) abluminal distributions and (Dii-Diii) organizational maps of CD235a, CD45, OSx, and SDF-1 co-localised with DAPI, comparisons of growth factor concentrations throughout culture for (Ei) M-CSF, Ang-2, EGF, and HGF, and (Eii) IL-6 and SCF, and (F) representative CD235a/CD71 flow cytometry plots of viable filtered cells gated on Calcein AM Violet from day 28. (N=1 biological replicate for (C), (D), and (E), n=9 image replicates for (C), n=1 image replicate for (D), (E), shaded regions in (C) represent standard error about the mean from n internal replicates).

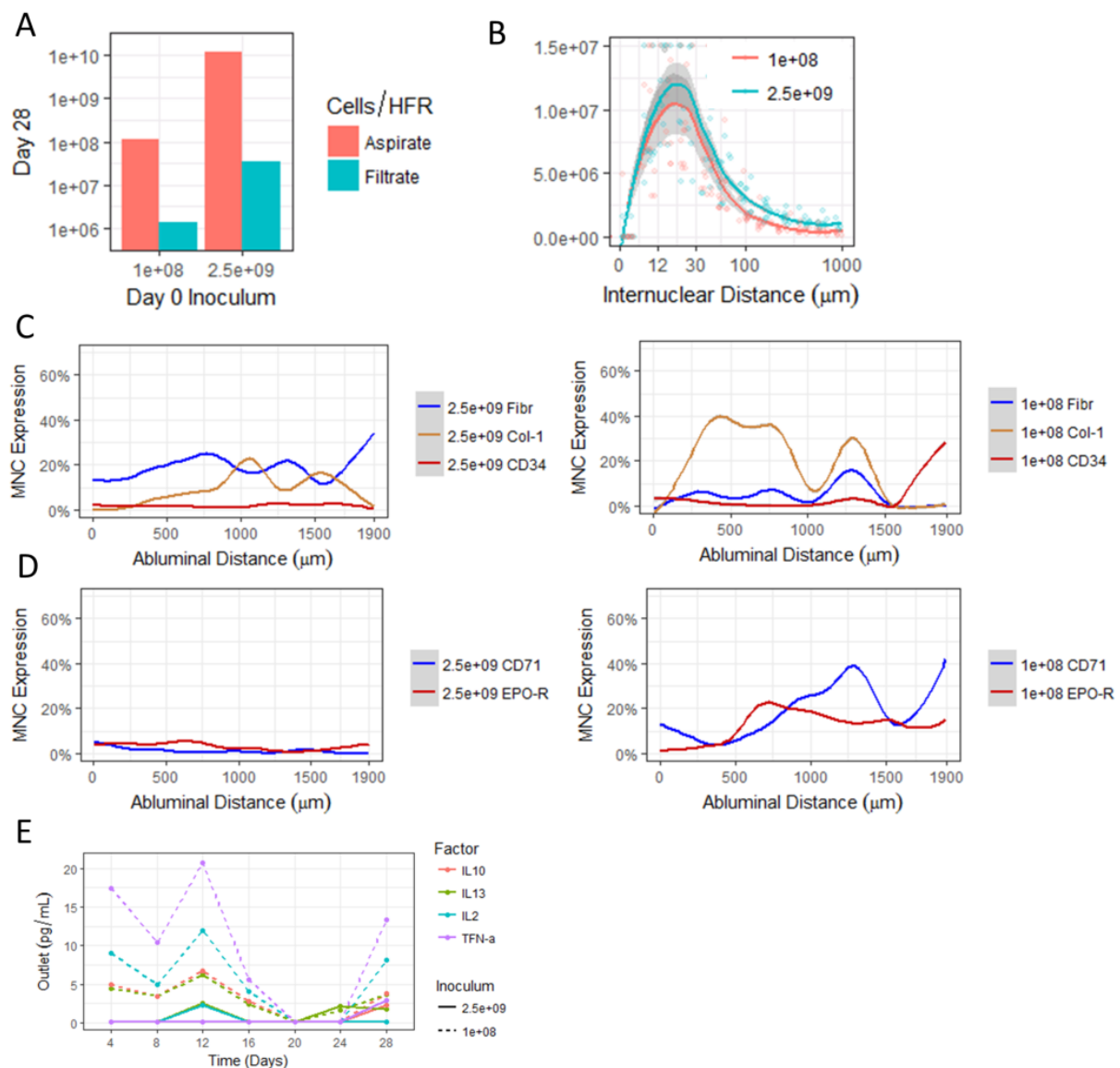


Figure 40: Comparisons of HFR inoculum densities.

(A) Total viable cell harvest at day 28 from normal (10^8 MNC/HFR) and high inoculum ($2.5 \cdot 10^9$ MNC/HFR with 5 mL/HFR) reactors, both populations were stained with trypan blue and manually counted by hemocytometer ($N=1$, $n=4$). (B) Intercellular association densities for DAPI⁺ MNC imaged within normal and high inoculum reactors at day 28. (C) Abluminal distribution of fibronectin, collagen type-1, and CD34 within high (left) and normal (right) inoculum reactors. (D) Abluminal distribution of CD71 and EPO-R within high (left) and normal (right) inoculum reactor. (E) Production of various ILs and TFN- α at high and normal inoculum HFR outlets. The high inoculum reactor produced virtually no IL-10 -13, -2, and TFN- α throughout culture (shaded region in (B) represents standard error for $n=9$ image replicates for $N=1$ biological replicate).

6.5. Discussion

A HFR platform of spatially characterized CBMNC erythropoiesis is proposed. While biomaterials or co-culture platforms demonstrate physiological context, and while HEMA platforms demonstrate efficient HSC expansion, the fabricated platform models hematopoietic niche structure and multilineal cellularity and interactions, from a single CB donor, under defined conditions, and produces billions of cells, reaching the highest cell densities to date while using 10% of current HEMA cytokine concentrations.

The HFR provides hBM-mimicking structural elements to aid physiological erythropoiesis: a porous, adherent 3D cell scaffolding, regional nutrient perfusion, and filtered cell harvest. Porous scaffolds allow for a more physiological expansion and differentiation of hematopoietic cells, employing porosity and surface modifications to approximate the ECM-coated hBM trabeculae (75-90% porous, 300-900 μm pore size) (Rnjak-Kovacina et al. 2014; Mortera-Blanco et al. 2011; Nelson & Roy 2016). Recent scaffolds include hollow channels for the static inclusion (Rnjak-Kovacina et al. 2014; Rodenhizer et al. 2016) or continuous perfusion (Kolesky et al. 2016; Zhang et al. 2016; Di Buduo et al. 2015) of fresh media, producing biochemical gradients for a distribution of microenvironmental conditions. Recently, wall shear stress (WSS) within perfusion HFRs has promoted the short-term generation of functional human platelets (Di Buduo et al. 2015; Thon et al. 2014). A WSS of 100 mPa was employed, comparable to an equivalent mass of rat marrow with a sinus WSS of 150 mPa (Thon et al. 2014; Mazo et al. 1998; Brookes 1967). These three structural elements have been incorporated in long-term culture as murine scaffold explants, and were able to recapitulate murine BM cell distributions, multilineal interactions, growth factor secretion, and cellular egress to provide an accurate *ex vivo* murine model to investigate drug response (Torisawa et al. 2014; Holzapfel et al. 2015).

A key innovation of the HFR is its generation of a stromal environment alongside erythropoiesis without exogenous stromal-acting factors, undefined animal serum, or secondary cell sources. CB mesenchymal cells proliferated, underwent osteogenesis, secreted ECM proteins, and associated in dense cellular neighborhoods where 22 detected and unsupplemented growth factors were endogenously produced. The exogenous addition of EPO may have aided osteogenic differentiation, as found in murine models (Singbrant et al. 2011), however OPN⁺ osteoblasts were not upregulated near

perfused HF as erythropoiesis was. This stromal environment interacted with hematopoietic progenitors and erythroid precursors in local neighbourhoods where effective concentrations of secreted growth factors may be higher than detected. Other *ex vivo* co-culture platforms have studied the impact of mesenchymal and osteoblast cells on hematopoietic progenitor function via physical cues and growth factor secretion (Leisten et al. 2012; Jing et al. 2010), and have included these cells in hematopoietic scaffold cultures to aid in murine transplantation (Ventura Ferreira et al. 2016).

The benefit of a culture platform supported by cellular interactions is further highlighted by culturing hUCB MNCs at a 25-fold higher, tissue-like, inoculum ($5 \cdot 10^8$ MNC/mL in the 5 mL HFR) under the same medium supplementation. After 28 days of culture, the HFR harvested $3 \cdot 10^7$ CD235a⁺ cells by filtration and $2.2 \cdot 10^9$ total cells/mL could be extracted at the end of 28 days, similar to hBM densities of 10^{8-9} MNC/mL (Lee et al. 2014; Choi et al. 2013). Current HEMA platforms are limited to a maximum batch culture density of $2\text{-}5 \cdot 10^6$ MNC/mL (Rousseau et al. 2014) and are supplemented with abnormal cytokine stimulation (3 U/mL EPO, 100 ng/mL SCF, amongst others (Giarratana et al. 2011; Timmins et al. 2011)) to inhibit negative signalling (Caldwell et al. 2015), requiring separate culture steps promoting stress erythropoiesis then subsequent maturation (Migliaccio et al. 2012). This culture platform supplements at least 10-fold lesser quantities of SCF and EPO, comprised of an initial stimulation of 50 ng/mL SCF which decreases below 5 ng/mL at day 8, and 75 mU/mL EPO on day 2 which increases to a maximum of 225 mU/mL between day 24 to 28, similar to plasma concentrations (Jelkmann 2011), which may have promoted red cell maturation alongside progenitor expansion.

6.6. Conclusion

In summary, a hollow fibre bioreactor culture system was designed and implemented which better mimics physiological erythropoiesis than current *ex vivo* culture systems. This reactor implemented a collagen-coated 3D porous scaffold similar to marrow trabeculae, 4 microporous cell-filtering perfused ceramic hollow fibres similar to central sinuses of the marrow (fabricated and assessed by Asma Tahlawi), reduced, more normal cytokine supplementation, and a heterogeneous CBMNC inoculum. This reactor expanded multi-lineal, interactive, and spatially distributed cell populations with similarities to human marrow endosteal, peri-vascular, and vascular niches, and could reach marrow cell densities, 1000-fold higher than current state of the art, while using one tenth the

concentrations of only EPO and SCF in serum-free medium. This HFR is proposed to be a translational platform to study human erythropoiesis and design cell expansion protocols in a more physiologically-relevant environment.

7. Development of high-cell-density mini-bioreactors toward producing blood.

Hematopoietic cell therapy biomanufacturing has demonstrated efficient rates of expansion and clinical utility, but remains too expensive for clinical translation due to low cell culture densities and high cytokine supplementations. The fabrication of 3D perfusion bioreactors (BRs) which can viably expand human hematopoietic at higher cell densities (10- to 100-fold, here 1,000-fold) and, in this thesis, lower cytokine concentrations (10-fold) than current liquid suspension methods toward clinically relevant costs in the tissue engineering field for cell therapy bioprocesses. 3D culture platforms have been limited from cell therapy biomanufacturing due to difficulties in product harvest similar to current liquid suspension methods. Therefore, parallelised “mini-BRs” are proposed for the expansion of human umbilical cord blood (hUCB) mononuclear cells (MNCs) at higher cell densities and lower cytokine supplementation than liquid suspension which can facilitate continuous enucleate red blood cell egress for collection.

In this section, Mark C. Allenby and Edwin Newn (supervisor: Mark C. Allenby) performed all computational design, Asma Tahlawi fabricated hollow fibres when used, Mark C. Allenby and José C.F. Morais (supervisor: Mark C. Allenby) performed all bioreactor fabrication and culture, and Mark C. Allenby performed all analyses.

7.2. Introduction

Within the last decade, the manufacturing of cell therapy products has greatly expanded. A 2016 analysis of cell-based markets indicated more than 500 companies are currently involved in cell therapy, with a 2013 market share of \$6-7 billion, and market prediction project expansive growth through 2026 (Jain 2017; Mason et al. 2013). Hematopoietic cell therapy products have been used for 200 years as blood transfusions, and within the last 60 years for marrow reconstitution post-chemotherapy (Lipsitz et al. 2016; Kirouac & Zandstra 2008), and current progress in red blood cell production *ex vivo* has reached impressive rates of cell expansion (Miharada et al. 2006; Timmins et al. 2011), proven clinical utility (Giarratana et al. 2011), and recently been implemented from an immortalised cell source (Trakarnsanga et al. 2017).

The clinical expense of using *ex vivo* generated red blood cells remains at least 40-fold more expensive than normal blood transfusion and 5- to 8-fold more expensive than rare blood transfusions by conservative estimates (Timmins et al. 2011). Recent studies have revealed the majority of red blood cell bioprocess costs and limitations can be contributed to medium expenses, as current liquid suspension methods require cells to be cultured at low densities ($\leq 10^6$ cells/mL) such that reaching a single transfusable unit of RBCs (10^{12}) would require nearly a basketball court of T-75 flasks supplemented with unphysiologically high concentrations of expensive growth factors (10-100x found *in vivo*) (Rousseau et al. 2014; Misener et al. 2014). Therefore, advances in red blood cell therapy manufacture have transferred the burden of cost from the procurement of seed stem cells to medium supplementation.

3D perfusion biomaterial platforms have allowed for the culture of hematopoietic cells at increased cell densities (10 to 100-fold higher) (Housler et al. 2012) and decreased growth factor concentrations (10-fold less) methods (Mantalaris et al. 1998; Mortera-Blanco et al. 2011) in comparison to current liquid suspension and reducing medium costs which limit red blood cell production from clinical utility. Therefore, efforts within the design, fabrication, and analysis of perfused biomaterial platforms for red blood cell biomanufacturing at tissue-like cell densities ($>10^9$ cells/mL) have the potential to resolve cost limitations of cellular therapeutics.

However, biomaterial platforms suffer from invasive methods of cell harvest. While red blood cells produced in liquid suspension can be continuously sampled and extracted, cells seeded into 3D scaffolds require culture termination to be extracted (Allenby et al. 2017). Therefore, techniques to continually separate cell therapy products from proliferative progenitor cells have been utilised to allow for continuous cell harvest (Severn et al. 2016). Herein, the design and fabrication of a hollow fibre bioreactor (HFBR) which has been miniaturised is reported. This mini-BR allowed for the 28-day serum-free, low-cytokine culture of high densities of hUCB MNCs, and continuous cellular egress was enhanced through the removal of filtering hollow fibres from central channels.

7.3. Methodology

The combination of secreted protein and metabolite detection, *in situ* quantitative spatial analyses, and harvested cell analysis provided a thorough characterisation of *ex vivo* hematopoietic environment remodelling toward erythropoiesis within the device from Section 6. While this platform demonstrated significant accomplishments with the viable quantity and range of cell types cultured, this system was still limited towards cell biomanufacturing by: a lack of cells continuously filtered (only $10^7/28$ -day culture on average), and an infeasible inoculum demand for the high-density HFR ($2.5 \cdot 10^9$ MNCs, while only $0.5 \cdot 10^9$ MNCs are typically isolated from 1 hUCB). Therefore, the HFR design was further developed by miniaturising and parallelising it while exploring methods to improve continuous cell harvest, such as omitting the hollow fibre in favour of a porous hollow channel included within the scaffold. The mini-BRs demonstrated promising results regarding the high-density expansion of cells, and an improved phenotypic red cell harvest, and further experiments to enhance mini-BR reproducibility and cell product harvest are suggested.

7.3.1. Mathematical design

The design of the cylindrical mini-BR size (diameter, length) was dictated by calculating the limiting krogh radius away from a central hollow fibre at which oxygen would reach anoxic ($<1\%$ dO_2) concentrations. Oxygen is well-described as the limiting nutrient for *in vivo* and 3D *ex vivo* cell culture (Chow et al. 2001), and would be dependent on: O_2 diffusion, cellular O_2 consumption, cell type density, and flow rate. An ideal bioreactor would display a broad oxygen gradient from levels between 1% and 20%, similar to what is present in human bone marrow, without having large volumes of toxic concentrations of oxygen ($<1\%$ dO_2). Bioreactor length can be calculated from a known cylindrical volume determined by cell number isolated, N_c , and desired inoculum cell density, D_c . This inoculated full cylindrical volume ($\pi L R_F^2$) must subtract hollow fibre volume ($\pi L N_{HF} R_2^2$). To solve for bioreactor length, L :

$$L = \frac{N_c}{\pi D_c (R_F^2 - N_{HF} R_2^2)} \quad [12]$$

The krogh cylinder design equations as presented as Equation 17 in Misener et al. 2014 can be solved at its furthestmost krogh cylinder point (R_3, L) as:

$$C_{k,3} = \frac{V_k}{D_{k,3}} \left[\frac{R_3^2}{2} \ln \left(\frac{R_3}{R_2} \right) - \left(\frac{R_3^2 - R_2^2}{4} \right) \right] - \frac{V_k}{D_{k,3}} (R_3^2 - R_2^2) \left(\frac{11}{48} + \frac{\ln \frac{R_2}{R_1}}{2\varepsilon_{HF}} \right) + \left(R_2 - \frac{R_3^2}{R_2} \right) \left(\frac{N_{HF} V_k}{U_z} \right) + C_{k,in} \quad [13]$$

This equation can be rearranged as:

$$R_3 = \left[\frac{C_{k,3} - \frac{V_k R_2^2}{D_{k,3}} \left(\frac{11}{48} + \frac{\ln \frac{R_2}{R_1}}{2\varepsilon_{HF}} \right) - \frac{V_k R_2^2}{4D_{k,3}} \frac{N_{HF} V_k R_2}{U_z} - C_{k,in}}{\frac{V_k}{D_{k,3}} \left(\frac{R_3}{2} - \frac{1}{4} \right) - \frac{N_{HF} V_k}{R_2 U_z} - \frac{V_k}{D_{k,3}} \left(\frac{11}{48} + \frac{\ln \frac{R_2}{R_1}}{2\varepsilon_{HF}} \right)} \right]^{\frac{1}{2}} \quad [14]$$

In this re-arranged form, R_3 is also in the denominator of the equation. Therefore, [14] must be iteratively solved from an initial value for R_3 . For proposed parameters displayed in Table 13, 100 random numbers were drawn from a uniform distribution between 0 and 1 mm from the outer surface of the fibre, R_2 , (0.45 to 1.45 mm from Krogh axis) as initial conditions for R_3 . New values for R_3 was iteratively calculated from [14] until subsequent calculations reached a convergence of 10^{-100} m.

Table 13: Mathematical parameters for krogh cylinder BR model.

To survey the effect of changing parameters, cellular O_2 consumption, cell density, and flow rate were changed in Figure 41A-C. Operator-defined parameters, in red, were investigated for their effect on toxic krogh radius.

| Variable | Value | Units | Description |
|--------------------|--------------------------------|----------------------|-------------------------------|
| R_1 | $2.6 \cdot 10^{-4}$ | m | Inner radius hollow fibre |
| R_2 | $4.5 \cdot 10^{-4}$ | m | Outer radius hollow fibre |
| R_3 | -- | m | Toxic Krogh radius |
| R_F | -- | m | Full bioreactor radius |
| $C_{k,in}$ | 0.26 | mol/m ³ | Inlet O_2 concentration |
| $C_{k,3}$ | 0.026 | mol/m ³ | Furthest O_2 concentration |
| $D_{k,3}$ | $3.29 \cdot 10^{-9}$ | m ² /s | O_2 diffusion into scaffold |
| V_k | $D_c \cdot 1.8 \cdot 10^{-16}$ | mol/m ³ s | Cellular O_2 consumption |
| D_c | $1.8 \cdot 10^{13}$ | cells/m ³ | Cell density |
| U_z | $7.1 \cdot 10^{-3}$ | m/s | Flow rate |
| ε_{HF} | 0.8 | -- | Hollow fibre porosity |
| N_{HF} | 1 | -- | Hollow fibre number |

Two parameters of interest include the radius at which low oxygen concentrations become toxic to culture cells, and how that radius changes as a function of the cellular consumption rate of oxygen, which increases or decreases for different human normal or abnormal cell types. Oxygen tension in the marrow reaches concentrations as low as 1.5% dO_2 , where quiescent HSCs reside (Spencer et al. 2014). In these calculations, Krogh radii was calculated at which oxygen concentrations drop to 1, 2, 3, 4, and 5% dO_2 at different flow rates, cell densities, and cellular oxygen consumption rates one-at-a-time, with other parameters defined in Table 13 and toxic Krogh radii displayed in Figure 41A-C.

7.3.2. Mini-BR fabrication

Mini-BR shells and caps were tailor-machined out of a large poly-fluoro-alkoxy (PFA) rod. PFA had been extensively used in prior experimentation, and is well-used in biomedical applications due to its low protein adherence, its ability to withstand autoclave and cryogenic temperatures, ethanol and UV sterilisation, and its relatively transparency to allow visual inspection of cell growth. A mini-BR shell was machined from PFA as a 6 mm rod, a 4.5 mm hole was bored through, and 3 top-caps of 2.5 mm were bored. The inlet and outlet of the polymeric shell was then filed to accept custom made 1/8 inch barbed tubing caps, and small top caps were made to seal the mini-BR after cell inoculation. The final fabricated PFA shell is shown in Figure 41D.

Ceramic hollow fibres (HFs) were fabricated by Asma Tahlawi through the dissolution, milling, and degassing of 58.6 wt% 1 µm aluminum oxide powder (VWR, Lutterworth, UK) with 1.3 wt% Arlcel P135 (Sigma-Aldrich, Dorset, UK) in N-methylpyrrolidone (Sigma-Aldrich) solution, followed by extrusion through a tube-in orifice spinneret prior to sintering with a temperature profile rising to 1350°C. A hollow fibre was adhered within the mini-BR shell by applying a quick drying two-component resin (Araldite, Basel, Switzerland) on both the inlet and outlet of the reactor. If a mini-BR was made without a hollow fibre, but with a hollow inner channel, a 21-gauge needle was inserted into a glass Pasteur pipette within the mini-BR shell instead, and carefully removed after forming the following polymeric scaffolding.

A solution of 5% polyurethane (PU; Noveon, Brussels, Belgium) in 1,4-dioxane (Sigma-Aldrich) was dissolved as previously, where the 1,4-dioxane was selectively sublimed through thermally induced phase separation (TIPS) to leave a porous PU scaffold, as shown in Figure 41E. The mini-BR was coated by bovine collagen type 1 (Sigma-Aldrich) and sterilised, then medium-conditioned as previously described to appear as Figure 41F after which scaffold and fibre porosity was analysed by SEM as down in Figure 41G-I.

The HFR was fitted into a perfusion assembly of silicon tubing and polycarbonate adapters including 100 mL and 500 mL bottle reservoirs, oxygen permeable tubing, stopcock adapters for sampling, and peristaltic pump tubing and pumps (Cole Parmer, Hanwell, UK; Smith's Medical, Watford, UK; VWR; Instech Technologies, Plymouth Meeting, USA) that were sterilized by either

autoclave sterilisation or ethanol and UV light sterilisation as described above and photographed in **Figure 41J**

7.3.3. Long-term hUCBMNC culture

Fresh human umbilical cord blood (hUCB) units (NHSBT, Colindale, UK) were isolated for mononuclear cells by Ficoll-Paque Plus according to manufacturer's instructions (Sigma-Aldrich). A suspension of $5 \cdot 10^7$ hUCB MNCs in culture medium was seeded into HFRs and incubated for 1 hour without perfusion. 4 reactors were perfused with medium which was recycled through a reservoir of 60 mL, and 27 mL of the reservoir was exchanged every second day. Reactors were sacrificed at days 0, 7, 14, 21, and 28, providing a greater amount of medium per reactor nearer the end of culture. Culture medium consisted of serum-free expansion medium (Stemspan SFEM) supplemented with 1% penicillin-streptomycin, 200 mg/L transferrin, 10 or 100 mg/L insulin, and 200 mg/L cholesterol, as described in Table 14.

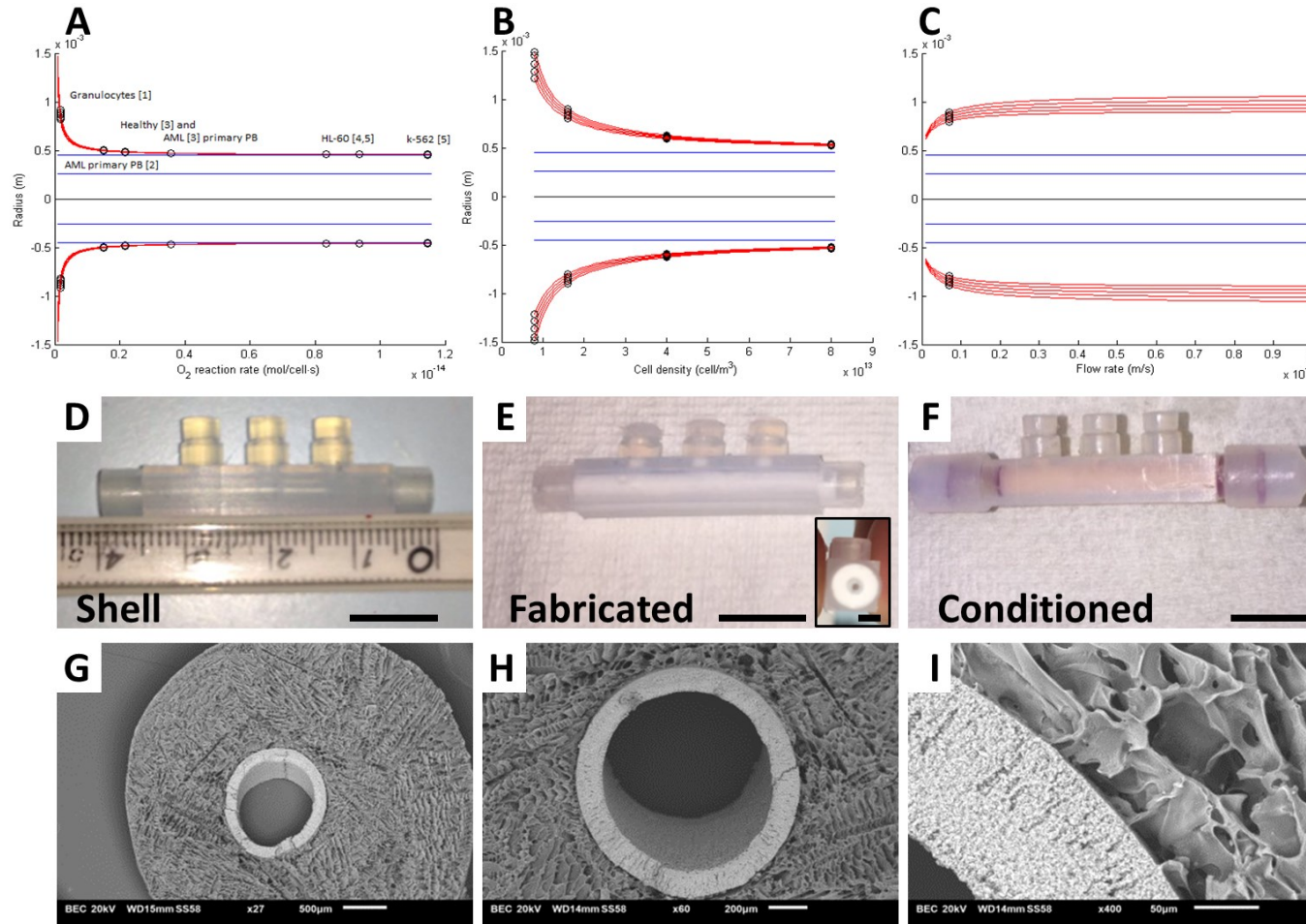


Figure 41: Mathematical design and fabrication of mini-BRs.

A theoretical study determined the BR radius at which oxygen becomes depleted from 20% to 1, 2, 3, 4, 5% dO_2 for (A) different cell types, (B) different cell densities, and (C) different flow rates, where a mini-BR diameter of 4.5 mm was selected to avoid anoxia. (D) The fabricated mini-BR shell and after (E) scaffolding and (F) conditioning with media, scale bars are 10 mm, inset of (E) is 2 mm. SEM images of a fibre-containing mini-BR cross-sections with (G) 500 μ m (H) 200 μ m (I) 50 μ m scale bars. In A, citations are: [1] (Collins et al. 1998), [2] (Souid et al. 2003), [3] (Škrtić et al. 2011), [4] (Wagner et al. 2011), [5] (Herst & Berridge 2007).

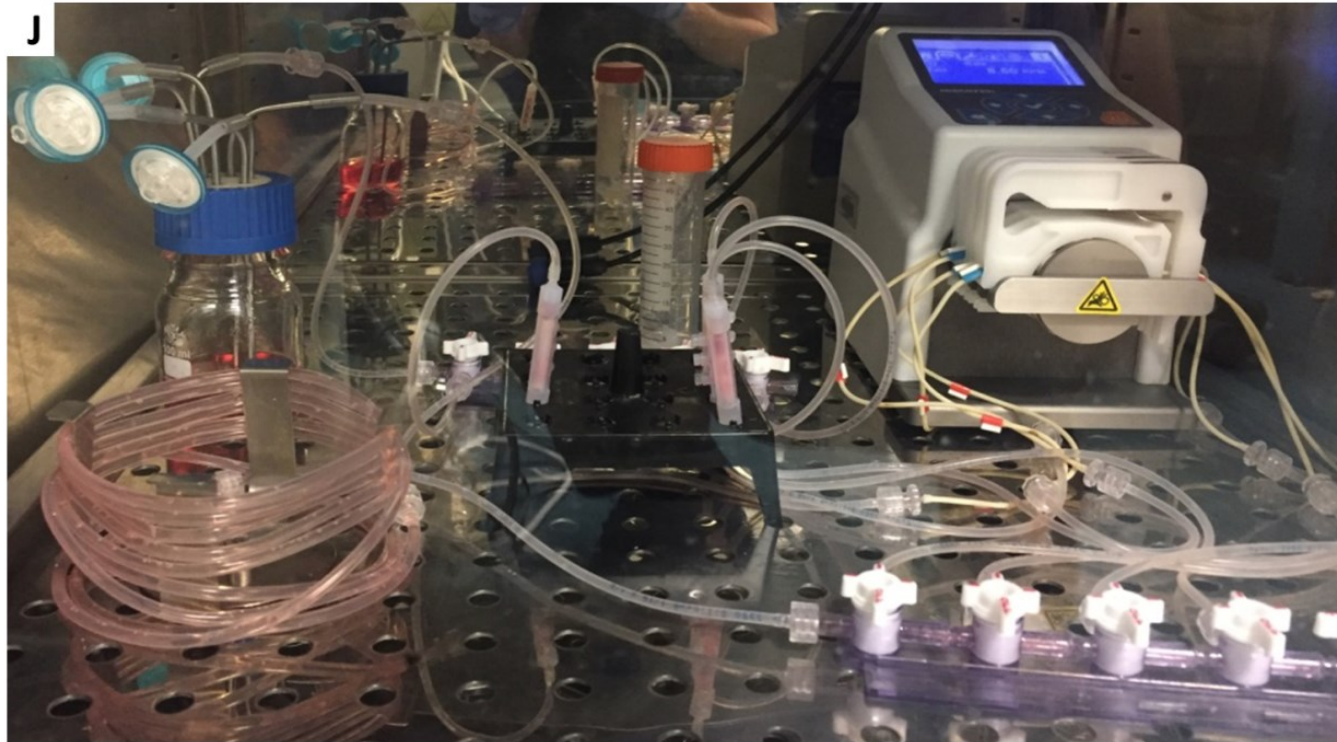


Figure 41 (continued): (J) Perfusion platform for 4 mini-BRs with (left) recycled reservoir and oxygen permeable tubing loop (right) line splitter and micropump and (center) mini-BRs.

One of two growth factor supplementation schedules were followed: in the first instance, 30 ng/mL SCF was supplemented in medium from day 0 to 20, and 0.3 IU/mL EPO was supplemented from day 8 to 28. In the second instance, 10 ng/mL SCF was supplemented from day 0 to 28, and 0.1 IU/mL EPO was supplemented from day 8 to 28, and at day 20, EPO supplementation was spiked to 1 IU/mL total concentration. The difference between mini-BR experiments and culture design are detailed in Table 14.

Table 14: Summary of successful design mini-BR medium profiles implemented up to 04/2017.

| Fibre Number (Section 4) | EPO (IU/mL)/ SCF (ng/mL) | Supplemented Insulin | Flow Rate | Add'l Notes | Date |
|--------------------------|--------------------------|----------------------|------------|--------------------------|---------|
| 8 | 0.3/30 | 10 mg/L | 460 mL/day | D20 no SCF | 04/2016 |
| 6 (DMSO) | 0.3/30 | 10 mg/L | 460 mL/day | -- | 08/2016 |
| 6 (DMSO) | 0.3/30 | 100 mg/L | 460 mL/day | -- | 10/2016 |
| 6 (DMSO) | 0.1/10 | 10 mg/L | 60 mL/day | D20 EPO spike to 1 IU/mL | 11/2016 |
| No Fibre | 0.1/10 | 10 mg/L | 60 mL/day | D20 EPO spike to 1 IU/mL | 04/2017 |

7.3.4. Flow cytometry analysis

Flow cytometry was performed on isolated MNCs on day 0 prior to inoculation, cells collected from perfused medium at days 7, 14, 21, and 28. Flow cytometry was performed on aliquots of $2 \cdot 10^5$ viable fresh cells which were first stained with Calcein AM and Hoechst 33342 or Calcein Violet AM, and second stained with antibodies CD36-APC, CD71-PECy5, and CD235a-PE and without or with CD45-FITC as described in prior sections. Positive antibody samples were prepared identically alongside isotype controls, analysed on a BD LSR Fortessa (Becton Dickinson), compensated against single-stain compensation bead controls, then gated against debris (SSC/FSC) and on viable (Calcein positive) cells, and bivariate isotype gates were set for 99% negative/negative events.

7.3.5. Scanning electron microscopy analysis

Frozen mini-BR sections were prepared as detailed in Section 6, briefly: fixed in glutaraldehyde, post-fixed in OsO_4 , serially dehydrated in ethanol, serially dehydrated in hexamethyldisilazane, mounted and gold-coated before imaging.

7.3.6. Confocal microscopy analysis

Frozen mini-BR sections were fixed, permeabilised, blocked, stained, and imaged as previously described in Section 5. Primary antibodies used include anti-human rat CD235a [ab111033] or IgG2b [ab18541] at 100 µg/mL, rabbit CD71 [ab84036] or IgG [ab172730] at 80 µg/mL, and mouse CD68 [ab955] or IgG1 at 10 µg/mL, and rat CD45 [ab30446] or IgG2b at 100 µg/mL, rabbit SDF-1 [ab155090] or IgG [ab172730] at 9 µg/mL, and mouse C-KIT [ab111033] or IgG1 [ab18437] at 9 µg/mL (AbCam). All positive samples and isotype controls were stained with secondary antibodies donkey anti-rat Alexa Fluor 488, anti-rabbit Alexa Fluor 555, and anti-mouse Alexa Fluor 647 at 1:500 dilution and counterstained with DAPI at 1:200 dilution (Life Technologies), then imaged on a Leica SP5 inverted confocal microscope with Leica LAS AF software (Leica, Milton Keynes, UK). Images were manipulated within figures only by adjusting contrast and brightness of both sample and negative isotype controls identically.

7.4. Results

7.4.1. Mathematical design of mini-bioreactor (BR) fabrication

The diameter of the cylindrical mini-BR was selected to include regions of marrow-like hypoxia (1 – 5% dO₂), which could have promoted the expansion and maintenance of supportive hematopoietic and stromal cell types found in prior studies, but to avoid regions of toxic anoxia (<1% dO₂). Cellular oxygen consumption, cell density, and flow rate were all critical factors in supporting the oxygenation of a hollow fibre bioreactor inoculated with high densities of cells. Cellular oxygen consumption varies widely for different normal and abnormal hematopoietic cell types, where hUCB granulocyte oxygen consumption rate (10¹⁶ mol O₂/cell·s) represents the highest rate of hematopoietic cells (0.05-1·10¹⁶) but is 3 orders of magnitude less than leukemic cell lines (10¹⁹ mol O₂/cell·s) (Chow et al. 2001; Wagner et al. 2011). To conservatively estimate oxygen demand for this hematopoietic culture, a granulocytic oxygen consumption rate for all cells was employed.

Higher cellular densities increased oxygen consumption, and therefore, decreased the mini-BR radius for well-oxygenated cell culture. While cell densities in liquid suspension culture are typically limited to a maximum of 10⁶ cells/mL, 3D biomaterial and perfusion cultures have demonstrated densities 1 to 3 orders of magnitude higher than liquid suspension (Rousseau et al. 2014; Mortera-Blanco et al. 2011; Housler et al. 2012, Section 6). To take advantage of the higher cell densities permitted by 3D perfusion culture systems, the effect of a range of cell densities from 10⁷-10⁸ cells/mL on viable mini-BR radius was investigated. Higher flow rates additionally improved the diffusion of viable oxygen tensions to further Krogh radii. Available pumps could perfuse flow velocities roughly between 0.01 to 1 mm/s within the 0.26 mm hollow fibre inner radius, where higher flow rates improve oxygen diffusion into the scaffold to increase viable Krogh radii.

From these mathematical design equations, a mini-BR where 50 million MNCs could be inoculated into a 0.5 mL cylindrical bioreactor with 4.5 mm inner diameter (or 2.25 mm krogh radius) and 40 mm length. Although mathematical equations dictate a much thinner mini-BR (1 mm; 0.5 mm krogh radius) for a 10⁸ MNC/mL inoculum density, the mini-BR scaffolding could not be formed in such a thin radius. To cope with the longer krogh radius utilised, the mini-BR was perfused at a maximal rate, with 460 mL recycled medium per day, corresponding to a velocity of 25.1 mm/s. These mini-BR

dimensions were dictated by the PFA shell, with the viable Krogh radii diameter and mini-BR length selected dictating the PFA shell inner diameter and length. Mini-BR hollow fibre fabrication, incorporation, scaffold formation, collagen coating, and sterilisation were identical to prior methods with larger bioreactors. Scaffolding porosity appeared to be similar to prior methods as observed by SEM.

7.4.2. Mini-BR culture of hUCB MNCs forms large, confluent cell clusters in 3D

Reactors were inoculated with 50 million hUCB MNCs per mini-BR, and when concentrated within 100 μ L for injection into the 500 μ L scaffold volume, the suspension resembled a thick red suspension of cells. Once injected, the reactor became heterogeneously coloured similarly as the suspension was absorbed into the scaffold, and can be seen in Figure 41J and in detail in Figure 42A. Within 2 and 4 days after inoculation and perfusion, millions of nonadherent cells could be collected within the filtrate, and the colour of the reactor turned a neutral light pink by day 6, demonstrating a dilution of oxygen-binding haemoglobin (Figure 42B). In the first bioreactor system tested in Table 14, a dark red cell suspension could be observed forming in reactors as early as day 14, most significantly near the reactor inlet at day 21 (Figure 42C). While these red masses were maintained until day 28, they did not further increase in size.

The reactor was then snap-frozen and sliced into cross sections for SEM and confocal microscopy at both the mini-BR inlet, where the red mass was located, and the centre, where the reactor was colored a more neutral light pink. SEM images of the mini-BR at day 21 indicated that the dark red inlet contained fibre-proximal scaffold regions which were completely filled with small, spherical hematopoietic cells while the light pink mini-BR centre contained a large, but not filled, density of both round and adherent cell types both in the scaffold and on the hollow fibres (Figure 42D-I).

Cross-sections from the same two regions were imaged by confocal microscopy. While the mini-BR was almost entirely filled with cell nuclei (DAPI; blue), a relatively scarce expression of red cell (CD235a, CD71) and myeloid (CD68) antigens existed, demonstrating that although the reactor was packed with MNCs, it may not necessarily come from an erythroid lineage (Figure 42J). This finding was further clarified when imaging the less dense mini-BR center with non-erythroid phenotypes. The centre mini-BR sections had a significantly smaller nuclear density, but nearly all cells expressed either

pan-hematopoietic CD45, or hematopoietic chemoattractant SDF-1, while SCF-responsive hematopoietic progenitors could be identified with C-KIT (Figure 42K). These results indicated that these high-density reactors can support nearly 3D-confluent cell densities after long-term culture, but despite supplementation with EPO and transferrin, these expanding cell numbers were not necessarily associated with erythroid markers, and rather expressed markers typical with pan-hematopoietic and mesenchymal cells. However, while prior experiments demonstrate hollow fibres can filter cells, very few cells egressed from the mini-BR ($<5 \cdot 10^5$ total at any time) in comparison to densities found *in situ*.

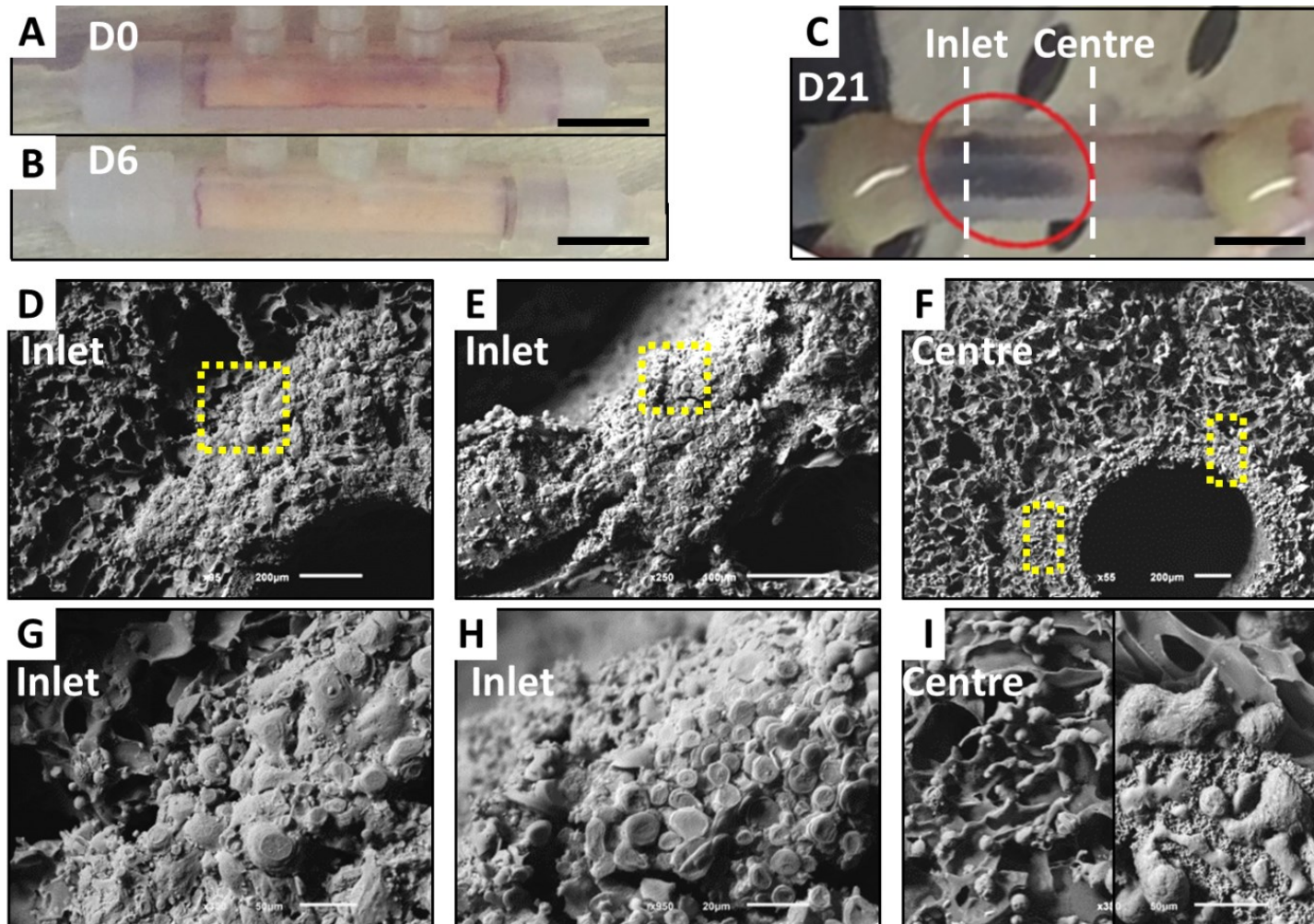


Figure 42: Mini-BR culture formed dense cellular clusters in 3D.

Gross images demonstrating red blood cell color (A) upon hUCB MNC inoculation, (B) at day 6, and (C) at day 21 with schematic of two mini-BR regions surveyed (inlet and centre; 1 mm scale bars). SEM images of day 21 inlet (D, E; 200, 100 μm scale, respectively) and centre cross-sections (F, 200 μm scale) with magnified regions (G,H,I; 50, 20, 50 μm scale bars).

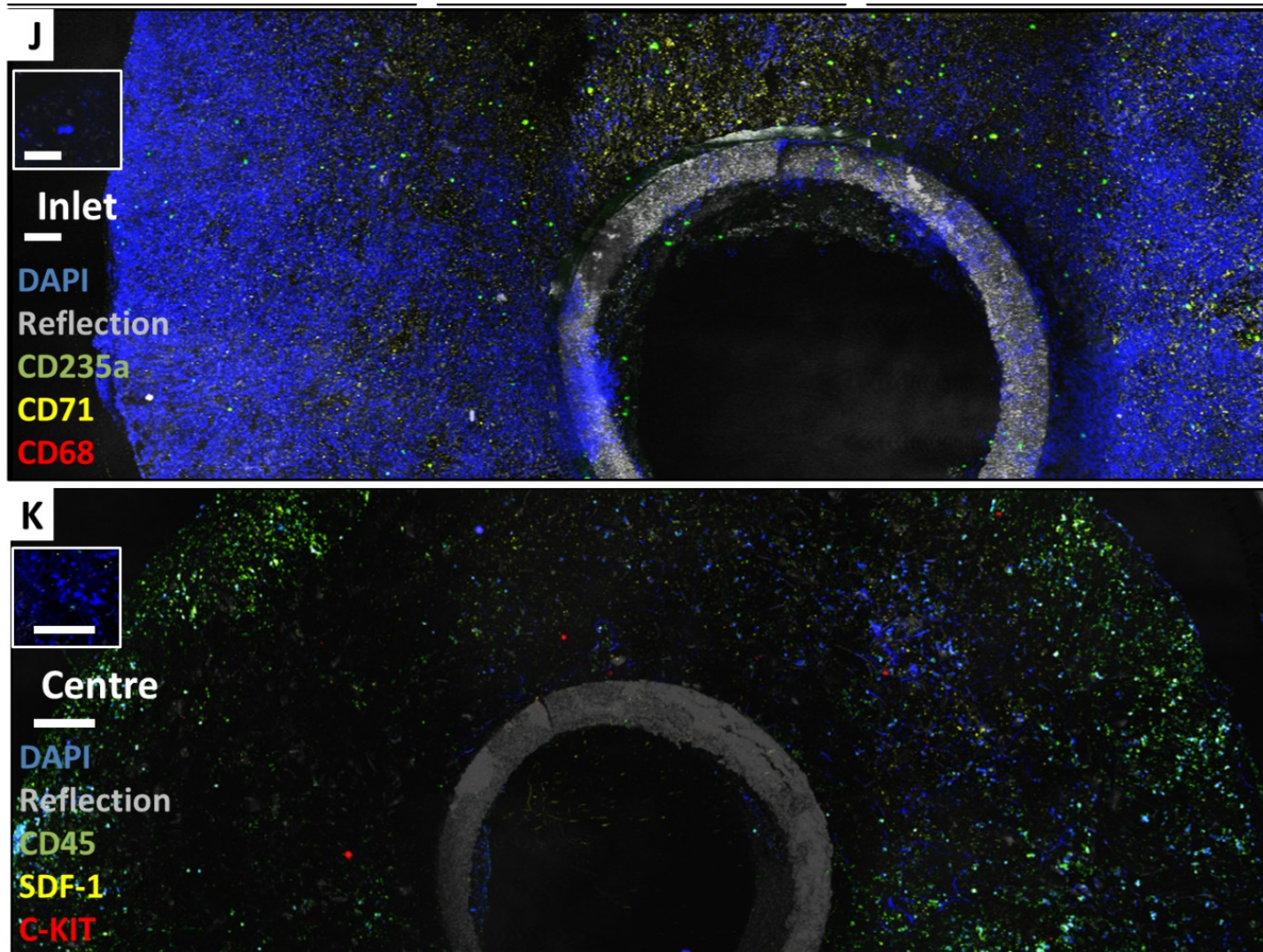


Figure 42 (continued): Immunofluorescent images of day 21 mini-BR: (J) inlet cross section staining for DAPI, CD235a, CD71, and CD68 and (K) centre cross section with CD45, SDF-1, and C-KIT, scale bars of 100 μ m.

7.4.3. Exclusion of hollow fibre improves phenotypic RBC egress

To determine if hollow fibres (fabricated by Asma Tahlawi) were blocking cell egress from mini-BRs, experiments were performed to compare mini-BRs with hollow fibres versus with a hollow cylinder void of scaffolding. As cells were theorized to egress much more easily from the reactor, and nutrients were theorized to diffuse much more easily; the flow rate was dropped from 460 mL/day, or a velocity of 25.1 m/s, to 60 mL/day or 3.26 m/s, and growth factor supplementation was adjusted to lower concentrations: EPO from 0.3 IU/mL to 0.1 IU/mL and SCF from 30 ng/mL to 10 ng/mL. To further promote erythroid differentiation, a spike of EPO was introduced at day 20 to bring perfused concentrations to 1 IU/mL.

The fabrication of the no-fibre mini-BRs created a void cylindrical region with a larger diameter (1 mm) as the inner diameter of the hollow fibres in the fibre-containing mini-BRs (0.52 mm), leaving 1.75 mm of scaffold space remaining until the mini-BR PFA shell (Figure 43A). After scaffold formation, regions of the scaffold adhered to the glass-covered needle forming the void cylinder, which tore regions of the scaffold when removed. These torn scaffold regions demonstrated an open pore architecture towards the central sinus (Figure 43B), while regions of the scaffold which did not adhere and tear formed a closed architecture (Figure 43C).

Throughout culture of both the no-fibre and fibre-containing mini-BRs, a red mass of cells did not appear as found for the prior fibre-containing mini-BRs implementing higher cytokine concentrations, but a larger number of cells continuously egressed from mini-BRs across the culture duration. While cumulative cell, viable cell, and MNC numbers egressed per no-fibre or fibre-containing mini-BR were similar, their dynamics varied (Figure 43D). The no-fibre mini-BR lost a large number of cells immediately upon perfusion (day 2), and egress cell number increased after the late high-dose spike of EPO (days 20, 21, 22). In contrast, the fibre-containing mini-BR filtered cells at a consistent rate until day 20, whereupon cellular egress stagnated.

Cells which egressed were assessed for phenotypic expression of red cell maturation phenotypes CD36, CD71, and CD235a at days 7, 14, 21, and 28, and compared to day 0 inoculate (Figure 43E). During culture, fibre-containing mini-BR filtrate expressed very little erythroid phenotypes (<4% for all markers), while, in contrast, egressed cells from no-fibre mini-BRs increased

expression of CD235a (from 12% to 30%), while decreasing the expression of more immature red cell markers CD71 and CD36 (from >65% to <10%) when compared to inoculate expression. The cells had a low forward and side scatter profile during flow cytometry, suggesting cells egressing fibre-containing mini-BR were mostly cellular debris, sheared into pieces from stress during filtration.

The co-expression of erythroid markers and nuclear marker Hoescht was compared on no-fibre mini-BR effluent (Figure 43F): CD235a was brightly expressed on rare, contaminating enucleate cells within the day 0 inoculate, but then alternated between moderate and dim CD235a expression on a much larger enucleate cell fraction. CD71 and CD36, which comprised a majority of enucleated cells and similar co-expressions with CD235a, but increased in single-positive expression (e.g. nucleated CD71⁺CD235a⁻ or CD36⁺CD235a⁻). The enucleate fraction analysed by flow cytometry (25% in inoculum, 70% in egress), was in agreement with that counted by methylene blue dye-exclusion differential counts. Altogether, this data demonstrates hollow fibres may be unnecessary to separate more-adherent hematopoietic MNCs from their less-adherent enucleate red cell progeny, but further optimisation is required to balance medium flow rate for appropriate diffusion and cellular while maintain cellular adherence within mini-BRs.

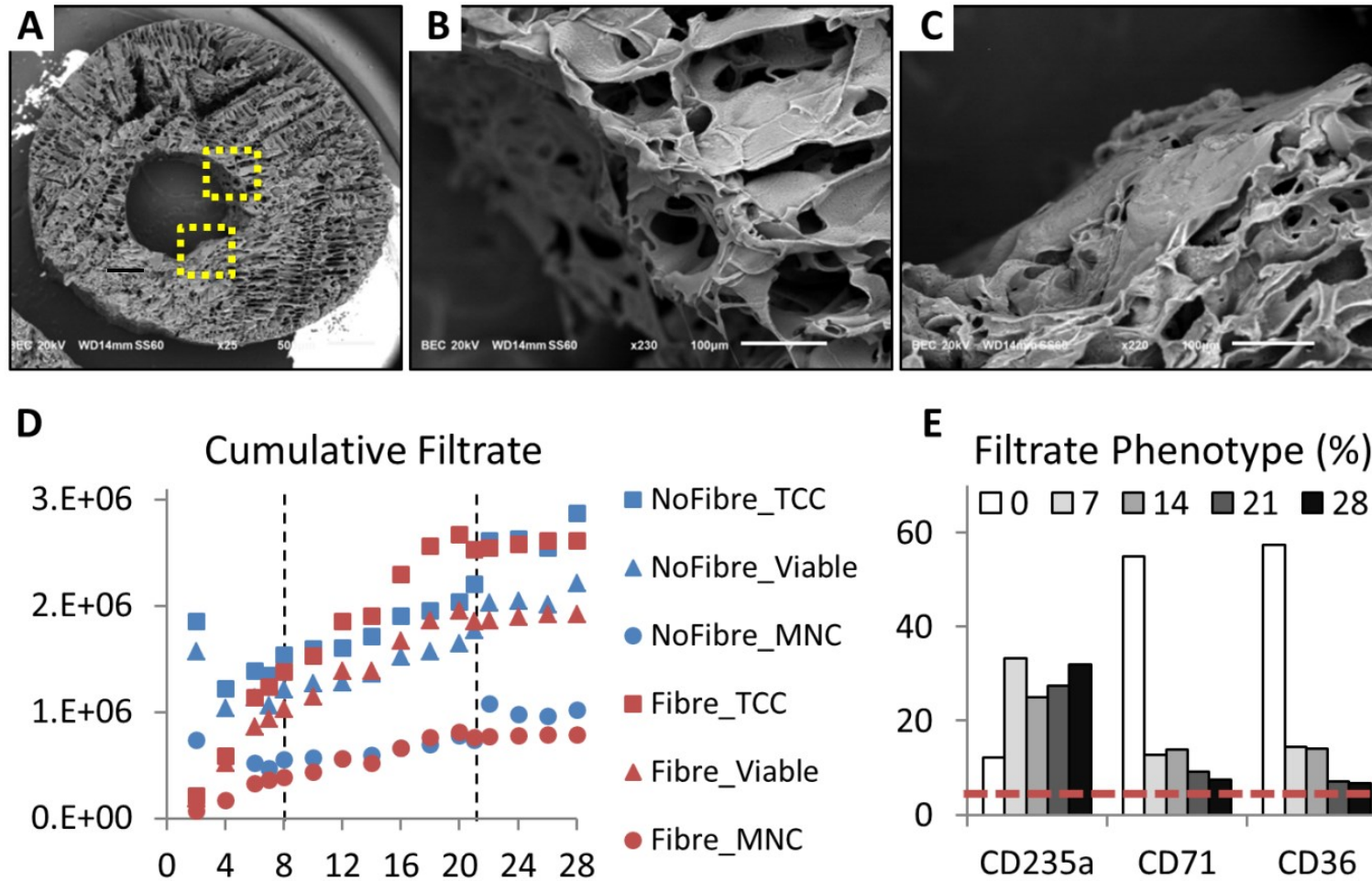


Figure 43: Comparison of mini-BR cultures with and without hollow fibres.

SEM images of no-fibre mini-BR post-fabrication with (A) 500 µm and (B, C) 50 µm scale bars within highlighted regions. (D) Effluent cell kinetics from 1-2 day collections including total cell number (TCC), viable cell number (viable), and mononuclear cell number (MNC) of fibre-free mini-BR (NoFibre) and a comparable fibre-containing culture (Fibre) where at day 8 (line) EPO was gradually introduced at 0.1 IU/mL and at day 20 (line) and EPO spike was introduced at day 20 at 1 IU/mL. (E) Collected viable cell single-phenotype expression of no-fibre mini-BR (gated on Calcein AM). Fibre-containing mini-BR cells never expressed above 4% of the phenotypes surveyed (red line).

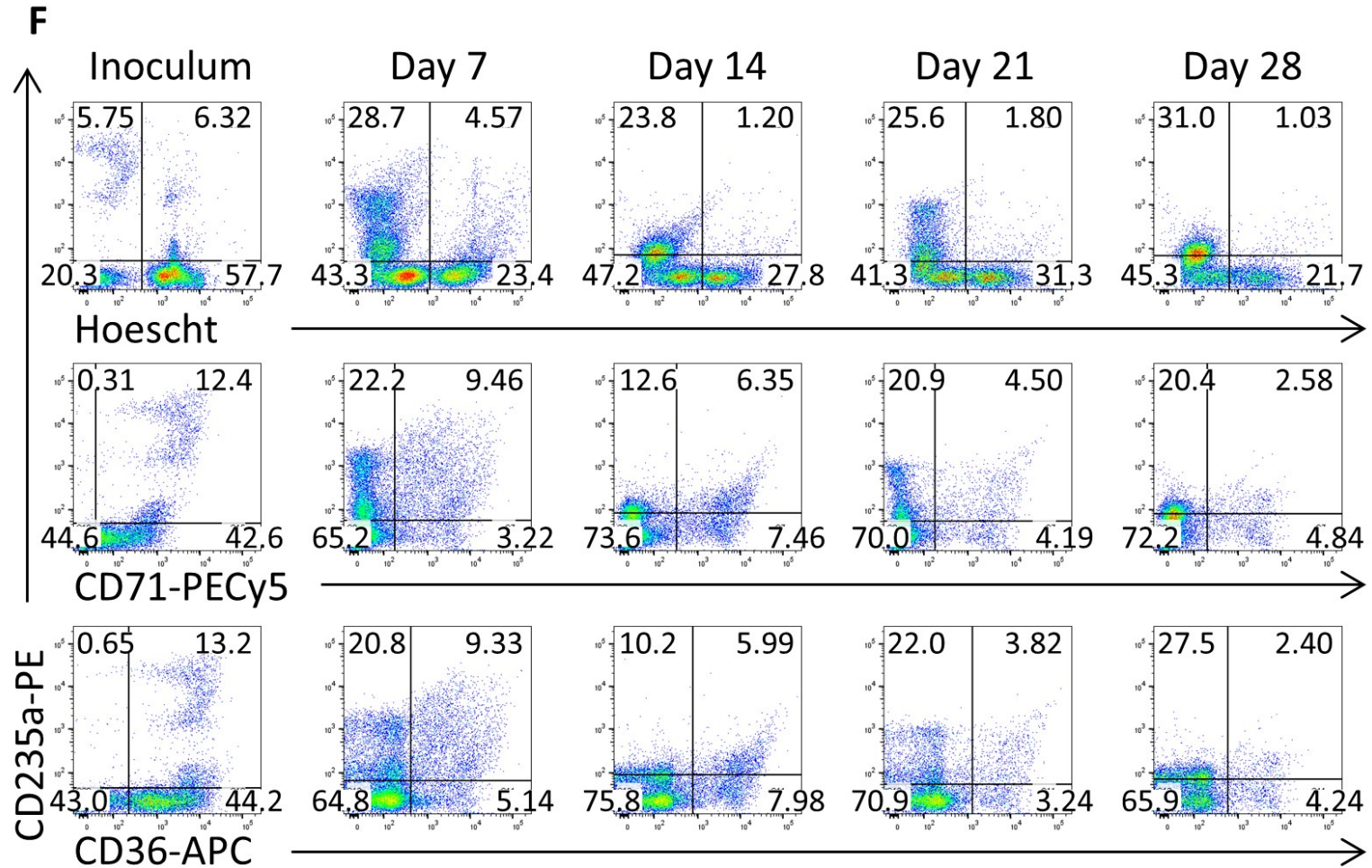


Figure 43 (continued): (F) Flow cytometry plots of collected no-fibre mini-BR cell effluent at inoculum, day 7, day 14, day 21, and day 28 while staining for markers Hoescht (nuclei), CD235a, CD71, and CD36.

7.5. Discussion

The engineering of cell therapy manufacturing platforms which can support growth at tissue-like cell densities would bring *ex vivo* red blood cell production toward clinically relevant costs. In prior studies, the dense inoculation ($5 \cdot 10^8$ MNC/mL) of a 5 mL perfusion hollow fibre bioreactor (HFBR) platform supported the expansion of hUCB MNCs to a density greater than $2 \cdot 10^9$ cells/mL. In this manuscript, similar and smaller 0.5 mL “mini-BRs” were designed and fabricated comprised of a collagen-coated polyurethane scaffolding surrounding either a ceramic hollow fibre (fabricated by Asma Tahlawi) or void channel which was continuously perfused with culture medium. When inoculated with high hUCB MNC densities (10^8 MNC/mL), these mini-BR supported cells for 28 days, and in some cultures, generated dark red confluent cell masses confluent in three-dimensions, and the exclusion of the ceramic hollow fibres aided the egress of viable enucleate red cells (Calcein AM⁺ Hoescht CD235a⁺) and not erythroid precursor phenotypes (CD71 or CD36).

The design of mini-BR dimensions was directed to avoid oxygen depletion within the reactor. While other nutrients (e.g. glucose, glutamine) may also effect cell quiescence, proliferation, and differentiation, oxygen has been well-studied as the limiting nutrient for cell viability *in vitro* and *in vivo* (Chow et al. 2001; Misener et al. 2014). Although not significantly affecting culture viability, the depletion of supplemented growth factors (e.g. EPO, SCF) could also be characterized. A similar analysis has been generated for prior HFBR designs, where growth factor supplementation was the most cost-intensive parameter for the model-based optimisation of red blood cell production (Misener et al. 2014). A comparable liquid suspension culture utilizing 2-day half-medium exchanges and simply maintaining $5 \cdot 10^7$ hUCB MNCs for 28 days would require 400 mL of medium, 30 μ g SCF, and 553 IU EPO, whereas the dense mini-BR requires 217 mL of medium containing a total of 3.3 μ g SCF and 55 IU EPO, reducing the quantity of the most expensive cell culture components to one-half the volume of medium and one-tenth the quantity of cytokines.

These calculations suggested viable oxygen concentration would only exist within scaffolding closer than 0.5 mm from the hollow fibre, and advised a bioreactor diameter of approximately 2 mm. Such a bioreactor design was not physically possible to fabricate, and instead the thinnest possible bioreactor diameter (4.5 mm) where a hollow channel could be formed. As an effort to reduce anoxic

volumes within this larger mini-BR, medium was perfused at the maximal rate possible. At day 21 of culture, the most confluent regions existed far from the hollow fibre, suggesting oxygen was not toxically deprived within the mini-BR. However, few cells could be filtered from these cell-dense mini-BRs, and imaging indicated small and tortuous hollow fibre pores may have prevented the egress of cells.

The confluent cell densities found within the first mini-BR experiments were not replicated, both in similar culture conditions, or in the two cultures implementing one-third the basal cytokine supplementation and a day 20 spike of EPO to a total medium concentration of 1 IU/mL (2 IU/mL in 30 mL fresh medium in a half-medium exchange). These mini-BRs implemented fibres with less tortuous pores (see prior sections), or omitted fibres in favour of hollow channels for medium perfusion. Both these mini-BRs were better able to filter and harvest small bodies compared to the earlier cell-dense mini-BR, but only egress from the fibre-free mini-BR contained erythroid phenotypes and were purified for enucleate red cell CD235a during culture. Potentially, the large number of small bodies collected from fibre-containing mini-BR effluent may have been comprised of sheared cellular membranes or hollow fibre aluminium oxide particulates resembling small cells unstained by trypan blue during differential counts.

7.6. Conclusion

In summary, a miniaturised red blood cell therapy culture platform is designed which can expand hUCB MNCs at densities above 10^8 per mL with a continuous egress of enucleate red blood cells. These “mini-BRs” allow for the culture of hematopoietic cells at 100-fold higher densities than liquid suspension, require 10-fold lower donor cell inoculum, and utilise 10- to 50-fold lower cytokine concentrations. Continuous collection of cell therapy product was improved by the removal of ceramic hollow fibre membranes (fabricated by Asma Tahlawi), which restricted the egress of mature cell types. 3D biomaterials implemented as perfusion culture platforms are promising candidates for expanding cell therapy products at tissue-like cell densities, and could be utilised to reduce biomanufacturing expenses to clinically-useful costs.

8. Conclusions

In this thesis, a cell culture platform was developed as a bone-marrow mimicry bioreactor to develop a model of personalised healthcare. As a more faithful model of the organ for human blood genesis; such a reactor could be applied for the bio-mimetic production of transfusable cell therapies and also be useful in future studies of the progression of abnormal blood production, such as leukemic cancers of the blood, and test relevant treatment strategies. This thesis focuses on the development and characterisation of bioreactor elements which are advantageous in normal blood production; such as the incorporation of perfused hollow fibres which can harvest cells, the characterization of interactive and supportive blood-stroma-bone environments, and the implementation of these studies to improve bioreactor design towards RBC production. This work was supported by prior research by prior members of the laboratory.

In a previous PhD thesis, this culture platform was developed as a hollow fibre bioreactor (HFBR) where both polymeric or polymeric and ceramic hollow fibres were incorporated within 10 mL of PU scaffolding; using polymeric hollow fibres which could filter nutrients, metabolites, but not proteins nor cells. In this prior thesis, a 4-polymeric HFBR reproducibly expanded $1.6 \cdot 10^7$ hUCB MNCs/mL 10-fold across 28 days; and, in a single experiment, a 4-ceramic and 4-polymeric HFBR expanded 10^8 hUCB MNCs/mL 33.5-fold across 31 days, reaching scaffold densities of $7.4 \cdot 10^8$ cells/mL and filtering $3 \cdot 10^{10}$ cells, 5% of which were enucleate red cells (Macedo 2011; Panoskaltsis et al. 2012). These preliminary experiments was further modelled and a framework for model-based optimisation of cost-effective RBC production was advised (Misener et al. 2014). However, the RBC-producing HFBR was only successfully cultured as one experimental replicate, in high concentrations of animal serum (30%), without rigorous characterisation of the medium components required, and without spatially characterizing the HFBR platform in supporting a physiological hematopoietic environment. This PhD thesis aims to further develop these preliminary and promising prior outcomes by designing and thoroughly characterizing a reproducible hUCB-derived RBC production platform whose culture design could then be explored.

In the first stage of this project (**Section 4**), new ceramic hollow fibres were produced by Asma Tahlawi, a current member of the lab, whose porosity and filtration properties were characterised. These

fibres could be used to purify a 80% MNC : 20% enucleate mixture of hUCB isolate to 10% MNC : 90% enucleate in a passive, cross-flow filtration, and could filter half a trillion enucleate red blood cells per hour in an aggressive, dead-end filtration which increased reticulocyte content from 19% to as high as 90% of a blood solution. While commercial and new microfluidic leukoreduction filters may offer better filtrate purity with less shear stress (Xia et al. 2016), the innovative quality of the ceramic hollow fibres is their ability to be incorporated within perfused 3D porous scaffold biomaterials to both diffuse fresh nutrients and harvest cells long-term. A ceramic hollow fibre was incorporated within 5 mL of polyurethane scaffolding which was collagen coated, sterilized, and cultured with hUCB MNCs for 21 days in 30% serum, 100 ng/mL SCF, and 1 IU/mL EPO as a 5 mL ceramic HFBR.

These hollow fibres were designed to mimic the central marrow sinus: the site of mature cell egress into peripheral blood circulation, where red blood cells (RBCs) can cross its endothelial wall by deforming through tight gaps between cells (2-3 μm) (Leblond et al. 1971). The endothelial sinus not only diffuses nutrients into the marrow, but also acts as a natural filter to purify small, deformable RBCs from neighbouring mononuclear cells (MNCs), as RBCs comprise <25% of marrow cells, but >95% of peripheral blood cells (Lansdorp & Dragowska 1992). In current studies, incorporating perfused hollow fibres into 3D porous biomaterials has (1) been utilised to promote mature cell product egress from biomaterials (Di Buduo et al. 2015), (2) enhanced nutrient diffusion for long-term high-cell-density culture platforms (Housler et al. 2012) and (3) provided biochemical gradients to structure multi-component cell co-cultures (Kolesky et al. 2016; Zhang et al. 2016). In these HFBRs, it likewise became clear cellular distribution became dictated by distance from hollow fibre placement.

The second stage of this project (**Section 5**), a mathematical toolkit to quantitate the distribution of cells in 3D materials was developed. For the first time, the density of cells could be estimated at continuous 2D and 3D distances away from a point of interest throughout an entire 3D image. These image analytics were developed to quantitate how the placement of specific nucleated or enucleated cell phenotypes (e.g. blood, stromal, bone cells; at different maturations) was reliant on distance from the engineered perfused hollow fibres, or on distance from other cell types (forming cell-to-cell association networks).

The study of animal marrow distributions of hematopoietic, mesenchymal, and osteogenic cells has been investigated using stereology since the 1970's and 80's by observing the placement of erythroid colonies and niches near and far from marrow sinuses from microsectioned histology and transmission EM sections (Mohandas & Prenant 1978; Leblond et al. 1971; Carlsson 1977; Weiss 1984). Recently, the use of 3D confocal microscopy for large-tissue-volume analyses has led to the study of rare HSC distributions and niche environments (Nombela-Arrieta et al. 2013; Itkin et al. 2016; Greenbaum et al. 2017; among many others), and has challenged traditional views of what comprises the HSC niche.

Our imaging analyses expand on current tools which calculate cellular association metrics (Bjornsson et al. 2008; Delarue et al. 2014; Meddens et al. 2013) by estimating cell densities within peripheral regions of 3D imaged space to quantitatively assess 2.1-fold more cells and 23-fold longer distances. The estimation of cellular distribution metrics throughout the image captured is very important for large and expensive samples where the entire tissue sample cannot be imaged. Current state-of-the-art qualitatively compare imaged experimental results against random distributions by counting cells within a given region (Acar et al. 2015; Takaku et al. 2010), while these methods can automatically calculate region volumes to provide cell densities, not just relative cell numbers.

The third stage of this project (**Section 6**) focused on the characterization of the marrow-mimetic environment the HFBR provided. The 21-day platform used in **Section 4** was inoculated with $4 \cdot 10^7$ hUCB MNCs/mL and extended to 28-days, and medium containing 30% serum was exchanged for serum-free expansion medium supplemented with lower SCF and EPO concentrations. Over the 28-day culture, phenotypically mature RBC populations could be filtered and harvested in the HFBR effluent, and 23 unsupplemented hematopoietic and stromal growth factors were detected. *In situ* imaging methods demonstrated an autonomously formed stromal component undergoing osteogenic differentiation, ECM deposition, and forming dense hematopoietic associations. The imaging algorithms developed in **Section 5** were applied to quantitate and make simulations of nucleated and enucleated phenotype numbers, distributions from hollow fibres, and associations with specific cell types. The inoculum density could be scaled 25-fold higher at an identical medium and cytokine replenishment, and expand hUCB MNCs 4-fold ($2.2 \cdot 10^9$ cells/mL) to become the highest density

hematopoietic culture to date, while this higher density increased produced and harvested red cell phenotype purity (CD235a⁺CD71⁻) continuously collected by filtration.

The culture of hUCB MNCs in the HFBR was characterized for its ability to recapitulate aspects of *in vivo* marrow erythropoiesis *ex vivo*, focusing on niche components, their spatiotemporal distributions, and the formation of supportive microenvironments throughout the marrow-mimicry environment. Contributions of accessory cells have recently been studied as nearby ($\leq 40 \mu\text{m}$) mesenchymal, osteoprogenitor, and mature osteoblast growth factor secretion and physical cues to promote HSC niche proliferation, differentiation, or quiescence (Kfoury & Scadden 2015; Boulais & Frenette 2015; Silberstein et al. 2016). The erythropoietic niche has been traditionally investigated as late erythroblasts physically contacting ($\leq 15 \mu\text{m}$) other macrophagic and erythroblast neighbors in support of red cell enucleation (Manwani & Bieker 2008; Chow et al. 2013). These two defined niches may paint an incomplete portrait of what may be a continuum of niche states during quiescence, proliferation, then erythroid differentiation and maturation of HSCs. Even so, the observed adhesive surface motifs and secreted growth and migratory factors from HSC and erythropoietic niches realised from *in vivo* animal studies provided insight for analyses of bio-mimetic niche formation.

The novelty of this system is three-fold. First, no group to date has studied the multi-lineal differentiation (e.g. stroma, osteogenic, hematopoietic) of hUCB MNCs *ex vivo* in defined medium components, wherein this project focused on an erythroid application. Second, no group has provided a model framework to study the distribution and association of these cells throughout a large scale tissue engineering device. Third, this HFBR allowed for the most dense culture of hUCB MNCs to date, which further improved erythroid differentiation and harvest. This HFBR platform may represent a more physiologically relevant culture system to study *ex vivo* erythropoiesis and could potentially provide a platform for translational cell expansion protocols.

The fourth stage of this project (**Section 7**) sought to improve the 5 mL HFBR design from **Section 6** by designing, fabricating, and culturing 0.5 mL mini-BRs which require less inoculated hUCB MNCs ($5 \cdot 10^7$) to take advantage of benefits found during high-density culture ($\geq 10^8$ MNC/mL). These mini-BRs were able to expand hematopoietic cells to a 3D confluent density across 28-days using lower concentrations of cytokines and smaller medium requirements. However, cell filtration and

harvest of these reactors were limited by fibres, and mini-BRs with hollow fibres were compared to those with a hollow channel in its place under otherwise similar conditions. Cellular egress from these no-fibre mini-BRs were enriched for enucleate erythroid cells (CD235a⁺ CD71⁻ Hoescht⁻ Calcein AM⁺), but were not able to reach *in situ* confluent cellular densities as found during higher cytokine supplementation. Therefore, the experiments suggest that growth factor supplementation should be higher than human serum values (0.3 IU/mL versus 0.015 IU/mL) and medium should be perfused at higher rates (460 mL/day versus 60 mL/day) to sustain high density HFBR cultures (10⁸ MNCs/mL), but further analyses should assess the different requirements of a fibre-free system (e.g. retaining cells within scaffold, shear stress, biochemical diffusion).

In conclusion, a hollow fibre bioreactor was developed toward mimicking and towards characterising physiological red blood cell production *ex vivo*. This development has spanned bioreactor fabrication and analysis (**Section 4**), quantitative image tools to characterize culture development (**Section 5**), analyses of physiological development of the reactor over long-term culture (**Section 6**), and a proposal for bioreactor optimisation through miniaturised, parallelised design (**Section 7**). These developments improve the current state-of-the-art for erythroid cell culture by proposing a hUCB MNC culture platform implementing higher cell densities (100 to 1000-fold) and lower (10-fold) cytokine supplementation able to maintain hematopoietic progenitors for longer-term culture (1.5-fold) where red cells could be produced and harvested throughout. These developments also improve the current state-of-the-art for 3D biomaterial culture platforms by proposing strategies for the continuous, non-invasive extraction of mature blood products and tools for the quantitative characterisation of the engineered 3D cellular environment. This body of research has the potential to be further developed through a better understanding of hematopoietic processes, control of output cell product, and comparison and application with normal and abnormal hematopoiesis under different conditions. Relevant future work concerning bioreactor characterisation, optimisation, and application is proposed in the following section.

9. Future Work

The developed bioreactor has recapitulated benefits of physiological marrow production: dense cell proliferation, reduced cytokine expenditure, multilineal growth for long-term production, continuous cell product egress, and a model of cellular distribution and interaction. However, its potential for cell therapy production and disease-treatment models remains limited by: inconsistent proliferation to tissue densities ($>10^8/\text{mL}$), inefficient RBC product egress ($<10^8/\text{BR}$), and could be extended by: assessment of produced RBC clinical utility, a more thorough analysis of endogenous cellular support, and recapitulation of abnormal hematopoiesis. Herein, future work is proposed to address these uncertainties:

9.2. Identify and exploit biomarkers in proliferative hUCB donations

The expansion of densely-innoculated hUCB MNCs in serum-free 0.5 mL mini-BRs was remarkably inconsistent (Section 7) in contrast to the robust 5 mL HFBRs (Section 6). Although a range of conditions were examined, only one high-density mini-BR produced 3D-confluent cell growth across 28 days, while other mini-BR cultures did not significantly expand the density of cells *in situ*. The factors for this unique mini-BR culture success was unclear: other cultures which maintained the same inoculum density, flow rate, and medium composition did not fare as well. hUCB has demonstrated donor-to-donor variability for the 2D expansion of CD34⁺ HSCs (Koller et al. 1996) and adherent MSCs (Lambrechts et al. 2016), which could be a result of metabolic, secretory, or genetic donation profiles, and could be controlled by providing essential growth factors, screening hUCB units cultured, and providing interactions with a consistent accessory cell batch. Therefore, it would be important to compare more proliferative hUCB units against more quiescent units using: common birth diagnostics (weight, size), hUCB unit size and cell composition, surface marker expression, intracellular metabolomics and proteomics, or secretory profile during early stages of culture; in order of complexity and invasiveness, where a less complex and less invasive hUCB screening metric would be optimal to determine which hUCB donations are most worthwhile as cell sources for *ex vivo* biomanufacturing, or to identify the optimal cytokine stimulation profile for more or less proliferative cell types as a patient-specific culture platform.

9.3. Further develop the a mini-BR for dense hUCB MNC expansion and RBC egress

This thesis did not report the best expansion of hUCB cells, but may be in the competition for reporting the best yield of extractable cells, because of the use of high inoculum cell densities. The current state-of-the-art have reported expansions as high as 10^6 -fold in 21 days (Timmins et al. 2011), but are initiated with rare $CD34^+$ which comprise 1% of hUCB MNCs, or $5 \cdot 10^6$ $CD34^+$ cells per hUCB donation (Fritsch et al. 1996), and are seeded at 10^4 /mL in 2D culture, whose growth and dilution would require 400 litres of medium to produce a unit of RBCs, assuming a maximal density of $5 \cdot 10^6$ cells/mL (Timmins & Nielsen 2009). The largest single-culture scale and expansion HEMA culture finished with a 1 litre culture maintained at 10^5 cells/mL, producing approximately 10^8 cells (Timmins et al. 2011). This thesis' HFBR expanded hUCB MNCs only 4-fold in 28 days, but started with a density of $5 \cdot 10^8$ MNCs/mL, and its harvest contained $2.2 \cdot 10^9$ cells/mL (cells include viable mononuclear and enucleate), such that $1.1 \cdot 10^{10}$ cells were within the 5 mL device at day 28, and if appropriately developed and scaled-up, may produce a unit-worth of RBCs (10^{12}) within less than 1 litre of reactor volume (Section 6).

The scale up of 3D biomaterials remains a challenge due to oxygenation, growth factor delivery, and cell inoculum and harvest. Therefore, the scale-up of mini-BRs occurred by scaling out: instead of increasing bulk reactor volume, scaling up by increasing the number of parallelised reactors. This method allows us to maintain similar nutrient diffusion and cellular kinetics while employing higher production, creating mini-BRs which expanded to tissue-like cell confluency. However, inconsistent hUCB MNC production of RBCs and ineffective RBC harvest through hollow fibres limited these studies. To further realise the platform as a RBC production device: biomarkers and process conditions (as above) must be identified to consistently produce large quantities of RBCs, and materials and culture conditions must be developed to allow for the extraction of RBCs, as hollow fibres or otherwise. Effective materials would contain bio-mimetic pore sizes for RBC filtration (2-3 μm) with low tortuosity employing perfusion flow rates adequately approximating *in vivo* shear rates.

9.4. Qualitatively assess RBC product quality

In these studies, collected RBC product was only assessed by morphology, enucleation, and phenotypic markers (Sections 6 - 7). These analyses lack functional characterisation of RBCs, including haemoglobin detection, oxygen binding, deformability measurements, and *in vivo* transfusion efficacy models. Susana Dos Santos, a fellow BSEL colleague, produced and aspirated hUCB MNC-derived RBCs within a similar static 3D biomimicry (similar to Section 4), who expressed fetal haemoglobin which later switched to adult haemoglobin when cultured at specific, more physiological, oxygen profiles (Dos Santos et al. 2016). Oxygen binding activity has been assessed by tonometer using *ex vivo* produced RBCs within the prior HFBR model and demonstrated similar binding curves to fresh hUCB RBCs (Macedo 2011). In addition, deformability of nucleated and enucleated hUCB cells has been assessed by optical tweezers at a collaborator institution, and should be applied to *ex vivo* RBCs produced by the bioreactor (Agrawal et al. 2016). Once large quantities of RBCs can be consistently produced and harvested from the BR, such analyses must be used as quality control before progressing towards *in vivo* transfusion.

9.5. Quantify and exploit endogenous hematopoietic support provided by accessory cells

Within all hUCB MNC bioreactor cultures, non-erythroid cell types were inoculated and proliferated for 28 days. Comprising mesenchymal, osteogenic, and macrophagic phenotypes and morphologies, these accessory cells appeared to support erythropoiesis through physical contact, growth factor secretion, and protein deposition; which occurred within static porous scaffolds as well as the HFBR (Santos et al. 2016). The variety of accessory phenotypes changed with serum-containing or serum-free medium, as initial experiments containing 30% fetal bovine serum in IMDM generated CD31⁺ cells, which was absent from serum-free conditions. It is likely the factors secreted from this stromal component promoted dense hematopoietic expansion under low cytokine, serum-free conditions, which could be further utilized to reduced costs, and directed towards erythroid differentiation. The support provided by accessory cells should be better understood through “knockout” experiments; removing specific stromal or hematopoietic phenotypes within the reactor. This support could be further exploited either by providing stromal growth factors at the start of culture,

first inoculating stromal cells before hematopoietic cells, or by re-seeding the reactor multiple times to make use of prior stromal deposition.

9.6. Model and treat abnormal hematopoiesis *ex vivo*

A cell therapy production platform that serves as a faithful mimicry of physiological hematopoiesis *ex vivo* could also serve to recapitulate blood diseases in the laboratory. This would provide mechanistic understanding as to the pathology, progression, and treatment of human diseases. During the very beginning of this thesis, an early bioreactor model of Dr. Maria Rende was inoculated with mixed phenotype acute leukemia and perfused with IMDM containing 30% serum and 1% penicillin-streptomycin. This bioreactor was maintained for 35 days without endogenous cytokines. Throughout culture, growth factors were continuously secreted by bioreactor cells throughout culture and a new leukemic clone emerged throughout the *ex vivo* culture which was not present at day 0 (Rende et al. 2013). In future experiments, the effect of well-studied or candidate therapeutics targeting leukemic clones could be studied and administration regimen could be optimised in this *ex vivo* system, as observed for static models (Fuentes-Gari et al. 2015).

10. References

- Acar, M. et al., 2015. Deep imaging of bone marrow shows non-dividing stem cells are mainly perisinusoidal. *Nature*, 526(7571), pp.126–30. Available at: <http://www.ncbi.nlm.nih.gov/pubmed/26416744>.
- Afonso, M. & Yaez, R., 2001. Nanofiltration of wastewater from the fishmeal industry. *Desalination*, 139(1–3), p.429.
- Agrawal, R. et al., 2016. Assessment of red blood cell deformability in type 2 diabetes mellitus and diabetic retinopathy by dual optical tweezers stretching technique. *Scientific reports*, 6(May 2015), p.15873. Available at: <http://dx.doi.org/10.1038/srep15873>.
- Alakel, N. et al., 2009. Direct contact with mesenchymal stromal cells affects migratory behavior and gene expression profile of CD133+ hematopoietic stem cells during ex vivo expansion. *Experimental Hematology*, 37(4), pp.504–513. Available at: <http://dx.doi.org/10.1016/j.exphem.2008.12.005>.
- Allen, J.E. & Henshaw, D.L., 2001. An in situ study of CD34(+) cells in human fetal bone marrow. *British journal of haematology*, 114(1), pp.201–10. Available at: <http://www.ncbi.nlm.nih.gov/pubmed/11472369>.
- Allenby, M.C. et al., 2017. A quantitative three-dimensional (3D) image analysis tool for maximal acquisition of spatial heterogeneity data. *Tissue Engineering Part C: Methods*, 23(2), p.ten.TEC.2016.0413. Available at: <http://online.liebertpub.com/doi/10.1089/ten.TEC.2016.0413>.
- An, X. et al., 2014. Global transcriptome analyses of human and murine terminal erythroid differentiation. *Global Transcriptome Analyses of Human and Murine Terminal Erythroid Differentiation*, 123(22), pp.3466–3478.
- Anon, 2017a. *Chronic Myelogenous Leukemia Treatment (PDQ®) - Patient Version*,
 Anon, 2017b. Efficient Monte Carlo Procedures for Generating Points Uniformly Distributed Over Bounded Regions Author (s): Robert L. Smith Published by: INFORMS Stable URL: <http://www.jstor.org/stable/170949> Efficient Monte Carlo Procedures for Generating, 32(6), pp.1296–1308.
- Anthony, B.A. & Link, D.C., 2014. Regulation of hematopoietic stem cells by bone marrow stromal cells. *Trends in Immunology*, 35(1), pp.32–37. Available at: <http://dx.doi.org/10.1016/j.it.2013.10.002>.
- Appel, A.A. et al., 2013. Imaging challenges in biomaterials and tissue engineering. *Biomaterials*, 34(28), pp.6615–6630. Available at: <http://dx.doi.org/10.1016/j.biomaterials.2013.05.033>.
- Baek, E.J. et al., 2008. In vitro clinical-grade generation of red blood cells from human umbilical cord blood CD34+ cells. *Transfusion*, 48(10), pp.2235–2245.
- Bagley, J. et al., 1999. Extended culture of multipotent hematopoietic progenitors without cytokine augmentation in a novel three-dimensional device. *Exp Hematol*, 27(3), pp.496–504.
- Baker, B.M. & Chen, C.S., 2012. Deconstructing the third dimension - how 3D culture microenvironments alter cellular cues. *Journal of Cell Science*, 125(13), pp.3015–3024.
- Bartl, R. & Frisch, B., 2012. *Biopsy of bone in internal medicine: an atlas and sourcebook* 21st ed., Springer Science and Business Media.
- De Bartolo, L. et al., 2009. Human hepatocyte functions in a crossed hollow fiber membrane bioreactor. *Biomaterials*, 30(13), pp.2531–2543. Available at: <http://dx.doi.org/10.1016/j.biomaterials.2009.01.011>.
- Bertrand, J.Y. et al., 2007. Definitive hematopoiesis initiates through a committed erythromyeloid progenitor in the zebrafish embryo. *Development (Cambridge, England)*, 134(23), pp.4147–4156.
- Binder, V. & Zon, L.I., 2013. High throughput in vivo phenotyping: The zebrafish as tool for drug discovery for hematopoietic stem cells and cancer. *Drug Discovery Today: Disease Models*, 10(1), pp.e17–e22. Available at: <http://dx.doi.org/10.1016/j.ddmod.2012.02.007>.
- Bjornsson, C.S. et al., 2008. Associative image analysis: A method for automated quantification of 3D multi-parameter images of brain tissue. *Journal of Neuroscience Methods*, 170(1), pp.165–178.

- Blood, N.H.S. & Transplant, 2010. Annual Review. *NHSBT Customer Services*.
- Blood, N.H.S. & Transplant, 2013. Annual Review. *NHSBT Customer Services*.
- Bolte, S. & Cordelieres, F.P., 2006. A guided tour into subcellular colocalisation analysis in light microscopy. *Journal of Microscopy*, 224(3), pp.13–232.
- De Boodt, S. et al., 2013. A Semiautomatic Cell Counting Tool for Quantitative Imaging of Tissue Engineering Scaffolds. *Tissue Eng Part C Methods*, 19(9), p.130226063303000. Available at: <http://dx.doi.org/10.1089/ten.tec.2012.0486>.
- Boulais, P. & Frenette, P., 2015. Making sense of hematopoietic stem cell niches. *Blood*, 125(17), pp.2621–2630. Available at: <http://www.bloodjournal.org/content/125/17/2621.abstract>.
- Breems, D. a et al., 1998. Stroma-contact prevents loss of hematopoietic stem cell quality during ex vivo expansion of CD34+ mobilized peripheral blood stem cells. *Blood*, 91(1), pp.111–7. Available at: <http://www.ncbi.nlm.nih.gov/pubmed/9414274>.
- Bronzino, J.D., 1999. *The Biomedical Engineering Handbook*, CRC Press.
- Brookes, M., 1967. Blood flow rates in compact and cancellous bone, and bone marrow. *J. Anat*, 101(3), pp.533–541.
- Di Buduo, C.A. et al., 2015. Programmable 3D silk bone marrow niche for platelet generation ex vivo and modeling of megakaryopoiesis pathologies. *Blood*, 125(14), pp.2254–2264.
- Cabrita, G.J.M. et al., 2003. Hematopoietic stem cells: from the bone to the bioreactor. *Trends Biotech*, 21(5), pp.233–240.
- Caldwell, J., Wang, W. & Zandstra, P.W., 2015. Proportional-Integral-Derivative (PID) control of secreted factors for blood stem cell culture. *PLoS ONE*, 10(9), pp.1–20.
- Carlsson, J., 1977. A proliferation gradient in three-dimensional colonies of cultures human glioma cells. *Int J Cancer*, 20(1), pp.129–136.
- Cells, C.D., Mcintosh, K. & Park, B., 2014. ERYTHROCYTES DIFFERENTIATED IN VITRO FROM NANOFIBER EXPANDED CD133+ CELLS. , 2(12), pp.69–74.
- Lo Celso, C. et al., 2009. Live-animal tracking of individual haematopoietic stem/progenitor cells in their niche. *Nature*, 457(7225), pp.92–6. Available at: <http://dx.doi.org/10.1038/nature07434>.
- Cha, C. et al., 2012. Designing biomaterials to direct stem cell fate. *ACS Nano*, 6(11), pp.9353–9358.
- Chen, L.-Y. et al., 2012. Effect of the surface density of nanosegments immobilized on culture dishes on ex vivo expansion of hematopoietic stem and progenitor cells from umbilical cord blood. *Acta Biomaterialia*, 8(5), pp.1749–1758. Available at: <http://dx.doi.org/10.1016/j.actbio.2012.01.002>.
- Chenouard, N. et al., 2014. Objective comparison of particle tracking methods. *Nature methods*, 11(3), pp.281–9. Available at: <http://www.pubmedcentral.nih.gov/articlerender.fcgi?artid=4131736&tool=pmcentrez&rendertype=abstract>.
- Chesney, A., Good, D. & Reis, M., 2011. Chapter 13 - Clinical Utility of Flow Cytometry in the Study of Erythropoiesis and Nonclonal Red Cell Disorders. In Z. Darzynkiewicz et al., eds. *Recent Advances in Cytometry, Part B Advances in Applications*. Methods in Cell Biology. Academic Press, pp. 311–332. Available at: <http://www.sciencedirect.com/science/article/pii/B9780123854933000139>.
- Choi, H.S. et al., 2013. Autonomous control of terminal erythropoiesis via physical interactions among erythroid cells. *Stem Cell Research*, 10(3), pp.442–453. Available at: <http://dx.doi.org/10.1016/j.scr.2013.02.003>.
- Choi, J.S., Mahadik, B.P. & Harley, B.A.C., 2015. Engineering the hematopoietic stem cell niche: Frontiers in biomaterial science. *Biotechnology Journal*, 10(10), pp.1529–1545.
- Chow, A. et al., 2013. CD169+ macrophages provide a niche promoting erythropoiesis under homeostasis and stress. *Nature medicine*, 19(4), pp.429–36. Available at: <http://www.pubmedcentral.nih.gov/articlerender.fcgi?artid=3983996&tool=pmcentrez&rendertype=abstract>.
- Chow, D.C. et al., 2001a. Modeling pO₂ distributions in the bone marrow hematopoietic compartment. II. Modified Kroghian models. *Biophysical journal*, 81(2), pp.685–696. Available at: [http://dx.doi.org/10.1016/S0006-3495\(01\)75732-3](http://dx.doi.org/10.1016/S0006-3495(01)75732-3).
- Chow, D.C. et al., 2001b. Modeling pO₂ distributions in the bone marrow hematopoietic compartment. II. Modified Kroghian models. *Biophysical journal*, 81(August), pp.685–696.

- Chow, D.C. et al., 2001. Modeling pO₂ Distributions in the Bone Marrow Hematopoietic Compartment. I. Krogh's Model. *Biophysical Journal*, 81(August), pp.675–684.
- Chua, K.-N. et al., 2006. Surface-aminated electrospun nanofibers enhance adhesion and expansion of human umbilical cord blood hematopoietic stem/progenitor cells. *Biomaterials*, 27(36), pp.6043–6051. Available at: <http://www.sciencedirect.com/science/article/B6TWB-4KF788N-2/2/64943476bae1f78edbf909f53a19687>.
- Collins, P.C. et al., 1998. Characterization of hematopoietic cell expansion, oxygen uptake, and glycolysis in a controlled, stirred-tank bioreactor system. *Biotechnology Progress*, 14(3), pp.466–472.
- Coutinho, L.D. et al., 1990. Effects of recombinant human granulocyte colony-stimulating factor (CSF), human granulocyte macrophage-CSF, and gibbon interleukin-3 on hematopoiesis in human long-term bone marrow culture. *Blood*, 75(11), pp.2118–2129.
- Cui, Y.F. et al., 1996. The relative spatial distribution of in vitro-CFCs in the bone marrow, responding to specific growth factors. *Cell Prolif*, 29(5), pp.243–257. Available at: http://www.ncbi.nlm.nih.gov/entrez/query.fcgi?cmd=Retrieve&db=PubMed&dopt=Citation&list_uids=8782487.
- Dao, M.A. et al., 1998. Adhesion to fibronectin maintains regenerative capacity during ex vivo culture and transduction of human hematopoietic stem and progenitor cells. *Blood*, 92(12), pp.4612–4621.
- Delarue, M. et al., 2014. Stress distributions and cell flows in a growing cell aggregate. *Interface focus*, 4(6), p.20140033. Available at: <http://rsfs.royalsocietypublishing.org/content/4/6/20140033>.
- Dexter, T.M., Allen, T.D. & Lajtha, L.G., 1977. Conditions controlling the proliferation of haemopoietic stem cells in vitro. *J Cell Physiol*, 91(3), pp.335–344.
- Ding, L. et al., 2012. Endothelial and perivascular cells maintain haematopoietic stem cells. *Nature*, 481(7382), pp.457–62. Available at: <http://www.pubmedcentral.nih.gov/articlerender.fcgi?artid=3270376&tool=pmcentrez&rendertype=abstract>.
- Doulatov, S. et al., 2012. Hematopoiesis: A Human Perspective. *Cell Stem Cell*, 10(2), pp.120–136.
- Ehninger, A. & Trumpp, A., 2011. The bone marrow stem cell niche grows up: mesenchymal stem cells and macrophages move in. *The Journal of experimental medicine*, 208(3), pp.421–8. Available at: <http://www.pubmedcentral.nih.gov/articlerender.fcgi?artid=3058583&tool=pmcentrez&rendertype=abstract>.
- Eng, G. et al., 2013. Assembly of complex cell microenvironments using geometrically docked hydrogel shapes. *Proceedings of the National Academy of Sciences of the United States of America*, 110(12), pp.4551–6. Available at: http://apps.webofknowledge.com/libproxy1.nus.edu.sg/full_record.do?product=UA&search_mode=GeneralSearch&qid=110&SID=Q2MwscAdxTcnBLIWxox&page=1&doc=26&cacheurlFromRightClick=no.
- Eshghi, S. et al., 2007. α 5 β 1 integrin and erythropoietin mediate temporally distinct steps in erythropoiesis: Integrins in red cell development. *Journal of Cell Biology*, 177(5), pp.871–880.
- Faiz, R. et al., 2013. Separation of Olefin Paraffin Gas Mixtures Using Ceramic Hollow Fiber Membrane Contactors. *Industrial and Engineering Chemistry Research*, 52(23), pp.7918–7929.
- Feng, Q. et al., 2006. Expansion of engrafting human hematopoietic stem/progenitor cells in three-dimensional scaffolds with surface-immobilized fibronectin. *J Biomed Mater Res A*, 78(4), pp.781–791.
- Flower, M.A., 2012. *Webb's physics of medical imaging*, Boca Raton: CRC Press.
- Frassoni, F., Testa, N.G. & Lord, B.I., 1982. The relative spatial distribution of erythroid progenitor cells (BFUe and CFUe) in the normal mouse femur.
- Fritsch, G. et al., 1996. The composition of CD34 subpopulations differs between bone marrow, blood and cord blood. *Bone Marrow Transplant*, 17(2), pp.169–78.
- Fuentes-Gari, M. et al., 2015. A systematic framework for the design, simulation and optimization of personalized healthcare: Making and healing blood. *Computers and Chemical Engineering*, 81, pp.80–93. Available at: <http://dx.doi.org/10.1016/j.compchemeng.2015.03.008>.

- Fujimi, A. et al., 2008. Ex vivo large-scale generation of human red blood cells from cord blood CD34+ cells by co-culturing with macrophages. *International Journal of Hematology*, 87(4), pp.339–350.
- Gattazzo, F., Urciuolo, A. & Bonaldo, P., 2014. Extracellular matrix: A dynamic microenvironment for stem cell niche. *Biochimica et Biophysica Acta - General Subjects*, 1840(8), pp.2506–2519. Available at: <http://dx.doi.org/10.1016/j.bbagen.2014.01.010>.
- Giarratana, M. et al., 2011. Proof of principle for transfusion of in vitro generated red blood cells. *Blood*, 118(19), pp.5071–5079. Available at: <http://www.bloodjournal.org/cgi/doi/10.1182/blood-2011-06-362038>.
- Giarratana, M.C. et al., 2005. Ex vivo generation of fully mature human red blood cells from hematopoietic stem cells. *Nature Biotechnology*, 23(1), pp.69–74. Available at: <http://www.ncbi.nlm.nih.gov/pubmed/15619619>.
- Gouveia Gil, A. et al., 2015. A highly permeable hollow fibre substrate for Pd/Al₂O₃ composite membranes in hydrogen permeation. *International Journal of Hydrogen Energy*, 40(8), pp.3249–3258.
- Greenbaum, A. et al., 2017. Bone CLARITY: Clearing, imaging, and computational analysis of osteoprogenitors within intact bone marrow. *Science Translational Medicine*, 9(387). Available at: http://stm.sciencemag.org/content/9/387/eaah6518?utm_campaign=toc_stm_2017-04-26&et rid=33807910&et cid=1295134.
- Greenbaum, A. et al., 2013. CXCL12 in early mesenchymal progenitors is required for haematopoietic stem-cell maintenance. *Nature*, 495(7440), pp.227–30. Available at: <http://www.pubmedcentral.nih.gov/articlerender.fcgi?artid=3600148&tool=pmcentrez&rendertype=abstract>.
- Grover, A. et al., 2014. Erythropoietin guides multipotent hematopoietic progenitor cells toward an erythroid fate. *The Journal of experimental medicine*, 211(2), pp.181–8. Available at: <http://www.pubmedcentral.nih.gov/articlerender.fcgi?artid=3920567&tool=pmcentrez&rendertype=abstract%5Cnhttp://www.ncbi.nlm.nih.gov/pubmed/24493804%5Cnhttp://www.pubmedcentral.nih.gov/articlerender.fcgi?artid=PMC3920567>.
- Hamlyn, L., 2016. *NHSBT 2015 Commercial Review*,
- Handel, B. V et al., 2010. The first trimester human placenta is a site for terminal maturation of primitive erythroid cells. *Blood*, 116(17), pp.3321–3330.
- Hanspal, M. & Hanspal, J.S., 1994. The association of erythroblasts with macrophages promotes erythroid proliferation and maturation: a 30-kD heparin-binding protein is involved in this contact. *Blood*, 84(10), pp.3494–504. Available at: <http://www.bloodjournal.org/content/84/10/3494.abstract>.
- Hawkins, E.D. et al., 2016. T-cell acute leukaemia exhibits dynamic interactions with bone marrow microenvironments. *Nature*, 538(7626), pp.518–522. Available at: <http://www.nature.com/doi/10.1038/nature19801>.
- Herst, P.M. & Berridge, M. V., 2007. Cell surface oxygen consumption: A major contributor to cellular oxygen consumption in glycolytic cancer cell lines. *Biochimica et Biophysica Acta - Bioenergetics*, 1767(2), pp.170–177.
- Holzapfel, B.M. et al., 2015. Tissue engineered humanized bone supports human hematopoiesis in vivo. *Biomaterials*, 61, pp.103–114.
- Housler, G.J. et al., 2012. Compartmental hollow fiber capillary membrane-based bioreactor technology for in vitro studies on red blood cell lineage direction of hematopoietic stem cells. *Tissue engineering. Part C, Methods*, 18(2), pp.133–42. Available at: <http://www.pubmedcentral.nih.gov/articlerender.fcgi?artid=3262978&tool=pmcentrez&rendertype=abstract>.
- Itkin, T. et al., 2016. Distinct bone marrow blood vessels differentially regulate haematopoiesis. *Nature*, 532(7599), pp.323–8. Available at: <http://www.ncbi.nlm.nih.gov/pubmed/27074509>.
- Jain, K.K., 2017. *Cell Therapy - Technologies, Markets and Companies*,
- Jelined, N. et al., 2002. Novel Bioreactors for the ex vivo Cultivation of Hematopoietic Cells. *Eng Life Sci*, 2(1), pp.15–18.
- Jelkmann, W., 2011. Regulation of erythropoietin production. *The Journal of Physiology*, 589(6), pp.1251–1258. Available at: <http://jp.physoc.org/content/589/6/1251.abstract>.

- Ji, P., Murata-Hori, M. & Lodish, H.F., 2011. Formation of mammalian erythrocytes: Chromatin condensation and enucleation. *Trends in Cell Biology*, 21(7), pp.409–415. Available at: <http://dx.doi.org/10.1016/j.tcb.2011.04.003>.
- Jiang, X.S. et al., 2006. Surface-immobilization of adhesion peptides on substrate for ex vivo expansion of cryopreserved umbilical cord blood CD34+ cells. *Biomaterials*, 27(13), pp.2723–2732.
- Jing, D. et al., 2010. Hematopoietic stem cells in co-culture with mesenchymal stromal cells - modeling the niche compartments in vitro. *Haematologica*, 95(4), pp.542–550.
- Johnstone, R.M., 1992. Maturation of reticulocytes: formation of exosomes as a mechanism for shedding membrane proteins. *Biochem. Cell. Biol.*, 70, pp.179–189.
- Kathryn, M. et al., 2016. Markov Chain Monte Carlo Convergence Diagnostics : A Comparative Review Stable URL : <http://www.jstor.org/stable/2291683> Linked references are available on JSTOR for this article : Markov Chain Monte Carlo Convergence Diagnostics : A Comparative Review. , 91(434), pp.883–904.
- Kfoury, Y. & Scadden, D.T., 2015. Mesenchymal Cell Contributions to the Stem Cell Niche. *Cell Stem Cell*, 16(3), pp.239–253. Available at: <http://linkinghub.elsevier.com/retrieve/pii/S1934590915000752>.
- Khademhosseini, A. & Bong, G.C., 2009. Microscale technologies for tissue engineering. 2009 *IEEE/NIH Life Science Systems and Applications Workshop, LiSSA 2009*, 103(8), pp.56–57.
- Khorshed, R.A. et al., 2015. Automated Identification and Localization of Hematopoietic Stem Cells in 3D Intravital Microscopy Data. *Stem Cell Reports*, 5(1), pp.139–153. Available at: <http://dx.doi.org/10.1016/j.stemcr.2015.05.017>.
- Kingsbury, B.F.K., Wu, Z. & Li, K., 2010. A morphological study of ceramic hollow fibre membranes: A perspective on multifunctional catalytic membrane reactors. *Catalysis Today*, 156(3–4), pp.306–315.
- Kirouac, D.C. & Zandstra, P.W., 2008. The Systematic Production of Cells for Cell Therapies. *Cell Stem Cell*, 3(4), pp.369–381.
- Klein, G., 1995. The extracellular matrix of the hematopoietic microenvironment. *Cell Mol Life Sci*, 51(9), pp.914–926.
- Kolesky, D.B. et al., 2016. Three-dimensional bioprinting of thick vascularized tissues. *Proceedings of the National Academy of Sciences of the United States of America*, 113(12), pp.3179–84. Available at: <http://www.ncbi.nlm.nih.gov/pubmed/26951646%5Cnhttp://www.pubmedcentral.nih.gov/articlerender.fcgi?artid=PMC4812707>.
- Koller, M.R. et al., 1998. Clinical-scale human umbilical cord blood cell expansion in a novel automated perfusion culture system. *Bone Marrow Transplant*, 21(7), pp.653–663.
- Koller, M.R. et al., 1996. Donor-to-donor variability in the expansion potential of human bone marrow cells is reduced by accessory cells but not by soluble growth factors. *Experimental Hematology*, 24(13), pp.1484–1493.
- Koller, M.R. et al., 1995. Long-term culture-initiating cell expansion is dependent on frequent medium exchange combined with stromal and other accessory cell effects. *Blood*, 86(5), pp.1784–93. Available at: <http://www.ncbi.nlm.nih.gov/pubmed/7544642>.
- Kondo, M. et al., 2003. Biology of hematopoietic stem cells and progenitors: implications for clinical application. *Annu Rev Immuno*, 21, pp.759–806.
- Kunisaki, Y. et al., 2013. Arteriolar niches maintain haematopoietic stem cell quiescence. *Nature*, 502(7473), pp.637–643. Available at: <http://www.ncbi.nlm.nih.gov/pubmed/24107994>.
- Kusumbe, A.P., Ramasamy, S.K. & Adams, R.H., 2014. Coupling of angiogenesis and osteogenesis by a specific vessel subtype in bone. *Nature*, 507(7492), pp.323–328. Available at: <http://eutils.ncbi.nlm.nih.gov/entrez/eutils/elink.fcgi?dbfrom=pubmed&id=24646994&retmode=ref&cmd=prlinks%5Cnpapers3://publication/doi/10.1038/nature13145>.
- Lambrechts, T. et al., 2016. Large-Scale Mesenchymal Stem/Stromal Cell Expansion: A Visualization Tool for Bioprocess Comparison. *Tissue Engineering Part B: Reviews*, 22(6), pp.485–498. Available at: <http://online.liebertpub.com/doi/10.1089/ten.teb.2016.0111>.
- Lane, S.W., Williams, D. a & Watt, F.M., 2014. Modulating the stem cell niche for tissue regeneration. *Nature biotechnology*, 32(8), pp.795–803. Available at:

- <http://www.nature.com/doi/10.1038/nbt.2978><http://www.ncbi.nlm.nih.gov/pubmed/25093887>.
- Lansdorp, P.M. & Dragowska, W., 1992. Long-term erythropoiesis from constant numbers of CD34+ cells in serum-free cultures initiated with highly purified progenitor cells from human bone marrow. *The Journal of experimental medicine*, 175(6), pp.1501–9. Available at: <http://www.pubmedcentral.nih.gov/articlerender.fcgi?artid=2119250&tool=pmcentrez&rendertype=abstract>.
- Lassailly, F. et al., 2013. Multimodal imaging reveals structural and functional heterogeneity in different bone marrow compartments : functional implications on hematopoietic stem cells. , 122(10), pp.1730–1740.
- Leberbauer, C. et al., 2005. Different steroids co-regulate long-term expansion versus terminal differentiation in primary human erythroid progenitors. *Blood*, 105(1), pp.85–94.
- Leblond, P.F., LaCelle, P.L. & Weed, R.I., 1971. Cellular Deformability: A Possible Determinant of the Normal Release of Maturing Erythrocytes From the Bone Marrow. *Blood*, 37(1), pp.40–46.
- Lee, E. et al., 2014. Red Blood Cell Generation by Three-Dimensional Aggregate Cultivation of Late Erythroblasts. *Tissue engineering. Part A*, 21, pp.1–30. Available at: <http://www.ncbi.nlm.nih.gov/pubmed/25314917>.
- Lee, J. et al., 2012. Implantable microenvironments to attract hematopoietic stem/cancer cells. *Proc Natl Acad Sci U S A*, 109(48), pp.19638–19643. Available at: <http://www.ncbi.nlm.nih.gov/pubmed/23150542>.
- Lee, M. et al., 2015. Formation of micro-channels in ceramic membranes - Spatial structure, simulation, and potential use in water treatment. *Journal of Membrane Science*, 483, pp.1–14.
- Lee, M. et al., 2014. Micro-structured alumina hollow fibre membranes - Potential applications in wastewater treatment. *Journal of Membrane Science*, 461, pp.39–48.
- Lee, M., Wu, Z. & Li, K., 2015. *Advances in ceramic membranes for water treatment*, Available at: <http://linkinghub.elsevier.com/retrieve/pii/B9781782421214000022>.
- Leisten, I. et al., 2012. 3D co-culture of hematopoietic stem and progenitor cells and mesenchymal stem cells in collagen scaffolds as a model of the hematopoietic niche. *Biomaterials*, 33(6), pp.1736–1747. Available at: <http://dx.doi.org/10.1016/j.biomaterials.2011.11.034>.
- Levee, M.G. et al., 1994. Microencapsulated human bone marrow cultures: A potential culture system for the clonal outgrowth of hematopoietic progenitor cells. *Biotechnology and Bioengineering*, 43(8), pp.734–739.
- Lichtman, J.C. and M., 1978. Marrow cell egress: specificity of the site of penetration into the sinus. , 52(5), pp.959–968.
- von Lindern, M. et al., 1999. The glucocorticoid receptor cooperates with the erythropoietin receptor and c-Kit to enhance and sustain proliferation of erythroid progenitors in vitro. *Blood*, 94(2), pp.550–559.
- Lipsitz, Y.Y., Timmins, N.E. & Zandstra, P.W., 2016. Quality cell therapy manufacturing by design. *Nat Biotechnol*, 34(4), pp.393–400. Available at: <http://dx.doi.org/10.1038/nbt.3525><http://10.1038/nbt.3525>.
- Liu, J. et al., 2010. Membrane remodeling during reticulocyte maturation. *Blood*, 115(10), pp.2021–2027.
- Liu, L. et al., 2006. Bio-ceramic hollow fiber membranes for immunoisolation and gene delivery. I: Membrane development. *Journal of Membrane Science*, 280(1–2), pp.375–382.
- Liu, Z. et al., 2015. Immune homeostasis enforced by co-localized effector and regulatory T cells. *Nature*, 528(7581), pp.225–30. Available at: <http://www.nature.com/doi/10.1038/nature16169><http://www.ncbi.nlm.nih.gov/pubmed/26605524><http://www.pubmedcentral.nih.gov/articlerender.fcgi?artid=PMC4702500>.
- Ma, Z. et al., 2015. Self-organizing human cardiac microchambers mediated by geometric confinement. *Nature communications*, 6(May), p.7413. Available at: <http://www.nature.com/ncomms/2015/150706/ncomms8413/full/ncomms8413.html>.
- Macedo, H., 2011. *A novel 3D dual hollow fibre bioreactor for the production of human red blood cells*. Imperial College London.
- Macedo, H.M., 2011. *A Novel 3D Dual Hollow Fibre Bioreactor for the Production of Human Red Blood Cells*. Imperial College London.

- Mahadik, B.P. et al., 2017. Regulating dynamic signaling between hematopoietic stem cells and niche cells via a hydrogel matrix. *Biomaterials*, 125, pp.54–64. Available at: <http://dx.doi.org/10.1016/j.biomaterials.2017.02.013>.
- Malleret, B. et al., 2013. Significant Biochemical, Biophysical and Metabolic Diversity in Circulating Human Cord Blood Reticulocytes. *PLoS ONE*, 8(10).
- Mantalaris, A. et al., 1998. Engineering a human bone marrow model: a case study on ex vivo erythropoiesis. *Biotechnol Prog*, 14(1), pp.126–133.
- Manwani, D. & Bieker, J., 2008. The erythroblastic island. *Curr Top Dev Biol*, 82, pp.23–52.
- Mason, C. et al., 2013. Cell therapy companies make strong progress from October 2012 to March 2013 amid mixed stock market sentiment. *Cell Stem Cell*, 12(6), pp.644–647. Available at: <http://dx.doi.org/10.1016/j.stem.2013.05.017>.
- Mazo, I.B. et al., 1998. Hematopoietic progenitor cell rolling in bone marrow microvessels: parallel contributions by endothelial selectins and vascular cell adhesion molecule 1. *The Journal of experimental medicine*, 188(3), pp.465–74. Available at: <http://www.pubmedcentral.nih.gov/articlerender.fcgi?artid=2212463&tool=pmcentrez&rendertype=abstract>.
- Meddens, M.B.M. et al., 2013. Automated podosome identification and characterization in fluorescence microscopy images. *Microscopy and microanalysis : the official journal of Microscopy Society of America, Microbeam Analysis Society, Microscopical Society of Canada*, 19(1), pp.180–9. Available at: <http://www.ncbi.nlm.nih.gov/pubmed/23347434>.
- Mendelson, A. & Frenette, P.S., 2014. Hematopoietic stem cell niche maintenance during homeostasis and regeneration. *Nature medicine*, 20(8), pp.833–846.
- Migliaccio, A.R. et al., 2012. Ex-vivo expansion of red blood cells: How real for transfusion in humans? *Blood Reviews*, 26(2), pp.81–95.
- Miharada, K. et al., 2006. Efficient enucleation of erythroblasts differentiated in vitro from hematopoietic stem and progenitor cells. *Nature Biotechnology*, 24(10), pp.1255–1256.
- Misener, R. et al., 2014. Global superstructure optimisation of red blood cell production in a parallelised hollow fibre bioreactor. *Computers and Chemical Engineering*, 71, pp.532–553. Available at: <http://dx.doi.org/10.1016/j.compchemeng.2014.10.004>.
- Mohandas, N. & Prenant, M., 1978. Three-dimensional model of bone marrow. *Blood*, 51(4), pp.633–643.
- Morales-Navarrete, H. et al., 2015. A versatile pipeline for the multi-scale digital reconstruction and quantitative analysis of 3D tissue architecture. *eLife*, 4(DECEMBER2015), pp.1–29.
- Mortera-Blanco, T. et al., 2012. Ex vivo Mimicry of Normal and Abnormal Human Hematopoiesis. *J Vis Exp*, (62).
- Mortera-Blanco, T. et al., 2011. Long-term cytokine-free expansion of cord blood mononuclear cells in three-dimensional scaffolds. *Biomaterials*, 32(35), pp.9263–9270.
- Mortera-Blanco, T.M., 2008. Development of an ex vivo three dimensional (3-D) model of acute myeloid leukaemia (AML). , (October). Available at: <http://ethos.bl.uk/OrderDetails.do?uin=uk.bl.ethos.513385>.
- Müller, E. et al., 2016. Distinguishing autocrine and paracrine signals in hematopoietic stem cell culture using a biofunctional microcavity platform. *Scientific Reports*, 6(1), p.31951. Available at: <http://www.nature.com/articles/srep31951>.
- Muta, K. et al., 1995. Stem cell factor retards differentiation of normal human erythroid progenitor cells while stimulating proliferation. *Blood*, 86(2), pp.572–580.
- Muth, C.A. et al., 2013. Regulation of Hematopoietic Stem Cell Behavior by the Nanostructured Presentation of Extracellular Matrix Components. *PLoS ONE*, 8(2).
- Neildez-Nguyen, T.M.A. et al., 2002. Human erythroid cells produced ex vivo at large scale differentiate into red blood cells in vivo. *Nature Biotechnology*, 20(5), pp.467–472.
- Nelson, M.R. & Roy, K., 2016. Bone-marrow mimicking biomaterial niches for studying hematopoietic stem and progenitor cells. *J. Mater. Chem. B*, 3490(4), pp.3490–3503. Available at: <http://dx.doi.org/10.1039/C5TB02644J>.
- Niklason, L.E. et al., 2010. Enabling tools for engineering collagenous tissues integrating bioreactors, intravital imaging, and biomechanical modeling. *Proceedings of the National Academy of Sciences of the United States of America*, 107(8), pp.3335–9. Available at:

- <http://www.pnas.org.ezp-prod1.hul.harvard.edu/content/107/8/3335>.
- Nilsson, S.K. et al., 1998. Immunofluorescence Characterization of Key Extracellular Matrix Proteins in Murine Bone Marrow In Situ. *The Journal of Histochemistry & Cytochemistry*, 46(3), pp.371–377.
- Nombela-Arrieta, C. et al., 2013. Quantitative imaging of haematopoietic stem and progenitor cell localization and hypoxic status in the bone marrow microenvironment. *Nature cell biology*, 15(5), pp.533–43. Available at: <http://www.ncbi.nlm.nih.gov/pubmed/23624405>.
- Ntziachristos, V., 2006. Fluorescence Molecular Imaging. *Http://Dx.Doi.Org/10.1146/Annurev.Bioeng.8.061505.095831*.
- Ntziachristos, V., 2010. Going deeper than microscopy: the optical imaging frontier in biology. *Nature methods*, 7(8), pp.603–614. Available at: <http://dx.doi.org/10.1038/nmeth.1483>.
- Pallotta, I. et al., 2011. Study of Megakaryocytes and Functional Platelet Production Using Silk-Based Vascular Tubes. *Tissue Engineering Part C: Methods*, 17(12), pp.1223–1232. Available at: <http://www.ncbi.nlm.nih.gov/pmc/articles/PMC3226422/pdf/ten.tec.2011.0134.pdf>.
- Palsson, B.O. et al., 1993. Expansion of human bone marrow progenitor cells in a high cell density continuous perfusion system. *Biotechnology (NY)*, 11(3), pp.368–372.
- Pampaloni, F., Reynaud, E.G. & Stelzer, E.H.K., 2007. The third dimension bridges the gap between cell culture and live tissue. *Nature reviews. Molecular cell biology*, 8(10), pp.839–845.
- Panoskaltis, N. et al., 2012. No Title. *Patent*, WO 2012/06.
- Parmar, K. et al., 2007. Distribution of hematopoietic stem cells in the bone marrow according to regional hypoxia. *Proceedings of the National Academy of Sciences of the United States of America*, 104(13), pp.5431–5436. Available at: <http://www.ncbi.nlm.nih.gov/pmc/articles/PMC1838452/%5Chttp://www.ncbi.nlm.nih.gov/pmc/articles/PMC1838452/pdf/zpq5431.pdf>.
- Paul, S.M. et al., 2010. How to improve R&D productivity: the pharmaceutical industry's grand challenge. *Nature Review Drug Discovery*, 9, pp.203–214.
- Paul Ducheyne, Kevin Healy, Dietmar E. Hutmacher, David W. Grainger, C.J.K., 2015. *Comprehensive Biomaterials, Volume 1*,
- Peng, W., Unutmaz, D. & Ozbolat, I.T., 2016. Bioprinting towards Physiologically Relevant Tissue Models for Pharmaceuticals. *Trends in Biotechnology*, 34(9), pp.722–732. Available at: <http://dx.doi.org/10.1016/j.tibtech.2016.05.013>.
- Placzek, M.R. et al., 2009. Stem cell bioprocessing: fundamentals and principles. *Journal of the Royal Society, Interface / the Royal Society*, 6(32), pp.209–32. Available at: <http://rsif.royalsocietypublishing.org/content/6/32/209>.
- Preibisch, S., Saalfeld, S. & Tomancak, P., 2009. Globally optimal stitching of tiled 3D microscopic image acquisitions. *Bioinformatics*, 25(11), pp.1463–1465.
- Rappold, I. et al., 1997. Functional and Phenotypic Characterization of Cord Blood and Bone Marrow Subsets Expressing FLT3 (CD135) Receptor Tyrosine Kinase. *Blood*, 90(1), pp.111–125.
- Ratcliffe, E. et al., 2012. A novel automated bioreactor for scalable process optimisation of haematopoietic stem cell culture. *Journal of Biotechnology*, 161(3), pp.387–390. Available at: <http://dx.doi.org/10.1016/j.jbiotec.2012.06.025>.
- Rende, M. et al., 2013. Biology Of Mixed Phenotype Acute Leukemia In Successful Long-Term Cytokine-Free Three-Dimensional (3D) Static and Perfused 3D Hollow-Fibre Bioreactor Culture. *Blood*, 122, p.2603.
- Reya, T. et al., 2001. Stem cells, cancer, and cancer stem cells. *Nature*, 414(6859), pp.105–111.
- Rnjak-Kovacina, J. et al., 2014. Arrayed hollow channels in silk-based scaffolds provide functional outcomes for engineering critically sized tissue constructs. *Advanced Functional Materials*, 24(15), pp.2188–2196.
- Rodenhizer, D. et al., 2016. A three-dimensional engineered tumour for spatial snapshot analysis of cell metabolism and phenotype in hypoxic gradients. *Nature materials*, 15(2), pp.227–34. Available at: <http://www.nature.com/doi/finder/10.1038/nmat4482%5Chttp://www.ncbi.nlm.nih.gov/pubmed/26595121%5Chttp://www.ncbi.nlm.nih.gov/pubmed/26595121>.
- Rousseau, G.F., Giarratana, M.C. & Douay, L., 2014. Large-scale production of red blood cells from stem cells: what are the technical challenges ahead? *Biotechnology journal*, 9(1), pp.28–38.

- Available at: <http://www.ncbi.nlm.nih.gov/pubmed/24408610>.
- Santos, S.B. Dos et al., 2016. Early Erythroid Development Is Enhanced with Hypoxia and Terminal Maturation with Normoxia in a 3D Ex Vivo Physiologic Erythropoiesis Model. *Blood*, 128, p.2453.
- Scannell, J.W. et al., 2012. Diagnosing the decline in pharmaceutical R&D efficiency. *Nature Reviews Drug Discovery*, 11, pp.191–200.
- Schaefer, A., Fane, A. & Waite, T., 2005. *Nanofiltration Principles and Applications*, Elsevier Science.
- Schindelin, J. et al., 2012. Fiji: an open-source platform for biological-image analysis. *Nature Methods*, 9(7), pp.676–682. Available at: <http://www.nature.com/doi/10.1038/nmeth.2019>.
- Schmal, O. et al., 2016. Hematopoietic stem and progenitor cell expansion in contact with mesenchymal stromal cells in a hanging drop model uncovers disadvantages of 3D culture. *Stem Cells International*, 2016.
- Schofield, R., 1978. The relationship between the spleen colony-forming cell and the haemopoietic stem cell. *Blood Cells*, 4(1–2), pp.7–25.
- Schoutens, A., 1993. *Bone circulation and vascularization in normal and pathological conditions*. ASI series., Plenum Press.
- Serafini, M. et al., 2007. Hematopoietic reconstitution by multipotent adult progenitor cells: precursors to long-term hematopoietic stem cells. *J Exp Med*, 204(1), pp.129–139.
- Severn, C.E. et al., 2016. Polyurethane scaffolds seeded with CD34(+) cells maintain early stem cells whilst also facilitating prolonged egress of haematopoietic progenitors. *Scientific reports*, 6(May), p.32149. Available at: <http://www.ncbi.nlm.nih.gov/pubmed/27573994><http://www.pubmedcentral.nih.gov/articlerender.fcgi?artid=PMC5004174>.
- Sharma, M.B., Limaye, L.S. & Kale, V.P., 2012. Mimicking the functional hematopoietic stem cell niche in vitro: Recapitulation of marrow physiology by hydrogel-based three-dimensional cultures of mesenchymal stromal cells. *Haematologica*, 97(5), pp.651–660.
- Sheu, J. et al., 2015. Large-scale production of lentiviral vector in a closed system hollow fiber bioreactor. *Molecular therapy. Methods & clinical development*, 2(April), p.15020. Available at: <http://www.nature.com/articles/mtm201520>.
- Shiozawa, Y. et al., 2010. Erythropoietin couples hematopoiesis with bone formation. *PLoS ONE*, 5(5).
- Silber, R., LoBue, J. & Gordon, A.S., 1978. Factors thought to contribute to the regulation of egress of cells from marrow. In *The year in hematology*. New York: Plenum Press, p. 243.
- Silberstein, L. et al., 2016. Proximity-Based Differential Single-Cell Analysis of the Niche to Identify Stem/Progenitor Cell Regulators. *Cell Stem Cell*, 19(4), pp.530–543.
- Singbrant, S. et al., 2011. Erythropoietin couples erythropoiesis, B-lymphopoiesis, and bone homeostasis within the bone marrow microenvironment. *Blood*, 117(21), pp.5631–5642.
- Škrtić, M. et al., 2011. Inhibition of Mitochondrial Translation as a Therapeutic Strategy for Human Acute Myeloid Leukemia. *Cancer Cell*, 20(5), pp.674–688.
- Souid, A.K. et al., 2003. Immediate effects of anticancer drugs on mitochondrial oxygen consumption. *Biochemical Pharmacology*, 66(6), pp.977–987.
- Spencer, J.A. et al., 2014. Direct measurement of local oxygen concentration in the bone marrow of live animals. *Nature*, 508(7495), pp.269–73. Available at: <http://www.nature.com/doi/10.1038/nature13034><http://www.pubmedcentral.nih.gov/articlerender.fcgi?artid=3984353&tool=pmcentrez&rendertype=abstract>.
- Sundaramurthy, V. et al., 2014. Deducing the mechanism of action of compounds identified in phenotypic screens by integrating their multiparametric profiles with a reference genetic screen. *Nature protocols*, 9, pp.474–90. Available at: <http://www.ncbi.nlm.nih.gov/pubmed/24481274>.
- Takaku, T. et al., 2010. Hematopoiesis in three dimensions: human and murine bone marrow architecture visualized by confocal microscopy. *Blood*, 116(15), pp.41–55. Available at: <http://www.ncbi.nlm.nih.gov/pubmed/20647571>.
- Tamir, A. et al., 2000. Stem cell factor inhibits erythroid differentiation by modulating the activity of G1-cyclin-dependent kinase complexes: a role for p27 in erythroid differentiation coupled G1 arrest. *Cell growth & differentiation: the molecular biology journal of the American Association*

- for *Cancer Research*, 11(5), pp.269–277.
- Thon, J.N. et al., 2014. Platelet bioreactor-on-a-chip. *Blood*, 124(12), pp.1857–1868.
- Timmins, N.E. et al., 2011. Ultra-High-Yield Manufacture of Red Blood Cells from Hematopoietic Stem Cells. *Tissue Engineering Part C Methods*, 17(11), pp.1131–1137.
- Timmins, N.E. & Nielsen, L.K., 2009. Blood cell manufacture: current methods and future challenges. *Trends in Biotechnology*, 27(7), pp.415–422.
- Toh, Y.C., Xing, J. & Yu, H., 2015. Modulation of integrin and E-cadherin-mediated adhesions to spatially control heterogeneity in human pluripotent stem cell differentiation. *Biomaterials*, 50(1), pp.87–97. Available at: <http://dx.doi.org/10.1016/j.biomaterials.2015.01.019>.
- Tordjman, R. et al., 2001. Erythroblasts are a source of angiogenic factors. *Blood*, 97(7), pp.1968–1974.
- Torisawa, Y. et al., 2014. Bone marrow-on-a-chip replicates hematopoietic niche physiology in vitro. *Nature methods*, 11(6), pp.663–9. Available at: <http://www.ncbi.nlm.nih.gov/pubmed/24793454>.
- Trakarnsanga, K. et al., 2017. An immortalized adult human erythroid line facilitates sustainable and scalable generation of functional red cells. *Nature Communications*, 8(May 2016), p.14750. Available at: <http://www.nature.com/doi/10.1038/ncomms14750>.
- Usuludin, S.B.M., Cao, X. & Lim, M., 2012. Co-culture of stromal and erythroleukemia cells in a perfused hollow fiber bioreactor system as an in vitro bone marrow model for myeloid leukemia. *Biotechnology and Bioengineering*, 109(5), pp.1248–1258.
- Ventura Ferreira, M.S. et al., 2016. An engineered multicomponent bone marrow niche for the recapitulation of hematopoiesis at ectopic transplantation sites. *Journal of hematology & oncology*, 9(1), p.4. Available at: <http://www.pubmedcentral.nih.gov/articlerender.fcgi?artid=4727380&tool=pmcentrez&rendertype=abstract>.
- Ventura Ferreira, M.S. et al., 2012. Cord blood-hematopoietic stem cell expansion in 3D fibrin scaffolds with stromal support. *Biomaterials*, 33(29), pp.6987–6997.
- Wagner, B.A., Venkataraman, S. & Buettner, G.R., 2011. The rate of oxygen utilization by cells. *Free Radical Biology and Medicine*, 51(3), pp.700–712. Available at: <http://dx.doi.org/10.1016/j.freeradbiomed.2011.05.024>.
- Wagner, W. et al., 2007. Molecular and secretory profiles of human mesenchymal stromal cells and their abilities to maintain primitive hematopoietic progenitors. *Stem cells*, 25(10), pp.2638–2647.
- Wang, T.Y. & Wu, J.H., 1992. A continuous perfusion bioreactor for long-term bone marrow culture. *Ann N Y Acad Sci*, 665, pp.274–284.
- Wagh, R.E. & Sassi, M., 1986. An in vitro model of erythroid egress in bone marrow. *Blood*, 68(1), pp.250–257.
- Webber, M.J. et al., 2015. A Perspective on the Clinical Translation of Scaffolds for Tissue Engineering. *Annals of Biomedical Engineering*, 43(3), pp.641–656.
- Weiss, L., 1983. Studies on the Organization and Regeneration of Bone Marrow: Origin, Growth, and Differentiation of Endocloned Hematopoietic Colonies. , 392, pp.369–392.
- Weiss, L., 1965. The structure of bone marrow. Functional interrelationships of vascular and hematopoietic compartments in experimental hemolytic anemia: An electron microscopic study. *Journal of Morphology*, 117(3), pp.467–537.
- Weiss, R.H.L. and L., 1984. A Model of Intramedullary Hematopoietic Microenvironments Based on Stereologic Study of the Distribution of Endocloned Marrow Colonies. *Blood*, 63(2), pp.287–297.
- Weissleder, R. & Nahrendorf, M., 2015. Advancing biomedical imaging. *Proceedings of the National Academy of Sciences*, 112(47), pp.14424–14428. Available at: <http://www.pnas.org/content/112/47/14424.short%5Cnhttp://www.pnas.org/lookup/doi/10.1073/pnas.1508524112>.
- Whitaker, B.I. & Henry, R.A., 2012. *The 2011 National Blood Collection and Utilization Survey Report*,
- Williams, D.A. et al., 1991. Fibronectin and VLA-4 in haematopoietic stem cell-microenvironment interactions. *Nature*, 352(6334), pp.438–41. Available at: <http://www.ncbi.nlm.nih.gov/pubmed/1861722>.

- Xia, H. et al., 2016. A high-throughput microfluidic approach for 1000-fold leukocyte reduction of platelet-rich plasma. *Scientific Reports*, 6(October), p.35943. Available at: <http://www.nature.com/articles/srep35943>.
- Yin, X. et al., 2016. Engineering Stem Cell Organoids. *Cell Stem Cell*, 18(1), pp.25–38. Available at: <http://dx.doi.org/10.1016/j.stem.2015.12.005>.
- Yokoyama, T. et al., 2003. Migration of erythroblastic islands toward the sinusoid as erythroid maturation proceeds in rat bone marrow. *The Journal of veterinary medical science / the Japanese Society of Veterinary Science*, 65(4), pp.449–52. Available at: <http://www.ncbi.nlm.nih.gov/pubmed/12736425>.
- Zhang, B. et al., 2016. Biodegradable scaffold with built-in vasculature for organ-on-a-chip engineering and direct surgical anastomosis. *Nature Materials*, 1(March), pp.1–42. Available at: <http://www.nature.com/doi/10.1038/nmat4570>.
- Zhu, J. & Emerson, S.G., 2002. Hematopoietic cytokines, transcription factors and lineage commitment. *Oncogene*, 21(21), pp.3295–3313.

11. Figure reprint permission

Table 15: Summary of figure reprint permissions.
with e-mailed permissions underneath.

| Figure # | Page # | Publication Reproduced | Reprint Permissions |
|----------|--------|---------------------------------------|--------------------------------------|
| 1 | 2 | (U.S. National Cancer Institute 2017) | Free use for academic non-profit. |
| 2 | 5 | (Mendelson & Frenette 2014) | Permission granted no. 4167031508028 |
| 7 | 15 | (Neildez-Nguyen et al. 2002) | Permission granted no. 4167110865457 |
| | | (Giarratana et al. 2011) | Permission attached below (06/09/17) |
| 8 | 23 | (Jing et al. 2010) | Permission attached below (11/09/17) |
| | | (Ventura Ferreira et al. 2016) | Free use for academic non-profit. |
| | | (Di Buduo et al. 2015) | Permission attached below (06/09/17) |
| 9 | 28 | (Lassailly et al. 2013) | Permission attached below (06/09/17) |
| | | (Nombela-Arrieta et al. 2013) | Permission granted no. 4178880107972 |
| | | (Kolesky et al. 2016) | Permission attached below (01/09/17) |




Mon 11/09/2017 15:00

Lorella Ripari <l.ripari@haematologica.org>

Re: Rights/Permissions: Reuse within Academic Thesis

To: Allenby, Mark

 We removed extra line breaks from this message.

Dear Mr. Allenby,
please use this mail as a permission granted to your needs.

To whom it may concern:

we herewith grant permission to re-use the figure cited in your message below free of charge: this publication is intended for no-profit use. Any other use is discouraged and it will remain under copyright laws of the Ferrata Storti Foundation, Pavia, Italy. You are also obliged to correctly quote the original article reference.

Best regards

Lorella Ripari
Haematologica Journal Office
c/o Fondazione Ferrata Storti
Via Belli 4
27100 Pavia, Italy
Phone: +39.0382.27129
Fax: +39.0382.394705

www.haematologica.org

> Dear Hematologica Editorial and Production Office,
>
> I would like to request rights and permissions to use Figure 1 of your publication:
>
> "Hematopoietic Stem Cells In Co-Culture With Mesenchymal Stromal Cells - Modeling The Niche Compartments In Vitro"
>
> DOI: "10.3324/haematol.2009.010736"
>
> Within an electronic thesis. This will be an academic thesis, and not for commercial use. Would this be possible?
>



Wed 06/09/2017 19:17

Blood Permissions <bloodpermissions@hematology.org>

RE: Rights/Permissions: Reuse within Academic Thesis

To: Allenby, Mark

Dear Mark,

Thank you again for contacting Blood.

You have permission to reuse the figure noted below for your thesis.

Kind regards,

Pat Baggott

From: Allenby, Mark [<mailto:mark.allenby@imperial.ac.uk>]

Sent: Thursday, August 31, 2017 5:14 AM

To: Blood Permissions <bloodpermissions@hematology.org>

Cc: Allenby, Mark <mark.allenby@imperial.ac.uk>

Subject: Rights/Permissions: Reuse within Academic Thesis

Dear American Society of Hematology and Blood Editorial and Production Office,

I would like to request rights and permissions to use Figure 1J of your publication:

“Multimodal imaging reveals structural and functional heterogeneity in different bone marrow compartments: functional implications on hematopoietic stem cells”

DOI: “10.1182/blood-2012-11-467498”

Volume: 122, Issue No.: 10, Pages: 1730-1740, Date: 2013

Authors: Francois Lassailly, Katie Foster, Lourdes Lopez-Onieva, Erin Currie and Dominique Bonnet

Within my electronic thesis, entitled, “Development of a bio-inspired *in silico-in vitro* platform: towards personalised healthcare through optimisation of a bone-marrow mimicry bioreactor”. This will be a nonprofit academic thesis, and not for commercial use. Would this be possible?

Thank you for your help, kind regards,

Mark Allenby, PhD Candidate
Biological Systems Engineering Laboratory
Department of Chemical Engineering
South Kensington Campus, SW7 2BZ



Wed 06/09/2017 19:17

Blood Permissions <bloodpermissions@hematology.org>

RE: Rights/Permissions: Reuse within Academic Thesis

To Allenby, Mark

Dear Mark,

Thank you again for contacting Blood.

You have permission to reuse the figure noted below for your thesis.

Kind regards,

Pat Baggott

Patrick Baggott
Sr. Manager, Publications
American Society of Hematology
2021 L Street, NW
Suite 900
Washington, DC 20036
pbaggott@hematology.org

www.bloodadvances.org
www.bloodjournal.org
www.ashclinicalnews.org
www.hematology.org

From: Allenby, Mark [<mailto:mark.allenby@imperial.ac.uk>]
Sent: Thursday, August 31, 2017 5:14 AM
To: Blood Permissions <bloodpermissions@hematology.org>
Cc: Allenby, Mark <mark.allenby@imperial.ac.uk>
Subject: Rights/Permissions: Reuse within Academic Thesis

Dear American Society of Hematology and Blood Editorial and Production Office,

I would like to request rights and permissions to use Figure 5 of your publication:

“Programmable 3D silk bone marrow niche for platelet generation ex vivo and modeling of megakaryopoiesis pathologies”

DOI: 10.1182/blood-2017-08-167100



Wed 06/09/2017 19:15

Blood Permissions <bloodpermissions@hematology.org>

RE: Rights/Permissions: Reuse within Academic Thesis

To: Allenby, Mark

Dear Mark,

Thank you for contacting Blood.

You have permission to reuse figures 1 and 4 as noted below.

Kind regards,

Pat Baggott

Patrick Baggott
Sr. Manager, Publications
American Society of Hematology
2021 L Street, NW
Suite 900
Washington, DC 20036
pbaggott@hematology.org

www.bloodadvances.org

www.bloodjournal.org

www.ashclinicalnews.org

www.hematology.org

From: Allenby, Mark [<mailto:mark.allenby@imperial.ac.uk>]
Sent: Thursday, August 31, 2017 5:13 AM
To: Blood Permissions <bloodpermissions@hematology.org>
Cc: Allenby, Mark <mark.allenby@imperial.ac.uk>
Subject: Rights/Permissions: Reuse within Academic Thesis

Dear American Society of Hematology and Blood Editorial and Production Office,

I would like to request rights and permissions to use Figure 1 and Figure 4 of your publication:

“Proof of principle for transfusion of in vitro-generated red blood cells”

DOI: “10.1182/blood-2012-11-467498”

Volume 118, Issue No. 10, Pages 5071-5079, Dec 14, 2011



Fri 01/09/2017 17:41

PNAS Permissions <PNASPermissions@nas.edu>

RE: Rights/Permissions: Reuse within Academic Thesis

To: Allenby, Mark

Action Items

+ Get more add-ins

Permission is granted for your use of the figure as described in your message. Please list a full citation for the PNAS article when re-using the material. Because this material published after 2008, a copyright note is not needed. There is no charge for this material, either. Let us know if you have any questions.

Best regards,
Kay McLaughlin for
Diane Sullenberger
Executive Editor
PNAS

From: Allenby, Mark [<mailto:mark.allenby@imperial.ac.uk>]

Sent: Wednesday, August 30, 2017 1:12 PM

To: PNAS Permissions

Cc: Allenby, Mark

Subject: Rights/Permissions: Reuse within Academic Thesis

Dear Proceedings of the National Academy of Sciences Editorial and Production Office,

I would like to request rights and permissions to use Figure 3E of your publication:

“Three-dimensional bioprinting of thick vascularized tissues”

DOI: “10.1073/pnas.1521342113”

Volume: 113, Issue No.: 12, Date: 02/02/2016

Authors: David B. Kolesky, Kimberly A. Homan, Mark A. Skylar-Scott, Jennifer A. Lewis

Within my electronic thesis, entitled, “Development of a bio-inspired *in silico-in vitro* platform: towards personalised healthcare through optimisation of a bone-marrow mimicry bioreactor”. This will be a nonprofit academic thesis, and not for commercial use. Would this be possible?

Thank you for your help, kind regards,

Mark Allenby, PhD Candidate
Biological Systems Engineering Laboratory
Department of Chemical Engineering
South Kensington Campus, SW7 2AZ
+447447117085
Imperial College London